UNIVERSITÀ DEGLI STUDI DI MILANO

Scuola di Dottorato in Fisica, Astrofisica e Fisica Applicata
Dipartimento di Fisica

Corso di Dottorato in Fisica, Astrofisica e Fisica Applicata
Ciclo XXIX

Angular High-Order Correlation Functions in Cosmology: LSS Bispectrum and CMB Trispectrum

Settore Scientifico Disciplinare FIS/05

Supervisore Interno: Prof. Davide MAINO

Supervisore Esterno: Dott. Emiliano SEFUSATTI

Coordinatore: Prof. Francesco RAGUSA

Tesi di Dottorato di:
Antonino TROJA

Anno Accademico 2016/2017

Commission of the final examination:

Internal Member:
Prof. Davide MAINO

External Member:
Prof. Eiichiro KOMATSU

External Member:
Prof. Benjamin WANDELT

External Member:
Prof. Cristiano PORCIANI

External Referee:
Prof. Licia VERDE

External Referee:
Dr. Michele LIGUORI

External Referee:
Dr. Martin KILBINGER

Final examination:

Date 24/07/2017

Università degli Studi di Milano, Dipartimento di Fisica, Milano, Italy

A te, Odierno Sconosciuto.
E a quel telescopio giallo, senza il quale, oggi, non sarei qui.

Cover illustration:
Illustris Collaboration

MIUR subjects:
FIS/05 - Astronomy and Astrophysics

PACS:
98.80.Es - Observational Cosmology

Contents

List of Figures

Introduction

Motivation

Cosmic Microwave Background radiation (CMB) and the Large Scale Structure of the Universe (LSS) offer a great opportunity to study the primordial physics of the Universe. In fact, although several models have been developed in the last decades, understanding what exactly happened during the very early phase of the Universe is still a high task to accomplish.

The hot Big Bang model allows to explain two of the great discoveries of the last century, the expansion of the Universe and the CMB. Nevertheless, it presents some issue, like the horizon and the flatness problem, that only an accelerated expansion can explain. Inflation provides a mechanism whereby exponential expansion is attained, thus resolving the Hot Big Bang model flaws. Furthermore, it provides the existence of primordial fluctuations that seeded the anisotropies of the CMB and the LSS of galaxies we see today. Unfortunately, several models of inflation was developed, each of them providing the accelerated expansion, but specific fluctuations. The first aim of my work was to understand how to constrain all of these model by means of their forecasts. But this is not the only one.

In fact, CMB allows to understand what the Universe is composed of. Radiation and matter of course, but there are two more evanescent components, called dark matter and dark energy. The first one drove the formation of structure, the latter is the main cause of the accelerated expansion we see today. I wont go into details with dark energy during this thesis, since it is beyond the purpose of my work. Although dark matter and dark energy are so important to understand the physics of the present Universe, it is impossible to observe them directly, since dark matter interacts only gravitationally and dark energy is, so far, only a name for something we totally don't understand. We can derive information about them by studying LSS, thus making ordinary matter a great probe to the dark components.

So, the question is, how can we derive information from CMB and LSS? Lots of statistical methods were developed with this purpose, but there still room for new ones. During my work, I developed an angular bispectrum estimator for the LSS and a Needlet trispectrum for the CMB. Bispectrum and trispectrum are the Fourier counterpart of 3- and 4-points correlation function, thus giving information about the non-Gaussian features of the distribution they are evaluated from. Non-Gaussianity, i.e. any deviation from a Gaussian distribution, is in fact inherited by LSS due to the non-linear clustering of matter, that evolve from an homogeneous lattice of elementary particles in clusters

and filaments. CMB, instead, presents an high level of Gaussianity. But, the possible existence of deviation from Gaussianity in the anisotropies distribution would give hints about what kind of model of inflation best describes the actual physics of the primordial Universe, since each model provides a characteristic non-Gaussianity track in CMB.

Thesis overview

Main results

I based my work well within the spherical function framework. Spherical analysis allows to work with Spherical Harmonics, the orthonormal basis of function on the sphere. Each function on the sphere can be decomposed by Spherical Harmonics, the property of the function are inherited by the Harmonics coefficients, with wich is possible to write the n-points correlation functions and then the polyspectra. Furthermore, I exploit the Spherical Needlet system, a wavelet system on the sphere with properties that make it the closest system to spherical harmonics. The analysis was carried on both on simulations of LSS and CMB with the following results.

Angular Bispectrum of LSS: I derived the bispectrum estimator for simulated spherical shells of LSS. In order to make the estimator more computationally feasible, I derived an optimal binned estimator that allows to evaluate bispectrum on binned intervals of the multipoles. Both bispectrum and its variance were compared to the predicted ones, obtained by integrating the matter 3-dimensional bispectrum over the line-of-sight. The comparison shown that the harmonic bispectrum estimator is quite reliable and it would be interesting to apply to set of real data in order to constrain cosmological parameters.

Needlet Trispectrum of CMB: Trispectrum estimator was developed by means of the Spherical Needlet system. This system works on asymmetric binned intervals of multipoles with a reconstruction formula identical to the Spherical Harmonics one. Furthermore, thanks to their localization property in real space, Spherical Needlets are statistically stronger in presence of missing observation than Spherical Harmonics that, instead, lose their orthonormality introducing bias in the harmonic coefficients and then in the statistics. Needlet trispectrum was used in order to constrain the non-Gaussian parameter g_{NL} with the purpose of constrain non-Gaussianity and then the inflationary models. The results on g_{NL} shown that the estimator is suboptimal but also that it is possible, with a minimum computational effort, to constrain g_{NL} easily in order to test inflation and other g_{NL} estimators.

Organizational note

This thesis is divided into three parts, for a total of 10 chapters. Each part is devoted to the analysis of a different cosmological observable except for Part I. Part I is composed by Chapters 1,2 and 3 where polyspectra and modern cosmology are defined. In Part II, chapters from 4 to 6 analyze the bispectrum of LSS while Part III contains chapters from 7 to 10 with all the work about the Needlet trispectrum of CMB. Each part can be read individually, withouth reading the others. The Chapters are focused on what follows.

Chapter 1: Mathematical definition of polyspectra is given. Estimator of angular power spectrum, bispectrum and trispectrum together with their variance are the main subject of this chapter.

Chapter 2: The Hot Big Bang theory is explained, with a final focus on its flaws and how they were solved by Inflation theory.

Chapter 3: The particle that drove Universe dynamics is analyzed, both the constant part and the fluctuations, inherited by CMB and LSS in later times.

Chapter 4: I reviewed the Linear and non-Linear perturbation theory, showing how non-Gaussianity is implicit in the non-linear evolution of matter. Then I showed that one of the greatest problem in the analysis of the matter distribution is the degeneration of parameters.

Chapter 5: I show how take a spherical field out of a 3-dimensional field by means of an integration along the line of sight, i.e. the redshift coordinate. The prediction of angular power spectrum and bispectrum are developed.

Chapter 6: I show the first results of my work, i.e. the comparison between estimated statistics and predicted ones, with comments about the meaning of this comparison and their consequences.

Chapter 7: Non-Gaussianity in the primordial curvature field is defined by means of the Bardeen's potential and the non-Gaussian parameters f_{NL} and g_{NL} together with the state of the art in their estimation.

Chapter 8: I describe the Spherical Needlet wavelets and their properties, explaining why they are one of the strongest statistics in presence of missing observations.

Chapter 9: By means of the Needlets, a new trispectrum estimator is provided. It takes advantage of the Wick product, which allows to write an unbiased estimator with the lowest one among the estimators of the same orders.

Chapter 10: g_{NL} is estimate on Gaussian and non-Gaussian simulations, with different resolutions. An hyperbolic fit is applied in order to estimate the behavior of the converged covariance matrix withouth reaching convergences and comments on the results are showed.

Appendix a: Some mathematical results is described in order to make the reader aware of some obscure passage within the text.

Part I

Setting Up the Framework

CHAPTER 1

Everything You Always Wanted to Know About Polyspectra* (*But Were Afraid to Ask)

Spherical random fields are of great interest in cosmology. In fact, the two main observables in cosmology, CMB and LSS (when measured photometrically), can be viewed as 2-dimensional fields that can be described as a spherical random fields centered on the observer and randomly distributed accordingly to a probability function. The properties of a random field are due to its probability distribution, which can be fully described by mean of its *moments*. The moments of a distribution describe the shape of the distribution itself. The zeroth-order moment indicates the total probability of the distribution, i.e. 1, the first-order moment is the mean of the distribution, the second one the variance. Then the third-order moment is the skewness, that is the asymmetry of the distribution, and the fourth-order is the kurtosis, parameterizing the relative height of the tails of the distribution. Higher order moments describe other properties that are beyond the aim of this thesis.

When we speak about spherical random fields, we can describe moments using the angular *polyspectra*. The aim of this chapter is to understand the meaning of these moments and their relative angular polyspectra, in order to get a rock-solid base on which develop the models I'll deal with in the rest of this work.

1.1 Definitions

Let's take a zero-mean spherical random field $T(\theta, \phi) \equiv T(\mathbf{n})$. As long as the field is defined over the whole sphere, we can decompose $T(\mathbf{n})$ as well as each function defined on the sphere using the *Spherical Harmonics* $Y_{lm}(\mathbf{n})$. The set of $\{Y_{lm}(\mathbf{n}) : l = 0, 1, 2, \ldots; m = -l, -l+1, \ldots, l-1, l\}$ represents an orthonormal basis on the space of square-integrable function on the sphere $L^2(S^2)$, thus allowing to rewrite every square-integrable function on the sphere as a linear combination of $Y_{lm}(\mathbf{n})$ (Marinucci & Peccati 2011),

$$T(\mathbf{n}) = \sum_{l=0}^{\infty} \sum_{m=-l}^{l} a_{lm} Y_{lm}(\mathbf{n}). \tag{1.1}$$

where the a_{lm} are the *harmonic coefficients* defined by

$$a_{lm} = \int_{S^2} d\Omega \, T(\mathbf{n}) Y^*_{lm}(\mathbf{n}). \tag{1.2}$$

The collection of Spherical Harmonics coefficients $\{a_{lm}\}$ is composed by uncorrelated zero-mean square-integrable complex-valued random variables (Baldi & Marinucci 2006;

Baldi et al. 2007), which are also independent when the probability distribution is Gaussian. The a_{lm}'s contain all the properties of the field from which they are evaluated, thus studying the statistics of a_{lm} means study the physics of the field. The indexes $\{l : l = 0, 1, 2 \dots\}$ are called *multipoles* and are related to the physical angular scale, i.e.

$$\theta = \frac{\pi}{l}. \tag{1.3}$$

Thus, the higher the multipole, the smaller the physical scale of interest. The collection of $\{m : m = -l, \dots, l\}$ represents the azimuthal orientations of the Spherical Harmonics on the sky. Each Spherical Harmonic has $(2l + 1)$ azimuthal orientation, and $m = 0$ represents the azimuthally symmetric Spherical Harmonic,

$$Y_{00}(\theta, \phi) \equiv Y_{00}(\theta). \tag{1.4}$$

The moments of the distribution fully characterize the shape and thus the property of the distribution itself. We can write the nth-order moment as

$$\mu(\mathbf{n}) \equiv \langle (T(\mathbf{n}) - \langle T(\mathbf{n}) \rangle)^n \rangle \tag{1.5}$$

where $\langle \cdot \rangle$ stands for *ensemble average*, i.e. the average of the field among all the possible realizations. It's easy to see that, for zero-mean field, the nth-order moment is nothing but the correlation function of the field. The correlation functions of the field directly depend on the same-order correlation functions of the harmonic coefficient, i.e. inserting eq. (1.1) in eq. (1.5)

$$\langle T_1(x) \cdots T_n(x) \rangle = \sum_{l_1, \dots, l_n} \sum_{m_1, \dots, m_n} \langle a_{l_1 m_1} \cdots a_{l_n m_n} \rangle Y_{l_1 m_1}(x) \cdots Y_{l_n m_n}(x). \tag{1.6}$$

Thus, we need to understand how to calculate the number $\langle a_{l_1 m_1} \cdots a_{l_n m_n} \rangle$. Following (Marinucci & Peccati 2011) it is possible to do this in a mathematical elegant way. Let's first introduce the notion of *strongly isotropic field*.

Definition 1. *Let $T = \{T(\boldsymbol{n}) : \boldsymbol{n} \in S^2\}$ be a real-valued spherical random field. Indicating with $g \cdot \boldsymbol{n} = g\boldsymbol{n}$ the action of g on $\boldsymbol{n}$, that is, $g\boldsymbol{n}$ stands for the position of the point $\boldsymbol{n}$ after the rotation g, the field T is said to be* ***strongly isotropic*** *if, for every $k \in \mathbb{N}$, every $\boldsymbol{n}_1 \dots \boldsymbol{n}_k \in S^3$ and every $g \in SO(3)$ (the group of rotations in $\mathbb{R}^3$) the vectors $\{T(\boldsymbol{n}_1), \dots, T(\boldsymbol{n}_k)\}$ and $\{T(g\boldsymbol{n}_1), \dots, T(g\boldsymbol{n}_k)\}$ have the same finite-dimensional distribution, i.e.*

$$\equiv \{T(\boldsymbol{n}_1), \dots, T(\boldsymbol{n}_k)\} \stackrel{dist}{=} \{T(g\boldsymbol{n}_1), \dots, T(g\boldsymbol{n}_k)\}. \tag{1.7}$$

On large scale, the Universe represent an excellent example of isotropic 3-dimensional field. If we take spherical shells centered on our position of infinitesimal width, the distribution within is actually a strongly isotropic spherical field in the sense of Definition 1. Furthermore, also the CMB represents an outstanding realization of a strongly isotropic spherical field, thus its statistics can be analyzed in view of Definition 1. This considerably simplifies the definitions of the tools I'm going to define.

Consider $n = 1$. In this case $\langle a_{00} \rangle = \langle \bar{T} \rangle$, where $\bar{T}$ is the spatial average of the field T, and it can be proved that the set of $\langle a_{lm} \rangle = 0$ for $l \geq 1$.

Let's consider the $n = 2$ case. A simple proposition comes in help to whomever is trying to define the results of $\langle a_{lm} a_{l'm'} \rangle$,

Proposition 1. *Let T be a strongly isotropic spherical field and $a_{l\cdot} = \{a_{lm} : m = -l, \dots, l\}$ the vector of harmonic coefficients associated with the scale l. Then the following hold*

1. *For all l such that $\langle ||a_{l\cdot}||^2 \rangle < \infty$,*

$$\langle a_{l\cdot} a_{l\cdot} \rangle = C_l I_{2l+1}, \tag{1.8}$$

where C_l is a non-negative constant depending only on l and I_{2l+1} denotes the $(2l+1) \times (2l+1)$ identity matrix. Whenever is well defined, the collection $\{C_l : l \geq 0\}$ is called ***angular power spectrum*** *of the field T.*

2. *For all l_1 and l_2 such that $\langle ||a_{l_1\cdot}||^2 \rangle < \infty$ and $\langle ||a_{l_2\cdot}||^2 \rangle < \infty$*

$$\langle a_{l_1\cdot} a_{l_2\cdot} \rangle = 0_{2l+1}, \tag{1.9}$$

where 0_{2l+1} is the $(2l_1+1) \times (2l_1+1)$ zero matrix.

The proof of Proposition 1 is shown in page 140 of (Marinucci & Peccati 2011). Here it is omitted because the math involved in goes far beyond the aim of this work. Proposition 1 can be summarized by simply writing

$$\langle a_{lm} a^*_{l'm'} \rangle = \delta_l^{l'} \delta_m^{m'} C_l, \tag{1.10}$$

that will be used as angular power spectrum definition hereafter.

For $n \geq 3$, the following theorem defines the form of polyspectra of every order (Marinucci & Peccati 2010),

Theorem 1. *If a random field is strongly isotropic with finite spectral moments of order $n \geq 3$, then for every $l_1, \dots, l_n$ there exist an array $P_{l_1 \dots l_n}(\lambda_1, \dots, \lambda_{n-3})$, with $|l_2 - l_1| \leq \lambda_1 \leq l_2 + l_1$,$|l_3 - \lambda_1| \leq \lambda_2 \leq l_3 + \lambda_1$,...,$|l_{n-2} - \lambda_{n-4}| \leq \lambda_{n-3} \leq l_{n-2} + \lambda_{n-4}$, such that*

$$\langle a_{l_1 m_1} \dots a_{l_n m_n} \rangle = (-1)^{m_n} \sum_{\lambda_1 = |l_2 - l_1|}^{l_2 + l_1} \dots \sum_{\lambda_{n-3}} C^{\lambda_1 \dots \lambda_{n-3} l_n, -m_n}_{l_1 m_1 \dots l_{n-1} m_{n-1}} P_{l_1 \dots l_n}(\lambda_1, \dots, \lambda_{n-3}) \tag{1.11}$$

$$C^{\lambda_1 \dots \lambda_{n-3} l_n, -m_n}_{l_1 m_1 \dots l_{n-1} m_{n-1}} = \sum_{\mu_1} \dots \sum_{\mu_{n-3}} C^{\lambda_1 \mu_1}_{l_1 m_1 l_2 m_2} C^{\lambda_2 \mu_2}_{\lambda_1 \mu_1 l_3 m_3} \dots C^{l_n - m_n}_{\lambda_{n-3} \mu_{n-3} l_{n-1} m_{n-1}} \tag{1.12}$$

with $\mu_n = -\lambda_n, \dots \lambda_n$.

For a fixed $n \geq 2$, the real-valued array $\{P_{l_1 \dots l_n}(\cdot) : l_1 \dots l_n \geq 0\}$ is called the **reduced angular polyspectrum** of order n-1 associated with the underlying strongly isotropic random field.

The $C^{\lambda_i \mu_i}_{l_j m_j l_j m_k}$ are the Clebsh-Gordan coefficients (Messiah 1962; Cohen-Tannoudji et al. 1977). Clebsh-Gordan coefficients arise in quantum mechanics when dealing with summation of angular momenta. Within this framework, $C^{l_3 m_3}_{l_1 m_1 l_2 m_2}$ parametrizes the probability amplitude of obtaining a single particle with angular momentum l_3 and z-projection m_3 as a result of a coupling process between two particle with angular momentum l_1 and l_2 and z-projection m_1 and m_2 respectively (Liboff 1999).

We can rewrite the Clebsh-Gordan coefficients as

$$\begin{pmatrix} l_1 & l_2 & l_3 \\ m_1 & m_2 & m_3 \end{pmatrix} := (-1)^{l_3 + m_3} \frac{1}{\sqrt{2l_3 + 1}} C^{l_3 m_3}_{l_1 - m_1 l_2 - m_2}, \tag{1.13}$$

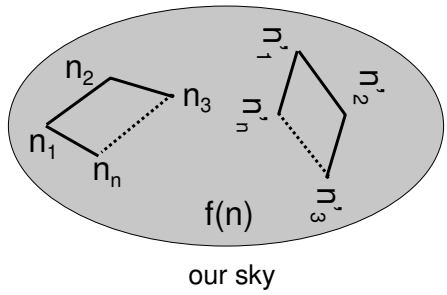

Figure 1.1: The statistical isotropy means that every correlation function in harmonic space is rotationally invariant. The figure shows this principle in real space, the function $f(n)$ is the same in both $\{n_1, n_2, \ldots, n_n\}$ and $\{n'_1, n'_2, \ldots, n'_n\}$ configurations that actually differ only by a roto-traslation (Bartolo et al. 2004).

$$C^{l_3 m_3}_{l_1 m_1 l_2 m_2} = (-1)^{l_1 - l_2 + m_3} \sqrt{2l_3 + 1} \begin{pmatrix} l_1 & l_2 & l_3 \\ m_1 & m_2 & -m_3 \end{pmatrix}. \tag{1.14}$$

The matrix-like object is called *Wigner 3j symbol* (Messiah 1962). It ensures that three multipoles form a closed triangle in harmonic space. In fact Wigner 3j coefficients are non-zero if and only if

$$l_1 + l_2 + l_3 = \text{integer}. \tag{1.15}$$

$$|l_i - l_j| \leq l_k \leq l_i + l_j, \qquad i, j, k = 1, 2, 3, \tag{1.16}$$

$$m_1 + m_2 + m_3 = 0. \tag{1.17}$$

First condition states that the sum of two multipole has to be a multipole itself. Condition (1.16) is the so-called *triangle rule*, ensuring that the three multipoles could form a triangle. The closeness of the triangle is ensured by the fact that the sum of the three orientations has to be zero (condition (1.17)). In the next sections, I'll show how the properties of Wigner 3j makes them the perfect choice when dealing with polyspectra.

Lastly, it must be noted that the strong isotropy of the field imposes a constraint on the form of the n-point correlation function and then on the form of polyspectra (Hu 2001). In fact, if statistical isotropy holds, the n-point correlation function must be invariant under the action of the group $SO(3)$. To see this, let us consider the effect of a rotation $g \in SO(3)$ expressed in terms of the Wigner-D function,

$$Y_{lm}(g\mathbf{n}) = \sum_{m'} D^l_{m'm}(g^{-1}) Y_{l'm'}(\mathbf{n}). \tag{1.18}$$

The action of the rotation on the field is thus

$$\begin{aligned} T(g\mathbf{n}) = \sum_l \sum_m a_{lm} Y_{lm}(g\mathbf{n}) = \sum_l \sum_{mm'} a_{lm} D^l_{m'm}(g^{-1}) Y_{lm'}(\mathbf{n}) = \\ = \sum_l \sum_{m'} a_{lm'} Y_{lm'}(\mathbf{n}) = T(\mathbf{n}), \end{aligned} \tag{1.19}$$

that is

$$a_{lm} = \sum_{m'} D^l_{mm'}(g^{-1}) a_{lm'} \equiv \sum_{m'} D^l_{mm'} a_{lm'}, \tag{1.20}$$

thus, the following identity must hold for every polyspectra with $n \geq 2$ for every rotation $g \in SO(3)$ (fig. 1.1)

$$\langle a_{l_1 m_1} \dots a_{l_n m_n} \rangle = \sum_{m'_1 \dots m'_n} \langle a_{l_1 m'_1} \dots a_{l_n m'_n} \rangle D^{l_1}_{m_1 m'_1} \dots D^{l_n}_{m_n m'_n}. \tag{1.21}$$

1.2 The Angular Power Spectrum

As we already saw, it is possible to write the 2-point correlation function using only the Spherical Harmonics coefficients properties. It is important to remark that if the probability distribution of the random field is Gaussian, then the 2-point correlation function, together with the mean, contains all the statistical properties of the field. The 2-point correlation function, i.e. the variance, is then the only parameter of a Gaussian distribution, while high-order correlation functions vanish. The only way to get non-vanishing higher-order term in the correlation function series is to introduce some non-Gaussianity in the distribution. Therefore, the existence of non-zero connected $n > 2$-order correlation functions is an evidence of the non-Gaussian nature of the distribution. In the next sections, we will see this and how to parametrize the level of non-Gaussianity.

Proposition 1 gives us the form of the 2-point correlation function in harmonic space,

$$\langle a_{lm} a^*_{l'm'} \rangle = \delta^{l'}_{l} \delta^{m'}_{m} C_l \tag{1.22}$$

and we called the sequence $\{C_l : l \in \mathbb{N}\}$ the angular power spectrum of the distribution. Physically, the power spectrum measures the amplitude of the fluctuations at a given scale π/l. The stronger the fluctuation at a given scale the higher the C_l amplitude at the same scale (fig. 1.2).

It is simple to show that eq. (1.22) obeys to the statistical isotropy (eq. (1.21)), i.e:

$$\begin{aligned}
\langle a_{l_1 m_1} a_{l_2 m_2} \rangle &= \sum_{m'_1 m'_2} \langle a_{l_1 m'_1} a_{l_2 m'_2} \rangle D^{l_1}_{m_1 m'_1} D^{l_2}_{m_2 m'_2} = \\
&= C_{l1} \sum_{m'_1 m'_2} (-1)^{m'_2} \delta^{l_2}_{l_1} \delta^{-m'_2}_{m'_1} D^{l_1}_{m_1 m'_1} D^{l_2}_{m_2 m'_2} = \\
&= C_{l_1} \delta^{l_2}_{l_1} \sum_{m'_1} (-1)^{m_1 - m'_1} (-1)^{-m_1} D^{l_1}_{m_1 m'_1} D^{l_2}_{m_2 - m'_1} = \\
&= (-1)^{-m_1} \delta^{l_2}_{l_1} \delta^{m_2}_{-m_1} C_{l_1},
\end{aligned} \tag{1.23}$$

in which I used the orthogonality condition for the Wigner-D functions

$$\sum_{m} (-1)^{m_2 - m} D^{l}_{m_1 m} D^{l}_{-m_2 - m} = \delta^{m_2}_{m_1}. \tag{1.24}$$

Optimal Estimator

An estimator is a method to measure the amplitude of a given quantity using a set of observed data. We define an *optimal estimator* the unbiased estimator with the lowest variance among the others, i.e. closest to the Cramer-Rao bound, expressing the lower bound of the variance of an estimator (Cramér 1946; Rao 1945; Borovkov 1998). Unbiased means that the ensemble average of the estimator is exactly the value of the quantity one

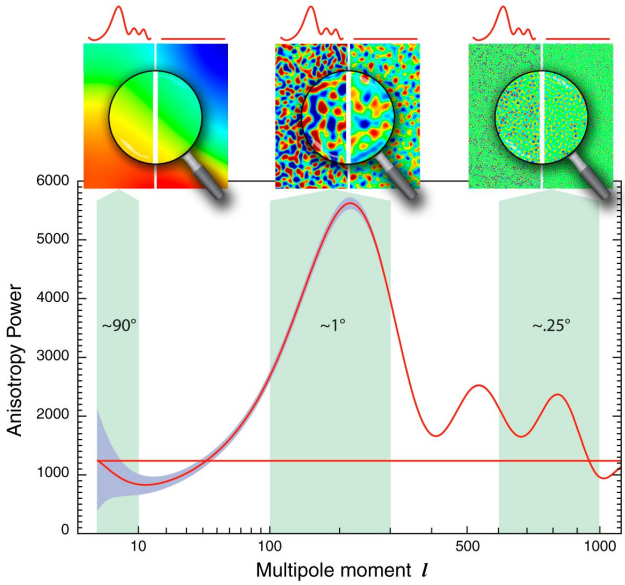

Figure 1.2: The CMB power spectrum (wiggly line) compared to a constant temperature field power spectrum (straight line) (NASA 2012). This image shows how the amplitude of the C_l (on the y-axis) depends on the strength of the fluctuations of the field. The top three images show the fluctuation of the CMB (on the left) and the constant field (on the right) at a given scale, locate in the bottom green region of the angular power spectrum. In the first region, in which $\pi/l \sim 90°$, the amplitude of CMB C_l is lower than that of constant field, this means the the fluctuations in the CMB field are weaker than that of the constant temperature one and this is cleary visible in the above figure in which the CMB fluctuations are smoother than in the constant field case. In the two other region, $\pi/l \sim 1°$ and $\pi/l \sim 0.25°$, we see that the CMB spectrum is higher, then the fluctuation are stronger than the constant temperature case.

wants to measure, i.e. given a quantity f and its estimator $\hat{f}$, the latter is unbiased if and only if $\langle \hat{f} \rangle = f$.

In principle, the optimal estimator for the angular power spectrum is:

$$\hat{C}_l = |a_{lm}|^2. \tag{1.25}$$

In fact, for any value of m we got $\langle \hat{C}_l \rangle = C_l$. Here comes the great issue of this chapter: how is it possible to perform an ensemble average within the real-data framework? Indeed, what we "have" its just one Universe, i.e. only one realization of the sky. We don't have an ensemble of universes among which average the estimator. We can take advantage, again, of the statistical isotropy of the Universe. In fact, isotropy ensures that there is no preferred direction in the sky, thus, since the integers m represent the azimuthal orientation of the spherical harmonics throughout the sphere, we can average the estimators over the collection of $\{m : |m| \leq l\}$, i.e. over different direction in the same sky, obtaining a way to perform ensemble average among different orientation in the sky instead of different sky. Unfortunately, the power of the m-average is reduced by its worst consequence, known as *cosmic variance*: since for low l the number of m is small, we'll have a greater variance as low is the multipole. As l increase, this effect tends to vanish, so that the estimation get more accurate as we go to smaller scales.

After this considerations, we can write the actual optimal estimator for the angular power spectrum as

$$\hat{C}_l = \frac{1}{2l+1} \sum_{m=-l}^{l} |a_{lm}|^2. \tag{1.26}$$

so that $\langle \hat{C}_l \rangle = C_l$ comes immediately introducing the C_l definition in eq. (1.10).

As small as we go with the size of physical scales, i.e. as more as we increase l, the evaluation of $\hat{C}_l$ could become more and more frustrating since we have to evaluate more and more harmonic coefficients ($(2l+1)$ per each l). Luckily, the solution to this "stronger-effort" requirement is quite simple and involve the harmonic transform of the original field. Following (Spergel & Goldberg 1999; Komatsu et al. 2002; Komatsu 2002), we can define the *azimuthally averaged harmonic transform* of the original spherical field

$$e_l(\mathbf{n}) = \sqrt{\frac{4\pi}{2l+1}} \sum_m a_{lm} Y_{lm}(\mathbf{n}) \,. \tag{1.27}$$

Thus, we can rewrite the starting field as

$$T(\mathbf{n}) = \frac{1}{\sqrt{4\pi}} \sum_{l=0}^{\infty} \sqrt{2l+1}\, e_l(\mathbf{n}), \tag{1.28}$$

hence, the field is decomposed by using the set of $e(\mathbf{n})$ that act like a basis, with constant coefficients depending on the multipole l, $\sqrt{2l+1}/\sqrt{4\pi}$. The advantage in the use of the e_l maps is that they are independent on the number of m, since they are an harmonic transformation of the starting field T, thus reducing the calculation effort.

The angular power spectrum estimator thus becomes

$$\hat{C}_l = \int_{S^2} \frac{d\Omega}{4\pi} |e_l(\mathbf{n})|^2, \tag{1.29}$$

i.e., the angular power spectrum is just the spatial average of the e_l^2.

Let's talk about variance. The variance of the C_l estimator is easily to obtain,

$$\begin{aligned}
\mathrm{Var}(\hat{C}_l) &\equiv \langle \hat{C}_l^2 \rangle - \langle \hat{C}_l \rangle^2 \\
&= \frac{1}{(2l+1)^2} \sum_{mm'} \langle a_{lm} a_{lm}^* a_{lm'} a_{lm'}^* \rangle - C_l^2 \\
&= \frac{1}{(2l+1)^2} \sum_{mm'} [\langle a_{lm} a_{lm}^* \rangle \langle a_{lm'} a_{lm'}^* \rangle + \langle a_{lm} a_{lm'}^* \rangle \langle a_{lm'} a_{lm}^* \rangle + \langle a_{lm} a_{lm'} \rangle \langle a_{lm}^* a_{lm'}^* \rangle \\
&+ \langle a_{lm} a_{lm}^* a_{lm'} a_{lm'}^* \rangle_c] - C_l^2 \\
&= \frac{1}{(2l+1)^2} \sum_{mm'} [C_l^2 + C_l \delta_m^{-m'} + C_l \delta_m^{m'} + \langle a_{lm} a_{lm}^* a_{lm'} a_{lm'}^* \rangle_c] - C_l^2 \\
&= \frac{2}{2l+1} C_l^2 + \frac{1}{(2l+1)^2} \sum_{mm'} \langle a_{lm} a_{lm}^* a_{lm'} a_{lm'}^* \rangle_c
\end{aligned}$$

The c subscript stands for *connect*, pointing at the connected 4-point correlation function, i.e. the *trispectrum*. The true meaning of the adjective connected is independent

from lower order statistics. It is important to distinguish between connected and non-connected component when talking about high-order statistics, since the non-Gaussian information about the distribution is stored only into the connected part of the statistics.

If the field is Gaussian, the trispectrum term vanishes and the variance becomes simply:

$$\mathrm{Var}^G(\hat{C}_l) = \frac{2}{2l+1} C_l^2. \tag{1.30}$$

1.3 The Angular Bispectrum

If the fluctuations of the random field have a non-Gaussian distribution, mean and variance are not enough anymore to describe the properties of the distribution. We need to go to higher order of the correlation function, since the higher order moments don't vanish. The lower order moment is the skewness, parametrized by the 3-point correlation function. It's harmonic counterpart is the *angular bispectrum*, which is possible to derive by means of theorem 1,

$$\begin{aligned}\langle a_{l_1 m_1} a_{l_2 m_2} a_{l_3 m_3} \rangle &= (-1)^{m_3} C^{l_3 - m_3}_{l_1 m_1 l_2 m_2} P_{l_1 l_2 l_3} \\ &= (-1)^{m_3} (-1)^{l_1 - l_2 - m_3} \sqrt{2l_3 + 1} \begin{pmatrix} l_1 & l_2 & l_3 \\ m_1 & m_2 & m_3 \end{pmatrix} P_{l_1 l_2 l_3} \\ &= \begin{pmatrix} l_1 & l_2 & l_3 \\ m_1 & m_2 & m_3 \end{pmatrix} B_{l_1 l_2 l_3}\end{aligned} \tag{1.31}$$

$$B_{l_1 l_2 l_3} = (-1)^{l_1 - l_2} \sqrt{2l_3 + 1} P_{l_1 l_2 l_3} \tag{1.32}$$

$B_{l_1 l_2 l_3}$ is the reduced angular bispectrum of the distribution. We already saw the matrix-like object in eqq. (1.13) and (1.14). It is the Wigner 3j coefficient, which role is to ensure that the three multipoles form a closed triangle in harmonic space, thus acting like a delta function. In fact, whenever one of the three condition in eqq. (1.15)-(1.16) is not satisfied, the Wigner 3j vanishes and so do the angular bispectrum. The reason for this behavior is quite simple. The 3-point correlation function measures the excess probability of finding three point of the distribution on the vertex of a triangle, i.e. the strength of fluctuations on triangular configurations. So we must have three multipoles that not only are able to from a triangle, but also they are oriented in such a way that the triangle is closed (fig. 1.3). Wigner 3j conditions (1.16) and (1.17) impose exactly this two statements respectively.

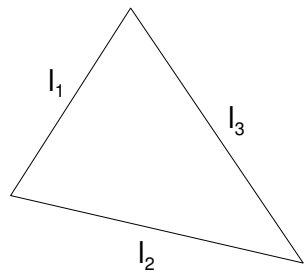

Figure 1.3: One admissible angular bispectrum configuration. Only when the three multipoles form a triangle in harmonic space the bispectrum doesn't vanish.

Altough the bispectrum is the first high-order statistics, it identifies with its connected part. In fact, since $\langle a_{lm}\rangle = 0$, we've got

$$\begin{aligned}\langle a_{l_1m_1}a_{l_2m_2}a_{l_3m_3}\rangle &= (\langle a_{l_1m_1}\rangle\langle a_{l_2m_2}a_{l_3m_3}\rangle + 2 \text{ cyc.}) + \langle a_{l_1m_1}a_{l_2m_2}a_{l_3m_3}\rangle_c \\ &= \langle a_{l_1m_1}a_{l_2m_2}a_{l_3m_3}\rangle_c\end{aligned} \tag{1.33}$$

It can be shown that, if the field is strongly isotropic, the 3-point correlation function could be written as (Hu 2001; Marinucci 2005, 2006)

$$\langle a_{l_1m_1}a_{l_2m_2}a_{l_3m_3}\rangle = \mathcal{G}\{l_1, m_1; l_2, m_2; l_3, m_3\} \times b_{l_1l_2l_3} \tag{1.34}$$

where $b_{l_1l_2l_3}$ is a real symmetric function of only the 3 multipoles (l_1, l_2, l_3). $\mathcal{G}$ is the *Gaunt integral* defined as follows

$$\begin{aligned}&\mathcal{G}\{l_1, m_1; \ldots; l_nm_n\} = \int_{S^2} Y_{l_1m_1}(x)\ldots Y_{l_nm_n}(x)dx \\ &= (-1)^{m_n}\sqrt{\frac{(2l_1+1)\cdots(2l_n+1)}{(4\pi)^{n-2}(2l_n+1)}}\sum_{\lambda_1\ldots\lambda_{n-3}} C^{\lambda_1 0}_{l_1 0 l_2 0}\cdots C^{l_n 0}_{\lambda_{n-3}0l_{n-1}0} \\ &\times \sum_{\mu_1\ldots\mu_{n-3}} C^{\lambda_1\mu_1}_{l_1m_1l_2m_2}\cdots C^{l_nm_n}_{\lambda_{n-3}\mu_{n-3}l_{n-1}m_{n-1}}\end{aligned} \tag{1.35}$$

where the $C^{lm}_{l_1m_1l_2m_2}$ are the Clebsh-Gordan coefficients.

Then, using the definition of Wigner 3j coefficients (eq. 1.14), for n=3

$$\begin{aligned}&\mathcal{G}\{l_1, m_1; l_2m_2; l_3m_3\} = (-1)^{m_3}\sqrt{\frac{(2l_1+1)(2l_2+1)}{4\pi(2l_3+1)}}C^{l_3-m_3}_{l_1m_1l_2m_2}C^{l_30}_{l_10l_20} \\ &= \sqrt{\frac{(2l_1+1)(2l_2+1)(2l_3+1)}{4\pi}}\begin{pmatrix} l_1 & l_2 & l_3 \\ m_1 & m_2 & m_3\end{pmatrix}\begin{pmatrix} l_1 & l_2 & l_3 \\ 0 & 0 & 0\end{pmatrix}\end{aligned} \tag{1.36}$$

So, the function $P_{l_1l_2l_3}$, defined in eq. 1.31, must satisfies the relationship

$$\begin{aligned}P_{l_1l_2l_3} &= b_{l_1l_2l_3}(-1)^{l_1-l_2}\sqrt{2l_3+1}\begin{pmatrix} l_1 & l_2 & l_3 \\ 0 & 0 & 0\end{pmatrix}\sqrt{\frac{(2l_1+1)(2l_2+1)}{4\pi(2l_3+1)}} \\ &= b_{l_1l_2l_3}C^{l_30}_{l_10l_20}\sqrt{\frac{(2l_1+1)(2l_2+1)}{4\pi(2l_3+1)}}\end{aligned} \tag{1.37}$$

and the angular bispectrum (1.32) assumes the form

$$B_{l_1l_2l_3} = \sqrt{\frac{(2l_1+1)(2l_2+1)(2l_3+1)}{4\pi}}\begin{pmatrix} l_1 & l_2 & l_3 \\ 0 & 0 & 0\end{pmatrix}b_{l_1l_2l_3}. \tag{1.38}$$

The difference between $B_{l_1l_2l_3}$ and $b_{l_1l_2l_3}$ is in the geometry of the field, i.e. the presence of regions in which the field is not defined, the shape of this regions and so on. Geometry is contained in $B_{l_1l_2l_3}$, but not in $b_{l_1l_2l_3}$, which contains only informations about the properties of the spherical random field.

Applying the identity 1.21, we can show that the 3-point correlation function calculated above (eq. 1.31) satisfies the statistical isotropy

$$\begin{aligned}
&\langle a_{l_1m_1}a_{l_2m_2}a_{l_3m_3}\rangle = \sum_{m_1'm_2'm_3'}\langle a_{l_1m_1'}a_{l_2m_2'}a_{l_3m_3'}\rangle D^{l_1}_{m_1m_1'}D^{l_2}_{m_2m_2'}D^{l_3}_{m_3m_3'} = \\
&= \sum_{m_1'm_2'm_3'} B_{l_1l_2l_3}\begin{pmatrix} l_1 & l_2 & l_3 \\ m_1' & m_2' & m_3'\end{pmatrix}\sum_{LMM'}\begin{pmatrix} l_1 & l_2 & L \\ m_1 & m_2 & -M\end{pmatrix}\times \\
&\times\begin{pmatrix} l_1 & l_2 & L \\ m_1' & m_2' & -M'\end{pmatrix}(2L+1)(-1)^{M+M'}D^{L}_{MM'}D^{l_3}_{m_3m_3'} = \\
&= \sum_{m_3'LMM'} B_{l_1l_2l_3}\delta^{L}_{l_3}\delta^{-M'}_{m_3'}\begin{pmatrix} l_1 & l_2 & L \\ m_1 & m_2 & -M\end{pmatrix}(-1)^{M+M'}D^{L}_{MM'}D^{l_3}_{m_3m_3'} = \\
&= \sum_{m_3'M} B_{l_1l_2l_3}\begin{pmatrix} l_1 & l_2 & L \\ m_1 & m_2 & -M\end{pmatrix}\sum_{m_3'}(-1)^{M-m_3'}D^{l_3}_{M-m_3'}D^{l_3}_{m_3m_3'} = \\
&= \sum_{m_3'M} B_{l_1l_2l_3}\begin{pmatrix} l_1 & l_2 & L \\ m_1 & m_2 & -M\end{pmatrix}\delta^{-M}_{m_3} = \\
&= B_{l_1l_2l_3}\begin{pmatrix} l_1 & l_2 & L \\ m_1 & m_2 & m_3.\end{pmatrix}
\end{aligned} \tag{1.39}$$

where I used the orthogonality relation (eq. 1.24) and the group multiplication property for Wigner-D function

$$D^{l_1}_{m_1m_1'}D^{l_2}_{m_2m_2'} = \sum_{LMM'}\begin{pmatrix} l_1 & l_2 & L \\ m_1 & m_2 & -M\end{pmatrix}\begin{pmatrix} l_1 & l_2 & L \\ m_1' & m_2' & -M'\end{pmatrix}(2L+1)(-1)^{M+M'}D^{L}_{MM'} \tag{1.40}$$

and the identity

$$\sum_{m_1m_2}\begin{pmatrix} l_1 & l_2 & L \\ m_1 & m_2 & M\end{pmatrix}\begin{pmatrix} l_1 & l_2 & L' \\ m_1' & m_2' & M'\end{pmatrix} = \frac{\delta^{L'}_{L}\delta^{M'}_{M}}{2L+1}. \tag{1.41}$$

1.3.1 Optimal Estimator

Let's multiply each side of eq. (1.31) by a single Wigner 3j coefficient

$$\begin{pmatrix} l_1 & l_2 & l_3 \\ m_1 & m_2 & m_3\end{pmatrix} \tag{1.42}$$

and sum both l.h.s and r.h.s. over the three azimuthal orientation m_1, m_2, m_3 as follows

$$\sum_{m_1m_2m_3}\begin{pmatrix} l_1 & l_2 & l_3 \\ m_1 & m_2 & m_3\end{pmatrix}\langle a_{l_1m_1}a_{l_2m_2}a_{l_3m_3}\rangle = B_{l_1l_2l_3}\sum_{m_1m_2m_3}\begin{pmatrix} l_1 & l_2 & l_3 \\ m_1 & m_2 & m_3\end{pmatrix}^2. \tag{1.43}$$

Introducing the following property of Wigner 3-j coefficients,

$$\sum_{m_1m_2m_3}\begin{pmatrix} l_1 & l_2 & l_3 \\ m_1 & m_2 & m_3\end{pmatrix}^2 = 1, \tag{1.44}$$

we get

$$\sum_{m_1 m_2 m_3} \begin{pmatrix} l_1 & l_2 & l_3 \\ m_1 & m_2 & m_3 \end{pmatrix} \langle a_{l_1 m_1} a_{l_2 m_2} a_{l_3 m_3} \rangle = B_{l_1 l_2 l_3}. \tag{1.45}$$

This is enough to define the optimal estimator for the angular bispectrum,

$$\hat{B}_{l_1 l_2 l_3} = \sum_{m_1 m_2 m_3} \begin{pmatrix} l_1 & l_2 & l_3 \\ m_1 & m_2 & m_3 \end{pmatrix} a_{l_1 m_1} a_{l_2 m_2} a_{l_3 m_3}, \tag{1.46}$$

that is unbiased by definition ($\langle \hat{B}_{l_1 l_2 l_3} \rangle = B_{l_1 l_2 l_3}$ is obvious).

Let's take the azimuthally averaged harmonic transform (eq. 1.27) of the original field in order to rewrite the bispectrum estimator in a more feasible way (Komatsu 2002; Komatsu et al. 2002),

$$\begin{aligned} &\int_{S^2} \frac{d\Omega}{4\pi} \, e_{l_1}(\mathbf{n}) e_{l_2}(\mathbf{n}) e_{l_3}(\mathbf{n}) = \\ &= \sqrt{\frac{(4\pi)^3}{(2l_1+1)(2l_2+1)(2l_3+1)}} \sum_{m_1 m_2 m_3} a_{l_1 m_1} a_{l_2 m_2} a_{l_3 m_3} \mathcal{G}\{l_1, m_1; l_2 m_2; l_3 m_3\} \\ &= \sum_{m_1 m_2 m_3} a_{l_1 m_1} a_{l_2 m_2} a_{l_3 m_3} \begin{pmatrix} l_1 & l_2 & l_3 \\ m_1 & m_2 & m_3 \end{pmatrix} \begin{pmatrix} l_1 & l_2 & l_3 \\ 0 & 0 & 0 \end{pmatrix} \\ &= \hat{B}_{l_1 l_2 l_3} \begin{pmatrix} l_1 & l_2 & l_3 \\ 0 & 0 & 0 \end{pmatrix} \end{aligned} \tag{1.47}$$

So the bispectrum estimator takes in account a map resulting in the multiplication of three e_l, each of them at one of the requested frequency l,

$$\hat{B}_{l_1 l_2 l_3} = \begin{pmatrix} l_1 & l_2 & l_3 \\ 0 & 0 & 0 \end{pmatrix}^{-1} \int_{S^2} \frac{d\Omega}{4\pi} \, e_{l_1}(\mathbf{n}) e_{l_2}(\mathbf{n}) e_{l_3}(\mathbf{n}). \tag{1.48}$$

Equation eq. (1.48) is efficient, because the e_l's can be calculated only once and tabulated in advance, leaving only the integration that is then performed over the whole sphere.

The variance of the bispectrum estimator depends on the *pentaspectrum*, just like the C_l variance that depends on the trispectrum. Let's write the definition of the variance,

$$\begin{aligned} \mathrm{Var}(\widehat{B}_{l_1 l_2 l_3}) &= \langle B^2_{l_1 l_2 l_3} \rangle - \langle B_{l_1 l_2 l_3} \rangle^2 \\ &= \sum_{m_1 m_2 m_3} \sum_{m'_1 m'_2 m'_3} \langle a_{l_1 m_1} a_{l_2 m_2} a_{l_2 m_3} a_{l_1 m'_1} a_{l_2 m'_2} a_{l_2 m'_3} \rangle \\ &\times \begin{pmatrix} l_1 & l_2 & l_3 \\ m_1 & m_2 & m_3 \end{pmatrix} \begin{pmatrix} l_1 & l_2 & l_3 \\ m'_1 & m'_2 & m'_3 \end{pmatrix} - \langle B_{l_1 l_2 l_3} \rangle^2 \end{aligned} \tag{1.49}$$

We can decompose the pentaspectrum as the connected plus the non-connected part (Matarrese et al. 1997; Verde et al. 2000a),

$$\begin{aligned} \langle a_{l_1 m_1} a_{l_2 m_2} a_{l_2 m_3} a_{l_1 m'_1} a_{l_2 m'_2} a_{l_2 m'_3} \rangle &= \langle a_{l_1 m_1} a_{l_2 m_2} \rangle \langle a_{l_2 m_3} a_{l_1 m'_1} \rangle \langle a_{l_2 m'_2} a_{l_2 m'_3} \rangle + 14\text{cyc.} \\ &+ \langle a_{l_1 m_1} a_{l_2 m_2} a_{l_2 m_3} \rangle_c \langle a_{l_1 m'_1} a_{l_2 m'_2} a_{l_2 m'_3} \rangle_c + 9\text{cyc.} \\ &+ \langle a_{l_1 m_1} a_{l_2 m_2} \rangle \langle a_{l_2 m_3} a_{l_1 m'_1} a_{l_2 m'_2} a_{l_2 m'_3} \rangle_c + 14\text{cyc.} \\ &+ \langle a_{l_1 m_1} a_{l_2 m_2} a_{l_2 m_3} a_{l_1 m'_1} a_{l_2 m'_2} a_{l_2 m'_3} \rangle_c \end{aligned} \tag{1.50}$$

Let's consider $(n > 4)$-order polyspectra vanishing, so we are in a quasi-Gaussian regime. The symmetry of ensemble average ($\langle a_{lm} a_{l'm'} \rangle \equiv \langle a_{l'm'} a_{lm} \rangle$) allows us to restrict the calculation to the $l_1 \geq l_2 \geq l_3$ case. We can distinguish three sub-cases:

1. $l_1 > l_2 > l_3$,

$$\mathrm{Var}^{QG}(B_{l_1 l_2 l_3}) = C_{l_1} C_{l_2} C_{l_3} + 3 B^2_{l_1 l_2 l_3};$$

2. $l_1 = l_2 > l_3$,

$$\mathrm{Var}^{QG}(B_{l_1 l_1 l_3}) = C^2_{l_1} C_{l_3} \left[2 + \sum_{mm'} \begin{pmatrix} l_1 & l_1 & l_3 \\ m & -m & 0 \end{pmatrix} \times \begin{pmatrix} l_1 & l_1 & l_3 \\ m' & -m' & 0 \end{pmatrix} \right] + 5 B^2_{l_1 l_1 l_3};$$

Note that when $l_3 = 2l_1$, $\mathrm{Var}^{QG}(B_{l_1 l_1 l_3}) = C^2_{l_1} C_{l_3} [2 + \sqrt{2\pi l_1}/(1 + 4l_1)] + 5 B^2_{l_1 l_1 l_3}$;

3. $l_1 = l_2 = l_3 = l$,

$$\begin{aligned} \mathrm{Var}^{QG}(B_{lll}) &= C^3_l [6 + 9 \sum_{mm'} \begin{pmatrix} l & l & l \\ m & -m & 0 \end{pmatrix} \\ &\quad \times \begin{pmatrix} l & l & l \\ m' & -m' & 0 \end{pmatrix}] + 9 B^2_{l_1 l_2 l_3} \\ &\approx C^3_l [6 + 9 \frac{1.15}{2l + 1}] + 9 B^2_{l_1 l_2 l_3}. \end{aligned}$$

If the field is perfectly Gaussian, also the bispectrum vanishes and the bispectrum variance becomes:

$$\mathrm{Var}^{G}(B_{l_1 l_2 l_3}) \approx s_{123} C_{l_1} C_{l_2} C_{l_3}. \tag{1.51}$$

As long as the Wigner 3j symbols approach 0 as l increases, the above approximation holds. The parameter s_{123} allows to distinguish among scalene, isosceles and equilateral triangle configurations, assuming the values $1, 2$ and 6 respectively. For the sake of simplicity, we can define the product of three C_l with the shape function as $C_{l_1 l_2 l_3}$, thus the variance can be rewritten as

$$\mathrm{Var}^{G}(B_{l_1 l_2 l_3}) = C_{l_1 l_2 l_3}. \tag{1.52}$$

1.4 The Angular Trispectrum

The four-point correlation function contains information about the kurtosis of the distribution, that is, the height of the tails relative to a Gaussian distribution for which the kurtosis vanishes. As we already done for the three-point correlation function, we'll use

theorem 1 in order to derive the structure of the four-point correlation function,

$$\begin{aligned}\langle a_{l_1m_1}a_{l_2m_2}a_{l_3m_3}a_{l_4m_4}\rangle &= (-1)^{m_4}\sum_{L=|l_2-l_1|}^{l_2+l_1} C^{Ll_4-m_4}_{l_1m_1l_2m_2l_3m_3}P_{l_1l_2l_3l_4}(L)\\ &= (-1)^{m_4}\sum_{L}\sum_{M=-L}^{L} C^{LM}_{l_1m_1l_2m_2}C^{l_4-m_4}_{LMl_3m_3}P_{l_1l_2l_3l_4}\\ &= \sum_{LM}(-1)^{l_1-l_2-l_3+L+M}\sqrt{(2L+1)(2l_4+1)}\begin{pmatrix} l_1 & l_2 & L\\ m_1 & m_2 & -M\end{pmatrix}\times\\ &\quad\times\begin{pmatrix} L & l_3 & l_4\\ M & m_3 & m_4\end{pmatrix}P_{l_1l_2l_3l_4}(L)\\ &= \sum_{LM}(-1)^{M}\begin{pmatrix} l_1 & l_2 & L\\ m_1 & m_2 & -M\end{pmatrix}\begin{pmatrix} l_3 & l_4 & L\\ m_3 & m_4 & M\end{pmatrix}Q^{l_1l_2}_{l_3l_4}(L)\end{aligned} \tag{1.53}$$

where, to simplify the notation, I used the following substitution

$$Q^{l_1l_2}_{l_3l_4}(L) = (-1)^{l_1-l_2-l_3+L}\sqrt{(2L+1)(2l_4+1)}P_{l_1l_2l_3l_4}. \tag{1.54}$$

$Q^{l_1l_2}_{l_3l_4}(L)$ is the *angular trispectrum* of the distribution. If you are a keen observer you should have noted that the columns in the second Wigner 3j are different between the last two lines of eq. (1.53). I was allowed to do this because Wigner 3j symbols are invariant for even permutation of columns. This is a choice usually made in literature, in order to have resemblance between the two Wigner 3j symbols in the definition of trispectrum.

Just like the three-point correlation function, the four-point correlation function depends on the Wigner-3j coefficients that reduce the possible combinations of (l_1, l_2, l_3, l_4) to the ones for which the symbols are not vanishing. The four-point correlation function measures the excess probability of finding four point on the vertex of a quadrilateral, i.e. the strength of fluctuation on a quadrilateral configuration. This configuration is univocally identified by one of its diagonal L, which divides the quadrilateral into two adjacent triangles (l_1, l_2, L) and (l_3, l_4, L) (fig. 1.4). That's why two Wigner 3j symbols are present in the definition on the trispectrum: they ensure that the two triangles in which the quadrilateral is split exist and so the quadrilateral. The value of L thus lies in $max(|l_1 - l_2|, |l_3 - l_4|) \leq L \leq min(l_1 + l_2, l_3 + l_4)$. Furthermore, the major hint on the existence of the quadrilateral is given by the m's. In fact, from the first Wigner 3j we have

$$m_1 + m_2 - M = 0$$

while from the second we have

$$m_3 + m_4 + M = 0.$$

Thus

$$m_1 + m_2 + m_3 + m_4 = 0$$

stating that the four multipoles (l_1, l_2, l_3, l_4) must close to form a quadrilateral. It is important to note that the 4-point correlation function results in the sum of the polyspectra of every possible quadrilateral configuration for a given quadruplet (l_1, l_2, l_3, l_4). Indeed, we have got the sum of $Q^{l_1l_2}_{l_3l_4}(L)$ over the diagonal L. Changing L means change the

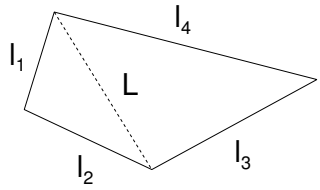

Figure 1.4: Quadrilateral configuration for the angular trispectrum. While the four multipoles (l_1, l_2, l_3, l_4) labelled the side of the quadrilateral, L is the diagonal between (l_1, l_2) and (l_3, l_4).

shape of the quadrilateral without changing its sides, giving birth to brand new quadrilateral on which the trispectrum is evaluated.

It worth noting that the trispectrum is the lowest order statistics for which there exist a non-vanishing non-connected component, i.e. a component due to the lower order statistics. In fact we can write

$$\langle a_{l_1 m_1} a_{l_2 m_2} a_{l_3 m_3} a_{l_4 m_4} \rangle = (\langle a_{l_1 m_1} a_{l_2 m_2} \rangle \langle a_{l_3 m_3} a_{l_4 m_4} \rangle + 2 \text{ cyc.}) + \langle a_{l_1 m_1} \cdots a_{l_4 m_4} \rangle_c. \quad (1.55)$$

For the trispectrum, the non-connected component is fully Gaussian. Furthermore it is non-vanishing if and only if the multipoles are equal in pairs, i.e. $l_1 = l_2$ and $l_3 = l_4$, because of the orhonogal property of the power spectrum (eq. 1.10). It is thus appropriate to distinguish the two components also in the reduced trispectrum, i.e.

$$Q^{l_1 l_2}_{l_3 l_4}(L) = G^{l_1 l_2}_{l_3 l_4}(L) + T^{l_1 l_2}_{l_3 l_4}(L), \quad (1.56)$$

where $G^{l_1 l_2}_{l_3 l_4}(L)$ labels the Gaussian part while $T^{l_1 l_2}_{l_3 l_4}(L)$ the actual trispectrum.

It is easy to show that also the four-point correlation function obeys the statistical

isotropy (eq. 1.21)

$$
\begin{aligned}
\langle a_{l_1 m_1} a_{l_2 m_2} a_{l_3 m_3} a_{l_4 m_4} \rangle &= \sum_{m_1' m_2' m_3' m_4'} \langle a_{l_1 m_1'} \cdots a_{l_4 m_4'} \rangle D^{l_1}_{m_1 m_1'} D^{l_2}_{m_2 m_2'} D^{l_3}_{m_3 m_3'} D^{l_4}_{m_4 m_4'} \\
&= \sum_{m_1' m_2' m_3' m_4'} \sum_{LM} (-1)^M Q^{l_1 l_2}_{l_3 l_4}(L) \begin{pmatrix} l_1 & l_2 & L \\ m_1' & m_2' & -M \end{pmatrix} \begin{pmatrix} l_3 & l_4 & L \\ m_3' & m_4' & M \end{pmatrix} \\
&\times \sum_{L_1 M_1 M_1'} \begin{pmatrix} l_1 & l_2 & L_1 \\ m_1' & m_2' & -M_1' \end{pmatrix} \begin{pmatrix} l_1 & l_2 & L_1 \\ m_1 & m_2 & -M_1 \end{pmatrix} (2L_1+1)(-1)^{M_1+M_1'} D^{L_1}_{M_1 M_1'} \\
&\times \sum_{L_2 M_2 M_2'} \begin{pmatrix} l_3 & l_4 & L_2 \\ m_3' & m_4' & -M_2' \end{pmatrix} \begin{pmatrix} l_3 & l_4 & L_2 \\ m_3 & m_4 & -M_2 \end{pmatrix} (2L_2+1)(-1)^{M_2+M_2'} D^{L_2}_{M_2 M_2'} \\
&= \sum_{LM} (-1)^M Q^{l_1 l_2}_{l_3 l_4}(L) \sum_{L_1 M_1 M_1'} \begin{pmatrix} l_1 & l_2 & L_1 \\ m_1 & m_2 & -M_1 \end{pmatrix} (-1)^{M_1+M_1'} D^{L_1}_{M_1 M_1'} \delta^L_{L_1} \delta^M_{M_1'} \qquad (1.57) \\
&\times \sum_{L_2 M_2 M_2'} \begin{pmatrix} l_3 & l_4 & L_2 \\ m_3 & m_4 & -M_2 \end{pmatrix} (-1)^{M_2+M_2'} D^{L_2}_{M_2 M_2'} \delta^L_{L_2} \delta^M_{-M_2'} \\
&= \sum_{L_1 M_1 M_2} (-1)^{M_1} Q^{l_1 l_2}_{l_3 l_4}(L_1) \begin{pmatrix} l_1 & l_2 & L \\ m_1 & m_2 & -M_1 \end{pmatrix} \begin{pmatrix} l_3 & l_4 & L \\ m_3 & m_4 & -M_2 \end{pmatrix} \\
&\times \sum_M (-1)^{M_2+M} D^L_{M_1 M} D^L_{M_2 -M} \\
&= \sum_{L_1 M_1} (-1)^{M_1} Q^{l_1 l_2}_{l_3 l_4}(L_1) \begin{pmatrix} l_1 & l_2 & L_1 \\ m_1 & m_2 & -M_1 \end{pmatrix} \begin{pmatrix} l_3 & l_4 & L_1 \\ m_3 & m_4 & M_1 \end{pmatrix}.
\end{aligned}
$$

To reach the last line we take advantage of eqq. (1.24), (1.40) and (1.41). Furthermore, we consider that $(-1)^{M_2+M} = (-1)^{-M_2-M}$.

1.4.1 Optimal Estimator

The estimator for $Q_{l_1 l_2 l_3 l_4}(L)$ is obtained by multiplying both l.h.s. and r.h.s of eq. 1.53 for

$$
(-1)^{M'} \begin{pmatrix} l_1 & l_2 & L' \\ m_1 & m_2 & -M' \end{pmatrix} \begin{pmatrix} l_3 & l_4 & L' \\ m_3 & m_4 & M' \end{pmatrix} \qquad (1.58)
$$

and then sum over $\{m_1, m_2, m_3, m_4, M'\}$. Exploiting the Wigner 3j orthonormality relations

$$
\sum_{m_1 m_2 m_3} \begin{pmatrix} l_1 & l_2 & l_3 \\ m_1 & m_2 & m_3 \end{pmatrix}^2 = 1; \qquad (1.59)
$$

$$
(2l_3+1) \sum_{m_1 m_2} \begin{pmatrix} l_1 & l_2 & l_3 \\ m_1 & m_2 & m_3 \end{pmatrix} \begin{pmatrix} l_1 & l_2 & l_3' \\ m_1 & m_2 & m_3' \end{pmatrix} = \delta^{m_3'}_{m_3} \delta^{l_3'}_{l_3}; \qquad (1.60)
$$

$$
\sum_{l_3 m_3} (2l_3+1) \begin{pmatrix} l_1 & l_2 & l_3 \\ m_1 & m_2 & m_3 \end{pmatrix} \begin{pmatrix} l_1 & l_2 & l_3 \\ m_1' & m_2' & m_3 \end{pmatrix} = \delta^{m_1'}_{m_1} \delta^{m_2'}_{m_2}, \qquad (1.61)
$$

the r.h.s of eq. 1.53 reduces as:

$$\begin{aligned}\sum_{LMM'}(-1)^{M+M'}\sum_{m_1m_2}\begin{pmatrix}l_1 & l_2 & L\\ m_1 & m_2 & -M\end{pmatrix}\begin{pmatrix}l_1 & l_2 & L'\\ m_1 & m_2 & -M'\end{pmatrix}\\ \times\sum_{m_3m_4}\begin{pmatrix}l_3 & l_4 & L\\ m_3 & m_4 & M\end{pmatrix}\begin{pmatrix}l_3 & l_4 & L'\\ m_3 & m_4 & M'\end{pmatrix}Q^{l_1l_2}_{l_3l_4}(L)\\ =\frac{Q^{l_1l_2}_{l_3l_4}(L)}{2L+1}\end{aligned} \tag{1.62}$$

and the reduced trispectrum estimator is then:

$$\begin{aligned}\hat{Q}^{l_1l_2}_{l_3l_4}(L)=(2L+1)\sum_{m_1m_2m_3m_4M}(-1)^M\begin{pmatrix}l_1 & l_2 & L\\ m_1 & m_2 & -M\end{pmatrix}\begin{pmatrix}l_3 & l_4 & L\\ m_3 & m_4 & M\end{pmatrix}\\ \times a_{l_1m_1}a_{l_2m_2}a_{l_3m_3}a_{l_4m_4}.\end{aligned} \tag{1.63}$$

It's easy to see that $\langle\hat{Q}^{l_1l_2}_{l_3l_4}(L)\rangle=Q^{l_1l_2}_{l_3l_4}(L)$, thus the estimator is unbiased.

We can rewrite the estimator using the azimuthally averaged harmonic transform of the starting field (eq. 1.27), again for reducing the calculation effort required to estimate the trispectrum. This time we have to deal with a double integration. In fact,

$$\begin{aligned}\int_{S^2}\frac{d\Omega}{4\pi}\,\frac{d\Omega'}{4\pi}\,e_{l_1}(\mathbf{n})e_{l_2}(\mathbf{n})e_{l_3}(\mathbf{n}')e_{l_4}(\mathbf{n}')P_L(\mathbf{n}\cdot\mathbf{n}')=\\ =\sqrt{\frac{(4\pi)^4}{(2l_1+1)(2l_2+1)(2l_3+1)(2l_4+1)}}\frac{4\pi}{2L+1}\sum_{m_1m_2m_3m_4}a_{l_1m_1}a_{l_2m_2}a_{l_3m_3}\\ \times(-1)^M\mathcal{G}\{l_1,m_1;l_2m_2;L,-M\}\mathcal{G}\{l_3,m_3;l_4m_4;LM\},\end{aligned} \tag{1.64}$$

where $P_L(\mathbf{n}\cdot\mathbf{n}')$ is the Legendre polynomial of order L, related to the Spherical Harmonics through the so-called *addition formula*:

$$\sum_M Y^*_{LM}(\mathbf{n})Y_{LM}(\mathbf{n}')=\frac{2L+1}{4\pi}P_L(\mathbf{n}\cdot\mathbf{n}'). \tag{1.65}$$

Expanding the 3-order Gaunt integral, we obtain the form for the integral estimator of the reduced bispectrum

$$\begin{aligned}\int_{S^2}\frac{d\Omega}{4\pi}\,\frac{d\Omega'}{4\pi}\,e_{l_1}(\mathbf{n})e_{l_2}(\mathbf{n})e_{l_3}(\mathbf{n}')e_{l_4}(\mathbf{n}')P_L(\mathbf{n}\cdot\mathbf{n}')=\\ =\begin{pmatrix}l_1 & l_2 & L\\ 0 & 0 & 0\end{pmatrix}\begin{pmatrix}l_3 & l_4 & L\\ 0 & 0 & 0\end{pmatrix}\hat{Q}^{l_1l_2}_{l_3l_4}(L).\end{aligned} \tag{1.66}$$

Since the trispectrum takes into account all of the possible quadrilateral configurations a quadruplet (l_1,l_2,l_3,l_4) can assume, it is more appropriate to write down an estimator that do the same. This aim is reached by performing the sum over the diagonal L of the reduced angular trispectrum estimator:

$$\hat{Q}^{l_1l_2}_{l_3l_4}=\sum_L\hat{Q}^{l_1l_2}_{l_3l_4}(L). \tag{1.67}$$

The integral form of this estimator takes into account only one integral,

$$\begin{aligned}\int_{S^2}\frac{d\Omega}{4\pi}\,e_{l_1}(\mathbf{n})e_{l_2}(\mathbf{n})e_{l_3}(\mathbf{n})e_{l_4}(\mathbf{n}) &= \\ &= \sqrt{\frac{(4\pi)^4}{(2l_1+1)(2l_2+1)(2l_3+1)(2l_4+1)}}\sum_{m_1m_2m_3m_4} a_{l_1m_1}a_{l_2m_2}a_{l_3m_3} \\ &\times \mathcal{G}\{l_1,m_1;l_2m_2;l_3,m_3;l_4,m_4\}.\end{aligned} \tag{1.68}$$

$\mathcal{G}\{l_1,m_1;l_2m_2;l_3,m_3;l_4,m_4\}$ is the fourth-order Gaunt integral, which, following eq. (1.35), assumes the form

$$\begin{aligned}\mathcal{G}\{l_1,m_1;l_2m_2;l_3,m_3;l_4,m_4\} &= \sqrt{\frac{(2l_1+1)(2l_2+1)(2l_3+1)(2l_4+1)}{(4\pi)^4}} \\ &\times \sum_l (2L+1)\begin{pmatrix}l_1 & l_2 & L\\ 0 & 0 & 0\end{pmatrix}\begin{pmatrix}l_3 & l_4 & L\\ 0 & 0 & 0\end{pmatrix} \\ &\times \sum_M (-1)^M \begin{pmatrix}l_1 & l_2 & L\\ m_1 & m_2 & -M\end{pmatrix}\begin{pmatrix}l_3 & l_4 & L\\ m_3 & m_4 & M\end{pmatrix}.\end{aligned} \tag{1.69}$$

Therefore, we get

$$\int_{S^2}\frac{d\Omega}{4\pi}\,e_{l_1}(\mathbf{n})e_{l_2}(\mathbf{n})e_{l_3}(\mathbf{n})e_{l_4}(\mathbf{n}) = \sum_L \begin{pmatrix}l_1 & l_2 & L\\ 0 & 0 & 0\end{pmatrix}\begin{pmatrix}l_3 & l_4 & L\\ 0 & 0 & 0\end{pmatrix} Q^{l_1l_2}_{l_3l_4}(L), \tag{1.70}$$

that is, the integral of the product of four e_l's is just a renormalization of the full trispectrum estimator.

Let's end this section with the variance of the trispectrum estimator,

$$\begin{aligned}\mathrm{Var}(\hat{Q}^{l_1l_2}_{l_3l_4}(L)) &= \langle \hat{Q}^{l_1l_2}_{l_3l_4}(L)^2\rangle - \langle \hat{Q}^{l_1l_2}_{l_3l_4}(L)\rangle^2 \\ &= (2L+1)^2 \sum_{m_1,\ldots,m_4}\sum_{m'_1,\ldots,m'_4}\sum_{MM'} \begin{pmatrix}l_1 & l_2 & L\\ m_1 & m_2 & -M\end{pmatrix}\begin{pmatrix}l_3 & l_4 & L\\ m_3 & m_4 & M\end{pmatrix} \\ &\times \begin{pmatrix}l_1 & l_2 & L\\ m'_1 & m'_2 & -M'\end{pmatrix}\begin{pmatrix}l_3 & l_4 & L\\ m'_3 & m'_4 & M'\end{pmatrix}\langle a_{l_1m_1}\cdots a_{l_4m_4}a_{l_1m'_1}\cdots a_{l_4m'_4}\rangle \\ &- \langle \hat{Q}^{l_1l_2}_{l_3l_4}(L)\rangle^2.\end{aligned} \tag{1.71}$$

The polyspectrum the variance depends on is the *eptaspectrum*, which decomposition using the lower-order statistics is:

$$\begin{aligned}\langle a_{l_1m_1}a_{l_2m_2}a_{l_3m_3}a_{l_4m_4}a_{l_1m'_1}a_{l_2m'_2}a_{l_3m'_3}a_{l_4m'_4}\rangle = & \\ &\langle a_{l_1m_1}a_{l_2m_2}\rangle\langle a_{l_3m_3}a_{l_4m_4}\rangle\langle a_{l_1m'_1}a_{l_2m'_2}\rangle\langle a_{l_3m'_3}a_{l_4m'_4}\rangle + 419 \text{ cyc. perms.} \\ &+ \langle a_{l_1m_1}a_{l_2m_2}\rangle\langle a_{l_3m_3}a_{l_4m_4}\rangle\langle a_{l_1m'_1}a_{l_2m'_2}a_{l_3m'_3}a_{l_4m'_4}\rangle + 419 \text{ cyc. perms.} \\ &+ \langle a_{l_1m_1}a_{l_2m_2}\rangle\langle a_{l_3m_3}a_{l_4m_4}a_{l_1m'_1}\rangle\langle a_{l_2m'_2}a_{l_3m'_3}a_{l_4m'_4}\rangle + 279 \text{ cyc. perms.} \\ &+ \langle a_{l_1m_1}a_{l_2m_2}\rangle\langle a_{l_3m_3}a_{l_4m_4}a_{l_1m'_1}a_{l_2m'_2}a_{l_3m'_3}a_{l_4m'_4}\rangle + 27 \text{ cyc. perms.} \\ &+ \langle a_{l_1m_1}a_{l_2m_2}a_{l_3m_3}\rangle\langle a_{l_4m_4}a_{l_1m'_1}a_{l_2m'_2}a_{l_3m'_3}a_{l_4m'_4}\rangle + 20 \text{ cyc. perms.} \\ &+ \langle a_{l_1m_1}a_{l_2m_2}a_{l_3m_3}a_{l_4m_4}\rangle\langle a_{l_1m'_1}a_{l_2m'_2}a_{l_3m'_3}a_{l_4m'_4}\rangle + 14 \text{ cyc. perms.} \\ &+ \langle a_{l_1m_1}a_{l_2m_2}a_{l_3m_3}a_{l_4m_4}a_{l_1m'_1}a_{l_2m'_2}a_{l_3m'_3}a_{l_4m'_4}\rangle_c.\end{aligned} \tag{1.72}$$

Due to the high number of cyclic permutation, I'll report only the Gaussian component of the variance (see the bispectrum variance eq. 1.51). Again, let's restrict the evaluation of variance to the $l_1 \geq l_2 \geq l_3 \geq l_4$ case and the subsequent cases

1. $l_1 > l_2 > l_3 > l_4$,
$$\mathrm{Var}^G(\hat{Q}^{l_1 l_2}_{l_3 l_4}(L)) = (2L+1) C_{l_1} C_{l_2} C_{l_3} C_{l_4};$$

2. $l_1 = l_2 > l_3 > l_4$,
$$\mathrm{Var}^G(\hat{Q}^{l_1 l_1}_{l_3 l_4}(L)) = (2L+1) C^2_{l_1} C_{l_3} C_{l_4} [2 + \sum_{m_1 m_1'} \begin{pmatrix} l_1 & l_1 & L \\ m_1 & m_1 & 0 \end{pmatrix} \begin{pmatrix} l_1 & l_1 & L \\ m_1' & m_1' & 0 \end{pmatrix}],$$
As well as with the bispectrum variance, we are dealing with a decreasing term in l. From now on, for simplicity reasons, I'll restrict the variance to non-decaying terms;

3. $l_1 = l_2 = l_3 > l_4$,
$$\mathrm{Var}^G(\hat{Q}^{l_1 l_1}_{l_1 l_4}(L)) = 6(2L+1) C^3_{l_1} C_{l_4};$$

4. $l_1 = l_2 = l_3 = l_4 = l$,
$$\mathrm{Var}^G(\hat{Q}^{ll}_{ll}(L)) = 24(2L+1) C^4_{l}.$$
We bump into a situation analogous to that of the bispectrum. We can rewrite variance in the compact form:
$$\mathrm{Var}^G(\hat{Q}^{l_1 l_2}_{l_3 l_4}(L)) = s_{1234}(2L+1) C_{l_1} C_{l_2} C_{l_3} C_{l_4} = (2L+1) C_{l_1 l_2 l_3 l_4}, \tag{1.73}$$
where $s_{l_1 l_2 l_3 l_4} = 1, 2, 6, 24$ depending on the sides of the quadrilateral are different from each other, two equal and two different, three equal and when the quadrilateral is equilateral respectively.

CHAPTER 2

A Very Brief History of Modern Cosmology

At the beginning of past century, the astronomer Edwin Hubble showed that there exist a relation between the radial velocity and the distance of galaxies, and in general, of any object outside the Milky Way (fig. 2.1) (Hubble 1929).

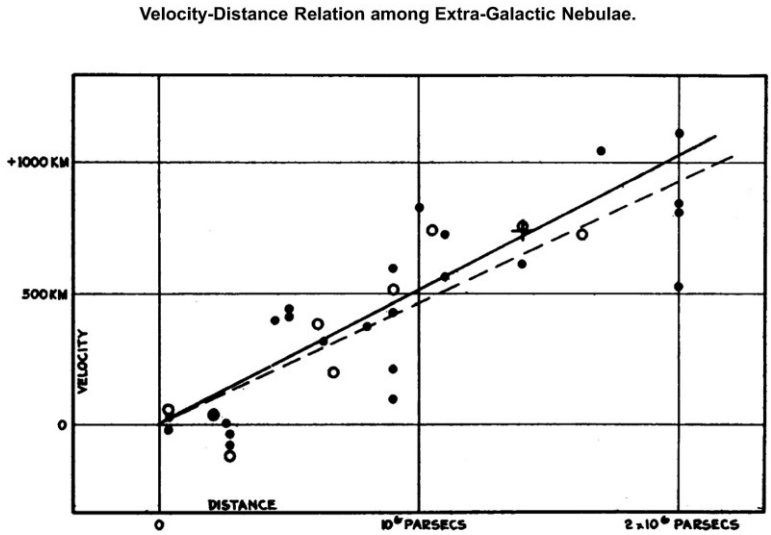

Figure 2.1: The original Hubble's plot for the velocity-distance relation (Hubble 1929). While the radial velocities were estimated easily by measuring galaxy redshifts, their distance were measured by means of the Cepheids variables inside the galaxies, acting like standard candles.

This relation is known as *Hubble's law*

$$\mathbf{V}_r = H_0 \cdot \mathbf{D}, \tag{2.1}$$

where $\mathbf{V}_r$ is the radial velocity, $\mathbf{D}$ is the distance and the constant of proportionality H_0 is the so-called *Hubble's constant*. The most recent estimate for H_0 comes from the Planck survey (Planck Collaboration et al. 2016c), fixing $H_0 = 67.8 \pm 0.9\,\mathrm{km\,s^{-1}\,Mpc^{-1}}$.

Hubble's law holds for any point in the Universe in fact, taking any three points in space, we have (fig: 2.2)

$$\mathbf{V}_{12} = \mathbf{V}_1 - \mathbf{V}_2 = H_0 \cdot (\mathbf{D}_1 - \mathbf{D}_2) = H_0 \cdot \mathbf{D}_{12} \tag{2.2}$$

where $\mathbf{V}_1, \mathbf{V}_2$ are the radial velocity of the galaxy located at the points 1 and 2 with respect to the point 0, $\mathbf{V}_{12}$ is the radial velocity of galaxy 1 with respect to galaxy 2, $\mathbf{D}$

represents the distance from one point to another one, following for the indices the same logic of the radial velocities. Then, every points of the Universe is receding from any other point with a velocity that grows with the distance, proving that the Universe is expanding.

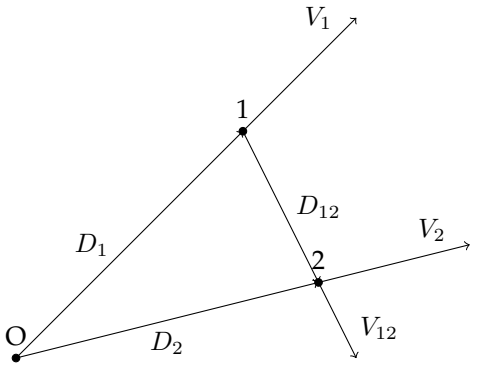

Figure 2.2: The effect of the existence of Hubble law. If Universe is receding linearly from one point, it recedes uniformly from each of its point, thus bringing to an overall expansion.

Several models were elaborated in order to explain the expansion of the Universe. The most accredited is the Big Bang theory, which is supported by many discoveries of the past century, namely the Cosmic Microwave Background radiation (CMB) (Penzias & Wilson 1965), the Large Scale Structure of the Universe (LSS) (Peebles 1980) and the abundance of light elements (Dodelson 2003).

According to the Big Bang theory, the Universe we live in is the result of an expansion process that started when all of its components were contained in about a single point, with density and temperature almost infinite. Then, the expansion brought this *singularity* to evolve into the Universe we see today. This primordial singularity must not be thought as embedded in a sort of "cosmic vacuum", because the space and time dimensions didn't exist until the Universe expansion started, both space and time born together with the Universe, and we can define them only within the Universe itself. As the Universe expands, its temperature decreases, allowing the formation of elementary particles. After 10^{-6} seconds, the Universe is well described by a mixture of protons, neutrons, electrons and photons, interacting by means of Compton scattering. Due to the frequent collisions with the electrons in this epoch, photons are thermalized. As the temperature decreases, ionized nuclei of hydrogen, helium and lithium were formed by protons and neutrons. When the temperature dropped to $T \sim 3000\ K$, electronic capture was allowed, making possible the formation of the firsts stable atoms. This period is called *recombination*. After recombination, matter and radiation decoupled and photons were free to propagate through the whole Universe, showing a blackbody spectrum. This radiation comes down to us as the CMB. Since the photons travelled freely through space, what we observe now using the CMB as probe is the Universe at the time of recombination. Meanwhile, matter began the process of fragmentation and accretion that gave birth to the LSS of galaxies we see today.

The expansion of the Universe takes away one point from each other, so that the physical distance between two objects grows with time. In order to define a distance that is invariant with respect to the expansion of the Universe, i.e. a *comoving distance*, we can define the scale factor $a(t)$. This scale factor is time-depending and it is used to

parametrize the expansion of the Universe. We can write

$$d(t) = a(t) \cdot d_0, \tag{2.3}$$

where $d(t)$ is the physical distance, d_0 is the comoving distance and $a(t)$ the scale factor. From now on, we can refer to the expansion of the Universe by using the scale factor $a(t)$. Conventionally, at the present time, indicated with t_0, the value of the scale factor is set equal to 1.

The scale factor together with the cosmological principle, i.e. the Universe is isotropic and homogeneous on large scales (hundreds of Mpc), allows one to write the metric of the Universe, describing the distance of any two points in terms of time and space coordinates. The metric of an homogeneous and isotropic Universe is known as *Friedmann-Lemaitre-Robertson-Walker metric* and it's the base of modern cosmology,

$$ds^2 = -dt^2 + a^2(t)\left[\frac{dr^2}{1-\kappa r^2} + r^2(d\theta^2 + \sin^2\theta d\phi^2)\right] \tag{2.4}$$

where κ is a constant related to the curvature of the Universe (fig. 2.3), that is:

- $\kappa = 1$, the Universe is *closed* and its geometry is represented by a 4-dimensional sphere where the sum of the angles of a triangle is greater than $180°$;
- $\kappa = -1$, the Universe is *open*, the 4-dimensional behavior is similar to the 3-dimension saddle, in which the sum of the angles of a triangle is lower than $180°$.
- $\kappa = 0$, the Universe is *flat* and behaves like a 4-dimensional hyper-plane, e.g. the sum of the angles of a triangle is $180°$;

It is possible to relate the geometry of the Universe to its energy content by means of Einstein's equations

$$R_{\mu\nu} - \frac{1}{2}g_{\mu\nu}R = 8\pi G T_{\mu\nu}, \tag{2.5}$$

where $R_{\mu\nu}$ is the *Ricci's tensor* describing the curvature of the Universe, thus its geometry, R is the scalar curvature, obtained by taking the trace of the Ricci's tensor, G is the usual gravitational constant, $T_{\mu\nu}$ is the *energy-momentum tensor*, describing the energy density of the Universe. In the equation (2.4) and (2.5) I used the convention

$$c = k_B = 1, \tag{2.6}$$

where c is the speed of light and k_B is the Boltzmann's constant. I will use this convention throughout this thesis.

In a Universe described by the metric in eq. (2.4), the Einstein's equations (2.5) reduces to the so-called *Friedmann's equations*

$$\left(\frac{\dot{a}}{a}\right)^2 = \frac{8\pi G}{3}\rho - \frac{K}{a^2}, \tag{2.7}$$

$$\frac{\ddot{a}}{a} = -\frac{4\pi G}{3}(\rho + 3P) \tag{2.8}$$

where ρ is the energy density of the Universe and P the associated pressure. Energy and pressure are related by means of a *fluid equation*, that for a homogeneous and isotropic Universe is

$$\dot{\rho} + 3\frac{\dot{a}}{a}(\rho + P) = 0, \tag{2.9}$$

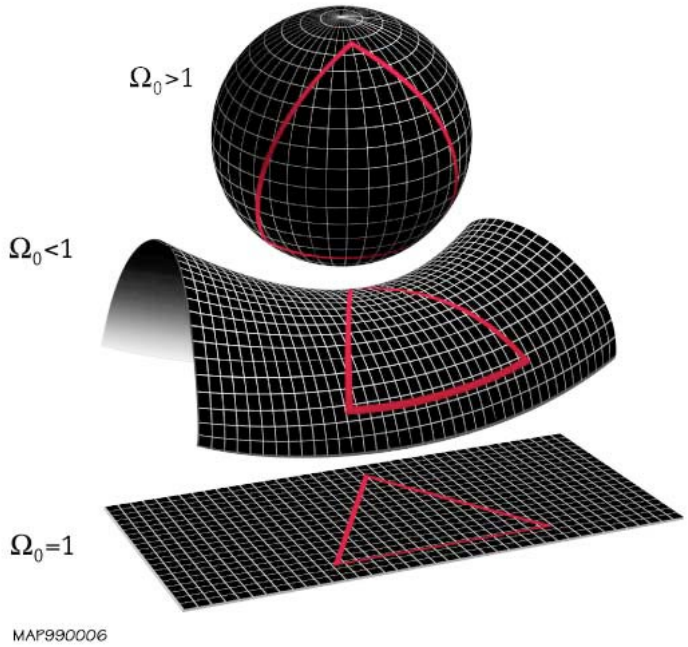

Figure 2.3: Geometry of the Universe in the closed (upper sphere), open (middle saddle) of flat (bottom plane) case. Red triangles show different behaviors depending on the geometry in which they are defined. The Ω_0 parameter is the total Universe energy density, which measurement allows to discriminate between different topologies as well as κ. (NASA 2014).

corresponding to the second thermodynamic principle applied to the Universe content with no exchange of heat between adjacent volumes. Thus, eq. (2.9) says that the expansion of the Universe is adiabatic. Unfortunately, eq. (2.7), (2.8) and (2.9) are not independent, since we can derive one of them from the other two. In order to complete the set of equation, we need an *equation of state*, i.e. an equation relating energy and pressure, of the form $P = P(\rho)$. For cosmology purposes, it was shown (Dodelson 2003; Ryden 2003) that we can simply write

$$P = w\rho. \tag{2.10}$$

At a first glance, the content of the Universe can be divided into matter (non-relativistic component) and radiation (relativistic component). There is a third unknown component, called *dark energy*, introduced in order to explain the acceleration of the Universe discovered by means of observation of type-Ia supernovae (Riess et al. 1998). Since this component is not relevant for the aim of this thesis I won't deal with it. We have $w = 0$ for non-relativistic component and $w = 1/3$ for the relativistic one.

As long as the Universe expands, the energy density decreases with time (fig. 2.4). The energy density of the matter scales with the increase in volume of the Universe, i.e.

$$\rho_m \propto a^{-3}. \tag{2.11}$$

For radiation, instead, we must consider also the cosmic redshift due to the expansion of the Universe, that adds a factor a^{-1} to the proportionality relation, giving

$$\rho_r \propto a^{-4}. \tag{2.12}$$

Comparing eq. 2.11 and eq. 2.12, it is easy to say that there was a moment in which the energy density of the Universe was dominated by radiation. Afterwards, the expansion of the Universe led the energy density of the radiation to decrease more quickly than the energy density of matter, that became the dominant component in the Universe. We can thus divide the history of the Universe into two eras, *radiation domination* (RD) and *matter domination* (MD) (fig. 2.4).

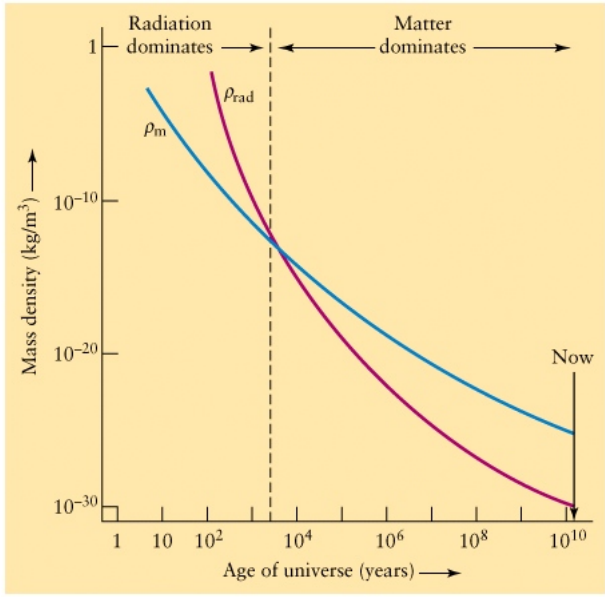

Figure 2.4: The energy content of the Universe is dominated by radiation or matter in different moments.

The Friedmann equations 2.7 and 2.8 allow us to evaluate the rate of the expansion of the Universe according to its energy density. In fact, according to the dominating component, the scale factor changes differently. We can derive the time-evolution of scale factor in different eras

$$a \propto t^{\frac{1}{2}} \qquad \text{RD}, \tag{2.13}$$

$$a \propto t^{\frac{2}{3}} \qquad \text{MD}. \tag{2.14}$$

It is important to remark that the Hubble constant is not really a constant. Indeed, it is a time-dependent parameter, and its value depends on the rate of the expansion of the Universe at the time in which it is calculated (Dodelson 2003). By means of back-envelope math it is possible to show that

$$\begin{aligned} \mathbf{V}(t) &= H(t)\mathbf{D}(t), \\ \dot{a}(t)\mathbf{d} &= H(t)a(t)\mathbf{d}, \end{aligned} \tag{2.15}$$

where $\mathbf{V}(t)$ is the receding velocity of a galaxy from another one calculated at time t, $\mathbf{D}(t)$ is the physical distance between this two galaxies and $\mathbf{d}$ is the comoving distance, then

$$H(t) = \frac{\dot{a}(t)}{a(t)}. \tag{2.16}$$

So, just like the scale factor, the Hubble parameter can be used to parametrizes the expansion of the universe. We can quantify how much the Universe expands between two moments with the number of e-folds, defined as follows

$$N = \int_{t_0}^{t_1} H(t)dt = \int_{a_0}^{a_1} \frac{da}{a} = \ln\left(\frac{a_1}{a_0}\right). \tag{2.17}$$

2.1 Big Bang flaws

The Hot Big bang model describes well the actual dynamics of the Universe. But nevertheless, it isn't free from problems that could undermine the confidence in it. Here, two of the main problems of the Hot Big Bang theory are listed, which bring scientist to formulate the so-called *inflationary paradigm*.

2.1.1 Horizon problem

For each point in the Universe it is possible to define a *casual horizon*, i.e. the distance to the farthest object for which the light emitted has got enough time to reach the observer,

$$d_{HOR} = a(t)\int_0^{t_0} \frac{dt}{a(t)} = \frac{a(t)}{H_0}\frac{2}{1+3w}. \tag{2.18}$$

Because of the presence of w, the dimension of the casual horizon changes depending on which era the horizon is defined at. Thus, two points separated by a distance greater than the horizon at any time could not be in casual contact.

Having said that, let's talk about history of cosmology. In the nineties, the COBE survey showed that the CMB is uniformely distributed over the sky, with a perfect blackbody spectrum at the temperature of 2.725K (Smoot et al. 1992). Deviation from this temperature, called *anisotropies* were found at level of

$$\frac{\Delta T}{T} \approx 10^{-5}, \tag{2.19}$$

where ΔT is the deviation of the temperature in a point of the sky from the mean value T. This low-level anisotropy shows the high isotropy level of the CMB. Such a uniform distribution requires a thermalizing process to be established, thus each point in the Universe should be in casual contact at the time of recombination. Unfortunately, this is not the case. In fact, we can define the angular size of the horizon on the *last scattering surface* at the moment of recombination. Isotropic CMB required an horizon angular size greater then 2π, i.e. the angular size of the circle. First, let's define the last scattering surface as the fictional surface from which CMB is emitted. Now, let's consider a flat geometry and define the *angular distance* as the ratio

$$d_A = \frac{l}{\theta} \tag{2.20}$$

where l is the proper length of an object in the sky and θ is the angular length from the observer. The angular distance of the last scattering surface is ≈ 13 Mpc. The horizon length during recombination is about $d_{HOR}(t_rec) \approx 0.4$ Mpc (Ryden 2003). Thus the angular size of the horizon on the last scattering surface is

$$\theta_{HOR} = \frac{d_{HOR}(t_{rec})}{d_A} \approx 2^\circ. \tag{2.21}$$

Hence, two points at a distance greater than 2° on the last scattering surface were not casual connected at the time of recombination, thus it was impossible to the photons to be thermalized over the whole Universe, unless the Universe have got the same temperature everywhere without any reason different by a universal fine tuning. The horizon problem is exactly the inability to account for the reason why the microwave sky is almost perfectly isotropic.

2.1.2 The Flatness Problem

The Horizon problem is not the only difficulty that affects the Big Bang model. Let's define the *critical* energy density as the density the content of the Universe must have at present time in order to be geometrically flat, i.e., using eq. (2.7) with $\kappa = 0$,

$$\rho_c = \frac{3H_0}{8\pi G}, \tag{2.22}$$

where H_0 is the Hubble parameter at present time. Then we can define the density parameter

$$\Omega = \frac{\rho}{\rho_c}. \tag{2.23}$$

The present value of the total energy density of the Universe, Ω_0, as well as κ, indicates its the geometry: open if $\Omega_0 < 1$, flat if $\Omega_0 = 1$ or close if $\Omega_0 > 1$. Ω_0 was found to be consistent with one (Hinshaw et al. 2009; Planck Collaboration et al. 2014c, 2016c), thus consolidating the flat geometry hypothesis.

Let's rewrite eq. (2.7) in this way

$$(\Omega - 1) = \frac{\kappa}{\dot{a}^2} \tag{2.24}$$

and insert it into eq. (2.8). Thus, we can analyze the evolution of Ω

$$\frac{d}{dt}(\Omega - 1) = (\Omega - 1)\frac{8\pi G}{3}\left(\frac{\rho + 3P}{H}\right). \tag{2.25}$$

We know that $P = 0$ for matter and $P = \rho/3$ for radiation, thus $\rho + 3P > 0$. This means that if we have $\Omega > 1$, Ω increase with time, while for $\Omega < 1$ it decrease with time. Then, to have $\Omega_0 \simeq 1$ today, Ω has been much closer to unity then it is now. In particular, at the Planck time $\tau_p = \sqrt{\hbar G} \simeq 10^{-44} s$, we must have $|\Omega_{\tau_p} - 1| \leq 10^{-60}$. Hence, the actual observation is justified only if Ω was fine tuned at a value close to one.

2.2 Inflation solutions

The inflationary paradigm was introduced just to account for the horizon and the flatness problems that Big Bang theory is not able to resolve (Guth 1981; Guth & Pi 1982). Although it was created "ad hoc", it can explain also the origin of the inhomogeneities that seeded the LSS of the Universe and the anisotropies of the CMB.

The main idea of the inflationary paradigm is that there was a period during the history of the Universe, between about 10^{-36} and 10^{-32} seconds after the Big Bang (Liddle & Lyth 2000), in which the expansions was accelerated, that is

$$\frac{d^2 a}{dt^2} > 0. \tag{2.26}$$

By means of eq. 2.8 we can explicitly write the condition that make inflation possible, i.e.

$$P < -\frac{\rho}{3}. \tag{2.27}$$

Assuming a flat Universe ($\kappa = 0$) and $P = -\rho$, it is easy to show that we have

$$\begin{aligned} \rho &= \text{constant}, \\ H &= \text{constant} \end{aligned} \tag{2.28}$$

then, using again eq. 2.8, we can write the time dependence of the scale factor during the inflationary period

$$a(t) = a_e e^{H(t-t_e)} \qquad t_i < t < t_e. \tag{2.29}$$

that is an exponential expansion. In eq. 2.29, t_i and t_e are the time at which inflation started and ended respectively.

2.2.1 Solution to the Big Bang problems

Inflation solves horizon and flatness problem. At the begin of inflation, the Universe is radiation dominated (Ryden 2003), thus we can write the size of the horizon as

$$d_{HOR}(t_i) = a(t_i)\int_0^{t_i}\frac{dt}{a(t)} = a(t_i)\int_0^{t_i}\frac{dt}{a(t_i)\left(\frac{t}{t_1}\right)^{\frac{1}{2}}} = 2t_i, \tag{2.30}$$

where t_i is the time at the begin of inflation. At the end of inflation, the horizon size is

$$\begin{aligned} d_{HOR}(t_f) &= a(t_f)\int_o^{t_f}\frac{dt}{a(t)} \\ &= a(t_i)e^N\left(\int_0^{t_i}\frac{dt}{a(t_i)\left(\frac{t}{t_1}\right)^{\frac{1}{2}}} + \int_{t_i}^{t_f}\frac{dt}{a(t_i)\exp(H(t_i)(t-t_i))}\right), \end{aligned} \tag{2.31}$$

where t_f is the time at the end of inflation and N is the number of e-folds the Universe was expanded of. If N is large, we have

$$d_{HOR}(t_f) = e^N(2t_i + H^{-1}). \tag{2.32}$$

Thus, considering $t_i \approx 10^{-36}$ s, $H^{-1} \approx 10^{36}$ s^{-1} and $N \approx 100$ e-foldings, we get

$$d_{HOR}(t_i) = 2t_i \approx 6 \times 10^{-28} m \tag{2.33}$$

and

$$d_{HOR}(t_i) = 3t_i \approx 6 \times 0.8 pc, \tag{2.34}$$

i.e. inflation generates a boost on the horizon. Thus the actual horizon has to be increased by a factor e^N, giving $d_{HOR}(t_{rec}) \approx 10^{43}$ Mpc, high enough to obtain a casual angular size many many times larger than 2π.

At the same time, flatness problem is solved by noting that, since $H \approx \text{constant}$ during inflation, we have

$$\Omega - 1 = \frac{\kappa}{a^2 H^2}, \tag{2.35}$$

then Ω is driven towards to one rather than away from it. We can easily check out how much the Universe has to be expanded to make Ω so close to one like it is today. Since $\Omega \propto a^{-2}$ during inflation, we have

$$\frac{|\Omega - 1|_{t_f}}{|\Omega - 1|_{t_i}} = \left(\frac{a_i}{a_f}\right)^2 = e^{-2N}, \tag{2.36}$$

where t_i and t_f are the times at which the inflation begins and ends respectively. Then, if we consider $|\Omega - 1|_{t_i}$ about unity, we must have

$$N = 30 \ln 10 \approx 70 \text{ e} - \text{folds}. \tag{2.37}$$

CHAPTER 3

The very first moments of the Universe: Inflation

Last chapter ended with the observation that the existence of a period in which the Universe expansion was accelerated brings solutions to the open issues of the Hot Big Bang model. The known components of the Universe, matter and radiation, don't have the needed prerequisites to give birth to a period of inflation. Furthermore, the time-evolution of the scale factor due to matter and radiation is known, equation (2.13) and (2.14), and it is far from an exponential one.

In order to satisfy the condition in eq. 2.27 and attain inflation, we must introduce a scalar field ϕ known as *inflaton*,

$$\phi(t, \mathbf{x}) = \phi_0(t) + \delta\phi(t, \mathbf{x}), \tag{3.1}$$

where ϕ_0 is the zero-order homogeneous part of the scalar field, whose value is the expectation value of the inflaton, and $\delta\phi$ is the quantum vacuum fluctuation.

Inflation caused by the only inflaton is a classical example of single-particle model, that is the simplest model allowing to achieve inflation, representing the so-called *standard scenario*. In order to obtain inflation, other models were developed, e.g. taking in account more then one scalar particle, the so-called multi-fields models. The interactions between particles gives rise to different vacuum fluctuation of the energy density with respect to the standard scenario. This fluctuation are inherited by curvature, which perturbations seeded LSS and CMB anisotropies.

3.1 Zero-order part of inflaton

The homogeneous part of the inflaton behaves like a perfect fluid, whose energy density and pressure are given by

$$T_{\mu\nu} = -g^{\alpha\nu}\frac{\partial\phi}{\partial x^\nu}\frac{\partial\phi}{\partial x^\beta} - g^\alpha_\beta\left[\frac{1}{2}g^{\mu\nu}\frac{\partial\phi}{\partial x^\mu}\frac{\partial\phi}{\partial x^\nu} + V(\phi)\right], \tag{3.2}$$

that is the equation for the energy-momentum tensor of a scalar field ϕ. Starting from eq. 3.2, we can rewrite energy and pressure of the inflaton as

$$\rho_\phi = \frac{1}{2}\dot{\phi}^2 + V(\phi), \tag{3.3}$$

$$P_\phi = \frac{1}{2}\dot{\phi}^2 - V(\phi), \tag{3.4}$$

respectively. Hence, in order to satisfies the condition in eq. (2.27), we must have

$$V(\phi) \gg \dot{\phi}^2, \tag{3.5}$$

thus the potential energy of the inflaton must be greater than its kinetic energy. This condition is achieved is we consider a scalar field *slowly rolling* down its potential, in a region where the potential is sufficiently flat (fig. 3.1). Solving eq. (2.7), we have

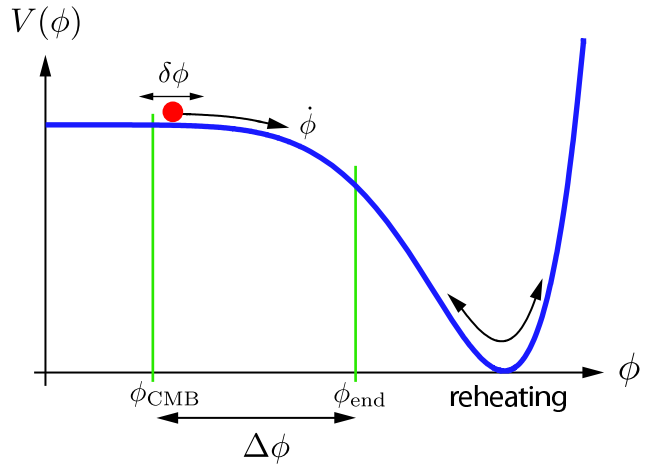

Figure 3.1: Potential for a slow-rolling scalar field. While the inflaton potential is almost constant, Universe expands exponentially. When the inflaton potential energy reaches the minimum, the field oscillates, decaying in matter and radiation.

$$H^2 \simeq \frac{8\pi G}{3} V(\phi), \tag{3.6}$$

so that, in presence of flat potential, $H \approx$ constant.

Slow-roll can be parametrized by means of two parameters,

$$\epsilon = \frac{M_p^2}{2}\left(\frac{V'}{V}\right)^2 = -\frac{\dot{H}}{H^2}, \quad \eta = M_p^2\left(\frac{V''}{V}\right), \tag{3.7}$$

where $M_p \equiv (8\pi G)^{-\frac{1}{2}} \simeq 2.4 \times 10^{18}$ GeV is the reduced Planck scale. In order to achieve inflation we must have $\epsilon, |\eta| \ll 1$ (Bartolo et al. 2004). By means of eq. 2.8, it is possible to show that the slow-roll parameter ϵ also constraints the end of inflation, that is

$$\frac{\ddot{a}}{a} = \dot{H} + H^2 = (1-\epsilon)H^2 > 0 \Leftrightarrow \epsilon < 1. \tag{3.8}$$

Then, as long as $\epsilon < 1$ inflation works. When this condition fails, inflation stops and begin the phase of monotonically expansion of Universe, driven by radiation first and matter later.

The end of inflation is achieved when the potential of the scalar field stops to slow-roll and reaches the minimum. Then, a phase of oscillatory motion of the inflaton about the minimum of potential begins, during which the scalar field decades into light particles. This phase is known as *reheating* because the temperature of the Universe, after the exponential cooling due to the extremely fast inflationary expansion, reaches pre-inflationary level (Ryden 2003).

3.2 Quantum fluctuations of the inflaton

Fluctuations of the matter and photon distribution, that seeded LSS of the Universe and CMB radiation, were associated to primordial energy density perturbations generated in the early phases of the Universe evolution, which survive after the inflation. When the Universe became matter dominated ($z \sim 3200$), primeval density inhomogeneities ($\delta\rho \sim 10^{-5}$) were amplified by gravity and grew up into the structures we see today (Peebles 1980; Coles & Lucchin 2002). Then, there must have been small preexisting fluctuations on relevant physical length scale (~ 1 Mpc, typically the scale of a galaxy), that behave as "seed" for the inhomogeneities, which left the Hubble radius during radiation dominated or matter dominated era. In the Big Bang model, perturbations on this small scales have to be put in by hand. Inflation, instead, provide a mechanism by which density perturbations (and gravitational waves) were generated.

In order to achieve a period of inflation, there must have been a scalar field such as that one in eq. (3.1) which dominates the energy density of the Universe in that moment. So, quantum perturbations of the scalar field imply fluctuations on the energy-momentum tensor $T_{\mu\nu}$, and hence, by means of the Einstein equations (2.5), on the metric $g_{\mu\nu}$ of the Universe, giving rise to perturbations of the curvature ζ (that may be loosely thought as a gravitational potential in the Universe). Then, these perturbations acts first on the coupled radiation-matter plasma and latter on matter, giving rise to matter and temperature perturbations $\delta\rho$ via the Poisson equation $\nabla^2\zeta = 4\pi G\delta\rho$. These fluctuations will then start growing, generating anisotropies in the photon distribution and fluctuation in the matter density field.

During inflation, the comoving Hubble radius $(aH)^{-1}$, that is the scale beyond which no casual processes can be attained, decrease with time. The quantum fluctuations of the scalar field that drives the inflation arise on scales smaller then the comoving Hubble radius, so, one can use the flat space-time quantum field theory to describe the scalar field vacuum fluctuations (Bartolo et al. 2004). Then, the inflationary expansion stretches the wavelength of the quantum fluctuations to outside the horizon were they follows a classical evolution (fig. 3.2). The amplitude of fluctuations is *frozen-in* since it is not affected by microscopic physics, and it is fixed at same value $\delta\phi$ at the horizon crossing, remaining almost unchanged, whereas its wavelength grows exponentially. (The same mechanism also generates stochastic gravitational waves (Starobinskiĭ 1985; Abbott & Wise 1984)).

The fluctuations of the scalar field produce primordial perturbations in the energy density ρ_ϕ, which are then inherited by the radiation and matter to which the inflaton decays during rehating phase after inflation. Once inflation has ended, the Hubble radius grows faster than the scale-factor, so the fluctuations eventually reenter the Hubble radius during radiation or matter dominated eras, giving rise to the structure we dealt above.

The physical wavelength in the range accessible to cosmological observations today exit the horizon around 60 e-foldings or so before. The spectra of these perturbations give us a direct observational connection to physics of inflation because they preserve a signature of inflation. As we shall see, the analysis of CMB anisotropies gives a powerful tools to measure the inflationary perturbations. The WMAP collaboration confirm for the very first time the detection of adiabatic super-horizon fluctuations (Peiris et al. 2003). These observations were confirmed afterwards by Planck survey (Planck Collaboration et al. 2014d,e).

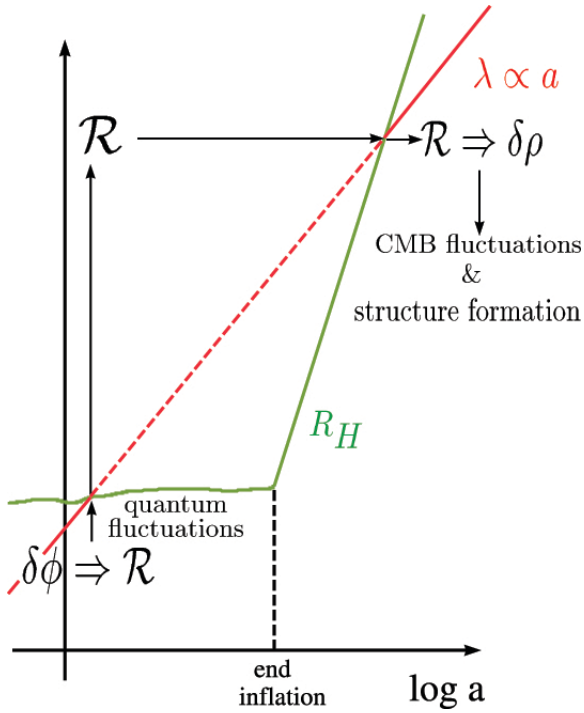

Figure 3.2: Behaviour of the quantum fluctuations during inflation. $\mathcal{R} = \zeta$ are the curvature perturbations, generated during inflation and their wavelengths λ are stretched from microscopic scales to astronomical scales during inflation.

3.2.1 Quantitative description of quantum perturbations

In order to describe quantitatively the behaviour of the fluctuations of the inflaton and their evolution during the inflation stage, we define a massless scalar field χ in a pure de Sitter stage, with $P_\chi = -\rho_\chi =$ constant and $H =$ constant, different from the inflaton (see Bartolo et al. 2004, for details)

$$\chi(t, \mathbf{x}) = \chi_0(t) + \delta\chi(t, \mathbf{x}), \tag{3.9}$$

where $\chi_0(t)$ is the homogeneous classical value of the scalar field and $\delta\chi$ is the quantum fluctuation of χ from the expected value.

Performing the Fourier transform of the quantum fluctuations

$$\delta\chi(t, \mathbf{x}) = \int \frac{d^3\mathbf{k}}{(2\pi)^{3/2}} e^{i\mathbf{k}\cdot\mathbf{x}} \delta\chi_k(t), \tag{3.10}$$

it is possible to write down the equation of motion for the fluctuations

$$\delta\ddot{\chi}_k + 3H\delta\dot{\chi}_k + \frac{k^2}{a^2}\delta\chi_k = 0, \tag{3.11}$$

that is simple the equation of motion of a damping harmonic oscillator. Then, we can consider two cases, depending on the relation between the wavelength λ of the fluctuations and the Hubble horizon H^{-1}:

- $\lambda \ll H^{-1}$, i.e. for wavelengths within the horizon, eq. (3.11) reduces to

$$\delta\ddot{\chi}_k + \frac{k^2}{a^2}\delta\chi_k = 0, \tag{3.12}$$

that is the equation of motion of an harmonic oscillator. Then, the solution for the quantum fluctuations is a plane wave

$$\delta\chi_k \propto e^{i\omega t} \tag{3.13}$$

where the frequency $\omega = k/a$ decrease with time because the scale factor grows exponentially during inflation. Then, as long as the wavelengths of the fluctuations are within the Hubble radius, the fluctuations oscillate with a wavelength that grows with time.

- $\lambda \gg H^{-1}$, i.e. for wavelengths beyond the horizon, eq. (3.11) reduces as

$$\delta\ddot{\chi}_k + 3H\delta\dot{\chi}_k = 0 \tag{3.14}$$

indicating that on super-horizon scales, $\delta\chi_k$ remains constant.

If we consider a scalar field with a non-vanishing mass, the amplitude of super-horizon fluctuations is not exactly constant, but it acquires a dependence upon time

$$|\delta\chi_k| = 2^{(\nu_\chi - 3/2)}\frac{\Gamma(\nu_\chi)}{\Gamma(3/2)}\frac{H}{\sqrt{2k^3}}\left(\frac{k}{aH}\right)^{3/2-\nu_\chi} \tag{3.15}$$

where

$$\nu_\chi^2 = \left(\frac{9}{4} - \frac{m_\chi^2}{H^2}\right). \tag{3.16}$$

then, eq. 3.15 is valid for $m_\chi \leq 3/2H$. On the other hand, if $m_\chi > 3/2H$, ν became imaginary and the amplitude or the perturbations oscillates with time.

If we consider a very light mass for the scalar field, such that $m_\chi \ll 3/2H$, we can introduce the parameter

$$\eta_\chi = \frac{m_\chi^2}{3H^2} \tag{3.17}$$

in analogy with the slow-roll parameters ϵ and η for the inflaton field (eq. 3.7). Then, we can expand the solution in eq. 3.15 in η_χ and take the lowest order component, i.e.

$$|\delta\chi_k| = \frac{H}{\sqrt{2k^3}}\left(\frac{k}{aH}\right)^{3/2-\nu_\chi} \tag{3.18}$$

where

$$\frac{3}{2} - \nu_\chi \simeq \eta_\chi. \tag{3.19}$$

Now, instead to consider a perfect de Sitter stage, we introduce a little deviation. In fact, during inflation, in a quasi de Sitter expansion, the Hubble parameter evolve with time as $\dot{H} = -\epsilon H^2$. Then, we have to put a correction of order ϵ in eq. 3.15

$$|\delta\chi_k| \simeq \frac{H}{\sqrt{2k^3}}\left(\frac{k}{aH}\right)^{\eta_\chi - \epsilon} \simeq \frac{H}{\sqrt{2k^3}}\left[1 + (\eta_\chi - \epsilon)ln\left(\frac{k}{aH}\right)\right], \tag{3.20}$$

so we get

$$|\delta\dot{\chi}_k| \simeq |H\eta_k\delta\chi_k| \ll |H\delta\chi|, \tag{3.21}$$

then, the variation of the amplitude of the fluctuations is negligible, so the fluctuations are (nearly) frozen on super-horizon scales.

3.2.2 The Power Spectrum

In order to characterize the properties of the fluctuations, we can introduce the *power spectrum*. Firstly, define the random scalar field $f(t, \mathbf{x})$ labelling the amplitude of the perturbations at a given moment t and at a given position $\mathbf{x}$. For such field, we can perform the Fourier transform as

$$f(t, \mathbf{x}) = \int \frac{d^3\mathbf{k}}{(2\pi)^{3/2}} e^{i\mathbf{k}\cdot\mathbf{x}} f_k(t), \tag{3.22}$$

the dimensionless power spectrum $\mathcal{P}(k)$ can be defined through

$$\langle f_{k_1} f^*_{k_2} \rangle \equiv \frac{2\pi^2}{k^3} \mathcal{P}_f(k)(\mathbf{k}_1 - \mathbf{k}_2), \tag{3.23}$$

where the angled brackets denote ensemble average. From the above definition, we can rewrite the mean square value of $f(t, \mathbf{x})$ in real space as

$$\langle f^2(t, \mathbf{x}) \rangle = \int \frac{dk}{k} \mathcal{P}_f(k), \tag{3.24}$$

then, the power spectrum $\mathcal{P}_f$ is the contribution to the variance of the field $f(t, \mathbf{x})$ per unit logarithmic interval in the wave number k. Thus, the power spectrum measures the amplitude of the fluctuations at a given scale k.

To describe the slope of the power spectrum it is standard practice to define a *spectral index* $n_f(k)$ through

$$n_f(k) - 1 \equiv \frac{d \ln \mathcal{P}_f}{d \ln k}. \tag{3.25}$$

In the case of a light mass ($m \ll 3/2H$) field χ in a de Sitter phase (but also in a quasi de Sitter phase, as already seen), we find from eq. (3.15) that the power spectrum on super-horizon scales is given by

$$\mathcal{P}_{\delta\chi}(k) = \left(\frac{H}{2\pi}\right)^2 \left(\frac{k}{aH}\right)^{3-2\nu_\chi}, \tag{3.26}$$

where ν_χ is given by eq. (3.16). Thus, in this case the dependence on time is tiny, and the spectral index slightly deviates from unity

$$n_{\delta_\chi} - 1 = 3 - 2\nu_\chi = 2\eta_\chi. \tag{3.27}$$

As we already have seen, fluctuations of the scalar field can be generated on super-horizon scales as in eq. (3.15) only if the scalar field is light. In fact, it can be shown that, for very massive scalar field, that is $m_\chi \gg 3/2H$, the fluctuations of the scalar field remain in the vacuum state and do not produce perturbations on cosmological relevant scales. Indeed, the amplitude of the power spectrum is damped exponentially as $e^{-2m_\chi^2}/H^2$ and the spectral index is equal to 4 (Pilo et al. 2004).

Part II

Bispectrum of Large Scale Structure

CHAPTER 4

Matter Power spectrum, Bispectrum and Parameter Degeneracy

4.1 Angular Statistics for 3-Dimensional Fields

In order to study the physics that drove matter in the Large Scale Structure we see today, the only visible observable is the galaxy distribution across the Universe. Assuming that galaxies trace the matter distribution, their distribution assumes a fundamental role. The galaxy distribution is described by means of the overdensity function:

$$\delta_g(\widehat{\mathbf{n}}, z) = \frac{n_g(\widehat{\mathbf{n}}, z) - \bar{n}(z)}{\bar{n}(z)}, \tag{4.1}$$

where $n_g(\widehat{\mathbf{n}}, z)$ is the number of galaxy in the direction $\widehat{\mathbf{n}}$ of the sky at redshift z and $\bar{n}$ is the averaged spatial density at the same redshift. Given its Fourier transform,

$$\delta_{\mathbf{k}}(z) = \int d^3r \; \delta_g(\widehat{\mathbf{n}}, z) e^{i\mathbf{k}\cdot\mathbf{r}}, \tag{4.2}$$

we can define the statistics used to describe the behavior of the distribution and therefore give hints about the physics of the galaxy clustering. The lowest order statistic is the *power spectrum*, i.e. the Fourier counterpart of the two-point correlation function,

$$\begin{aligned} \langle \delta_{\mathbf{k_1}} \delta_{\mathbf{k_2}} \rangle &= \int d^3r_1 d^3r_2 e^{-i\mathbf{k_1}\cdot\mathbf{r_1}} e^{-i\mathbf{k_2}\cdot\mathbf{r_2}} \langle \delta(\mathbf{r_1}) \delta(\mathbf{r_2}) \rangle \\ &= (2\pi)^3 \delta_D(\mathbf{k}_1 + \mathbf{k}_2) \int d^3x e^{-i\mathbf{k}\cdot\mathbf{x}} \xi(x) \\ &= (2\pi)^3 \delta_D(\mathbf{k}_1 + \mathbf{k}_2) P(k_1). \end{aligned} \tag{4.3}$$

The two-points correlation function $\xi(x)$ parametrizes the excess probability to find two galaxies separated by a certain distance. The power spectrum gives the same information, in the form of the power of the distribution at each physical-scale k^{-1}. The highest the excess probability at a physical scale, the highest is the power of $P(k)$ at the same scale. Eq. 4.3 shows that it doesn't matter the orientation of the two-galaxies system in the distribution, but just the distance between them. This follows directly from homogeneity and isotropy of the Universe. For this reason, P depends only on the modulus of $\mathbf{k}$, not on its orientation. The Dirac delta ensures that, in Fourier space, the two vectors $\mathbf{k}$ have the same modulus and opposite direction, with the starting-point of one located at the end-point of the other, and vice versa.

The first higher-order statistic is the *bispectrum*, that is the Fourier counterpart of the three-points correlation function:

$$\langle \delta_{\mathbf{k}_1} \delta_{\mathbf{k}_2} \delta_{\mathbf{k}_3} \rangle \equiv (2\pi)^3 \delta^D(\mathbf{k}_{123}) B(\mathbf{k}_1, \mathbf{k}_2, \mathbf{k}_3) \,, \tag{4.4}$$

where $\mathbf{k}_{i_1 \dots i_n} \equiv \mathbf{k}_{i_1} + \dots + \mathbf{k}_{i_n}$. The three-point correlation function express the excess probability to find three galaxies placed at the three vertex of a closed triangle, condition ensured by the presence of the Dirac delta in the above definition. We can use this information to study the physics of the galaxy clustering, a non-Gaussian process that introduces non-Gaussianity in the galaxy distribution, easily detectable through the bispectrum.

4.2 Evolution of fluctuations

4.2.1 Initial Conditions

The main legacy of inflation is the generation of curvature perturbations, inherited by matter. The fluctuations of matter eventually grow thus bringing to the Large Scale Structure of filaments and clusters of galaxies that we see today. The initial fluctuations are described by the power spectrum, set by inflation to

$$P_L(k) \propto \delta_H k^{n_s} T^2(k) \tag{4.5}$$

where the L subscript stands for *linear*, δ_h parametrizes the amplitude of fluctuations at earlier time, while $T(k)$ is the transfer function that describes the evolution of perturbations (Dodelson 2003). This power spectrum represents our initial condition, thus Gaussian, since a Gaussian distribution is fully described by its variance.

4.2.2 Perturbation Theory

Let's assume that

- Matter is (essentially) Cold Dark Matter (CDM);
- We live in a Einstein-De Sitter Universe, i.e. $\Omega_m = 1$;
- We are using a Newtonian approximation
  1. $k >> H$, scales smaller than casual horizon,
  2. $v_p << c$, velocity of particles is smaller than that of light.

We will use comoving coordinates, related to physical ones as follows:

- Position: $\mathbf{r}(t) = a(t)\mathbf{x}$;
- Velocity: $\mathbf{v}(t) = \frac{d\mathbf{r}(t)}{dt} = \dot{a}\mathbf{x} + a\frac{d\mathbf{x}}{dt} = Ha\mathbf{x} + \mathbf{u}(t)$, where u is the peculiar velocity of the particles;
- Conformal time: $d\tau = \frac{dt}{a(t)}$.

Using the definition of conformal time, we can rewrite the Hubble parameter as $\mathcal{H} = \frac{1}{a}\frac{da}{d\tau} = aH$ and thus the velocity becomes $\mathbf{v}(t) = \mathcal{H}x + u(t)$.

The expressions for the perturbation are:

- Matter Density: $\rho(\mathbf{x},t) = \bar{\rho}(t)[1+\delta(\mathbf{x},t)]$;
- Velocity: $\mathbf{v}(\mathbf{x},t) = \mathcal{H}\mathbf{x} + \mathbf{u}$;
- Gravitational Potential: $\Phi_{tot}(\mathbf{x},t) = \frac{2\pi G}{3}\bar{\rho}r^2 + \Phi(\mathbf{x},t)$.

In order to understand how the fluctuations evolve, we have to write the equation of motions, i.e.

1. Continuity eq. $\frac{\partial\rho}{\partial t} + \nabla_r \cdot \rho\mathbf{v} = 0$;
2. Euler eq. $\frac{\partial\mathbf{v}}{\partial t} + \mathbf{v}\cdot\nabla_r\mathbf{v} = -\nabla_r\phi_t$;
3. Poisson eq. $\nabla_r^2\phi_t = 4\pi G\rho$.

We consider a pressure-less fluid and the *single-stream approximation*, i.e. in each point in space it is defined a unique velocity (it is not possible in non-linearities where there are chaotic motions and galaxies in the same point may have different velocities). Thus, the equation of motion evolves as:

1. Continuity equation:
$$\frac{\partial\delta}{\partial\tau} + \nabla\cdot[(1+\delta)\mathbf{u}] = 0 \tag{4.6}$$
2. Euler equation:
$$\frac{\partial\mathbf{u}}{\partial\tau} + \mathbf{u}\nabla\cdot\mathbf{u} + \mathcal{H}\mathbf{u} + \nabla\phi = 0 \tag{4.7}$$
3. Poisson equation:
$$\nabla^2\phi = \frac{3}{2}\mathcal{H}^2\delta \tag{4.8}$$

4.2.3 Linear Theory

Eq. (4.6), (4.7) and (4.8) are actually *non-linear* because of the quadratic term in Euler equation. Linearize the equations means take the first-order component of the equations, i.e.
$$\frac{\partial\delta}{\partial\tau} + \theta = 0, \tag{4.9}$$
$$\frac{\partial\theta}{\partial\tau} + \mathcal{H}\theta + \frac{3}{2}\mathcal{H}^2\delta = 0, \tag{4.10}$$
where θ is the divergence of the velocity, i.e. $\theta(\mathbf{x},t) = \nabla\cdot\mathbf{u}(\mathbf{x},t)$.

Let's move on Fourier space. Single-stream approximation is expected to work also in Fourier space (for small k's). Inserting eq. (4.9) in eq. (4.10) we get
$$\frac{\partial^2\delta_\mathbf{k}}{\partial\tau^2} + \mathcal{H}\frac{\partial\delta_\mathbf{k}}{\partial\tau} - \frac{3}{2}\mathcal{H}^2\delta_\mathbf{k} = 0. \tag{4.11}$$
Consider solution of the type $\delta_\mathbf{k} = D(\tau)A_\mathbf{k}$, the above equation becomes
$$\frac{\partial^2 D}{\partial\tau^2} + \mathcal{H}\frac{\partial D}{\partial\tau} - \frac{3}{2}\mathcal{H}^2 D = 0. \tag{4.12}$$

Let's do the ansatz $D(\tau) = a^n$. The eq. of motion becomes

$$n^2 + \frac{n}{2} - \frac{3}{2} = 0, \tag{4.13}$$

with solution $n = 1, -3/2$. The first solution is the growing mode, the second the decaying mode. Thus we have solution for the density and velocity

$$\delta_{\mathbf{k}} = A_{\mathbf{k}} a + B_{\mathbf{k}} a^{-3/2}. \tag{4.14}$$

$$\theta_{\mathbf{k}} = -\frac{\partial \delta_{\mathbf{k}}}{\partial \tau} = -\mathcal{H}\left(A_{\mathbf{k}} a - \frac{3}{2} B_{\mathbf{k}} a^{-3/2}\right). \tag{4.15}$$

The physical meaning of this solution is clear. If we set up initial condition in growing mode, i.e. $A_{\mathbf{k}} \neq 0$ and $B_{\mathbf{k}} = 0$, we have peculiar velocities pointing toward the center of a perturbation, while in decaying mode it happens the contrary. Since decaying mode vanishes with time, the net effect of the evolution of perturbation is to cluster around overdensities.

Solution in ΛCDM

Consider a ΛCDM with $\Omega_m + \Omega_\Lambda = 1$. The equations of motions reduce as

$$\frac{d^2 D}{d\eta} + \left[2 + \frac{d \ln H}{d\eta}\right] \frac{d \ln D}{d\eta} + \frac{d \ln H}{d\eta} D = 0, \tag{4.16}$$

where $\eta = \ln a$. In this case, the decaying mode scales as $D_-(a) \propto H(a)$ while the growing mode

$$D_+(a) = \frac{5}{2} H_0^2 \Omega_{m0} H(a) \int_0^a \frac{da}{a^3 H^3(a)} \equiv g(a) H(a). \tag{4.17}$$

We can define the *growth rate*

$$f = \frac{d \ln D}{d \ln a}. \tag{4.18}$$

For EdS model, $f = 1$ while for ΛCDM cosmology is $f \approx \Omega_m^{0.55}$.

4.2.4 Non-Linear Theory

In Linear theory we have $\delta, \theta << 1$. These assumptions break down on small scales and small redshifts, thus we cannot neglect the quadratic term in Euler equation. Let's define

$$\delta_{NL} = \delta_L + \delta^{(2)} + \delta^{(3)} + \dots,$$

where $\delta^{(2)} \propto \delta_L^2$, $\delta^{(3)} \propto \delta_L^3$ and so on.

Let's assume an EdS Universe. The non-linear equations of motions become

$$\frac{\partial \delta}{\partial \eta} - \Theta = \nabla \cdot (\delta \mathbf{V}), \tag{4.19}$$

$$\frac{\partial \Theta}{\partial \eta} + \frac{1}{2}\Theta - \frac{3}{2}\delta = \nabla[(\mathbf{V} \cdot \nabla)\mathbf{V}], \tag{4.20}$$

where $\mathbf{V} = -\frac{\mathbf{u}}{\mathcal{H}}$ and $\Theta = \nabla \cdot \mathbf{V}$. Let's move again in Fourier space. Now it is more difficult because of the quadratic terms. The r.h.s of continuity eq. transforms like

$$\mathcal{F}[\nabla \cdot (\delta \mathbf{V})] = \int d^3k_1 d^3k_2 \delta_D(\mathbf{k_{12}} - \mathbf{k}) \frac{\mathbf{k_{12}} \cdot \mathbf{k_2}}{k_2^2} \delta_{\mathbf{k_1}} \Theta_{\mathbf{k_2}}, \tag{4.21}$$

with $\mathbf{k}_{12} = \mathbf{k}_1 + \mathbf{k}_2$. The r.h.s of Euler eq. instead

$$\mathcal{F}[\nabla \cdot ((\mathbf{V} \cdot \nabla)\mathbf{V})] = \int d^3k_1 d^3k_2 \delta_D(\mathbf{k_{12}} - \mathbf{k}) \frac{(\mathbf{k_1} \cdot \mathbf{k_2}) k_{12}^2}{2k_1^2 k_2^2} \Theta_{\mathbf{k_1}} \Theta_{\mathbf{k_2}}. \tag{4.22}$$

Let's define

$$\psi = \begin{pmatrix} \delta \\ \Theta \end{pmatrix}. \tag{4.23}$$

The equations of motion can be reduced as

$$\frac{\partial \psi_a(\mathbf{k})}{\partial \eta} + \Omega_{ab} \psi_b(\mathbf{k}) = \int d^3k_1 d^3k_2 \gamma_{abc}(\mathbf{k}, \mathbf{k_1}, \mathbf{k_2}) \psi_b(\mathbf{k_1}) \psi_c(\mathbf{k_2}) \tag{4.24}$$

with

$$\Omega_{ab} = \begin{pmatrix} 0 & -1 \\ -3/2 & 1/2 \end{pmatrix}. \tag{4.25}$$

γ_{abc} has only two non-vanishing terms

$$\begin{aligned} \gamma_{112}(\mathbf{k}, \mathbf{k_1}, \mathbf{k_2}) &= \frac{\mathbf{k} \cdot \mathbf{k_2}}{k_2^2} \delta_D(\mathbf{k} - \mathbf{k_{12}}) \equiv \alpha(\mathbf{k_1}, \mathbf{k_2}) \delta_D(\mathbf{k} - \mathbf{k_{12}}) \\ \gamma_{222}(\mathbf{k}, \mathbf{k_1}, \mathbf{k_2}) &= \frac{k^2 (\mathbf{k_1} \cdot \mathbf{k_2})}{2k_1^2 k_2^2} \delta_D(\mathbf{k} - \mathbf{k_{12}}) \equiv \beta(\mathbf{k_1}, \mathbf{k_2}) \delta_D(\mathbf{k} - \mathbf{k_{12}}) \end{aligned} \tag{4.26}$$

We try to find solution of the type

$$\psi_a(\mathbf{k}, \eta) = \sum_{n=1}^{\infty} a^n \psi_a^{(n)}(\mathbf{k}). \tag{4.27}$$

Substituting ψ_a in the equation of motions we get the nth-order solution

$$\psi_a^{(n)}(\mathbf{k}) = \sigma_{ab}(n) \int d^3k_1 d^3k_2 \gamma_{bcd}(\mathbf{k}, \mathbf{k_1}, \mathbf{k_2}) \sum_{m=1}^{n-1} \psi_c^{(n-m)}(\mathbf{k_1}) \psi_d^{(m)}(\mathbf{k_2}), \tag{4.28}$$

where

$$\sigma_{ab}(n) = \frac{1}{(2n+3)(n-1)} \begin{pmatrix} 2n+1 & 2 \\ 3 & 2n \end{pmatrix}. \tag{4.29}$$

It is important to note that every solution is written using the low order solutions. As an example, let's calculate the second-order correction in perturbation theory,

$$\psi_a^{(2)}(\mathbf{k}) = \sigma_{ab}(2) \int d^3k_1 d^3k_2 \gamma_{bcd} \psi_c^{(1)}(\mathbf{k_1}) \psi_d^{(1)}(\mathbf{k_2}), \tag{4.30}$$

with

$$\sigma_{ab}(2) = \frac{1}{7} \begin{pmatrix} 5 & 2 \\ 3 & 4 \end{pmatrix}. \tag{4.31}$$

$\psi^{(1)}$ was evaluated in the linear case. Considering only the growing mode, the solution for the second order correction is

$$\psi^{(2)}(\mathbf{k}) = \begin{pmatrix} \delta^{(2)}_{\mathbf{k}} \\ \Theta^{(2)}_{\mathbf{k}} \end{pmatrix} = \int d^3k_1 d^3k_2 \delta_D(\mathbf{k} - \mathbf{k_{12}}) \begin{pmatrix} F_2(\mathbf{k_1}, \mathbf{k_2}) \\ G_2(\mathbf{k_1}, \mathbf{k_2}) \end{pmatrix} \delta^{(1)}_{\mathbf{k_1}} \delta^{(1)}_{\mathbf{k_2}}, \tag{4.32}$$

with

$$F_2(\mathbf{k_1}, \mathbf{k_2}) = \frac{5}{7} + \frac{1}{2} \frac{\mathbf{k_1} \cdot \mathbf{k_2}}{k_1 k_2} \left(\frac{k_1}{k_2} + \frac{k_2}{k_1} \right) + \frac{2}{7} \frac{(\mathbf{k_1} \cdot \mathbf{k_2})^2}{k_1^2 k_2^2}, \tag{4.33}$$

and

$$G_2(\mathbf{k_1}, \mathbf{k_2}) = \frac{3}{7} + \frac{1}{2} \frac{\mathbf{k_1} \cdot \mathbf{k_2}}{k_1 k_2} \left(\frac{k_1}{k_2} + \frac{k_2}{k_1} \right) + \frac{4}{7} \frac{(\mathbf{k_1} \cdot \mathbf{k_2})^2}{k_1^2 k_2^2}. \tag{4.34}$$

Eq. (4.32) can be generalized to higher-order as

$$\psi^{(n)}(\mathbf{k}) = \begin{pmatrix} \delta^{(n)}_{\mathbf{k}} \\ \Theta^{(n)}_{\mathbf{k}} \end{pmatrix} = \int d^3k_1 ... d^3k_n \delta_D(\mathbf{k} - \mathbf{k_{1...n}}) \begin{pmatrix} F_n(\mathbf{k_1}, ..., \mathbf{k_n}) \\ G_n(\mathbf{k_1}, ..., \mathbf{k_n}) \end{pmatrix} \delta_{\mathbf{k_1}} ... \delta_{\mathbf{k_n}}. \tag{4.35}$$

Given $F_1(\mathbf{k_1}..., \mathbf{k_n}) \equiv 1$ and $G_1(\mathbf{k_1}..., \mathbf{k_n}) \equiv 1$, we can iteratively calculate the F and the G functions:

$$\begin{aligned} F_n(\mathbf{k_1}, ..., \mathbf{k_n}) = \sum_{m=1}^{n-1} \frac{G_m(\mathbf{k_1}, ..., \mathbf{k_m})}{(2n+3)(n-1)} [(2n+1)\alpha(\mathbf{k_1}, \mathbf{k_2}) F_{n-m}(\mathbf{k_{m+1}}, ..., \mathbf{k_n}) \\ + 2\beta(\mathbf{k_1}, \mathbf{k_2}) G_{n-m}(\mathbf{k_{m+1}}, ..., \mathbf{k_n})] \end{aligned} \tag{4.36}$$

$$\begin{aligned} G_n(\mathbf{k_1}, ..., \mathbf{k_n}) = \frac{2n}{3} F_n(\mathbf{k_1}, ..., \mathbf{k_n}) \\ - \sum_{m=1}^{n-1} \frac{\mathbf{k} \cdot \mathbf{k_{1...n}}}{(\mathbf{k_{1...n}})^2} F_{n-m}(\mathbf{k_{m+1}}, ..., \mathbf{k_n}) G_m(\mathbf{k_1}, ...\mathbf{k_m}). \end{aligned} \tag{4.37}$$

It is interesting to note that the difference between the solution of EdS model and ΛCDM are below the percent level, thus it is possible to use the solutions of EdS as solutions for the ΛCDM model.

Non-Linear Power Spectrum

Remember that the power spectrum is defined by $P(k) = |\delta_{\mathbf{k}}|^2$. So, substituting $\delta_{\mathbf{k}}$ as a series we obtain:

$$\begin{aligned} \langle \delta_{\mathbf{k_1}} \delta_{\mathbf{k_2}} \rangle = \left\langle \delta^{(1)}_{\mathbf{k_1}} \delta^{(1)}_{\mathbf{k_2}} \right\rangle + \left(\left\langle \delta^{(1)}_{\mathbf{k_1}} \delta^{(2)}_{\mathbf{k_2}} \right\rangle + \left\langle \delta^{(2)}_{\mathbf{k_1}} \delta^{(1)}_{\mathbf{k_2}} \right\rangle \right) \\ + \left(\left\langle \delta^{(1)}_{\mathbf{k_1}} \delta^{(3)}_{\mathbf{k_2}} \right\rangle + \left\langle \delta^{(3)}_{\mathbf{k_1}} \delta^{(1)}_{\mathbf{k_2}} \right\rangle + \left\langle \delta^{(2)}_{\mathbf{k_1}} \delta^{(2)}_{\mathbf{k_2}} \right\rangle \right) + ... \end{aligned} \tag{4.38}$$

The first term is of the second order and we know that it gives $(2\pi)^3 \delta_D(\mathbf{k_1} - \mathbf{k_2}) P_{lin}(k_1)$. The terms in the first brackets are of the third order, while the terms in the second brackets are of fourth order and so on.

Now the first term of the first brackets (the second term gives the same contribution):

$$\left\langle \delta^{(1)}_{\mathbf{k_1}} \delta^{(2)}_{\mathbf{k_2}} \right\rangle = \int d^3q_1 d^3q_2 \; F_2(\mathbf{q_1}, \mathbf{q_2}) \delta_D(\mathbf{k} - \mathbf{q_{12}}) \left\langle \delta^{(1)}_{\mathbf{k}} \delta^{(1)}_{\mathbf{q_1}} \delta^{(1)}_{\mathbf{q_2}} \right\rangle = 0 \tag{4.39}$$

for Gaussian initial condition. In the second bracket we have two equal term and a third one that are

$$\left\langle \delta^{(1)}_{\mathbf{k_1}} \delta^{(3)}_{\mathbf{k_2}} \right\rangle \equiv \delta(\mathbf{k_{12}}) P_{13}(k_1) = \delta(\mathbf{k_{12}}) P_{31}(k_1) \tag{4.40}$$

$$= 3P_{lin}(k_1)\delta_D(\mathbf{k_{12}}) \int d^3q F_3(-\mathbf{k_1}, \mathbf{q}, -\mathbf{q}) P_{lin}(q), \tag{4.41}$$

$$\begin{aligned} \left\langle \delta^{(2)}_{\mathbf{k_1}} \delta^{(2)}_{\mathbf{k_2}} \right\rangle &\equiv \delta_D(\mathbf{k_{12}}) P_{22}(k_1) \\ &= 2\delta_D(\mathbf{k_{12}}) \int d^3q F_2^2(\mathbf{q}, \mathbf{k} - \mathbf{q}) P_{lin}(q) P_{lin}(|\mathbf{k} - \mathbf{q}|). \end{aligned} \tag{4.42}$$

Tree-Level Bispectrum

The bispectrum at the lowest order in perturbation theory is

$$\begin{aligned} \langle \delta_{\mathbf{k_1}} \delta_{\mathbf{k_2}} \delta_{\mathbf{k_3}} \rangle &= \left\langle \delta^{(1)}_{\mathbf{k_1}} \delta^{(1)}_{\mathbf{k_2}} \delta^{(1)}_{\mathbf{k_3}} \right\rangle \\ &\quad + \left\langle \delta^{(1)}_{\mathbf{k_1}} \delta^{(1)}_{\mathbf{k_2}} \delta^{(2)}_{\mathbf{k_3}} \right\rangle + 2 \text{ Perm.} \end{aligned} \tag{4.43}$$

The first term vanishes because of Gaussian initial condition. The second term reduces as

$$\begin{aligned} \left\langle \delta^{(1)}_{\mathbf{k_1}} \delta^{(1)}_{\mathbf{k_2}} \delta^{(2)}_{\mathbf{k_3}} \right\rangle &\propto \delta_D(\mathbf{k_{123}}) B(\mathbf{k_1}, \mathbf{k_2}, \mathbf{k_3}) \\ &= \left\langle \delta^{(1)}_{\mathbf{k_1}} \delta^{(1)}_{\mathbf{k_2}} \int d^3q_1 d^3q_2 \; \delta_D(\mathbf{k_3} - \mathbf{q_{12}}) F_2(\mathbf{q_1}, \mathbf{q_2}) \delta^{(1)}_{\mathbf{q_1}} \delta^{(1)}_{\mathbf{q_2}} \right\rangle = \\ &= \int d^3q_1 d^3q_2 \; \delta_D(\mathbf{k_3} - \mathbf{q_{12}}) F_2(\mathbf{q_1}, \mathbf{q_2}) \left\langle \delta^{(1)}_{\mathbf{k_1}} \delta^{(1)}_{\mathbf{k_2}} \delta^{(1)}_{\mathbf{q_1}} \delta^{(1)}_{\mathbf{q_2}} \right\rangle \end{aligned} \tag{4.44}$$

Expanding the trispectrum into connected and non-connected part and introducing the lower order term in perturbation theory allows to gets

$$B(\mathbf{k_1}, \mathbf{k_2}, \mathbf{k_3}) = 2 \left[F_2(\mathbf{k_1}, \mathbf{k_2}) P_{lin}(k_1) P_{lin}(k_2) + 2 \text{ Perm. } \right]. \tag{4.45}$$

that is the so called *tree-level bispectrum*. In order to get rid of the scale-dependence of the triangles, we can define the reduced bispectrum

$$Q(\mathbf{k_1}, \mathbf{k_2}, \mathbf{k_3}) = \frac{B(\mathbf{k_1}, \mathbf{k_2}, \mathbf{k_3})}{P(k_1)P(k_2) + 2 \text{ Perm.}} \tag{4.46}$$

Let's fix $\mathbf{k_1}$ and $\mathbf{k_2}$ and vary the angle between them. Calculations show that it is easier to find galaxies in a row than in an equilateral configuration ($B(\mathbf{k_1}, \mathbf{k_2}, 0) > B(\mathbf{k_1}, \mathbf{k_2}, \pi/2)$). Physically, this means that filaments are the preferred structures in the Universe. Thus, non-linear perturbation theory provides the results of measurements.

4.3 Parameter Degeneracy

Let's call n_g the number counts of the galaxies in real space. Thus, we can define the fluctuations of this number count just like we did for the matter density field, i.e.

$$n_g = \bar{n}[1 + \delta_g]. \tag{4.47}$$

This quantity is important because it is impossible to directly measure the matter density field because of the dark matter component. What we assume is that galaxies trace the matter field, i.e.

$$\delta_g = b\delta \tag{4.48}$$

where δ represents the overdensity field of the matter distribution while b is the linear prefactor that relate the two field.

As well as it is not possible to directly measure the matter field, it is not possible to measure the position of galaxies in real space because of their proper motion that affects the measured distribution. What we get is a distribution in redshift space which power spectrum is slightly different from the real one. Kaiser (1987) first shows how to relate the actual power spectrum with the measured ones

$$P^s(k, \mu) = \left(1 + \frac{f}{b}\mu^2\right)^2 b^2 P_L(k) \tag{4.49}$$

where $\mu = \mathbf{k} \cdot \mathbf{r}$, $f = \frac{\partial \log D}{\partial \log a}$ and $P_L(k)$ is the power spectrum of the matter. The normalization of the power spectrum can be set using σ_8. What happens is that in the power spectrum estimate, σ_8 is degenerate with f and b (Pezzotta et al. 2016). This means that we need new statistics in order to remove parameter degeneracy. This role is undertaken by the bispectrum. Estimators of the 3-dimensional bispectrum were developed through the last years, but yet, it is not sufficient to completely remove degeneracy. For this reason, I introduce a new bispectrum estimator in harmonic space, with the aim of combining it with the matter power spectrum and the 3-dimensional bispectrum estimator and help in the task of removing degeneracy.

CHAPTER 5

Analysis of angular density fields

The aim of this work is to study the behavior of the angular statistics of the distribution of matter lying on a shell of radius z. Although it seems there are no advantages, since the number of triangles is lower in 2-dimensional case with respect to the 3-dimensional one, it is important to derive and work with angular estimators because of the development of photometric surveys, in which only the position of galaxy at a given redshift is measured, so that the result of these measurements is a shell of projected galaxies along the line of sight. Ongoing and future surveys are going in this direction, i.e. the Dark Energy Survey (DES), the Physics of Accelerating Universe survey (PAU) and Euclid survey.

The aim of this work is to develop (and apply to data) estimators of both power spectrum and bispectrum. It was showed, in fact, that the combined use of both these statistics allow to improve the results on the constraints (Fry 1994; Scoccimarro et al. 2004; Sefusatti et al. 2012; Sefusatti & Komatsu 2007). Example of projected statistics are present in literature, for example in (Buchalter et al. 2000; Verde et al. 2000b; Hashimoto et al. 2016a,b).

5.1 Spherical Projection

Since the distribution of galaxies is clearly 3-dimensional, we need to integrate it along the line of sight, obtaining a 2-dimensional scalar field defined on the sphere. The integrated distribution is:

$$\delta(\widehat{\mathbf{n}}) = \int dz\, \phi(z)\delta_g(\widehat{\mathbf{n}}, z), \tag{5.1}$$

where $\phi(z)$ is the radial selection function. In our analysis we will consider all the galaxies within a redshift bin centered at the z of interest. The observed galaxy distribution along the line of sight inside the bin is described by the radial selection $\phi(z)$ that characterizes the probability of finding a galaxy within the bin, normalized to unity within the redshift range of interest

$$\int\limits_{z\in\Delta z} dz'\ \phi(z') = 1. \tag{5.2}$$

In case of zero-width redshift bin, i.e. the case in which we are considering only the galaxy located at an exact redshift, the radial selection behaves like a Dirac delta. Otherwise, the radial selection is composed by a window function $W(z)$, that takes in account the selection characteristic of the bin, convolved with the probability that a galaxy is located inside the bin (Crocce et al. 2011). We can define this probability term according to the galaxies redshift, the true one or the photometric one, case in which the photo-z

error of the photometric galaxy survey is taken into account. In the exact case, the radial selection is simply the number of galaxies N_g per unit of redshift times the window function:

$$\phi(z) = \frac{dN_g}{dz} W(z). \tag{5.3}$$

In the photo-z case, the window function is convolved with the probability that the photometric measured redshift of the galaxy is the actual redshift of the galaxy $P(z|z_p)$ (Budavári et al. 2003)

$$\phi(z) = \frac{dN_g}{dz} \int dz_p \; P(z|z_p) W(z_p) \tag{5.4}$$

where $W(z_p)$ is the photometric redshift window function. In what follows, we will consider the photo-z contribution to the radial selection, considering a top-hat window function with same extrema as the redshift bin. Furthermore, we consider the photometric error probability as a Gaussian distribution around the true redshift of the galaxy (Ma et al. 2006).

5.2 Spherical decomposition

The integrated matter distribution in eq. (5.1) is actually a spherical field, making possible its decomposition with the Spherical Harmonics. Inserting eq. (4.2) and eq. (5.1) in eq. (1.2), we obtain the harmonic coefficients for the $\delta(\hat{\mathbf{n}})$:

$$a_{lm} = \int d\Omega \delta(\hat{\mathbf{n}}) Y^*_{lm}(\hat{\mathbf{n}}) \tag{5.5}$$

$$= \int dz \phi(z) \int_{S^2} d\Omega \int \frac{d^3k}{(2\pi)^3} \, \delta_{\mathbf{k}}(z) e^{i\mathbf{k}\cdot\mathbf{r}} Y^*_{lm}(\hat{\mathbf{n}}). \tag{5.6}$$

The plane-wave expansion:

$$e^{i\mathbf{k}\cdot\mathbf{r}} = e^{ikr\hat{\mathbf{k}}\cdot\hat{\mathbf{n}}} = 4\pi \sum_{l=0}^{\infty} \sum_{m=-l}^{m=l} i^l j_l(kr) Y^*_{lm}(\hat{\mathbf{k}}) Y_{lm}(\hat{\mathbf{n}}), \tag{5.7}$$

gives us the possibility to get rid of the integration over the solid angle Ω exploiting the orthonormalisation property of the Spherical Harmonics[1]:

$$a_{lm} = 4\pi i^l \int dz \phi(z) \int \frac{d^3k}{(2\pi)^3} \, \delta_{\mathbf{k}}(z) j_l(kr(z)) Y^*_{lm}(\hat{\mathbf{k}}). \tag{5.8}$$

In the next sections I'll exploit eq. 5.8 in order to get the prediction models for the angular spectrum and bispectrum in the integrated galaxy distribution framework.

[1] $\int_{S^2} d\Omega \; Y^*_{lm}(\hat{\mathbf{n}}) Y_{l'm'}(\hat{\mathbf{n}}) = \delta_l^{l'} \delta_m^{m'}$

5.2.1 The angular power spectrum C_l

Recalling eq. (1.10) and (5.8), we can write the angular spectrum of the integrated density fluctuations as follows:

$$\begin{aligned}\langle a_{l_1 m_1} a^*_{l_2 m_2}\rangle =&(4\pi)^2 i^{l_1-l_2}\int dz_1 dz_2 \phi(z_1)\phi(z_2)\\ &\times\int \frac{d^3k_1}{(2\pi)^3}\frac{d^3k_2}{(2\pi)^3}\langle\delta_{\mathbf{k}_1}(z_1)\delta_{\mathbf{k}_2}(z_2)\rangle\\ &\times j_{l_1}(k_1\, r(z_1))j_{l_2}(k_2\, r(z_2))Y^*_{l_1 m_1}(\hat{\mathbf{k}}_1)Y_{l_2 m_2}(\hat{\mathbf{k}}_2)\,,\end{aligned} \tag{5.9}$$

where $r_i \equiv r(z_i)$. As we already saw in eq. (4.3), the product $\langle\delta_{\mathbf{k}_1}(z_1)\delta_{\mathbf{k}_2}(z_2)\rangle$ defines the power spectrum of the full distribution. Introducing it in eq. (5.9), we can rewrite:

$$\begin{aligned}\langle a_{l_1 m_1} a^*_{l_2 m_2}\rangle =& (4\pi)^2 i^{l_1-l_2}\int dz_1 dz_2 \phi(z_1)\phi(z_2)\\ &\times\int \frac{d^3k_1}{(2\pi)^3}\frac{d^3k_2}{(2\pi)^3}(2\pi)^3 P_L(k_1,z_1,z_2)\delta^D(\mathbf{k}_1+\mathbf{k}_2)\\ &\times j_{l_1}(k_1 r(z_1))j_{l_2}(k_2 r(z_2))Y^*_{l_1 m_1}(\hat{\mathbf{k}}_1)Y_{l_2 m_2}(\hat{\mathbf{k}}_2).\end{aligned} \tag{5.10}$$

Using the properties of the δ^D in spherical coordinate system:

$$\delta^D(\mathbf{k}+\mathbf{k}_0) = \frac{1}{k^2}\delta^D(k+k_0)\delta^D(\hat{\mathbf{k}}+\hat{\mathbf{k}}_0), \tag{5.11}$$

we get:

$$\begin{aligned}\langle a_{l_1 m_1} a^*_{l_2 m_2}\rangle =& \frac{(4\pi)^2}{(2\pi)^3} i^{l_1-l_2}\int dz_1 dz_2 \phi(z_1)\phi(z_2)\\ &\times\int d^3k_1 P_L(k_1,z_1,z_2) j_{l_1}(k_1 r(z_1)))Y^*_{l_1 m_1}(\hat{\mathbf{k}}_1)\\ &\times j_{l_2}(-k_1 r(z_2))Y_{l_2 m_2}(-\hat{\mathbf{k}}_1).\end{aligned} \tag{5.12}$$

Now, exploiting the parity symmetry of the Spherical Bessel functions and of the Spherical Harmonics,

$$j_l(-x) = (-1)^l j_l(x) \tag{5.13}$$

$$Y_{lm}(-x) = (-1)^l Y_{lm}(x) \tag{5.14}$$

and the orthonormality of the Spherical Harmonics, we get:

$$\begin{aligned}\langle a_{l_1 m_1} a^*_{l_2 m_2}\rangle =& \delta^{l_2}_{l_1}\delta^{m_2}_{m_1}(4\pi)^2 i^{l_1-l_2}\int dz_1 dz_2 \phi(z_1)\phi(z_2)\\ &\times\int \frac{dk_1}{(2\pi)^3}k_1^2 P_L(k_1,z_1,z_2) j_{l_1}(k_1 r(z_1))j_{l_2}(k_2 r(z_2)).\end{aligned} \tag{5.15}$$

Thus, the angular spectrum is

$$C_l = \frac{2}{\pi}\int k^2 dk \int dz_1 dz_2\ \phi(z_1)\phi(z_2) j_l(kr_1)j_l(kr_2)P(k,z_1,z_2). \tag{5.16}$$

The angular spectrum changes with respect to the scales at which we are evaluating it. In addition, as we go to smaller and smaller scales, the evaluation of C_l gets computationally harder because of the oscillatory behavior of the spherical Bessel function $j_l(x)$ for $x \gg 1$. Moreover, on the largest scales the redshift space distortions (RSD) become important, forcing us to add this contribution to the calculation. If we divide the interval of k into two, small and large scales, we can deal with C_l in two separate ways, allowing us to write it in a more computationally feasible way.

Large Scales

On the largest scales, we can take advantage of the linear approach to describe the galaxy power spectrum. In the linear approach the time-dependency of the power spectrum is simply factorized-out,

$$P(k,z) \simeq D(z)^2 P_L(k), \tag{5.17}$$

where $D(z)$ is the growth function characterizing the time-evolution of the matter fluctuations in the linear regime:

$$\delta(z) = D(z)\delta_L. \tag{5.18}$$

We can then rewrite the exact formula of the angular power spectrum as:

$$C_l = \frac{2}{\pi}\int k^2 dk P_L(k)\Psi_l^2(k), \tag{5.19}$$

with integrated selection function:

$$\Psi_l(k) = \int dz \phi(z) D(z) j_l(kr)\,, \tag{5.20}$$

where we left implicit the redshift dependence of the line-of-sight distance $r = r(z)$.

As I said earlier, the redshift space distorsions (RSD) play an important role in biasing the statistics at large scales, while they vanish at the smallest scale. Following Padmanabhan et al. (2007) and Crocce et al. (2011), in order to account for the RSD effect, we modified the integrated radial selection $\Psi_l(k)$ as follows:

$$\begin{aligned}\Psi_l^{RSD}(k) = \int dz \phi(z) D(z) \Bigg[& \frac{(2l^2+2l-1)}{(2l_3)(2l-1)} j_l(kr) \\ & - \frac{l(l+1)}{(2l-1)(2l1+1)} j_{l-2} \\ & - \frac{(l+1)(l+2)}{(2l+1)(2l+3)} j_{l+1}(kr) \Bigg]\,.\end{aligned} \tag{5.21}$$

.

Small Scales

Evaluate the angular power spectrum in eq. (5.16) may be computationally hard. Howevere, it's possible to make eq. (5.16) more feasible by exploiting the so-called Limber approximation (Limber 1953; Kaiser 1992, 1998) that follows from the orthogonality relation of the spherical Bessel functions:

$$\int dk\; k^2 j_l(kr_1) j_l(kr_2) f(k) \simeq \frac{\pi}{2}\frac{\delta^D(r_1 - r_2)}{r_1^2} f\left(\frac{l+1/2}{r_1}\right). \tag{5.22}$$

The higher the l the closer are the approximation results to the exact ones. This approximation leads to the following expression for C_l's:

$$C_l^{limb} = \int dz \, \frac{\phi^2(z)}{r^2(z)|r'(z)|} \, P\left(\frac{l+1/2}{r(z)}, z\right). \tag{5.23}$$

where we use the well-known property of Dirac's delta:

$$\delta^D(f(x)) = \sum_i \frac{\delta^D(x - x_i)}{|f'(x_i)|}, \tag{5.24}$$

where the x_i's are the zeros of the function $f(x)$. As well as the galaxy distribution, with the Limber approximation the angular spectrum is just the integral along the line of sight of the full galaxy power spectrum, convolved with a selection functions.

5.2.2 Angular Bispectrum

Recalling the definition of the harmonic coefficients for the integrated galaxies distribution (eq. 5.8), we can write the angular bispectrum (1.31) as:

$$\begin{aligned}\langle a_{l_1 m_1} a_{l_2 m_2} a_{l_3 m_3} \rangle = \\ = \frac{1}{\pi^3} \left\{ \prod_{i=1}^{3} i^{l_i} \int dz_i \phi(z_i) \int d^3 k_i \, j_{l_i}(k_i r(z_i)) \, Y^*_{l_i m_i}(\hat{\mathbf{k}}_i) \right\} \\ \times \, \delta_D(\mathbf{k}_{123}) \, B(k_1, k_2.k_3, z_1, z_2, z_3) \,,\end{aligned} \tag{5.25}$$

where $\mathbf{k}_{123} = \mathbf{k}_1 + \mathbf{k}_2 + \mathbf{k}_3$. The next step is to replace the Dirac delta with its integral representation and take advantage of the plane-wave expansion, eq. (5.7), that is

$$\begin{aligned}\delta_D(\mathbf{k}_{123}) = \int \frac{d^3x}{(2\pi)^3} \prod_{i=1}^{3} e^{-i\mathbf{k}_i \cdot \mathbf{x}} \\ = 8 \int d^3x \prod_{i=1}^{3} \sum_{l_i', m_i'} i^{l_i'} j_{l_i'}(-k_i x) Y_{l_i' m_i'}(\hat{\mathbf{k}}_i) Y^*_{l_i' m_i'}(\hat{\mathbf{x}}),\end{aligned} \tag{5.26}$$

Then, exploiting the orthonormality of the spherical harmonics and the symmetry properties of the Bessel functions (eq. (5.13)), remembering that $i^{2l} = (-1)^l$, we obtain

$$\begin{aligned}\langle a_{l_1 m_1} a_{l_2 m_2} a_{l_3 m_3} \rangle = \frac{8}{\pi^3} \prod_{i=1}^{3} \left\{ \int dz_i \phi(z_i) \int dk_i k_i^2 j_{l_i}(k_i r(z_i)) \right\} \\ B(k_1, k_2, k_3; z_1, z_2, z_3) \int dx x^2 \; j_{l_1}(k_1 x) j_{l_2}(k_2 x) j_{l_3}(k_3 x) \\ \times \int d^2\hat{x} \; Y^*_{l_1 m_1}(\hat{\mathbf{x}}) Y^*_{l_2 m_2}(\hat{\mathbf{x}}) Y^*_{l_3 m_3}(\hat{\mathbf{x}}).\end{aligned} \tag{5.27}$$

The last line in eq. 5.27 is nothing but the Gaunt's integral (eq. 1.36). In fact:

$$\begin{aligned}\int d^2\hat{x} \; Y^*_{l_1 m_1}(\hat{\mathbf{x}}) Y^*_{l_2 m_2}(\hat{\mathbf{x}}) Y^*_{l_3 m_3}(\hat{\mathbf{x}}) = \\ = (-1)^{m1+m2+m3} \int d^2\hat{x} \; Y_{l_1 -m_1}(\hat{\mathbf{x}}) Y_{l_2 -m_2}(\hat{\mathbf{x}}) Y_{l_3 -m_3}(\hat{\mathbf{x}}) \\ = \mathcal{G}^{l_1 l_2 l_3}_{-m_1 -m_2 -m_3} = (-1)^{l_1+l_2+l_3} \mathcal{G}^{l_1 l_2 l_3}_{m_1 m_2 m_3} = \mathcal{G}^{l_1 l_2 l_3}_{m_1 m_2 m_3}.\end{aligned} \tag{5.28}$$

In the second line we used the reality condition for the Spherical Harmonics

$$Y^*_{lm}(x) = (-1)^m Y_{l-m}(x).$$

In the third line, we consider the fact that $\mathcal{G}^{l_1 l_2 l_3}_{m_1 m_2 m_3} \neq 0$ only if $m_1 + m_2 + m_3 = 0$, property heired by the Wigner-3j symbol $\begin{pmatrix} l_1 & l_2 & l_3 \\ -m_1 & -m_2 & -m_3 \end{pmatrix}$. We considered also the property of the Wigner-3j

$$\begin{pmatrix} l_1 & l_2 & l_3 \\ -m_1 & -m_2 & -m_3 \end{pmatrix} = (-1)^{l_1+l_2+l_3} \begin{pmatrix} l_1 & l_2 & l_3 \\ m_1 & m_2 & m_3 \end{pmatrix}$$

and the fact that $l_1 + l_2 + l_3$ must be even because of the presence of $\begin{pmatrix} l_1 & l_2 & l_3 \\ 0 & 0 & 0 \end{pmatrix}$ in the Gaunt integral explicit form. Hence, recalling the definition of the reduced angular bispectrum, eq. (1.38), we can write

$$\begin{aligned} b_{l_1 l_2 l_3} &= \frac{8}{\pi^3} \int dx x^2 \prod_{i=1}^{3} \left\{ \int dk_i k_i^2 dz_i \phi(z_i) j_{l_i}(k_i r(z_i)) j_{l_i}(k_i x) \right\} \\ &\quad \times B(k_1, k_2, k_3, z_1, z_2, z_3) \end{aligned} \tag{5.29}$$

Unlike the angular spectrum, the angular bispectrum is hard to provide even at the smallest scale. The introduction of linear theory, in fact, doesn't help us to reduce the amount of computation power we need to evaluate the seven integrals the bispectrum is composed of. Anyway, we can treat the small scales as well as we've done with the C_l's, obtaining an extremely simple form for the bispectrum, as we'll see below.

Limber Approximation

Similarly to the power spectrum, we can apply the Limber approximation, eq. (5.22), to the integrals over the k_i in eq. (5.29) in order to derive a simpler expression expected to be valid at small scales. We obtain

$$\begin{aligned} b_{l_1 l_2 l_3} &\simeq \int dx x^2 \prod_{i=1}^{3} \left\{ \int dz_i \frac{\phi(z_i)}{r_i^2} \delta_D(r_i - x) \right\} \\ &\quad \times B\left(\frac{l_1 + \frac{1}{2}}{r_1}, \frac{l_2 + \frac{1}{2}}{r_2}, \frac{l_3 + \frac{1}{2}}{r_3}; z_1, z_2, z_3 \right) \end{aligned} \tag{5.30}$$

Introducing $f(x) = \delta_D(r_1 - x)\delta_D(r_2 - x)$, the integral over x in the previous equation becomes

$$\begin{aligned} \int dx x^2 \, f(x) \delta_D(r_3 - x) &= f(r_3)\delta_D(r_1 - r_3)\delta_D(r_2 - r_3) \\ &= \frac{\delta_D(z_1 - z_3)}{|r_3'|} \frac{\delta_D(z_2 - z_3)}{|r_3'|}, \end{aligned} \tag{5.31}$$

with $r_3' \equiv dr_3(z)/dz$. Finally, integrating over z_1 and z_2, we obtain the Limber approximation for the angular bispectrum as

$$\begin{aligned} b_{l_1 l_2 l_3} &= \int dz \phi(z)^3 \frac{1}{r(z)^4 |r(z)'|^2} \\ &\quad B\left(\frac{l_1 + \frac{1}{2}}{r(z)}, \frac{l_2 + \frac{1}{2}}{r(z)}, \frac{l_3 + \frac{1}{2}}{r(z)}; z \right), \end{aligned} \tag{5.32}$$

where we reinstated the explicit dependence of the line-of-sight distance r on redshift.

5.3 Angular Estimators

We already reviewed the estimators for the angular statistics in chapter 1. The purpose of this section is to analyze two different aspects of the estimators. First, the case of incomplete sky maps, then the fact that we have to take into account a large number of multipoles combinations.

In the case of incomplete maps, what happens is simple. The Spherical Harmonics orthonormality doesn't hold anymore, thus introducing some bias in the Harmonic coefficients, as we will see in the next section. As long as we work with sky fractions, we have to reduce this bias as much as possible. Luckily, there exist a powerful approximation that allows to reconstruct the true statistics starting from a biased one.

The second aspect is quite important since it affects the required computational efforts because of the number of bispectrum configurations, which scales as l^3_{max}. Even at low multipoles, i.e. $l_{max} = 100$, the number of bispectrum configurations is too high to be computed in a short time. I'll introduce then a binning in the multipoles interval, in order to evaluate the statistics on the multipole bins. Thus, binned estimators are required and they will be showed in the respective section.

5.3.1 Incomplete sky coverage

As we have seen, spherical harmonics form an orthonormal basis on the sphere. This means that the properties of spherical harmonic stand as far as we deal with full-spherical field. What if the spherical field contains some "gaps", i.e. region of the sphere in which the field is not defined? This is the normal routine in cosmological data analysis. For example, in CMB analysis, to prevent spurious contribution from galaxy emission or other foregrounds, it is customery to mask the region where non-cosmological components are present (i.e. the galactic plane). In LSS analysis, instead, the surveys do not look at the entire sky, but they are limited within a well-defined region of the sky. This means that the field that we want to analyse (the photon anisotropy or the number of galaxies distribution), represent an incomplete-spherical field.

In this case, the spherical harmonics lose their orthonormality. We can define the *coupling integral* (Peebles 1980)

$$\begin{aligned} W_{ll'mm'} &\equiv \int_{S^2} d\Omega\, W(\widehat{\mathbf{n}}) Y^*_{lm}(\widehat{\mathbf{n}}) Y_{l'm'}(\widehat{\mathbf{n}}) \\ &= \int_{S^2/G} d\Omega\, Y^*_{lm}(\widehat{\mathbf{n}}) Y_{l'm'}(\widehat{\mathbf{n}}), \end{aligned} \tag{5.33}$$

where $W(\widehat{\mathbf{n}})$ is a step function, equal to 0 within the gaps G, 1 otherwise. S^2/G indicates the sky region in which the field is defined.

The coupling integral $W_{ll'mm'}$ has an important physical meaning. It is the bias affecting the harmonic coefficients evaluated in incomplete-sky analysis, $\tilde{a}_{lm}$, with respect to the *exact* coefficients a_{lm} that are supposed to describe the field if it is measured on the full sky

$$\tilde{a}_{lm} = \int_{S^2/G} d\Omega\, T(\widehat{\mathbf{n}}) Y^*_{lm}(\widehat{\mathbf{n}}) = \sum_{l'} \sum_{m'} a_{l'm'} W_{ll'mm'}. \tag{5.34}$$

Power spectrum

Since the power spectrum is estimated starting from the a_{lm}'s evaluated from the *measured* map, in the incomplete sky analysis it is affected by the bias carried by the harmonic coefficients. It is possible to show (see, e.g. Komatsu et al. 2002), that the power spectrum defined by the incomplete-sky coeffients $\tilde{a}_{lm}$'s can be approximated as

$$\begin{aligned}
\langle \widetilde{C}_l \rangle &\equiv \frac{1}{2l+1} \sum_m \langle \tilde{a}_{lm} \tilde{a}^*_{lm} \rangle \\
&= \frac{1}{2l+1} \sum_{l'} C_{l'} \sum_{mm'} |W_{ll'mm'}|^2 \\
&\simeq \frac{1}{2l+1} C_l \sum_m \sum_{l'm'} \int_{S^2} d\Omega \; W(\widehat{\mathbf{n}}) Y^*_{lm}(\widehat{\mathbf{n}}) Y_{l'm'}(\widehat{\mathbf{n}}) \\
&\quad \times \int_{S^2} d\Omega' \; W(\widehat{\mathbf{n}}') Y^*_{lm}(\widehat{\mathbf{n}}') Y_{l'm'}(\widehat{\mathbf{n}}') \\
&= \frac{1}{2l+1} C_l \sum_m \int_{S^2} d\Omega \; W(\widehat{\mathbf{n}}) Y^*_{lm}(\widehat{\mathbf{n}}) \\
&\quad \times \int_{S^2} d\Omega' \; W(\widehat{\mathbf{n}}') Y^*_{lm}(\widehat{\mathbf{n}}') \delta^D(\widehat{\mathbf{n}} - \widehat{\mathbf{n}}') \\
&= \frac{1}{2l+1} C_l \int_{S^2} d\Omega \; W(\widehat{\mathbf{n}}) \frac{2l+1}{4\pi} P_l(1) \\
&\simeq f_{sky} C_l,
\end{aligned} \tag{5.35}$$

with C_l denoting the exact, full-sky power spectrum, while

$$f_{sky} \equiv \frac{\Delta\Omega}{4\pi}, \tag{5.36}$$

indicates the fraction of the sky the spherical field is defined on. We used the Spherical Harmonics properties:

$$\sum_{lm} Y_{lm}(\widehat{\mathbf{n}}) Y^*_{lm}(\widehat{\mathbf{n}}') = \delta^D(\widehat{\mathbf{n}} - \widehat{\mathbf{n}}'), \tag{5.37}$$

and

$$\sum_m Y_{lm}(\widehat{\mathbf{n}}) Y^*_{lm}(\widehat{\mathbf{n}}') = \frac{2l+1}{4\pi} P_l(\widehat{\mathbf{n}} \cdot \widehat{\mathbf{n}}') \tag{5.38}$$

and the fact that $P_l(1) = 1, \forall l$. The approximation is justified by the fact that $|W_{ll'mm'}|^2$ peaks very sharply at $l = l'$, while $C^{exact}_{l'}$ varies much slower than $|W_{ll'mm'}|^2$ in l'. Thus, we can consider it almost constant and take it out from the summation. This approximation works as long as the gaps are small and have simple geometry. In fact, the rapidity of $|W_{ll'mm'}|^2$ depends both on the size and of the shape of the mask! Once the approximation is done, the calculation involves only the discrete properties of the Spherical Harmonics orthogonality (in fact, we use only the property involving the summation, never the ones with the integral), so that the result depends only on the the number of l's and m's involved in the analysis and never on the integral over the (incomplete) sphere. The f_{sky} result is exact and depends only on the size of the mask, because, the assumption on the shape are done when we put $C_{l'}$ outside the $\sum_{l'}$.

Thus, in first approximation, the bias is simply parametrized by a constant f_{sky} depending only on the dataset we are interested in.

The diagonal variance of the estimator changes accordingly,

$$Var(\widetilde{C}_l) \approx \frac{Var(C_l)}{f_{sky}}. \tag{5.39}$$

The more the sky is covered by gaps, the less C_l configurations are detectable in the distribution, making the variance higher as a consequence of this *cosmic variance* effect.

Bispectrum

As we have seen, in the cases in which the spherical field is not fully defined, the spherical harmonics are affected by a bias, described by the coupling integral (eq. 5.33), and this bias is inherited by the angular spectrum as the parameters f_{sky}, that is, the fraction of the sky without gaps.

We can derive the bias inherited by the bispectrum simply considering the product:

$$\begin{aligned}\langle \tilde{a}_{l_1 m_1} \tilde{a}_{l_2 m_2} \tilde{a}_{l_3 m_3} \rangle &= \sum_{l_1' l_2' l_3'} \sum_{m_1' m_2' m_3'} \langle a_{l_1' m_1'} a_{l_2' m_2'} a_{l_3' m_3'} \rangle \\ &\times W_{l_1 l_1' m_1 m_1'} W_{l_2 l_2' m_2 m_2'} W_{l_3 l_3' m_3 m_3'} \\ &= \sum_{l_1' l_2' l_3'} b_{l_1' l_2' l_3'} \sum_{m_1' m_2' m_3'} \int_{S^2} d\Omega Y^*_{l_1 m_1}(\widehat{\mathbf{n}}) Y^*_{l_2 m_2}(\widehat{\mathbf{n}}) Y^*_{l_3 m_3}(\widehat{\mathbf{n}}) \\ &\times W_{l_1 l_1' m_1 m_1'} W_{l_2 l_2' m_2 m_2'} W_{l_3 l_3' m_3 m_3'},\end{aligned} \tag{5.40}$$

where, in the second equality, we exploit the fact that $m_1 + m_2 + m_3 = 0$ for the Gaunt integral and the parity of the summation on the m's. By means of the same argument we used for C_l's, that is $b_{l_1' l_2' l_3'}$ varies much slower than the coupling integral, and after a little math, the relation between the incomplete-sky bispectrum and the full-sky one reduces as (Komatsu et al. 2002):

$$\begin{aligned}\langle \tilde{a}_{l_1 m_1} \dots \tilde{a}_{l_3 m_3} \rangle &\simeq b_{l_1 l_2 l_3} \int_{S^2} d\Omega\, Y^*_{l_1 m_1}(\widehat{\mathbf{n}}) Y^*_{l_2 m_2}(\widehat{\mathbf{n}}) Y^*_{l_3 m_3}(\widehat{\mathbf{n}}) \\ &\times \sum_{l_1' m_1'} \int_{S^2} d\Omega_1 W(\widehat{\mathbf{n}}_1) Y_{l_1' m_1'}(\widehat{\mathbf{n}}_1) Y^*_{l_1 m_1}(\widehat{\mathbf{n}}_1) \\ &\times \sum_{l_2' m_2'} \int_{S^2} d\Omega_2\; W(\widehat{\mathbf{n}}_2) Y_{l_2' m_2'}(\widehat{\mathbf{n}}_2) Y^*_{l_2 m_2}(\widehat{\mathbf{n}}_2) \\ &\times \sum_{l_3' m_3'} \int_{S^2} d\Omega_3\; W(\widehat{\mathbf{n}}_3) Y_{l_3' m_3'}(\widehat{\mathbf{n}}_3) Y^*_{l_3 m_3}(\widehat{\mathbf{n}}_3) \\ &= b_{l_1 l_2 l_3} \int_{S^2} d\Omega\; W(\widehat{\mathbf{n}}) \\ &\times Y^*_{l_1 m_1}(\widehat{\mathbf{n}}) Y^*_{l_2 m_2}(\widehat{\mathbf{n}}) Y^*_{l_3 m_3}(\widehat{\mathbf{n}}),\end{aligned} \tag{5.41}$$

where we used the Spherical Harmonics property showed in eq. (5.37). Clearly, $[W(\widehat{\mathbf{n}}_1)]^3 = W(\widehat{\mathbf{n}}_1)$ since it is a step function. Introducing this in the bispectrum estimator (eq. 1.38),

using the definition of 3rd-order Gaunt integral (eq. 1.36) we obtain:

$$\begin{aligned}\langle\widetilde{b}_{l_1l_2l_3}\rangle &\simeq b_{l_1l_2l_3}\sum_{m_1m_2m_3}\int_{S^2}d\Omega_1 Y_{l_1m_1}(\widehat{\mathbf{n}}_1)Y_{l_2m_2}(\widehat{\mathbf{n}}_1)Y_{l_3m_3}(\widehat{\mathbf{n}}_1)\\ &\times\int_{S^2}d\Omega\, W(\widehat{\mathbf{n}})Y^*_{l_1m_1}(\widehat{\mathbf{n}})Y^*_{l_2m_2}(\widehat{\mathbf{n}})Y^*_{l_3m_3}(\widehat{\mathbf{n}})\\ &= b_{l_1l_2l_3}\int_{S^2}\frac{d\Omega}{4\pi}\frac{d\Omega_1}{4\pi}W(\widehat{\mathbf{n}})\times P_{l_1}(\widehat{\mathbf{n}}\cdot\widehat{\mathbf{n}_1})P_{l_2}(\widehat{\mathbf{n}}\cdot\widehat{\mathbf{n}_1})P_{l_3}(\widehat{\mathbf{n}}\cdot\widehat{\mathbf{n}_1})\\ &= f_{sky}b_{l_1l_2l_3},\end{aligned} \tag{5.42}$$

where $b_{l_1l_2l_3}$ is the full-sky bispectrum. Following Komatsu et al. (2002), we used the property in eq. (5.38) and the identity:

$$\int_{-1}^{1}\frac{dx}{2}P_{l_1}(x)P_{l_2}(x)P_{l_3}(x)=\begin{pmatrix}l_1 & l_2 & l_3\\ 0 & 0 & 0\end{pmatrix}^2. \tag{5.43}$$

Just like the angular spectrum, the bias introduced in the bispectrum from a incomplete-sky analysis is parametrized, in first approximation, by a factor that is the fraction of the sky in which the field is defined. The reliability of the approximation depends both on the size and the shape of the mask. As well as the C_l variance, the bispectrum variance increases due to the cosmic variance, i.e.:

$$Var(\widetilde{b}_{l_1l_2l_3})\approx\frac{Var(b_{l_1l_2l_3})}{f_{sky}}. \tag{5.44}$$

5.3.2 Binned estimators

We will consider, for our measurements, large l-bins both to increase the numerical efficiency of the bispectrum estimator code, but also to account for the mode-coupling induced by a relatively small window function and its effect on the power spectrum and bispectrum variance.

We define the binned estimator for the power spectrum given by

$$\widehat{C}_L\equiv\frac{\sum_{l\in L}(2l+1)\widehat{C}_l}{\sum_{l\in L}(2l+1)}, \tag{5.45}$$

corresponding to a simple weighted average of the C_l estimator, the weights being just the number of pairs for each multipole.

The variance of the binned estimator is evaluated after a bit of math, following the same passages that brought to the C_l estimator variance, obtaining:

$$\begin{aligned}\mathrm{Var}(\widehat{C}_L) &= \frac{\sum_{l\in L}(2l+1)\mathrm{Var}^G(\widehat{C}_l)}{\left[\sum_{l\in L}(2l+1)\right]^2}\\ &+\frac{\sum_{l\in L}\sum_{l'\in L}\sum_{m\in l}\sum_{m'\in l'}\langle a_{lm}a^*_{lm}a_{l'm'}a^*_{l'm'}\rangle}{\left[\sum_{l\in L}(2l+1)\right]^2}.\end{aligned} \tag{5.46}$$

If we take just the Gaussian component of (5.46), we obtain

$$\begin{aligned}\mathrm{Var}^G(\widehat{C}_L) &= \frac{\sum_{l\in L}(2l+1)\frac{2\widehat{C}_l}{(2l+1)}}{\left[\sum_{l\in L}(2l+1)\right]^2} \\ &= \frac{2\widehat{C}_L}{\sum_{l\in L}(2l+1)}\end{aligned} \tag{5.47}$$

Note that the form of eq. (5.47) is the same of eq. (1.30).

We can make the C_l estimation more efficient by replacing the numerator of eq. (5.45) with an integral of the non-normalized binned azimutally averaged harmonic transform of the spherical field (eq. (1.27)):

$$\begin{aligned}e_L(\widehat{\mathbf{n}}) &= \sum_{l\in L}\sqrt{2l+1}e_l(\widehat{\mathbf{n}}) \\ &= \sum_{l\in L}\sum_{m=-l}^{l}\sqrt{4\pi}a_{lm}Y_{lm}(\widehat{\mathbf{n}}).\end{aligned} \tag{5.48}$$

Thus

$$\begin{aligned}\int_{S^2}\frac{d\Omega}{4\pi}|e_L(\widehat{\mathbf{n}})|^2 &= \sum_{ll'}\sum_{mm'}a_{lm}a^*_{l'm'}\int_{S^2}d\Omega Y_{lm}(\widehat{\mathbf{n}})Y^*_{l'm'}(\widehat{\mathbf{n}}) \\ &= \sum_{l\in L}\sum_{m}|a_{lm}|^2 \\ &= \sum_{l\in L}(2l+1)\widehat{C}_l.\end{aligned} \tag{5.49}$$

Therefore, we can use the unit e_L, i.e.

$$I_L(\widehat{\mathbf{n}}) = \sum_{l\in L}\sum_{m=-l}^{l}\sqrt{4\pi}Y_{lm}(\widehat{\mathbf{n}}), \tag{5.50}$$

to get the number of pairs allowed inside a bin:

$$\begin{aligned}\int_{S^2}\frac{d\Omega}{4\pi}|I_L(\widehat{\mathbf{n}})|^2 &= \sum_{ll'}\sum_{mm'}\int_{S^2}d\Omega Y_{lm}(\widehat{\mathbf{n}})Y^*_{l'm'}(\widehat{\mathbf{n}}) \\ &= \sum_{ll'}\sum_{mm'}\delta^{l'}_{l}\delta^{m'}_{m} \\ &= \sum_{l\in L}(2l+1).\end{aligned} \tag{5.51}$$

so that we can rewrite eq. (5.45) in a more convenient (from the computational point of view) form:

$$\widehat{C}_L = \frac{\int_{S^2}\frac{d\Omega}{4\pi}|e_L(\widehat{\mathbf{n}})|^2}{\int_{S^2}\frac{d\Omega}{4\pi}|I_L(\widehat{\mathbf{n}})|^2} \tag{5.52}$$

In order to simplify the notation involved in the binned bispectrum formula, let's introduce

$$t_{123} \equiv \{l_1, l_2, l_3\} \tag{5.53}$$

and

$$T_{123} \equiv \{L_1, L_2, L_3\} \tag{5.54}$$

so that, assuming a l-bin size ΔL

$$\sum_{l_1,l_2,l_3 \in T_{123}} \equiv \sum_{t_{123} \in T_{123}} \equiv \sum_{l_1=L_1-\Delta L/2}^{L_1+\Delta L/2} \sum_{l_2=L_2-\Delta L/2}^{L_2+\Delta L/2} \sum_{l_3=L_3-\Delta L/2}^{L_3+\Delta L/2} \tag{5.55}$$

The binned bispectrum estimator is thus defined as:

$$\begin{aligned} \widehat{b}_{L_1L_2L_3} &= \frac{\sum\limits_{t_{123} \in T_{123}} h^2_{l_1l_2l_3} \widehat{b}_{l_1l_2l_3}}{\sum\limits_{t_{123} \in T_{123}} h^2_{l_1l_2l_3}} \\ &= \frac{\sum\limits_{t_{123} \in T_{123}} N_{trip} \widehat{b}_{l_1l_2l_3}}{\sum\limits_{t_{123} \in T_{123}} N_{trip}} \end{aligned} \tag{5.56}$$

where N_{trip} is the number of triangles in multipole space *with different m's* corresponding to the triplet defined by (l_1, l_2, l_3). The variance of the binned estimator is derived exploiting the pentaspectrum already seen in (1.50). What we get is:

$$\begin{aligned} \mathrm{Var}(\widehat{b}_{L_1L_2L_3}) = &\frac{\sum\limits_{t_{123} \in T_{123}} h^4_{l_1l_2l_3} \mathrm{Var}^G(\hat{b}_{l_1l_2l_3})}{\left[\sum\limits_{t_{123} \in T_{123}} h^2_{l_1l_2l_3}\right]^2} \\ &+ \frac{\sum\limits_{t_{123} \in T_{123}} \sum\limits_{t'_{123} \in T_{123}} h^2_{l_1l_2l_3} h^2_{l'_1l'_2l'_3} \langle \hat{b}_{l_1l_2l_3} \hat{b}_{l'_1l'_2l'_3} \rangle^{NG}}{\left[\sum\limits_{t_{123} \in T_{123}} h^2_{l_1l_2l_3}\right]^2}. \end{aligned} \tag{5.57}$$

The NG superscript indicates the non-Gaussian term that arise from the pentaspectrum, while $\mathrm{Var}^G(\hat{b}_{l_1l_2l_3})$ is the Gaussian variance we already saw in eq. (1.30)

$$\begin{aligned} \mathrm{Var}^G(\hat{b}_{l_1l_2l_3}) &= \frac{\sum\limits_{t_{123} \in T_{123}} h^2_{l_1l_2l_3} s_{l_1l_2l_3} C_{l_1} C_{l_2} C_{l_3}}{\left[\sum\limits_{t_{123} \in T_{123}} h^2_{l_1l_2l_3}\right]^2} \\ &= \frac{1}{\sum\limits_{t_{123} \in T_{123}} h^2_{l_1l_2l_3}} C_{L_1L_2L_3} \end{aligned} \tag{5.58}$$

Again, the binned variance assumes the same form of the unbinned one (eq. (1.52)).

Now let's take the full binned harmonic transform:

$$e_L(\widehat{\mathbf{n}}) \quad = \quad \sum_{l\in L}\sum_{m=-l}^{l} a_{lm}Y_{lm}(\widehat{\mathbf{n}}). \tag{5.59}$$

and its unit counterpart, multiplied by a tuned factor:

$$I_L(\widehat{\mathbf{n}}) \quad = \quad \sum_{l\in L}\sqrt{(4\pi)^{-1/3}(2l+1)}\sum_{m=-l}^{l} Y_{lm}(\widehat{\mathbf{n}})\delta_0^m. \tag{5.60}$$

Starting from (5.59) and (5.60), it is straightforward to obtain :

$$\widehat{b}_{L_1L_2L_3} = \frac{\int_{S^2}\frac{d\Omega}{4\pi}e_{L_1}(\widehat{\mathbf{n}})e_{L_2}(\widehat{\mathbf{n}})e_{L_3}(\widehat{\mathbf{n}})}{\int_{S^2}\frac{d\Omega}{4\pi}I_{L_1}(\widehat{\mathbf{n}})I_{L_2}(\widehat{\mathbf{n}})I_{L_3}(\widehat{\mathbf{n}})}. \tag{5.61}$$

CHAPTER 6

N-Body simulations

We are interested in comparing measurements of bispectra estimated using eq. (5.61) with predictions calculated with eq. (5.32). We applied the estimator to photometric mocks extracted from the N-body simulation named MICE7680 produced by the MICE collaboration[1] in order to match the specifications od the Dark Energy Survey (DES). This simulation involved 2048^3 dark matter particles in a volume of $L_{box} = 7680h^{-1}$Mpc assuming a ΛCDM cosmology with $\Omega_m = 0.25$, $\Omega_b = 0.044$ and $h = 0.7$ (see Fosalba et al. 2008; Crocce et al. 2010, 2011, for further details). We worked on spherical shells of varying width extracted from comoving outputs of MICE7680, centered on 125 different observers placed on a grid. Each shell is placed at redshift z=0.5 from the observer. The observers were placed in order to reduce the overlap between shells and get the lowest one among all the possible configurations (again see Crocce et al. 2011, for details).

These shells cover 1/8 of the sky, having right ascension and declination between $0^\circ - 90^\circ$ (fig. 6.1).

The radial distribution of the galaxies inside the bin follows the one expected in the Dark Energy Survey (DES), i. e.

$$\frac{dN}{dz} \propto \left(\frac{z}{\bar{z}}\right)^2 \exp\left[-\left(\frac{z}{\bar{z}}\right)^{1.5}\right], \tag{6.1}$$

where $\bar{z}$ is the redshift at the center of the bin, i.e. $\bar{z} = 0.5$.

The photo-z errors were introduced as random gaussian displacements on the position of the galaxies near $\bar{z}$, so that

$$d(z) = \frac{1}{\sqrt{2\pi}\sigma_z} \exp\left[-\frac{\delta z^2}{2\sigma_z}\right]. \tag{6.2}$$

Due to the presence of the photometric error, much of the small-scales radial information is lost. For this reason, we considered the amplitude of the redshift bins larger or comparable to the photo-z error (Simpson et al. 2009).

The 125 shells were extracted using different redshift bins and photo-z errors. The results are five different set of mocks with the following parameters:

Case	$\Delta z/(1+\bar{z})$	σ_z
1	0.03	0.03
2	0.05	0.03
3	0.03	0.06
4	0.05	0.06
5	0.15	0.06

[1] http://www.ice.cat/mice

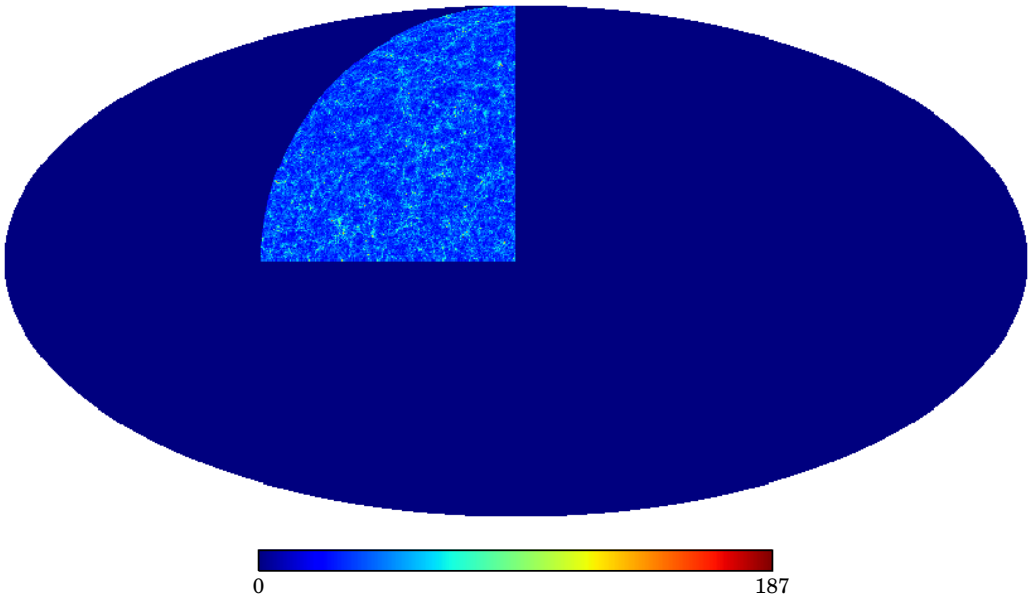

Figure 6.1: One of the 125 simulated shells. The visible sky cover only $1/8$ of the sphere.

6.1 Measurements vs Predictions I: C_l

We applied eq. (1.26) to the first four cases in the previous table in order to reproduce the C_l's of the mocked distribution of dark matter. The first case is shown in fig. 6.2. The measured C_l's are compared with the exact prediction both linear and non linear and that from the Limber approximation. The error bars on the C_l's are the mean standard deviation, i.e. $\sigma/\sqrt{N_{mocks}}$, that explains why the error bars are so small.

The linear predictions took in account the MICE power spectrum at $z = 0$. The non-linear power spectrum was extrapolated from the linear one using the halofit model (Takahashi et al. 2012). As we already wrote, the time-dependence of the linear power spectrum is factorizable out as the growth function at the z of interest (eq. (5.17)). In the non-linear regime, the time-dependence is slightly difficult to calculate, since it isn't scale-independent. Hence, the best way to get it is to interpolate several non-linear power spectra at redshift inside the bin. The problem is that it's not possible to apply this procedure when we deal with exact prediction because of the double integral in redshift in the C_l formula (eq. (5.16)). Since the bin width is quite smaller, the scale-dependence of the non-linear power spectrum should be negligible. For this reason, we approximated the non-linear time-dependence as

$$P_{NL}(z) = \frac{D^2(z)}{D^2(\bar{z})} P_{NL}(\bar{z}). \tag{6.3}$$

Anyway, we didn't get rid of the interpolation procedure. In fact, since the Limber approximated formula contains only one integral in redshift, we could apply the z-interpolation to it getting the best results for the predictions on small scales.

In the left bottom panel of fig. 6.2 it is possible to see how the exact prediction and the measurements agrees on the largest scales, where the linear regime is enough to describe the gravitational clustering ($\ell \lesssim 100$). On these scales the exact prediction,

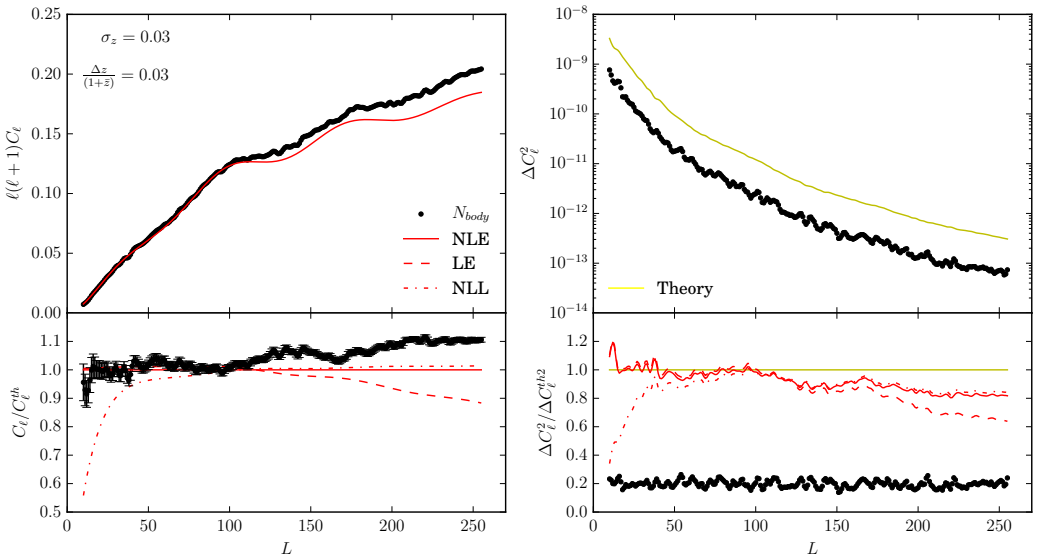

Figure 6.2: *Top panels*: Cl measured and the predicted one (left panels) and its variance (right panels). *Bottom panels*: Ratio between measurements and predictions, both for C_l and ΔC_l^2. The measurements are labeled with black points. NLE stands for non-linear exact prediction, LE for linear exact prediction, NLL for non-linear Limber approximated prediction. Theory is the variance calculated according to eq. (6.4)

both linear and non-linear, agree below the 1% level, while this is not the case for the Limber approximation as expected. On the smallest scales ($\ell \gtrsim 100$), the linear prediction deviates from the non-linear one and so do the measurements, that anyways stay below the 10% from the non-linear exact C_l's. It is reasonable to say that, when we deal with only one realization of the sky, the confidence level of measurements is well below the 2-σ level. The reason for this deviation is totally due to the non-linear effects in the mocked dark matter distribution and in some mask effects that the f_{sky} approximation isn't able to account for. Furthermore, the effects of the redshift bins and the photo-z error play an important role in the measurements-prediction deviation, as we will see further on. The Limber approximation with non-linear power spectrum is closer to the measurements because of the z-interpolation procedure we used in order to evaluate the correct time dependence of the matter power spectrum.

The effects of the mask are clearly visible in the right panels, where it is shown the measured Gaussian variance of the estimator compared to the theory that predicts it. The theory is evaluated using the measured C_l's, i.e.

$$\Delta C_l^{th2} = \frac{2}{2l+1}\langle C_l^{meas}\rangle^2. \tag{6.4}$$

The measurements are well below the theory, and this is explained by the diagonal 'leakage' of the C_l covariance matrix when measured on a incomplete sky (Crocce et al. 2011). The effect of the mask is to mix up the scales, thus leading to non-zero off-diagonal term in the covariance matrix. The first consequence is that the amplitude of the covariance diagonal decreases, while the one of the off-diagonal terms increase. In the Gaussian

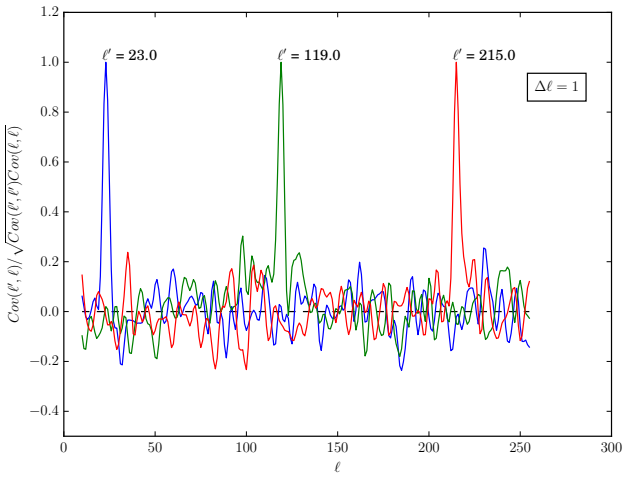

Figure 6.3: Trasversal cuts of the normalized C_l covariance matrix at different l's. The amplitude of the off-diagonal terms is non-zero even at the furthest scales. The peaks are normalized by the amplitude of diagonal covariance to show their relative height.

limit, this leakage is described by

$$\int dl' \; Cov(l, l') = \frac{2}{2l+1} C_l^2. \tag{6.5}$$

and is shown in fig. 6.3. This mask effect can be removed by taking the C_l's over multipole bins (eq. (5.52)) with $\Delta l \gtrsim 2 f_{sky}^{-1}$ (Cabré et al. 2007). In this case, in fact, the covariance matrix assumes a diagonal form closer to the full-sky one, while the off-diagonal terms approach to zero (without reaching it, fig. 6.4).

The effect of decreasing the off-diagonal terms is clear in fig. 6.5 where the binned C_l variances of the first case are shown, with $\Delta l = 16, 24$. In the binned case, the theory and the measured variances share the same order of magnitude. The tension between them is due to the sub-20% level off-diagonal terms that, although smaller than in the unbinned case, don't vanish at all.

It is important to remark that, at the same time, the theory doesn't agree with the variance coming from the predictions, and this happens whether or not the multipole binning is considered, reflecting the pre-existing tension between measured C_l's and predicted ones.

In fig. 6.6 the C_l's for the four cases are shown, compared to the predictions. Variance isn't shown because it behaves in the same way as the case 1. Fig. 6.6 tells us a lot about how the binning in redshift and the photo-z error affects the measured C_l's. In fact, the first thing that stands out is that increasing the z-bin width, the C_l's approach to zero, while the relative distance to the predictions decreases. This is explained by the fact that to the increase in the bin width corresponds an increase in the number of dark matter particles projected on the spherical shell taken into account, whose net effect is to homogenize the projected field thus decreasing the power of every scale. Indeed, the excess probability of finding two particles at a certain distance becomes lower as the homogeneity level grows. The decrease of the relative ratio between measurements and predictions shows how the incomplete-sky statistics become stronger increasing the amplitude of the field. Furthermore, it proves that the bin width plays an important role

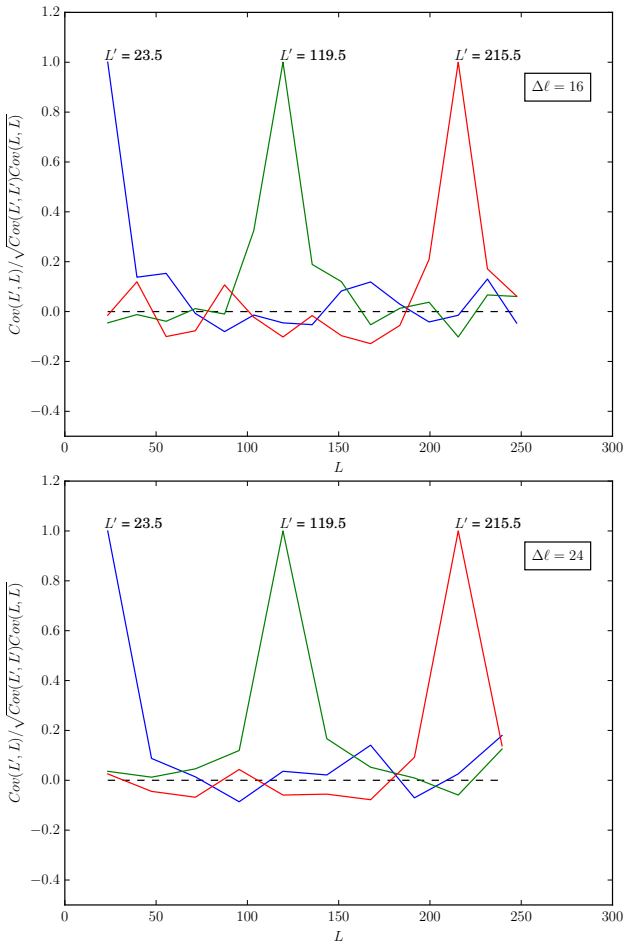

Figure 6.4: Transversal cuts of the C_l covariance matrix for two different binnings ($\Delta l = 16, 24$). The amplitude of the off-diagonal terms get close to zero as stronger is the binning. The height of the diagonal term approach to the real one.

when the C_l's are estimated from the observed sky.

At the same time, the photo-z error plays another important role, since as it increase, we have the homogenizing effect and the departure of the measurements from the predictions. The effect of the photo-z error is to include in the bin particles that are actually outside it and remove particles that, instead, are inside. In this way, the measurements are done over a field that is not actually the correct one, bringing an important systematic bias in the resulting statistics.

The same effects are expected to be observed also in the bispectrum as we are going to see in the next section.

6.2 Measurements vs Predictions II: Bispectrum

The estimation of the unbinned bispectrum is a highly time-consuming process. Furthermore, we already saw how the scale-mixing effect due to the mask makes useless to

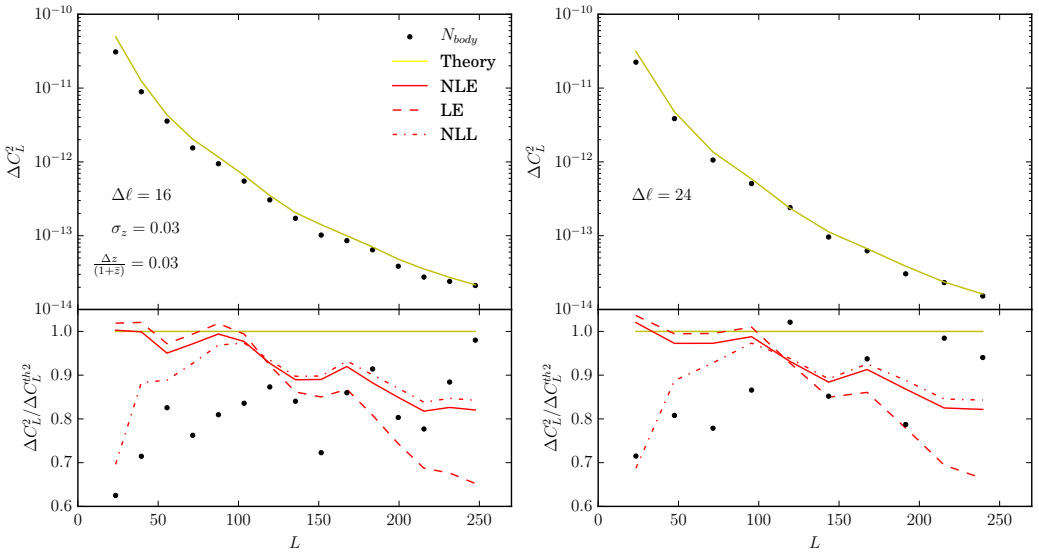

Figure 6.5: *Top panels*: Binned variance measured and their relative theory for $\Delta l = 16$(left panels) and $\Delta l = 24$(right panels). *Bottom panels*: Ratio between measurements and predictions.

estimate the variance for the unbinned case. For these reasons, we estimated directly the binned bispectra, considering $\Delta l = 16, 24$ and 40, i.e. $2f_{sky}^{-1}$, $3f_{sky}^{-1}$ and $5f_{sky}^{-1}$ respectively. In fig. 6.7 it is possible to see both bispectra and relative variances.

The x-axis is labeled by l_1, the first multipole of the triplet (l_1, l_2, l_3) on which the bispectrum is evaluated. The three multipole in the several configurations follows the $l_1 \geq l_2 \geq l_3$ rule, so that all the bispectra in plot below a certain l_1 have all of the three multipoles below l_1. The vertical lines mark the points in which the three l's have the same amplitude, i. e. the bispectrum equilateral configurations. We can immediately see how the bispectra are consistent with the predictions at 2σ level. Here the predictions are calculated using the Limber approximation, in order to get rid of the seven-integral form of eq. (5.29). We considered three form for the bispectrum, depending on which scales we are interested in. For the linear case we used tree-level (TL) bispectrum (eq. (4.45)).

For the non-linear regime, we considered two fitted formula. Both of them take the form of the tree-level bispectrum, but improving the kernel F_2, which becomes:

$$\begin{aligned} F_2^{eff}(\mathbf{k}_i, \mathbf{k}_j) = & \frac{5}{7} a(n_i, k_i) a(n_j, k_j) \\ & + \frac{1}{2} \frac{\mathbf{k}_1 \cdot \mathbf{k}_2}{k_1 k_2} \left(\frac{k_1}{k_2} + \frac{k_2}{k_1} \right) b(n_i, k_i) b(n_j, k_j) \\ & + \frac{2}{7} \left(\frac{\mathbf{k}_1 \cdot \mathbf{k}_2}{k_1 k_2} \right)^2 c(n_i, k_i) c(n_j, k_j). \end{aligned} \tag{6.6}$$

In the Scoccimarro-Couchman approach (Scoccimarro & Couchman 2001), the three func-

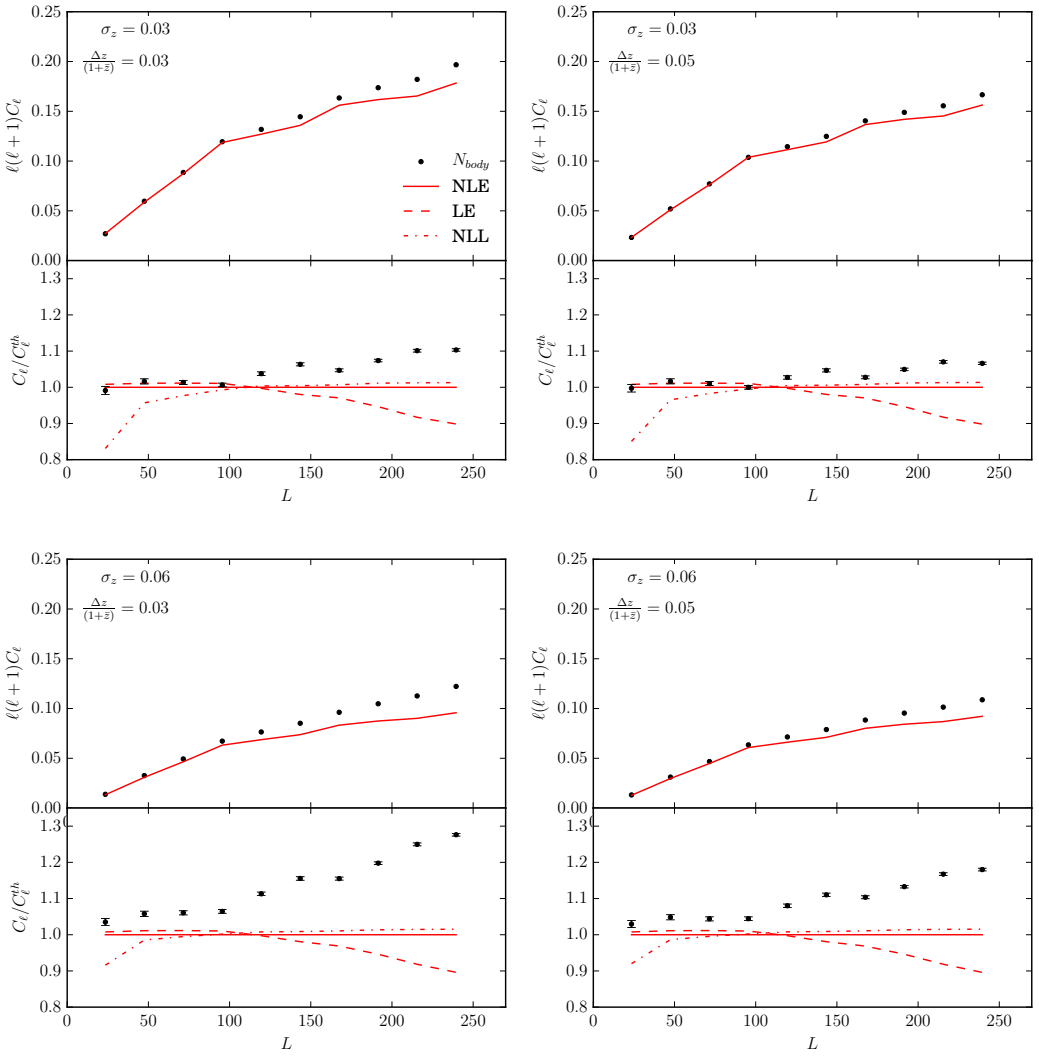

Figure 6.6: Comparison between measured and predicted binned C_l's for four out of five cases, with $\Delta l = 24$.

tions are written as:

$$
\begin{aligned}
a(n,k) &= \frac{1+\sigma_8^{a_6}(z)[0.7Q_3(n)]^{1/2}(qa_1)^{n+a_2}}{1+(qa_1)^{n+a_2}}, \\
b(n,k) &= \frac{1+0.2a_3(n+3)q^{n+3}}{1+q^{n+3.5}}, \\
c(n,k) &= \frac{1+4.5a_4/[1.5+(n+3)^4](qa_5)^{n+3}}{1+(qa_5)^{n+3.5}},
\end{aligned}
\tag{6.7}
$$

where n is the slope of the linear power spectrum at a given k,

$$
n \equiv \frac{d\log P_L(k)}{d\log k}, \tag{6.8}
$$

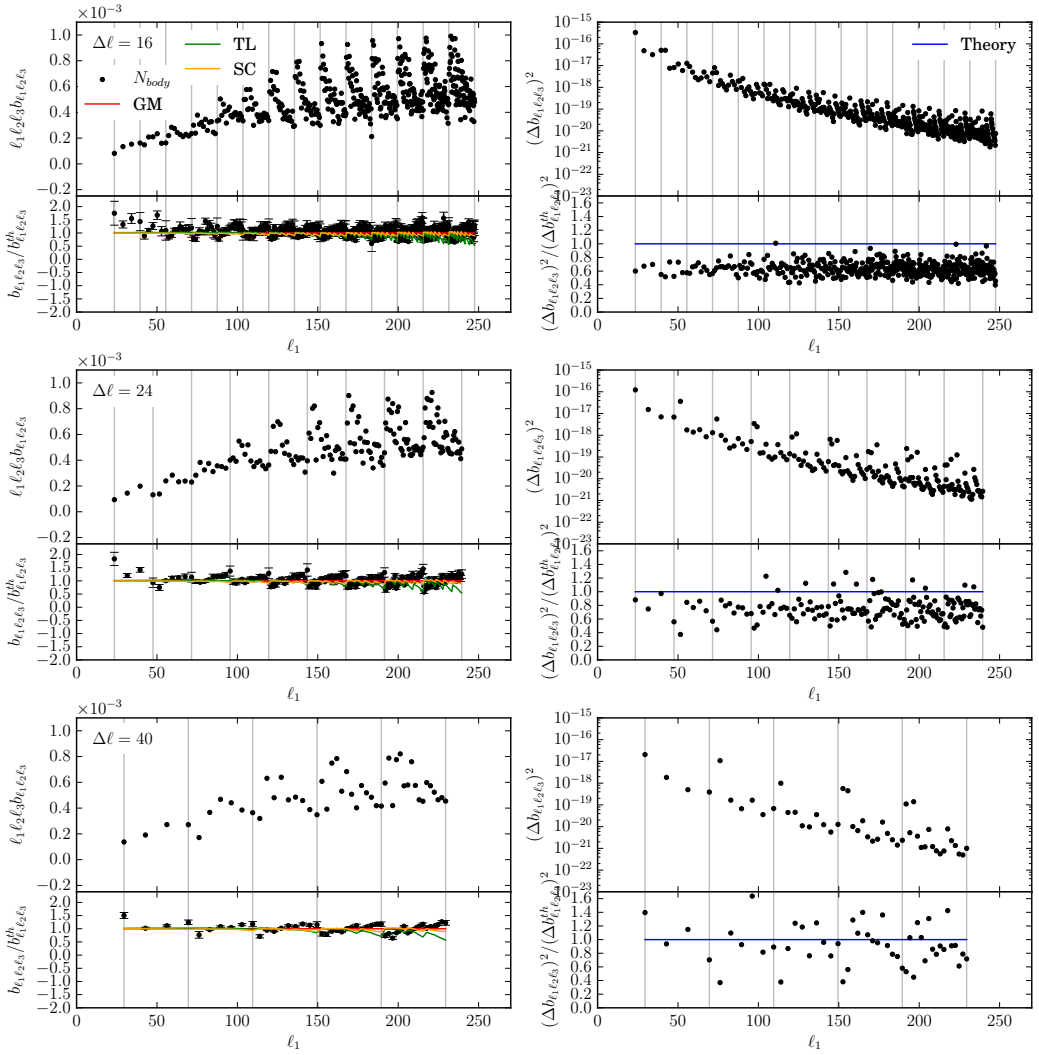

Figure 6.7: Bispectra measured and the predicted ones (left panels) and their variance (right panels), binned with $\Delta_l = 16$ (top panels), $\Delta_l = 24$ (middle panels) and $\Delta_l = 40$ (bottom panels) for the first case $\Delta z = 0.03(1 + \bar{z})$, $\sigma_z = 0.03$. The vertical lines label the position of the equilateral configuration. TL stands for Tree-Level bispectrum, SC for Scoccimarro-Couchman and GM for Gil-Marin. GM bispectra are considered as fiducial model for the bispectra comparison. Variance best model, i.e. the variance calculated using the measured C_l's, is taken as fiducial model for the variance comparison.

$q \equiv k/k_{nl}$, with k_{nl} representing the scale in which the non-linearities start to play a non-negligible role. We can define this scale as

$$\frac{k_{nl}P_L(k_{nl})}{2\pi^2} = 1. \tag{6.9}$$

Finally, the function Q_3 is defined as

$$Q_3(n) = \frac{4 - 2^n}{1 + 2^{n+1}}. \tag{6.10}$$

Note that on the linear regime we get $a, b, c \to 1$, recovering the usual tree-level formula.

The six parameters proposed by SC are

a_1=0.25	a_4=1
a_2=3.5	a_5=2
a_3=2	a_6=-0.2

Gil-Marin (Gil-Marín et al. 2012) improved this non-linear formula by adding three new a_i constant parameters, modifying the a, b, c functions as follows,

$$\begin{aligned}
\tilde{a}(n,k) &= \frac{1 + \sigma_8^{a_6}(z)[0.7Q_3(n)]^{1/2}(qa_1)^{n+a_2}}{1 + (qa_1)^{n+a_2}}, \\
\tilde{b}(n,k) &= \frac{1 + 0.2a_3(n+3)(qa_7)^{n+3+a_8}}{1 + (qa_7)^{n+3.5+a_8}}, \\
\tilde{c}(n,k) &= \frac{1 + 4.5a_4/[1.5 + (n+3)^4](qa_5 + a_9)^{n+3}}{1 + (qa_5)^{n+3.5+a_9}},
\end{aligned} \tag{6.11}$$

with

a_1=0.484	a_4=0.392	a_7=0.128
a_2=3.74	a_5=1.013	a_8=-0.722
a_3=-0.849	a_6=-0.575	a_9=-0.926

Note that GM→SC when $a_7 \to 1$ and $a_8, a_9 \to 0$.

Since the non-linear bispectrum prediction is evaluated using the Limber approximation, the z-dependence of the non-linear powers spectrum is interpolated, being this the best procedure to describe it correctly.

Let's come back to figure 6.7. The more we increase Δl the more consistent predictions and measurements are. This is especially true for the bispectrum Gaussian variance, where the effect of the off-diagonal terms on the bispectrum covariance matrix even in the binned case is shown. Unfortunately, the biasing effect of the off-diagonals is stronger than in the C_l case, so we must reach a very strong binning to reach complete consistency.

From now on, we consider $\Delta l = 24$, representing a good trade-off between accuracy in the estimation and reduction of triangle configurations. In fig. 6.8 we can see how the bispectrum behaves while measured on different binning and different photo-z errors. First of all, as the bin width increases, the power associated to each scale reduces, so that the bispectrum tends to zero when the bin is too wide. The explanation is again the homogenizing in the dark matter field, just like the C_l. Another affinity with the C_l's is the lowering effect due to the photo-z error, changing the dark matter number density

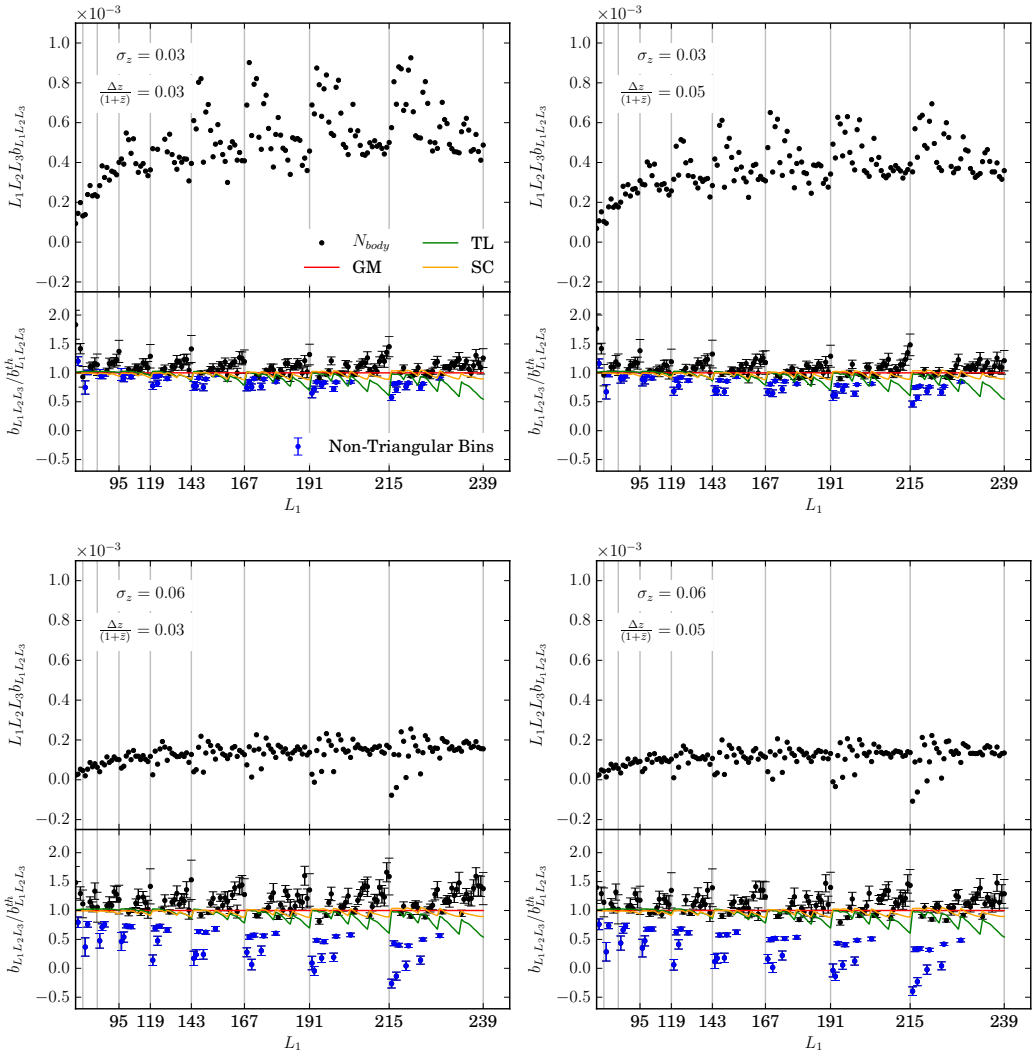

Figure 6.8: Bispectra measured for the four cases took in account. Each case presents a different photometric error and redshift width, both write in the top left corner of each plot. The convention for colors is the same of the previous plot. The blue points mark the *non-triangular* bins, which behavior seems depending strongly on the mocks parameters.

in a way that homogenize the density field and increase the error. The new and unexpected feature visible in fig. 6.8 is the behavior of what we called non-triangular bins, i.e. the binned configuration (L_1, L_2, L_3) with L_i center of the bin, for which the triangular property doesn't hold, i.e. $|L_j - l_k| \not\leq L_i \not\leq L_j + L_k$. This is possible because, even if the multipoles at the center of the bins doesn't form a triangle in harmonic space, the binned configuration contains at least one valid unbinned configuration. In particular, non-triangular bins are the bins containing the collapsed triangle, i.e. the triangle configurations (l_1, l_2, l_3) for which the identity $l_1 = l_2 + l_3$ holds. What fig. 6.8 tells is that one of the main effects of an high photo-z error is to destroy the collapsed configuration, especially the one composed by smallest scales among the others, thus bringing the bis-

pectrum power of this configuration to zero. And this is what we actually can see in fig. 6.8.

6.3 Comments

The comparison between the estimated C_l and bispectra and the predicted ones shows different behavior, depending on the size of the z-bin and of the photo-z error. Analyzing different cases, we understand the effect of these features, making us aware of possible difficulties in future analysis. Anyway, the common feature in all cases is the existence of repeated structure in the estimated bispectrum compared to the predicted ones, although in $\Delta l = 24$ case, measurements and prediction are consistent within 2σ. There are many possible explanation for this behavior that will be analyzed in a future work. For now, results show that an estimation of cosmological parameter is necessary to understand the power of angular bispectrum estimator in LSS case. This is the main goal of my future research, in which I hope to show that the angular bispectrum is a powerful tool, to be put together with the estimators that already are proven to be efficient in LSS analysis.

Part III

Trispectrum of Cosmic Microwave Background Radiation

CHAPTER 7

Non-Gaussianity in the photon distribution

7.1 Non-Gaussianity in the curvature perturbations

The *standard scenario* in inflationary cosmology is a model in which there exists only one scalar field whose potential energy drives inflation. But, what if there exist other scalar fields whose energy is not dominant? It is expected that their quantum fluctuations would influence those of the dominant field, usually dubbed inflaton, and hence the curvature perturbations. Many models were developed in order to provide alternatives to the standard scenario. Curvaton scenario (Mollerach 1990; Enqvist & Sloth 2002), inhomogeneous reheating scenario (Kofman 2003; Dvali et al. 2004), ghost inflation scenario (Hamed et al. 2004), D-celleretion scenario (Lyth & Riotto 1999) are some of these models, each of them provides a different mechanism to achieve inflation. One of the challenges of the new cosmology era is then to discriminate among these models of inflation, putting some constraints that must be able to rule out the larger possible number of models.

In order to constrain inflation models, the generic predictions of an accelerated de Sitter expansion must be tested. The main predictions are the generation of gravity-wave fluctuations, which produce B-mode polarization in the CMB (Kamionkowski et al. 1997; Seljak & Zaldarriaga 1997), spectral index of comoving curvature perturbations close to one (Lyth & Riotto 1999), and a distribution of primordial perturbations close to Gaussian. In particular, testing the Gaussianity offers stringent constraints on the inflationary scenario.

Introducing a collection of non-linearity parameters $\{f_{NL}, g_{NL}\}$, we can parameterizing the level of non-Gaussianity in the cosmological perturbations through the so-called *Bardeen's gravitational potential* (Bardeen 1980; Salopek & Bond 1990; Gangui et al. 1994; Verde et al. 2000b; Komatsu & Spergel 2001)

$$\Phi = \Phi_l + f_{NL}(\Phi_l^2 - \langle\Phi_l^2\rangle) + g_{NL}(\Phi_l^3), \tag{7.1}$$

where Φ_l represents the gravitational potential at linear order. Φ is related to the curvature perturbations by this simple relation (Bartolo et al. 2004)

$$\Phi(\mathbf{n}) = \frac{3}{5}\zeta(\mathbf{n}) \tag{7.2}$$

where ζ is the curvature perturbation field.

Since the beginning of the study of non-Gaussianity using the Bardeen's potential (Hodges et al. 1990; Latham & da Costa 1991; Falk et al. 1993), the attention was devoted to f_{NL}, because the g_{NL} is generally suppressed by inflationary models with respect to f_{NL}. Furthermore, there exists an optimal estimator compatible with the sensibility of

instruments used to measure CMB anisotropies (Komatsu et al. 2002; Komatsu & Spergel 2001; Santos et al. 2003; Smith et al. 2004; Yadav & Wandelt 2008a,b; Casaponsa et al. 2011; Planck Collaboration et al. 2014d). For g_{NL}, the Planck survey, although its precision in the measurements is well below the precision required, has introduced an improvement that can open the way for a third-order analysis of the curvature perturbations (The Planck Collaboration 2006; Planck Collaboration et al. 2016b).

As we have seen, the two-point correlation function and its Fourier transform, the power-spectrum, gives information about the amplitude of the curvature fluctuations. If they are Gaussian distributed, the power spectrum completely characterizes the statistic of the distribution of the curvature perturbations. In fact, consider a collection of centered random variables $\{\delta_i = \delta(x_i),\ i = 1, 2, \ldots\}$, the field $\Delta = \{\delta_i\}$ is Gaussian distributed if, for any $m \in \mathrm{card}\{\Delta\}$ their m-point joint probability distribution obeys the multi-variate Gaussian

$$P(x_1, \ldots, x_m) = \frac{1}{\sqrt{(2\pi)^m \det(M)}} \exp\left[-\sum_{i,j=1}^{m} \frac{1}{2} \delta_i (M)^{-1} \delta_j \right] \tag{7.3}$$

where $M_{ij} \equiv \langle \delta_i \delta_j \rangle$ is the covariance matrix and M^{-1} is its inverse. Eq. (7.3) implies that Gaussian fields are fully specified by the two-point correlation function and its linear combinations. If we consider higher-order correlation functions we find that the odd correlation functions vanish due to the property of the Gaussian moments of a distribution, while the even correlation function can be written in terms of the two-point correlation function. In fact, it is possible to divide the higher-order correlation functions into two parts, the connected and the unconnected part. The unconnected part can be expressed in terms of the lower-order correlation functions, while the connected part contains the true information about non-Gaussianity of the distribution. As we already have seen in chapter 1, for a zero-mean random field, the second and third-order connected correlation function coincide with the correlation function themselves, while at fourth-order one can write

$$\begin{aligned} &\langle f(\mathbf{x}_1) f(\mathbf{x}_2) f(\mathbf{x}_3) f(\mathbf{x}_4) \rangle \\ &= \langle f(\mathbf{x}_1) f(\mathbf{x}_2) \rangle \langle f(\mathbf{x}_3) f(\mathbf{x}_4) \rangle + \langle f(\mathbf{x}_1) f(\mathbf{x}_3) \rangle \langle f(\mathbf{x}_2) f(\mathbf{x}_4) \rangle \\ &+ \langle f(\mathbf{x}_1) f(\mathbf{x}_4) \rangle \langle f(\mathbf{x}_2) f(\mathbf{x}_3) \rangle + \langle f(\mathbf{x}_1) f(\mathbf{x}_2) f(\mathbf{x}_3) f(\mathbf{x}_4) \rangle_c \end{aligned} \tag{7.4}$$

where the subscript c denotes the connected part. For a Gaussian distribution, the connected part of the $n > 2$-order correlation functions is always vanishing. Otherwise, the presence of non-vanishing connected part of the $n > 2$-points gives information about the non-Gaussian behaviour of the distribution. Thus, the two and three-point correlation functions are the lowest-order statistics able to distinguish non-Gaussian from Gaussian perturbations. It is important to say that higher-order correlation functions are related with the self-interactions of the field (or the fields, in which case we have to consider the interactions between different fields too) that generated the curvature perturbations (Bartolo et al. 2004).

Just like the two-point correlation function and the power spectrum, we can take the Fourier transform the two and three-point correlation functions in order to evaluate the amount of non-Gaussianity of the curvature perturbations, i.e.

$$\langle \Phi(\mathbf{k}_1) \Phi(\mathbf{k}_2) \Phi(\mathbf{k}_3) \rangle = (2\pi)^3 \delta^{(3)}(\mathbf{k}_1 + \mathbf{k}_2 + \mathbf{k}_3) B_\Phi(k_1, k_2, k_3), \tag{7.5}$$

$$\langle \Phi(\mathbf{k}_1)\Phi(\mathbf{k}_2)\Phi(\mathbf{k}_3)\Phi(\mathbf{k}_4)\rangle = \\ = (2\pi)^3\delta^{(3)}(\mathbf{k}_1+\mathbf{k}_2+\mathbf{k}_3,\mathbf{k}_4)T_\Phi(k_1,k_2,k_3,k_4), \tag{7.6}$$

where $\delta^{(3)}$ is the tridimensional Dirac's delta. $B_\Phi(k_1,k_2,k_3)$ is the so-called *bispectrum*, while $T_\Phi(k_1,k_2,k_3,k_4)$ is the *trispectrum*. Bispectrum and trispectrum are strictly related with the parameters that characterize the non-Gaussian curvature perturbation in eq. 7.1. In fact, f_{NL} and g_{NL} parametrize the amplitude of the bispectrum and trispectrum respectively.

7.1.1 The Bispectrum

In general the bispectrum can be written as

$$B_\Phi(k_1,k_2,k_3) = f_{NL}F(k_1,k_2,k_3). \tag{7.7}$$

The bispectrum is measured on triangular configurations of the three wavenumber k_1, k_2 and k_3. The physics among the generation of the primordial perturbations (Babich et al. 2004) determines the shape of the triangles and the form of $F(k_1,k_2,k_3)$. $F(k_1,k_2,k_3)$ is a function that depends on the configuration of the three wavenumber k in the Fourier space and encodes the scale dependence of the bispectrum (Chen 2005, 2010)[1]. The possible shape that the harmonic triangle can assume are usually divided in squeezed, equilateral and orthogonal, related to the following kind of non-Gaussianity:

- *local non-Gaussianity* generating the squeezed triangles, i.e. $k_1 \ll k_2 \simeq k_3$ (Gangui et al. 1994; Verde et al. 2000b; Wang & Kamionkowski 2000; Komatsu & Spergel 2001; Maldacena 2003). This occurs when primordial non-Gaussianity is generated on super-horizon scales, e.g. multi-fields models of inflation;
- *equilateral non-Gaussianity* characterizing the equilateral triangles $k_1 \simeq k_2 \simeq k_3$ (Babich et al. 2004), which can occurs if the three perturbation modes mostly interact when they cross the horizon approximately at the same time, e.g. single field models such as *k-inflation* (Chen et al. 2007; Armendáriz-Picón et al. 1999), DBI inflation (Silverstein & Tong 2004; Alishahiha et al. 2004), ghost inflation (Arkani-Hamed et al. 2004) and models arising from effective field theories (Cheung et al. 2008);
- *orthogonal non-Gaussianity* (Senatore et al. 2010), it generates a signal with a positive peak at the equilateral configuration and a negative peak at the folded configuration, achieved by single-field model with higher-derivatives interactions.

However, there are exceptional cases which are out of the previous list, in which we have non-Gaussianity with intermediate shapes (Chen & Wang 2010a,b) or superposition of shapes (Langlois et al. 2008a,b; Arroja et al. 2008; Renaux-Petel 2009), but these models are beyond the aim of this work.

All of the models listed above predict $|f_{NL}| \gg 1$, i.e. a detectable non-Gaussianity behaviour. On the contrary, the single-field slow-roll inflation provides a quasi-Gaussian perturbation distribution, and the deviation from the Gaussian statistic is well below the range of detection, i.e. $|f_{NL}| \ll 1$ (Acquaviva et al. 2003; Maldacena 2003). In fact, in

[1] Although the parameter f_{NL} was found to be almost scale independent (Bartolo et al. 2004; Smidt et al. 2010)

the single-field slow-roll inflation, the non-linearity parameter should be $f_{NL} \simeq \mathcal{O}(\epsilon, \eta)$, where ϵ and η are the slow-roll parameters (eq. 3.7) (Gangui et al. 1994; Acquaviva et al. 2003; Maldacena 2003). Indeed, the main contribution to the non-Gaussianity in single-field slow-roll models comes from the non-linear gravitational perturbations, rather than the inflation self-interactions (Babich et al. 2004). As we have seen in the previous chapter, in order to have a period of inflation the inflaton potential must be very flat, (i.e. $\epsilon, |\eta| \ll 1$), therefore the self-interaction terms in the inflaton potential and the gravitational coupling must be very small and then non-linearities are suppressed too. On the other hand, if we consider an additional field χ, different from inflaton, whose energy density is negligible in comparison with that of the inflaton, its self-interactions are not constrained by slow-roll condition, thus sizeable non-Gaussianities can be generated. This is the simplest case in which a detectable non-Gaussianity can be produced. Then, a detection of non-Gaussianity in the curvature perturbations would rule out the single-field slow-roll models of inflation.

In recent papers (Planck Collaboration et al. 2014e, 2016b), f_{NL} has be found consistent with zero. A third-order analysis of the curvature perturbation, and then of g_{NL}, becomes necessary in order to evaluate the presence or not of primordial non-Gaussianity.

7.1.2 The Trispectrum

We can write the trispectrum as

$$T_\Phi(k_1, k_2, k_3, k_4) = \frac{25}{9}\tau_{NL}[P_\Phi(k_1)P_\Phi(k_2)P_\Phi(k_3) + (11\text{perm.})] \tag{7.8}$$

$$+6g_{NL}[P_\Phi(k_1)P_\Phi(k_2)P_\Phi(k_3) + (3\text{perm.})], \tag{7.9}$$

where $P_\Phi(k_i)$ is the power spectrum of the distribution, and $k_{ij} = |\mathbf{k}_i + \mathbf{k}_j|$. The trispectrum written above is divided into the non-connected component (eq. 7.8) and the connected one (eq. 7.9). The parameter g_{NL} introduced in eq. 7.1 is therefore the amplitude of the connected part of the trispectrum. The parameter τ_{NL} is also a non-Gaussianity parameter, but it is strictly related with the non-linearity parameter f_{NL} (see eq. 7.26 and eq. 7.41 in the next paragraph).

Moreover, the trispectrum can provide a tool to distinguish among the different inflationary models. In fact, the same interactions that led to the bispectrum might be responsible also for a large trispectrum (Planck Collaboration et al. 2014d). Several inflationary models have been found in which the bispectrum is suppressed, thus leaving the trispectrum as the largest higher-order correlator in the data. Large trispectra are possible in certain curvaton and multi-fields model (Byrnes et al. 2006; Sasaki et al. 2006; Byrnes & Choi 2010) and single-field models with high derivatives interactions (Chen et al. 2009; Arroja et al. 2008; Senatore & Zaldarriaga 2011; Bartolo et al. 2010). Recently, Planck collaboration (Planck Collaboration et al. 2016b) shown a g_{NL} consistent with zero, but with huge error bars making the statistics poor. New g_{NL} estimator could improve the statistics or, at least, make possible to do consistency checks on the previous and future results.

7.1.3 Non-Gaussianity for single-field and multi-fields model of inflation

It is possible to evaluate the amplitude of the three non-gaussianity parameters f_{NL}, τ_{NL} and g_{NL} by means of the δN formalism (see Smidt et al. 2010; Starobinsky 1982; Starobinskiĭ 1985; Byrnes et al. 2006; Lyth & Rodríguez 2005; Suyama & Yamaguchi 2008, for details).

During inflation, spacetime expands by a certain number of e-folds N. By Heisenberg's uncertainty principle, expansion for each point of the Universe ends at slightly different times producing a spatially dependent total e-folds:

$$N(\mathbf{n}) = \int_{t_i}^{t_f} H(t, \mathbf{x}) dt, \tag{7.10}$$

where t_i is the time at which the inflations begin and t_f the time at which it ends, while $H(t, \mathbf{x})$ is the Hubble parameter. Since point by point differences are small, we can define

$$N(\mathbf{n}) = \bar{N} + \delta N(\mathbf{n}). \tag{7.11}$$

The perturbations of the e-folds correspond to perturbation in local expansion, then we can identify δN with the curvature perturbations $\zeta = \delta N$. Moreover, we may parametrize the number of e-folds by the underlying fields $\zeta = N(\phi^A) - \bar{N}$ where ϕ^A represents the initial value for the scalar fields $\phi^A = \bar{\phi}^A + \delta\phi^A$. Then, we can expand the curvature perturbations as

$$\zeta = \delta N = \sum_n \frac{1}{n!} N_{A_1 A_2 \dots A_n} \delta\phi^{A_1} \delta\phi^{A_2} \dots \delta\phi^{A_n}, \tag{7.12}$$

where we used the Einstein summation convention and N_x is the derivative of N with respect to the fields x

$$N_{A_1 A_2 \dots A_n} = \frac{\partial^n N}{\partial\phi^{A_1} \partial\phi^{A_2} \dots \partial\phi^{A_n}}. \tag{7.13}$$

Then, the power spectrum of the curvature perturbations at first order is

$$\langle \zeta_{\mathbf{k}} \zeta_{\mathbf{k}'} \rangle = N_A N_B C^{AB}(k) (2\pi)^3 \delta^3(\mathbf{k} + \mathbf{k}'), \tag{7.14}$$

where, in the slow-roll limit, C^{AB} becomes the leading order $\delta^{AB} P(k)$. Likewise, we can calculate the bispectrum and trispectrum in this formalism

$$B_\zeta(k_1, k_2, k_3) = N_A N_{BC} N_D [C^{AC}(k_1) C^{BD}(k_2) + C^{AC}(k_2) C^{BD}(k_3) + C^{AC}(k_3) C^{BD}(k_1)] \tag{7.15}$$

$$\begin{aligned} T_\zeta(k_1, k_2, k_3, k_4) =& N_{A_1 A_2} N_{B_1 B_2} N_C N_D [C^{A_2 B_2}(k_{13}) C^{A_1 C}(k_2) C^{B_1 D}(k_4) + (11 \text{ perms})] \\ &+ N_{A_1 A_2 A_3} N_B N_C N_D [C^{A_1 B}(k_2) C^{A_2 C}(k_3) C^{A_3 D}(k_4) + (3 \text{ perms})] \end{aligned} \tag{7.16}$$

where $k_{ij} = |\mathbf{k}_i + \mathbf{k}_j|$. We can compare the above expression with the usual bispectrum and trispectrum calculated in the slow-roll limit for the curvature perturbation ζ, that are

$$B(k_1, k_2, k_3) = \frac{6}{5} f_{NL} [P_\zeta(k_1) P_\zeta(k_2) + P_\zeta(k_2) P_\zeta(k_3) + P_\zeta(k_3) P_\zeta(k_1)], \tag{7.17}$$

$$\begin{aligned} T(k_1, k_2, k_3, k_4) =& \tau_{NL} [P_\zeta(k_{13}) P_\zeta(k_3) P_\zeta(k_4) + (11 \text{ perms})] \\ &+ \frac{54}{25} g_{NL} [P_\zeta(k_2) P_\zeta(k_3) P_\zeta(k_4) + (3 \text{ perms})], \end{aligned} \tag{7.18}$$

where $P_\zeta(k) = N_A N_B C^{AB}(k)$ and therefore in the slow-roll limit $P_\zeta(k) = N_A N^A P(k)$. We thus obtain the values for each statistic

$$f_{NL} = \frac{5}{6}\frac{N_A N_B N^{AB}}{(N_C N^C)^2}; \tag{7.19}$$

$$\tau_{NL} = \frac{N_{AB} N^{AC} N^B N_C}{(N_D N^D)^3}; \tag{7.20}$$

$$g_{NL} = \frac{25}{54}\frac{N_{ABC} N^A N^B N^C}{(N_D N^D)^3}. \tag{7.21}$$

Single-field models

In the case where a single field dominates the energy density, we may expand ζ using the formalism in eq. 7.12, as:

$$\zeta = N'\delta\phi + \frac{1}{2}N''\delta\phi^2 + \frac{1}{6}N'''\delta\phi^3 + \dots, \tag{7.22}$$

where $N' = dN/d\phi$. Then, from equations 7.19-7.21, we have

$$f_{NL} = \frac{5}{6}\frac{N''}{(N')^2}; \tag{7.23}$$

$$\tau_{NL} = \frac{(N'')^2}{(N')^4}; \tag{7.24}$$

$$g_{NL} = \frac{25}{54}\frac{N'''}{(N')^3}. \tag{7.25}$$

The results in equations 7.23-7.25 holds for any single field whose energy dominates the energy density of the Universe during inflation, such as the inflaton or the curvaton.

Equations 7.23 and 7.24 yield a very important consequence of single-field models namely

$$\tau_{NL} = \left(\frac{6 f_{NL}}{5}\right)^2. \tag{7.26}$$

This is a general result and therefore, defining $A_{NL} = \tau_{NL}/(6f_{NL}/5)^2$, $A_{NL} \neq 1$ may be used to rule out single-field models all together.

In the case of standard single field inflation, we can calculate the non-linearity parameters f_{NL} and g_{NL} in terms of the slow-roll parameters at first (eq. 3.7) and second-order

$$\xi^2 \equiv M_p^4 \frac{V'V'''}{V^2}, \tag{7.27}$$

where M_p is the Planck mass. Then we have (see Byrnes et al. 2006, for details)

$$f_{NL} = \frac{5}{6}(\eta - 2\epsilon), \tag{7.28}$$

$$\tau_{NL} = (\eta - 2\epsilon)^2, \tag{7.29}$$

$$g_{NL} = \frac{25}{54}(2\epsilon\eta - 2\eta^2 + \xi^2). \tag{7.30}$$

Instead, in the curvaton scenario, there exist a weakly interacting scalar field χ together with the inflaton, whose energy density comes to contribute a significant fraction of the energy density of the Universe sometimes after inflation (Byrnes & Choi 2010; Byrnes et al. 2006; Enqvist & Nurmi 2005; Enqvist & Takahashi 2008; Enqvist et al. 2010). After the decays of the curvaton, its fluctuations produce the primordial curvature perturbations ζ.

The potential of the curvaton is parametrize as follow (Enqvist et al. 2010)

$$V = \frac{1}{2}m^2\chi^2 + \lambda\chi^{n+4}, \tag{7.31}$$

where m is the curvaton's mass and λ is a coupling constant. For such models, N in equation 7.12 has been worked out giving

$$f_{NL} = \frac{5}{4r_\chi}(1+h) - \frac{5}{3} - \frac{5r_\chi}{6}, \tag{7.32}$$

$$g_{NL} = \frac{25}{54}\left[\frac{9}{4r_\chi}(\tilde{h}+3h) - \frac{9}{r_\chi}(1+h) + \frac{1}{2}(1-9h) + 10r_\chi + 3r_\chi^2\right], \tag{7.33}$$

where

$$\begin{aligned} r_\chi &= \frac{3\Omega_{\chi,D}}{4-\Omega_{\chi,D}}, \\ h &= \frac{\chi_0\chi_0''}{\chi_0'^2} \\ \tilde{h} &= \frac{\chi_0^2\chi_0'''}{\chi_0'^3}. \end{aligned} \tag{7.34}$$

Here $\Omega_{\chi,D}$ is the energy density at time of curvaton decay, χ_0 is the curvaton field during oscillations just before decays and the primes here denotes derivatives with respect to time. Unlike the inflatons, in the curvaton models g_{NL} can be significantly large even f_{NL} is small because the curvaton can have large self interactions.

Multi-fields models

In general $\tau_{NL} \geq (6f_{NL}/5)^2$ and equality holds only if N_A is an eigenmode of N_{AB} (Suyama & Yamaguchi 2008). Models in which the equality doesn't holds are the multi-fields models.

For multi-fields models is nearly impossible to use the δN formalism, instead one is forced to work with specific models. For example, consider two-fields models with scalar fields ϕ and χ that have a separable potential (Byrnes & Choi 2010; Vernizzi & Wands 2006; Choi et al. 2007; Battefeld & Easther 2007; Seery & Lidsey 2007)

$$W = (\phi, \chi) = U(\phi)V(\chi). \tag{7.35}$$

The slow-roll parameters for this models are

$$\epsilon_\phi = \frac{M_p^2}{2}\left(\frac{U_{,\phi}}{U}\right)^2, \quad \epsilon_\chi = \frac{M_p^2}{2}\left(\frac{V_{,\chi}}{V}\right)^2, \tag{7.36}$$

$$\eta_{\phi\phi} = M_p^2 \frac{U_{,\phi\phi}}{U}, \quad \eta_{\phi\chi} = M_p^2 \frac{U_{,\phi} V_{,\phi}}{W}, \quad \eta_{\chi\chi} = M_p^2 \frac{V_{,\chi\chi}}{V}, \tag{7.37}$$

from which we can define

$$\tilde{r} = \frac{\epsilon_\chi}{\epsilon_\chi} e^{2(\eta_{\phi\phi} - \eta_{\chi\chi})N}. \tag{7.38}$$

For this class of models, in the region where $|f_{NL}| > 1$ we have

$$f_{NL} = \frac{5}{6} \eta_{\chi\chi} \frac{\tilde{r}}{(1+\tilde{r})^2} e^{2(\eta_{\phi\phi} - \eta_{\chi\chi})N}; \tag{7.39}$$

$$g_{NL} = \frac{10}{3} \frac{\tilde{r}(\eta_{\phi\phi} - 2\eta_{\chi\chi}) - \eta_{\chi\chi}}{1+\tilde{r}} f_{NL}; \tag{7.40}$$

$$\tau_{NL} = \frac{1+\tilde{r}}{\tilde{r}} \left(\frac{6 f_{NL}}{5} \right)^2; \tag{7.41}$$

$$A_{NL} = \frac{1+\tilde{r}}{\tilde{r}}. \tag{7.42}$$

Then, in this class of models, both g_{NL} and τ_{NL} are related to f_{NL} and we have $|g_{NL} < f_{NL}|$ which will therefore be harder to detect. On the other hand, $\tau_{NL} > (6 f_{NL}/5)^2$ so that non-Gaussianity may be easier to detect in the trispectrum than in the bispectrum for some multi-fields models.

7.2 Detecting Non-Gaussianity with the CMB anisotropies distribution

As we have just seen, the inflationary paradigm provides a mechanism which seeds the inhomogeneities we see today in the photon background (CMB). In particular, the vacuum fluctuations of the scalar field that generates the inflation (i.e. the inflaton in the single-field models) were transferred in curvature perturbation. Then, during inflation, they grows till they became larger than the casual horizon. When inflation ends, the horizon began to expand and the perturbations re-enter within the causal horizon during the radiation or the matter era, introducing density inhomogeneities in the coupled radiation-matter plasma. Then, this inhomogeneities were amplified by gravity and grew into structures we see today.

We can quantify the effect of curvature perturbations on the photon distribution by using the so-called *Sach-Wolfe* formula (Sachs & Wolfe 1967; Yadav & Wandelt 2010; Planck Collaboration et al. 2014e; Bartolo et al. 2004)

$$\frac{\Delta\theta}{\theta} = -\frac{1+\omega}{5+3\omega}\zeta, \tag{7.43}$$

where $\Delta\theta$ is the deviation of the temperature of the photons from the mean temperature θ, ζ is the curvature perturbation and $\omega = -P/\rho$ is related to the equation of state of the Universe. Then, during radiation domination era $\omega = 1/3$, while during the matter domination era $\omega = 0$. Since at recombination, the Universe was in the matter domination era, so $\omega = 0$, we observe adiabatic temperature fluctuations in the CMB of

$$\frac{\Delta\theta}{\theta} = -\frac{1}{3}\Phi = -\frac{1}{5}\zeta, \tag{7.44}$$

where Φ is the gravitational potential $\Phi = -3/5\zeta$.

After recombination, CMB photons became free to propagate throughout the Universe, without interacting with the now completely neutral matter. Then, the inhomogeneities of the photon background due to inflation don't change with time, thus the CMB anisotropies distribution that we see today is the same of that at the time of recombination.

By means of the anisotropy of the CMB, we can then study the primeval fluctuations of the inflation fields. Having defined the last scattering surface as the imaginary sphere around us from which the CMB was emitted, we can then define the CMB as a random field on this sphere (Dodelson 2003; Durrer 2008). Every function f on the sphere enjoys the following spectral decomposition (Marinucci & Peccati 2011)

$$f(\mathbf{n}) = \sum_{l=0}^{\infty} \sum_{m=-l}^{l} a_{lm} Y_{lm}(\mathbf{n}), \tag{7.45}$$

that is, the Fourier transform on the sphere. Y_{lm} are the orthonormal basis of the space of the functions on the sphere, known as *Spherical Harmonics*. If the field f represents the CMB anisotropies distribution on the sphere, we can easily relate the harmonic coefficients a_{lm} of the spectral decomposition of eq. 7.45 with the primordial fluctuations Φ (eq. 7.2) as (Yadav & Wandelt 2010; Planck Collaboration et al. 2014e)

$$a_{lm} = 4\pi(-i)^l \int \frac{d^3k}{(2\pi)^3} \Phi(\mathbf{k}) g_l(k) Y^*_{lm}(\hat{\mathbf{k}}), \tag{7.46}$$

where $\Phi(\mathbf{k})$ is the primordial curvature perturbations for a comoving wavevector $\mathbf{k}$ and $g_l(k)$ is the radiation transfer function.

Hence, the higher order correlation function for the temperature anisotropies field $T = \Delta\theta/\theta$ can be expressed by ensemble average of linear combination of the harmonic coefficients, e.g. the bispectrum

$$\langle T(\mathbf{x}_1)T(\mathbf{x}_2)T(\mathbf{x}_3)\rangle = \sum_{l_1 l_2 l_3} \sum_{m_1 m_2 m_3} \langle a_{l_1 m_1} a_{l_2 m_2} a_{l_3 m_3}\rangle Y_{l_1 m_1}(\mathbf{x}_1) Y_{l_2 m_2}(\mathbf{x}_2) Y_{l_3 m_3}(\mathbf{x}_3), \tag{7.47}$$

and thus, using eq. 7.46, we can relate them to the same order correlation functions of the curvature perturbation

$$\langle a_{l_1 m_1} a_{l_2 m_2} a_{l_3 m_3}\rangle \longleftrightarrow \langle \Phi(\mathbf{k}_1)\Phi(\mathbf{k}_2)\Phi(\mathbf{k}_3)\rangle. \tag{7.48}$$

Then, the evaluation of the higher-order correlation functions for the CMB allows to evaluate that of the primordial gravitational potential and then of the primordial curvature perturbations. Then, by means of the Bardeen's potential (eq. 7.1), we can evaluate f_{NL} and g_{NL} through the CMB anisotropy distribution analysis. The recent result on f_{NL} on the Planck survey data (Planck Collaboration et al. 2016b), show that the single-field models seems to be the excellent candidate to explain how the inflation was produced, i.e.

$$\begin{aligned} f_{NL}^{local} &= 0.8 \pm 5.0 \ \ (1\sigma), \\ f_{NL}^{equil} &= -4 \pm 43 \ \ (1\sigma), \\ f_{NL}^{ortho} &= -26 \pm 21 \ \ (1\sigma), \end{aligned} \tag{7.49}$$

while for g_{NL},

$$g_{NL}^{local} = (-9.0 \pm 7.7) \times 10^4 \ \ (1\sigma). \tag{7.50}$$

Note that the error bars on g_{NL} do not allows to consider significant the result above. In order to study high-order non-Gaussianity, a finer statistics must be provided.

CHAPTER 8

The Spherical Needlet Wavelets

Although the Spherical Harmonics enjoy several useful properties, they are not localized on the sphere in real space, that is, they shows a global character on the sphere. If the sphere presents a gap, some correlations are added to the $\{a_{lm}\}$, leading the harmonic coefficients to lose their uncorrelation properties. We can say that the global character of Spherical Harmonics implies that the effects of missing fraction of the sphere are spread throughout the whole $\{a_{lm}\}$ array (Marinucci & Peccati 2011). Denoting by G the gap of the sphere, the definition of harmonic coefficients became

$$a_{lm}^{G} = \int_{S^2/G} T(\mathbf{n}) Y_{lm}^{*}(\mathbf{n}) d\Omega \,. \tag{8.1}$$

So, the correlation between a_{lm} at different scales is provided by

$$\begin{aligned} \langle a_{l_1 m_1}^{G} a_{l_2 m_2}^{G*} \rangle &= \langle \left[\int_{S^2/G} T(\mathbf{n}) Y_{l_1 m_1}^{*}(\mathbf{n}) d\Omega \int_{S^2/G} T(\mathbf{n}') Y_{l_2 m_2}(\mathbf{n}') d\Omega' \right] \rangle \\ &= \sum_{l_1 m_1} \sum_{l_2 m_2} \langle a_{lm} a_{l'm'}^{*} \rangle \left[\int_{S^2/G} Y_{lm}(\mathbf{n}) Y_{l_1 m_1}^{*}(\mathbf{n}) d\Omega \int_{S^2/G} Y_{l'm'}^{*}(\mathbf{n}') Y_{l_2 m_2}(\mathbf{n}') d\Omega' \right] \\ &= \sum_{lm} C_l W_{lml_1 m_1} W_{l'm'l_2 m_2} \end{aligned} \tag{8.2}$$

where $W_{lml_1 m_1}$ denotes the so-called *coupling factors*

$$W_{lml_1 m_1} := \int_{S^2/G} Y_{lm}(\mathbf{n}) Y_{l_1 m_1}^{*}(\mathbf{n}) d\Omega \,. \tag{8.3}$$

Whenever $G = \emptyset$, i.e. when the spherical random field is fully observed, eq. 8.3 represents nothing but the orthonormality property of the Spherical Harmonics, thus

$$W_{lml_1 m_1} = \delta_l^{l_1} \delta_m^{m_1},$$

so the uncorrelation properties of harmonic coefficients is recovered

$$\langle a_{l_1 m_1} a_{l_2 m_2}^{*} \rangle = C_{l_1} \delta_{l_1}^{l_2} \delta_{m_1}^{m_2}.$$

The problem of incomplete spherical random fields is a relevant issue in CMB analysis. In fact, the last scattering surface is hiding by the Milky Way and other point sources spread throughout the sky, generating a radiation that affects the photon distribution of

the CMB. Although many software were developed in order to reduce the impact of this foregrounds, there are some regions that are irreversibly affected by spurious contributions. To improve the statistics, we have to remove this regions (Cabella et al. 2006).

In order to improve the statistics involving an incomplete sphere we can use the Spherical Wavelets (Potts et al. 1996; Freeden & Schreiner 1998; Wiaux et al. 2007; Antoine & Vandergheynst 1998). A wavelet is a wave-like oscillation localized both in real and in harmonic domain. When spectral decomposition of the field by means of wavelet transform is made, one is decomposing the field *locally* into contributions living at different scales. This, in principle, avoids the problems occurring due the global behavior of Spherical Harmonics and makes the statistics stronger in presence of gap and/or missing observations of the field. Different procedures in wavelet domain were developed in CMB and cosmology analysis since past years (McEwen et al. 2007; Barreiro et al. 2000; Cayón et al. 2001, 2003).

During my PhD, I worked with a specific class of spherical wavelets, the so-called *Spherical Needlets*. Since the introduction (Narcowich et al. 2006b,a), Spherical Needlets were studied in order to be applied to spherical field and therefore to the CMB (Baldi et al. 2006; Pietrobon et al. 2006; Marinucci et al. 2008). In the following paragraphs I'll describe the Spherical Needlets framework and the properties that make them different from other wavelet system (Baldi et al. 2006, 2007).

8.1 Standard Spherical Needlets

Spherical Harmonics form an orthonormal basis of the space of square-integrable functions on the two-dimensional sphere $L^2(S^2)$. Then, it is possible to decompose this space into the direct sum of orthogonal spaces which are spanned by the Spherical Harmonics

$$L^2(S^2) = \bigoplus_{l=0}^{\infty} \mathcal{H}_l, \tag{8.4}$$

where $\mathcal{H}_l = \mathcal{H}_l(S^2) = span\{Y_{lm}, m = -l \dots l\}$. Then, define $\mathcal{K}_l = \bigoplus_{k=0}^{l} \mathcal{H}_k$ as the space of restrictions to sphere S^2 of polynomials of degree less than l. Starting from (Narcowich et al. 2006b,a), it is possible to say that for all $j \in \mathbb{N}$, there exist a finite subset $\mathcal{X}_j$ of S^2, whose elements are called *cubature points* $\{\xi_{jk} \in S^2\}$, and positive real numbers $\lambda_{jk} > 0$ called *cubature weights*, indexed by elements of $\mathcal{X}_j$, such that

$$\forall f \in \mathcal{K}_l, \quad \int_{S^2} f(\mathbf{n}) d\Omega = \sum_{\xi_{jk} \in \mathcal{X}_j} \lambda_{jk} f(\xi_{jk}). \tag{8.5}$$

It is known that the points in $\{\mathcal{X}_j\}_{j=0}^{\infty}$ are almost ε_j distributed with $\varepsilon_j := \kappa B^{-j}$, and the coefficients $\{\lambda_{jk}\}$ are such that $\lambda_{jk} \approx cB^{-2j}$, card$\{\mathcal{X}\} \approx B^{2j}$. In other words, the cubature points and the cubature weights are such that, for all polynomials $Q_l(\mathbf{n})$ of degree smaller than B^{j+1},

$$\sum_k Q_l(\xi_{jk}) \lambda_{jk} = \int_{S^2} Q_l(\mathbf{n}) d\Omega \,. \tag{8.6}$$

The set of cubature points and related cubature weight have a deeper meaning within the framework of the sphere in view of the construction of the Needlet trispectrum (Marinucci & Peccati 2011; Baldi et al. 2007). First,it is useful to recall the definition of the standard open balls in S^2

$$B^{\circ}(a, \alpha) = \{x : (a, x) < \alpha\} \tag{8.7}$$

and that of close balls

$$B(a,\alpha)=\{x:(a,x)\leq\alpha\}, \tag{8.8}$$

having used $d(x,y)=\arccos(\langle x,y\rangle)$ to indicate the distance between x and y on the sphere. Then, define a *maximal net* as follows

Definition 2. *For any $\varepsilon>0$, $\Xi_\varepsilon=\{x_1,\ldots,x_n)$ is a maximal ε-net if $x_1,\ldots,x_n$ are in S^2, $\forall\, i\neq j$, $d(x_i,x_j)>\varepsilon$, and the set is maximal for this property, i.e.*

$$\forall\, x\in S^2, d(x,\Xi_\varepsilon)\leq\varepsilon,\ \ \cup_{x_i\in\Xi_\varepsilon}B(x_i,\varepsilon)=S^2, \tag{8.9}$$

$$\textit{and}\ \ \forall\, i\neq j,\ \ B(x_i,\varepsilon/2)\cap B(x_j,\varepsilon/2)=\emptyset. \tag{8.10}$$

An ε-net is then a grid of point at distance at least ε. On the sphere, the number of points can be bounded by the following lemma (Baldi et al. 2007)

Lemma 1. *Let $\Xi_\varepsilon=\{x_1,\ldots,x_n\}$ be a maximal ε-net. Then*

$$\frac{4}{\varepsilon^2}\leq N\leq\frac{4}{\varepsilon^2}\pi^2. \tag{8.11}$$

The ε-net can be used to construct a partition of the sphere into disjoint set, each of them associated with a single point in the net. This partition can be made by means of *Voronoi cells*

Definition 3. *Let Ξ_ε be a maximal ε-net. For all $x_i\in\Xi_\varepsilon$, the associated family of Voronoi cells is defined by:*

$$\mathcal{V}(x_i)=\{x\in S^2\ :\ \forall\, j\neq i,\ d(x,x_i)\leq d(x,x_j)\}. \tag{8.12}$$

From (Marinucci & Peccati 2011) and (Baldi et al. 2007), I recall some properties of the voronoi cells on the sphere. First, $B(x_i,\varepsilon/2)\subset\mathcal{V}\subset B(x_i,\varepsilon)$, hence, identifying with σ the area of a subset on the sphere, one has $\sigma(\mathcal{V}(x_i))\approx\varepsilon^2$. Also, if two Voronoi cells are adjacent, i.e. $\mathcal{V}(x_i)\cap\mathcal{V}(x_j)\neq\emptyset$, then $d(x_i,x_j)\leq 2\varepsilon$. Then, it is possible to recall the set of cubature points and weights in views of the framework of Voronoi cells:

- The cubature points $\{\xi_{jk}\}$ can be taken to form a maximal ε_j-net, with $\varepsilon_j\approx B^{-j}$;
- The cubature weights $\{\lambda_{jk}\}$ are of order B^{-2j}, i.e. for all j,k we have $\lambda_{jk}\approx\sigma(\mathcal{X}(\xi_{jk}))$, the area of the associated Voronoi cell.

The properties of cubature points and weights, such as the definition of Voronoi's cells, will be used in the derivation of the Needlet trispectrum.

Moreover, the set of cubature points is crucial in view of the definiton of Spherical Needlets, because Spherical Needlets are defined on this set,

Definition 4. *A family of Spherical Needlets $\{\psi_{jk}\}$ is defined by setting*

$$\psi_{jk}(\boldsymbol{n}):=\sqrt{\lambda_{jk}}\sum_l b\left(\frac{l}{B^j}\right)\sum_{m=-l}^{l}Y_{lm}(\xi_{jk})Y^*_{lm}(\boldsymbol{n}) \tag{8.13}$$

$$\psi_{jk}(\boldsymbol{n}):=\sqrt{\lambda_{jk}}\sum_l b\left(\frac{l}{B^j}\right)\frac{2l+1}{4\pi}P_l(\langle\xi_{jk},x\rangle), \tag{8.14}$$

where $x\in S^2$, $\{\lambda_{jk},\xi_{jk}\}$ are a set of cubature points and weights, $P_l(.)$ is the Legendre polynomial of l-th order, $B>1$ is a constant and $b(.)$ is a weight function satisfying the three follow conditions

- *compact support, $b(.) > 0$ in (B^{-1}, B), and it is equal to zero otherwise,*
- *partition of unity, for all $\zeta \geq 1$*

$$\sum_{j=0}^{\infty} b^2\left(\frac{\zeta}{B^j}\right) = 1 \tag{8.15}$$

- *smoothness $b(.) \in C^M$, i.e., it is M times continuously differentiable, for some $M = 1, 2, \ldots$ or $M = \infty$.*

There are many possible constructions satisfying the three conditions on $b(.)$ listed in definition 4. The following recipe (Baldi et al. 2006; Marinucci & Peccati 2011) allows to write the so-called *standard Needlets*:

- STEP 1: Construct the C^∞, compactly supported function

$$\phi_1(t) = \begin{cases} exp\left(-\frac{1}{1-t^2}\right), & -1 \leq t \leq 1 \\ 0, & \text{otherwise.} \end{cases} \tag{8.16}$$

- STEP 2: Construct the C^∞, non-decreasing function

$$\phi_2(u) = \frac{\int_{-1}^{u} \phi_1(t)}{\int_{-1}^{1} \phi_1(t)}. \tag{8.17}$$

  The function ϕ_2 is normalized so that $\phi_2(-1) = 0$, $\phi_2(1) = 1$.

- STEP 3: Construct the function

$$\phi(t) = \begin{cases} 1 & \text{if} \quad 0 \leq t \leq \frac{1}{B} \\ \phi_2\left[1 - \frac{2B}{B-1}\left(t - \frac{1}{B}\right)\right] & \text{if} \quad \frac{1}{B} < t \leq 1 \\ 0 & \text{if} \quad t > 1. \end{cases} \tag{8.18}$$

  this step implements a change of variables so that the resulting function $\phi(.)$ is constant on $(0, B^{-1})$ and monotonically decreasing to zero in the interval $(B^{-1}, 1)$. Indeed, it can be checked out that

$$1 - \frac{2B}{B-1}\left(t - \frac{1}{B}\right) = \begin{cases} 1 & \text{for} \quad t = \frac{1}{B} \\ -1 & \text{for} \quad t = 1 \end{cases} \tag{8.19}$$

  and

$$\begin{aligned} \phi\left(\frac{1}{B}\right) &= \phi_2(1) = 1 \\ \phi(1) &= \phi_2(-1) = 0. \end{aligned} \tag{8.20}$$

- STEP 4: Construct

$$b(\zeta) = \sqrt{\phi\left(\frac{x}{B}\right) - \phi(\mathbf{n})}, \quad -\infty < x < \infty. \tag{8.21}$$

  The resulting function $b(.)$ is C^∞ and satisfies the three condition listed in the Spherical Needlets definition, for all $M = 1, 2, \ldots$.

Spherical Needlet coefficients β_{jk} are provided by the analytical formula

$$\begin{aligned}\beta_{jk} &= \int_{S^2} T(\mathbf{n})\psi_{jk}(\mathbf{n})d\Omega \\ &= \sqrt{\lambda_{jk}}\sum_l b\left(\frac{l}{B^j}\right)\sum_{m=-l}^{l}\left\{\int_{S^2} T(\mathbf{n})Y^*_{lm}(\mathbf{n})\right\}Y_{lm}(\xi_{jk}) \\ &= \sqrt{\lambda_{jk}}\sum_l b\left(\frac{l}{B^j}\right)\sum_{m=-l}^{l} a_{lm}Y_{lm}(\xi_{jk}).\end{aligned} \tag{8.22}$$

It is easy to show that sample mean of Needlet coefficients is identically zero at all scales j

$$\begin{aligned}\sum_k \beta_{jk}\sqrt{\lambda_{jk}} &= \sum_{l=B^{j-1}}^{B^{j+1}}\sum_{m=-l}^{l} b\left(\frac{l}{B^j}\right)a_{lm}\left[\sum_k \lambda_{jk}Y_{lm}(\xi_{jk})\right] \\ &= \sum_{l=B^{j-1}}^{B^{j+1}}\sum_{m=-l}^{l} b\left(\frac{l}{B^j}\right)a_{lm}\left[\int_{S^2} Y_{lm}(\mathbf{n})d\Omega\right] = 0.\end{aligned} \tag{8.23}$$

The main difference between the Spherical Needlets and the spherical harmonics lies in the fact that the latter form an orthonormal basis for the space of square-integrable function on the sphere whereas Spherical Needlets don't because of redundant elements. Spherical Needlets, instead, form a *tight frame*, that can be viewed as the closer system to a basis

Definition 5. *Given a Hilbert space of functions $\mathcal{H}$ with inner product $\langle .,. \rangle$, a countable family of functions $\{e_k : k = 1, 2, 3, \ldots\}$ is called a frame if there exist universal constants c, C called frame bounds, such that for all $f \in \mathcal{H}$*

$$c||f||^2 \leq \sum_k |\langle f, e_k\rangle|^2 \leq C||f||^2. \tag{8.24}$$

The frame is called tight if $c = C$.

In order to deal with spherical random fields, $L^2(S^2)$ must be taken as the Hilbert space with the usual inner product

$$\langle f, g\rangle := \int_{S^2} f g d\Omega\,. \tag{8.25}$$

In particular, Spherical Needlets form a tight frame with $c = C = 1$ (Marinucci & Peccati 2011), so it is possible to rewrite eq. 8.24 as follows

$$\sum_k |\langle f, e_k\rangle|^2 \equiv \int_{S^2} f(\mathbf{n})^2 d\Omega\,. \tag{8.26}$$

This equation represents the norm-preserving property of the fields, property that is shared by all the orthonormal systems. In such sense, a tight frame is the closest system to an orthonormal basis.

The norm-preserving property can be rewritten as follows:

$$\begin{aligned}\sum_{jk}\beta_{jk}^2 &= \sum_{jk}\lambda_{jk}\left\{\sum_l b\left(\frac{l}{B^j}\right)\sum_m a_{lm}Y_{lm}(\xi_{jk})\right\}^2 \\ &= \sum_j\sum_{l_1l_2} b\left(\frac{l_1}{B^{j_1}}\right)b\left(\frac{l_2}{B^{j_2}}\right)\sum_{m_1m_2}a_{l_1m_1}a^*_{l_2m_2}\sum_k\lambda_{jk}Y_{l_1m_1}(\xi_{jk})Y^*_{l_2m_2}(\xi_{jk}) \\ &= \sum_j\sum_{l_1l_2} b\left(\frac{l_1}{B^{j_1}}\right)b\left(\frac{l_2}{B^{j_2}}\right)\sum_{m_1m_2}a_{l_1m_1}a^*_{l_2m_2}\delta^{l_2}_{l_1}\delta^{m_2}_{m_1} \\ &= \sum_j\sum_l b^2\left(\frac{l}{B^j}\right)\sum_m|a_{lm}|^2 = \sum_l(2l+1)\hat{C}_l,\end{aligned} \tag{8.27}$$

where

$$\hat{C}_l = \frac{1}{2l+1}\sum_m|a_{lm}|^2, \tag{8.28}$$

providing the correct normalization for Spherical Needlets. Then, Needlets coefficients seems to act just like the harmonic coefficients. This analogy become more strictly when we write the *reconstruction formula* for the Spherical Needlets, providing the way to reconstruct the starting field from the Spherical Needlets using the Needlet coefficients. Indeed, for all the functions $f\in L^2(S^2)$ with corresponding coefficients $\{\beta_{jk}=\beta_{jk}(f)\}$, we have

$$\begin{aligned}&\sum_{jk}\beta_{jk}\psi_{jk}(\mathbf{n}) \\ &= \sum_j\sum_{l_1}\sum_{m_1=-l_1}^{l_1} b\left(\frac{l_1}{B^j}\right)b\left(\frac{l_2}{B^j}\right)a_{l_1m_1}Y_{l_1m_1}(\mathbf{n})\sum_{l_2}\sum_{m_2=-l_2}^{l_2}\sum_k Y_{l_1m_1}(\xi_{jk})Y^*_{l_1m_1}(\xi_{jk})\lambda_{jk}\end{aligned} \tag{8.29}$$

Using the property of cubature points and weight in eq. 8.6, we have that

$$\sum_k Y_{l_1m_1}(\xi_{jk})Y^*_{l_1m_1}(\xi_{jk})\lambda_{jk} = \int_{S^2}Y_{l_1m_1}(\xi_{jk})Y^*_{l_1m_1}(\xi_{jk})d\Omega = \delta^{l_2}_{l_1}\delta^{m_2}_{m_1}, \tag{8.30}$$

then,

$$\begin{aligned}&\sum_{jk}\beta_{jk}\psi_{jk}(\mathbf{n}) \\ &= \sum_j\sum_{l_1}\sum_{m_1=-l_1}^{l_1} b\left(\frac{l_1}{B^j}\right)b\left(\frac{l_2}{B^j}\right)a_{l_1m_1}Y_{l_1m_1}(\mathbf{n})\sum_{l_2}\sum_{m_2=-l_2}^{l_2}\delta^{l_2}_{l_1}\delta^{m_2}_{m_1} \\ &= \sum_{l_1}\sum_{m_1=-l_1}^{l_1}a_{l_1m_1}Y_{l_1m_1}(\mathbf{n}),\end{aligned} \tag{8.31}$$

so that

$$f(\mathbf{n}) = \sum_{jk}\beta_{jk}\psi_{jk}(\mathbf{n}). \tag{8.32}$$

Eqq. 8.27 and 8.32 are directly consequence of the partion of unity property (eq. 8.15) characteristic of tight frames. This simple reconstruction formula is then typical of tight frame, and does not hold for other wavelet systems (Marinucci & Peccati 2011). Its similarity with the Spherical Harmonics reconstruction formula

$$f(\mathbf{n}) = \sum_{lm} a_{lm} Y_{lm}(\mathbf{n}) \tag{8.33}$$

makes the Spherical Needlets the best wavelet system usable to replace the Spherical Harmonics basis.

8.1.1 Properties

Localization property and missing observations

Spherical Needlets enjoy an excellent localization property in the real domain (Narcowich et al. 2006b,a).

Proposition 2. *Consider the function $\psi_{jk}(\boldsymbol{n})$ defined in 8.13; then there exist a constant $c_M > 0$ such that, for every $x \in S^2$:*

$$|\psi_{jk}(\boldsymbol{n})| \leq \frac{c_M B^j}{(1 + B^j \arccos\langle \xi_{jk}, x\rangle)^M} \quad uniformly\ in (j,k). \tag{8.34}$$

where $\langle ., . \rangle$ is the Euclidean inner product, whereas $\arccos\langle ., . \rangle$ is the natural distance on the unit sphere between two points. For $b(.) \in C^\infty$, eq. 8.34 holds for $M \in \mathbb{N}$, that is, Needlets are quasi-exponentially localized around any cubature point ξ_{jk}. Otherwise, the value of ψ_{jk} goes to zero quasi-exponentially as j goes to infinity. Hence, at smaller values of B, Needlets are more concentrated in harmonic space, because less multipoles entering in any Needlet, instead larger values of B ensure a faster decay in real space, and a stronger behaviour when the spherical field is not fully considered, that is, if there exist gaps in the sphere. The localization property, indeed, has a significant consequence: Spherical Needlets coefficients are asymptotically unaffected by the presence of gaps in the sphere (Baldi et al. 2006).

Let $G \subset S^2$ be a set of points removed from the sphere. Calling $\widetilde{T}$ the field obtained by subtraction of the field defined in G from the starting field T, then $\widetilde{T}(\mathbf{n}) = T(\mathbf{n})_{S^2/G}\mathbb{I}(\mathbf{n})$ and $G_\varepsilon := \{x \in S^2 : d(x, G) \leq \varepsilon\}$. Moreover, define the neighbourhood of radius ε around the set $G \subset S^2$. Then, write β^*_{jk} to indicate the random Needlet coefficients evaluated on the partially observed sphere, so that

$$\begin{aligned} \beta^*_{jk} &= \int_{S^2} \widetilde{T}(\mathbf{n})\psi_{jk}(\mathbf{n})d\Omega = \int_{S^2/G} T(\mathbf{n})\psi_{jk}(\mathbf{n})d\Omega \\ &= \beta_{jk} - \int_G T(\mathbf{n})\psi_{jk}(\mathbf{n})d\Omega \end{aligned} \tag{8.35}$$

Proposition 3. *For $\xi_{jk} \in S^2/G_\varepsilon$. We have*

$$\sqrt{\langle \left\{\beta^*_{jk} - \beta_{jk}\right\}^2 \rangle} \leq \frac{c_M B^j \Omega_G}{(1 + B^j\varepsilon)^M} \sqrt{\langle T^2(\boldsymbol{n})\rangle}. \tag{8.36}$$

As in the previous Proposition, for $b(.) \in C^\infty$, eq. 8.36 holds for $M \in \mathbb{N}$, so that the contributions of missing observations to the statistic of the field goes to zero asymptotically as j goes to infinity. Furthermore, the greater is parameter B, the stronger is the behaviour against incomplete sphere, that is in our framework, incomplete sky coverage.

Uncorrelation property

Spherical Needlets are asymptotically uncorrelated for any fixed angular distance, as the frequencies grows, going to infinity. To show this property, we first needs to recall some arguments and write some consequences of the Needlets properties. First of all, the compact support in harmonic domain entails that random Needlets coefficients are uncorrelated whenever $|j-j'| \geq 2$ due to the orthonormality of the Spherical Harmonics, indeed.

$$\begin{aligned}\langle \beta_{jk}\beta_{j'k'}\rangle &= \sqrt{\lambda_{jk}\lambda_{j'k'}}\sum_{ll'} b\left(\frac{l}{B^j}\right) b\left(\frac{l'}{B^{j'}}\right)\sum_{mm'}\langle a_{lm}a_{l'm'}\rangle Y_{lm}(\xi_{jk})Y_{l'm'}(\xi_{j'k'}) \\ &= \sqrt{\lambda_{jk}\lambda_{j'k'}}\sum_{ll'} b\left(\frac{l}{B^j}\right) b\left(\frac{l'}{B^{j'}}\right)\sum_{mm'} C_l\delta_l^{l'}\delta_m^{m'} Y_{lm}(\xi_{jk})Y^*_{l'm'}(\xi_{j'k'}).\end{aligned} \tag{8.37}$$

If $|j-j'| \geq 2$ the two sum in eq. 8.37 don't have common multipoles, then $\delta_l^{l'} = 0$ and we have

$$\langle \beta_{jk}\beta_{j'k'}\rangle = 0. \tag{8.38}$$

For $j = j'$, it is possible to write the variance of the Needlet coefficients as

$$\begin{aligned}\langle \beta_{jk}^2\rangle &= \lambda_{jk}\sum_l b^2\left(\frac{l}{B^j}\right) C_l \sum_{m=-l}^{l} Y_{lm}(\xi_{jk})Y^*_{lm}(\xi_{jk}) \\ &= \lambda_{jk}\sum_l \frac{2l+1}{4\pi} b^2\left(\frac{l}{B^j}\right) C_l =: \sigma_{jk}^2 > 0\end{aligned} \tag{8.39}$$

Note that we have $\sigma_{jk}^2 \approx: \sigma_j^2$ uniformly over k (Marinucci & Peccati 2011), where

$$\sigma_j^2 := \frac{1}{N_j}\sum_l \frac{2l+1}{4\pi} b^2\left(\frac{l}{B^j}\right) C_l, \quad N_j := card\{\mathcal{X}_j\}. \tag{8.40}$$

The follows conditions is necessary so that the uncorrelation property holds

Condition 1. *There exist $M \in \mathbb{N}, \alpha > 2$ and a sequence of functions $\{g_j(.)\}$ such that*

$$C_l = l^{-\alpha} g_j\left(\frac{l}{B^j}\right) > 0, \qquad for\ \ B^{j-1} < l < B^{j+1}, \tag{8.41}$$

where

$$c_0^{-1} \leq g_j \leq c_0 \quad for\ \ all\ \ j \in \mathbb{N}, \tag{8.42}$$

and for $r = 1, \ldots, M$

$$\sup_j \sup_{B^{-1}\leq u\leq B}\left|\frac{d^r}{du^r} g_j(u)\right| \leq c_r \quad some\ \ c_1, \ldots, c_M > 0. \tag{8.43}$$

Condition 1 entails a weak smothness requirment on the behaviour of the angular power spectrum, which is trivially satisfied by cosmological revelant models (Marinucci & Peccati 2011), where power spectrum usually behaves as an inverse polynomial (Dodelson 2003; Scodeller et al. 2011)

$$C_l = \langle |a_{lm}|^2\rangle \simeq G(l) l^{-\alpha}, \tag{8.44}$$

where $G(l)$ is some smooth function,

The correlation coefficients can be then derived as

$$\begin{aligned} Corr(\beta_{jk}, \beta_{jk'}) &= \frac{\langle \beta_{jk} \beta_{jk'} \rangle}{\sqrt{\langle \beta_{jk}^2 \rangle \langle \beta_{jk'}^2 \rangle}} \\ &= \frac{\sqrt{\lambda_{jk}\lambda_{jk'}} \sum_l b^2 \left(\frac{l}{B^j}\right) \frac{2l+1}{4\pi} C_l P_l(\langle \xi_{jk}, \xi_{jk'} \rangle}{\sqrt{\lambda_{jk}\lambda_{jk'}} \sum_l b^2 \left(\frac{l}{B^j}\right) \frac{2l+1}{4\pi} C_l} \end{aligned} \tag{8.45}$$

then (Baldi et al. 2006)

Lemma 2. *Under Condition 1 the following inequality holds*

$$|Corr(\beta_{jk}, \beta_{jk'})| \leq \frac{C_M}{(1 + B^j d(\xi_{jk}, \xi_{jk'}))^M}, \qquad some \;\; C_M > 0, \tag{8.46}$$

where $d(\xi_{jk}, \xi_{jk'}) = \arccos(\langle \xi_{jk}, \xi_{jk'} \rangle)$ *is the standard distance on the sphere.*

Spherical Needlets coefficients are then asymptotically uncorrelated at any fixed angular distance $d(\xi_{jk}, \xi_{jk'})$ as the frequency j grows to infinity. This property is not a consequence of the localization property. In fact, it is possible to find many counterexample in the functional analysis literature (Marinucci & Peccati 2011).

8.1.2 Mexican Needlets

Another definition of Spherical Needlets alternative to the tandard Needlets is the so-called *Mexican Needlets* (Geller & Mayeli 2007b, 2009, 2007a; Freeden & Schreiner 1998). Mexican Needlets were introduced removing the condition on the compact support of the kernel of Spherical Needlets. This means that in the harmonic space, mexican Needlets are larger than Spherical Needlets, because they contain all the multipoles. The resulting kernel thus involves polynomials of infinitely large order, making exact cubature formula no more holding. In place of eq. 8.21 we have

$$b\left(\frac{l}{B^j}\right) = \left(\frac{l(l+1)}{B^{2j}}\right)^p \exp\left(-\frac{l(l+1)}{B^{2j}}\right) \tag{8.47}$$

that, inserted in definition 8.13, brings to

$$\psi_{jk}(x; p) := \sqrt{\lambda_{jk}} \sum_{l=0}^{\infty} \left(\frac{l(l+1)}{B^{2j}}\right)^p \exp\left(-\frac{l(l+1)}{B^{2j}}\right) \frac{2l+1}{4\pi} P_l(\langle x, \xi_{jk} \rangle). \tag{8.48}$$

Remark 1. *It is important to note that for* $p = 1$*, mexican Needlets provide a very good approximation of the so-called Spherical Mexican Hat Wavelets (SMHW) as the frequency* j *grows to infinity. This kind of wavelets has been used in many works of statistical cosmology and in particular in the study of the CMB (Curto et al. 2009, 2011, 2012).*

The introduction of high order terms is allowed by the absence of a compact support in the harmonic domain. This brings to an improvement of the localization property of the mexican Needlet in the harmonic domain, but also to a worsening of the localization properties in the real space, due to the "uncertainty principle" of Fourier transform, for which is not possible for a function and its Fourier transform to be simultaneously very small (Marinucci & Peccati 2011; Havin & Joricke 1994). Otherwise, mexican Needlets

are better concentrated in real space than standard ones, due the fact they introduce a Gaussian decay at each scale. This property together with the fact they are well-defined by formula in eq. 8.47 in real space (unlike the standard Needlets due the lack of usable formulas), allows to implement mexican Needlets directly on the sphere (Geller & Mayeli 2007b, 2009) rather than only in the frequencies domain.

The mexican Needlet coefficients are given by

$$\begin{aligned}\beta_{jk}(p) &= \int_{S^2} T(\mathbf{n})\psi_{jk}(x;p)d\Omega = \int_{S^2}\sum_{lm} a_{lm}Y_{lm}(\mathbf{n})\psi_{jk}(x;p)d\Omega \\ &= \sqrt{\lambda_{jk}}\sum_{l}\left(\frac{l(l+1)}{B^{2j}}\right)^{p}\exp\left(-\frac{l(l+1)}{B^{2j}}\right)\sum_{m} a_{lm}Y_{lm}(\xi_{jk}).\end{aligned} \tag{8.49}$$

Due the lack of an exact cubature formula, it is no longer possible use the mexican Needlets coefficients to write an exact reconstruction formula just like the one obtained for the standard Needlets (eq. 8.32). But, it can be easily show that mexican Needlets provide a more powerful uncorrelation property with respect to the standard Needlets (Lan & Marinucci 2008a; Mayeli 2008). The explicitly expression for the correlation coefficient is

$$Corr(\beta_{jk_1;p},\beta_{jk_2;p}) = \frac{\sum_l (\frac{l(l+1)}{B^{2j}})^{2p} e^{-\frac{2l(l+1)}{B^{-2j}}}(2l+1)C_l P_l(\langle \xi_{jk_1}\xi_{jk_2}\rangle)}{\sum_l (\frac{l(l+1)}{B^{2j}})^{2p} e^{-\frac{2l(l+1)}{B^{-2j}}}(2l+1)C_l}. \tag{8.50}$$

Then, we have

Proposition 4. *Assume Condition 1 holds with $\alpha < 4p+2$ and $M \geq 4p+2-\alpha$; then there exist some constant $C_M > 0$ such that*

$$|Corr(\beta_{jk_1;p},\beta_{jk_2;p})| \leq \frac{C_M}{(1+j^{-1}B^j \arccos(\langle \xi_{jk_1}\xi_{jk_2}\rangle))^{(4p+2-\alpha)}} \tag{8.51}$$

The parameter α is linked to angular power spectrum, representing its decaying rate (Marinucci & Peccati 2011). Random mexican Needlet coefficients are correlated if the parameter α is greater than or equal to $4p+2$, whereas they present a better uncorrelation property with respect to standard Needlets when $\alpha < 4p+2$, due to the j^{-1} in the denominator of eq. 8.51. This is expressed by the following proposition

Proposition 5. *Under Condition 1, for $\alpha > 4p+2$, $\forall \varepsilon \in (0,1)$, there exist a positive $\delta = \delta_\varepsilon$, such that*

$$\lim_{j\to\infty} \inf Corr(\beta_{jk_1;p},\beta_{jk_2;p}) > 1-\varepsilon, \tag{8.52}$$

for all $\{\xi_{jk},\xi_{jk'}\}$ such that $d(\xi_{jk},\xi_{jk'}) \leq \delta$.

The explanation of this different behaviour of Needlet coefficients between standard and mexican Needlets is quite simple and depends on the lack of compact support for the latters. In fact, the lowest scale taking in account the lowest multipoles that are the most affected by cosmic variance. Because of the standard Needlets compact support in the frequencies domain, these low-frequency components are dropped out, ensuring the uncorrelation of random coefficients at high frequencies. This doesn't happen with the mexican Needlets, in which none of the components are ruled out due to the lack of compact support. The low frequencies components become then relevant for mexican

Needlets when the condition on α of proposition 4 is not satisfied, i.e. the spectrum decays too fast. Instead, when the angular power spectrum is decaying "slowly enough", asymptotic uncorrelation of the random coefficients is ensured. It should be noted that for cosmological application $\alpha = 2$ provides an excellent fit to the data, granting asymptotic uncorrelation even for $p = 1$ (Marinucci & Peccati 2011). In (Scodeller et al. 2011), numerical results show that for CMB-like power spectra, the uncorrelation property of mexican Needlets is more powerful than standard Needlets, justifying the use of this new kind of Spherical Needlets.

CHAPTER 9

The Needlet Trispectrum

The main effort in constraining non-Gaussianity was focused on the bispectrum, and then in constraining f_{NL}, because of the fact that inflationary trispectrum is generally suppressed with respect to the bispectrum. There is a significant literature on the trispectrum estimator (Smith et al. 2015; Fergusson et al. 2010; Regan et al. 2015; Kogo & Komatsu 2006; Hu 2001), showing how it is possible to constrain g_{NL} optimally using Spherical Harmonics based estimator. The aim of my work is to introduce an estimator stronger than the Spherical Harmonics one in presence of masks, able to constrain g_{NL}, thus giving an independent way to measure inflationary parameter that can support all of the existing methods. An estimator close to mine was developed by (Regan et al. 2015), but it was tested only on low resolution maps, thus not giving reliable information with respect to the data we have today from, i.e., Planck survey (Planck Collaboration et al. 2014a, 2016a). In what follows, I'll derive the optimal Needlet system based trispectrum estimator and I will show how does it behave when applied to high-resolution CMB data, with the aim to apply it to the real high resolution data of Planck and thus obtaining a brand new estimation for g_{NL}.

9.1 Derivation of the Optimal Trispectrum Estimator

In order to provide a rigorous trispectrum estimator, I have to introduce a new method to calculate the polyspectrum of a spherical random field. This section is based upon the conclusions of (Marinucci & Wigman 2012).

Let $T(\mathbf{n})$ be a zero-mean Gaussian and isotropic spherical random field and consider the spectral decomposition

$$T(\mathbf{n}) = \sum_l T_l(\mathbf{n}), \tag{9.1}$$

where

$$T_l(\mathbf{n}) = \sum_m a_{lm} Y_{lm}(\mathbf{n}). \tag{9.2}$$

Consider functionals of the form

$$Z_l = \sum_{q=0}^{Q} b_q \int_{S^2} \left[\frac{T_l(\mathbf{n})}{\sqrt{\langle T_l^2(\mathbf{n}) \rangle}} \right]^q d\Omega\,, \quad \text{for some } Q \in \mathbb{N}, b_q \in \mathbb{R}. \tag{9.3}$$

This polynomial statistics represent a *renormalization of the sum of the polyspectra* of the random field T. Then, there exist coefficients $\beta_0 \dots \beta_p$ such that it is possible to rewrite

the functionals Z_l in terms of Hermite polynomials

$$Z_l = \sum_{q=0}^{Q} \beta_q \int_{S^2} H_q \left(\frac{T_l(\mathbf{n})}{\sqrt{\langle T_l^2(\mathbf{n}) \rangle}} \right) d\Omega \tag{9.4}$$

where H_q is the q-th order Hermite polynomial (see (Marinucci & Wigman 2012) for the details). The Hermite polynomials are the polynomials with the lowest variance among the other polynomials (Marinucci & Peccati 2011). This fact make the new definition of polyspectra in eq. 9.4 suitable for the construction of the optimal estimator for these statistics.

While for the bispectrum we have to consider the third-order Hermite polynomial $H_3(\mathbf{n}) = x^3 - 1$, for the trispectrum the fourth-order Hermite polynomial must be used

$$H_4(x) = x^4 - 6x^2 + 3. \tag{9.5}$$

A difficulty in the case of Hermite polynomials is that they are functions of a variable, that is, the ratio $\frac{T_l(\mathbf{n})}{\sqrt{\langle T_l^2(\mathbf{n}) \rangle}}$. Instead, polyspectra are functions of two or more random variables, labelled by the multipoles l_i. Therefore, in the next paragraph, I 'll introduce a multi-variate form of the Hermite polynomials, called *Wick Product*, with the same property of low variance of the Hermite polynomials.

9.1.1 Wick Product

Wick product was introduced in (Wick 1950) and it is often used in applied mathematics (Hu & Yan 2009; Kaligotla & Lototsky 2010). It is defined by this recursive formula

$$\begin{cases} ::= 1 \\ \frac{\partial :X_1,\ldots,X_k:}{\partial X_i} =: X_1, \ldots, X_{i-1}, X_{i+1}, \ldots, X_k : \quad \text{for } k \geq 1 \end{cases}$$

and the property of null mean holds, $\langle : x_1 \ldots x_k : \rangle = 0$ for $k \geq 1$.

In order to apply Wick product to polyspectra, I had to derive the first four order polynomials. At the first order, Wick product is simply the subtraction of the expected value from the variables itself:

$$: X := X - \langle X \rangle \tag{9.6}$$

for $k = 2$ one has:

$$: X_1, X_2 := X_1 X_2 - \langle X_1 \rangle X_2 + \langle X_1 \rangle X_2 + 2\langle X_1 \rangle \langle X_2 \rangle - \langle X_1 X_2 \rangle \tag{9.7}$$

for $k = 3$:

$$\begin{aligned} : X_1, X_2, X_3 : = & X_1 X_2 X_3 \\ & - \langle X_1 \rangle X_2 X_3 - \langle X_2 \rangle X_1 X_3 - \langle X_3 \rangle X_1 X_2 \\ & + 2\langle X_1 \rangle \langle X_2 \rangle X_3 + 2\langle X_1 \rangle \langle X_3 \rangle X_2 + 2\langle X_2 \rangle \langle X_3 \rangle X_1 \\ & - \langle X_1 X_2 \rangle X_3 - \langle X_1 X_3 \rangle X_2 - \langle X_2 X_3 \rangle X_1 \\ & - \langle X_1 X_2 X_3 \rangle \\ & + 2\langle X_1 \rangle \langle X_2 X_3 \rangle + 2\langle X_2 \rangle \langle X_1 X_3 \rangle + 2\langle X_3 \rangle \langle X_1 X_2 \rangle \\ & - 2\langle X_1 \rangle \langle X_2 \rangle \langle X_3 \rangle - 2\langle X_1 \rangle \langle X_3 \rangle \langle X_2 \rangle - 2\langle X_2 \rangle \langle X_3 \rangle \langle X_1 \rangle \end{aligned} \tag{9.8}$$

then, for $k = 4$:

$$
\begin{aligned}
: X_1, X_2, X_3, X_4 : = & X_1X_2X_3X_4 \\
& - \langle X_1\rangle X_2X_3X_4 - \langle X_2\rangle X_1X_3X_4 \\
& - \langle X_3\rangle X_1X_2X_4 - \langle X_4\rangle X_1X_2X_3 \\
& + 2\langle X_1\rangle\langle X_2\rangle X_3X_4 + 2\langle X_1\rangle\langle X_3\rangle X_2X_4 + 2\langle X_1\rangle\langle X_4\rangle X_2X_3 \\
& + 2\langle X_2\rangle\langle X_3\rangle X_1X_4 + 2\langle X_2\rangle\langle X_4\rangle X_1X_3 + 2\langle X_3\rangle\langle X_4\rangle X_1X_2 \\
& - \langle X_1X_2\rangle X_3X_4 - \langle X_1X_3\rangle X_2X_4 - \langle X_1X_4\rangle X_2X_3 \\
& - \langle X_2X_3\rangle X_1X_4 - \langle X_2X_4\rangle X_1X_3 - \langle X_3X_4\rangle X_1X_2 \\
& - \langle X_1X_2X_3\rangle X_4 - \langle X_1X_3X_4\rangle X_2 \\
& - \langle X_1X_2X_4\rangle X_3 - \langle X_2X_3X_4\rangle X_2 \\
& + 2\langle X_1\rangle\langle X_2X_3\rangle X_4 + 2\langle X_2\rangle\langle X_1X_3\rangle X_4 + 2\langle X_3\rangle\langle X_1X_2\rangle X_4 \\
& + 2\langle X_1\rangle\langle X_2X_4\rangle X_3 + 2\langle X_2\rangle\langle X_1X_4\rangle X_3 + 2\langle X_4\rangle\langle X_1X_2\rangle X_3 \\
& + 2\langle X_1\rangle\langle X_3X_4\rangle X_2 + 2\langle X_3\rangle\langle X_1X_4\rangle X_2 + 2\langle X_4\rangle\langle X_1X_3\rangle X_2 \\
& + 2\langle X_2\rangle\langle X_3X_4\rangle X_1 + 2\langle X_3\rangle\langle X_2X_4\rangle X_1 + 2\langle X_4\rangle\langle X_2X_3\rangle X_1 \\
& - 6\langle X_1\rangle\langle X_2\rangle\langle X_3\rangle X_4 - 6\langle X_1\rangle\langle X_2\rangle\langle X_4\rangle X_3 \\
& - 6\langle X_1\rangle\langle X_3\rangle\langle X_4\rangle X_2 - 6\langle X_2\rangle\langle X_3\rangle\langle X_4\rangle X_1 \\
& + 2\langle X_1\rangle\langle X_2X_3X_4\rangle + 2\langle X_2\rangle\langle X_1X_3X_4\rangle \\
& + 2\langle X_3\rangle\langle X_1X_2X_4\rangle + 2\langle X_4\rangle\langle X_1X_2X_3\rangle \\
& - 6\langle X_1\rangle\langle X_2\rangle\langle X_3X_4\rangle - 6\langle X_1\rangle\langle X_3\rangle\langle X_2X_4\rangle \\
& - 6\langle X_1\rangle\langle X_4\rangle\langle X_2X_3\rangle - 6\langle X_2\rangle\langle X_3\rangle\langle X_1X_4\rangle \\
& - 6\langle X_2\rangle\langle X_4\rangle\langle X_1X_3\rangle - 6\langle X_3\rangle\langle X_4\rangle\langle X_1X_2\rangle \\
& + 2\langle X_1X_2\rangle\langle X_3X_4\rangle + 2\langle X_1X_3\rangle\langle X_2X_4\rangle + 2\langle X_1X_4\rangle\langle X_2X_3\rangle \\
& + 24\langle X_1\rangle\langle X_2\rangle\langle X_3\rangle\langle X_4\rangle - \langle X_1X_2X_3X_4\rangle.
\end{aligned}
\tag{9.9}
$$

Consider then Gaussian centered random variables, $\langle X_i\rangle = 0$, $\langle X_i^2\rangle = \sigma_i$ and $\langle X_iX_j\rangle = \sigma_{ij}$. Due to the vanishing property of the Gaussian variables odd moments, the fourth-order Wick product (eq. 9.9) reduces as follows

$$
\begin{aligned}
: X_1, X_2, X_3, X_4 : = & X_1X_2X_3X_4 \\
& - \sigma_{12}X_3X_4 - \sigma_{13}X_2X_4 - \sigma_{23}X_1X_4 \\
& - \sigma_{14}X_2X_3 - \sigma_{24}X_1X_3 - \sigma_{34}X_1X_2 \\
& + 2\sigma_{12}\sigma_{34} + 2\sigma_{13}\sigma_{24} + 2\sigma_{14}\sigma_{23} \\
& - \langle X_1X_2X_3X_4\rangle.
\end{aligned}
\tag{9.10}
$$

Thanks to Diagram Formula (appendix A) we can decompose the term in the last line of eq. (9.10) as

$$
\langle X_1X_2X_3X_4\rangle = \sigma_{12}\sigma_{34} + \sigma_{13}\sigma_{24} + \sigma_{14}\sigma_{23}, \tag{9.11}
$$

thus obtaining:

$$
\begin{aligned}
: X_1, X_2, X_3, X_4 : = & X_1X_2X_3X_4 \\
& - \sigma_{12}X_3X_4 - \sigma_{13}X_2X_4 - \sigma_{23}X_1X_4 \\
& - \sigma_{14}X_2X_3 - \sigma_{24}X_1X_3 - \sigma_{34}X_1X_2 \\
& + \sigma_{12}\sigma_{34} + \sigma_{13}\sigma_{24} + \sigma_{14}\sigma_{23}.
\end{aligned}
\tag{9.12}
$$

If we consider only one gaussian centered random variable $\langle X_i \rangle = 0$, $\langle X_i^2 \rangle = \sigma_i$, one has

$$: X, X, X, X := X^4 - 6\sigma X^2 + 3\sigma^2 \tag{9.13}$$

When $\sigma = 1$, the fourth-order Wick product is the Hermite polynomial of order four becomes

$$: X, X, X, X := X^4 - 6X^2 + 3 \tag{9.14}$$

confirming the first hypothesis about Wick product, that is, Wick product is the multidimensional analogue of Hermite polynomials (9.5).

When the variables involved in the Wick product are non-Gaussian, what we get taking the expected value of the Wick product is:

$$\langle : X_1, X_2, X_3, X_4 : \rangle = \langle X_1 X_2 X_3 X_4 \rangle - (\sigma_{12}\sigma_{34} + \sigma_{13}\sigma_{24} + \sigma_{14}\sigma_{23}) \tag{9.15}$$

that is the definition of the connected part of the trispectrum (see eq. (1.55), exactly what we want to measure with our estimator.

In order to prove the property of lowest variance of the Wick polynomials, consider a fourth-order polynomials in four variables, written as follows

$$\begin{aligned} P(X_1, X_2, X_3, X_4) = {} & X_1 X_2 X_3 X_4 \\ & + c_1 X_2 X_3 X_4 + c_2 X_1 X_3 X_4 \\ & + c_3 X_1 X_2 X_4 + c_4 X_1 X_2 X_3 \\ & + c_{12} X_3 X_4 + c_{13} X_2 X_4 + c_{14} X_2 X_3 \\ & + c_{23} X_1 X_4 + c_{24} X_1 X_3 + c_{34} X_1 X_2 \\ & + c_{123} X_4 + c_{124} X_3 + c_{134} X_2 + c_{234} X_1 \\ & + c_{1234}. \end{aligned} \tag{9.16}$$

It is possible to rewrite this polynomial in terms of Wick product

$$\begin{aligned} P(X_1, X_2, X_3, X_4) =: {} & X_1 X_2 X_3 X_4 : \\ & + c_1 X_2 X_3 X_4 + c_2 X_1 X_3 X_4 + c_3 X_1 X_2 X_4 + c_4 X_1 X_2 X_3 \\ & + (c_{12} + \langle X_1 X_2 \rangle) X_3 X_4 + (c_{13} + \langle X_1 X_3 \rangle) X_2 X_4 \\ & + (c_{14} + \langle X_1 X_4 \rangle) X_2 X_3 + (c_{23} + \langle X_2 X_3 \rangle) X_1 X_4 \\ & + (c_{24} + \langle X_2 X_4 \rangle) X_1 X_3 + (c_{34} + \langle X_3 X_4 \rangle) X_1 X_2 \\ & + c_{123} X_4 + c_{124} X_3 + c_{134} X_2 + c_{234} X_1 \\ & + c_{1234} - 2\langle X_1 X_2 \rangle \langle X_3 X_4 \rangle - 2\langle X_1 X_3 \rangle \langle X_2 X_4 \rangle \\ & - 2\langle X_2 X_3 \rangle \langle X_1 X_4 \rangle + \langle X_1 X_2 X_3 X_4 \rangle \\ =: {} & X_1 X_2 X_3 X_4 : + Q(X_1, X_2, X_3, X_4), \end{aligned} \tag{9.17}$$

where $Q(X_1, X_2, X_3, X_4)$ is a third order polynomial in (X_1, X_2, X_3, X_4). It is readily seen that $: X_1 X_2 X_3 X_4 :$ is uncorrelated with any polynomials of order smaller than four in the same variables. In fact, the uncorrelation with polynomials of order three or one is provided by the property of Gaussian variables, whose odd moments are always equal

to 0

$$\begin{aligned}\langle : X_1, X_2, X_3, X_4 : X_1X_2X_3\rangle &= \langle X_1^2X_2^2X_3^2X_4\rangle \\ &- \langle X_1X_2\rangle\langle X_1X_2X_3^2X_4\rangle - \langle X_1X_3\rangle\langle X_1X_2^2X_3X_4\rangle \\ &- \langle X_2X_3\rangle\langle X_1^2X_2X_3X_4\rangle - \langle X_1X_4\rangle\langle X_1X_2^2X_3^2\rangle \\ &- \langle X_2X_4\rangle\langle X_1^2X_2X_3^2\rangle - \langle X_3X_4\rangle\langle X_1^2X_2^2X_3\rangle \\ &+ (2\langle X_1X_2\rangle\langle X_3X_4\rangle + 2\langle X_1X_3\rangle\langle X_2X_4\rangle \\ &+ 2\langle X_2X_3\rangle\langle X_1X_4\rangle - \langle X_1X_2X_3X_4\rangle) \times \langle X_1X_2X_3\rangle \\ &= 0,\end{aligned} \tag{9.18}$$

while the uncorrelation with second order polynomials is provided by means of the *Diagram Formula* (see appendix A)

$$\begin{aligned}\langle : X_1, X_2, X_3, X_4 : X_1X_2\rangle &= \langle X_1^2X_2^2X_3X_4\rangle \\ &- \langle X_1X_2\rangle\langle X_1X_2X_3X_4\rangle - \langle X_1X_3\rangle\langle X_1X_2^2X_4\rangle \\ &- \langle X_2X_3\rangle\langle X_1^2X_2X_4\rangle - \langle X_1X_4\rangle\langle X_1X_2^2X_3\rangle \\ &- \langle X_2X_4\rangle\langle X_1^2X_2X_3\rangle - \langle X_3X_4\rangle\langle X_1^2X_2^2\rangle \\ &+ 2\langle X_1X_2\rangle^2\langle X_3X_4\rangle + 2\langle X_1X_3\rangle\langle X_2X_4\rangle\langle X_1X_2\rangle \\ &+ 2\langle X_2X_3\rangle\langle X_1X_4\rangle\langle X_1X_2\rangle - \langle X_1X_2X_3X_4\rangle\langle X_1X_2\rangle \\ &= 0\end{aligned} \tag{9.19}$$

Hence we have:

$$\begin{aligned}Var\{P(X_1, X_2, X_3, X_4)\} &= Var\{: X_1X_2X_3X_4 : + Q(X_1, X_2, X_3, X_4)\} \\ &= Var\{: X_1X_2X_3X_4 :\} + Var\{Q(X_1, X_2, X_3, X_4)\} \\ &+ 2Cov\{: X_1X_2X_3X_4 :, Q(X_1, X_2, X_3, X_4)\} \\ &= Var\{: X_1X_2X_3X_4 :\} + Var\{Q(X_1, X_2, X_3, X_4)\} \\ &\geq Var\{: X_1X_2X_3X_4 :\}.\end{aligned} \tag{9.20}$$

Then, eq. 9.20 entails the property of lowest variance for Wick Product. Although the proof is limited to the case of fourth order Wick product, that is, the case strictly related to the trispectrum, conclusions are more general and holds for every order of the Wick polynomials.

9.2 The Optimal Trispectrum Estimator

In order to write the Trispectrum estimator, we recall eq. 9.4, replacing Wick product instead of the Hermite polynomials

$$\begin{aligned}\int_{S^2} : \hat{T}_{l_1}(\mathbf{n})\hat{T}_{l_2}(\mathbf{n})\hat{T}_{l_3}(\mathbf{n})\hat{T}_{l_4}(\mathbf{n}) : d\Omega \;= \int_{S^2} &[\hat{T}_{l_1}(\mathbf{n})\hat{T}_{l_2}(\mathbf{n})\hat{T}_{l_3}(\mathbf{n})\hat{T}_{l_4}(\mathbf{n}) \\ &- (\Gamma_{l_1l_2}\hat{T}_{l_3}(\mathbf{n})\hat{T}_{l_4}(\mathbf{n}) + 5\text{cyc.}) \\ &+ (\Gamma_{l_1l_2}\Gamma_{l_3l_4} + 2\text{cyc.})]d\Omega\,,\end{aligned} \tag{9.21}$$

where $d\Omega$ is the *Lebesgue measure* of S^2, $\hat{T}_{l_i}(\mathbf{n}) = \frac{T_{l_i}(\mathbf{n})}{\langle T_{l_i}^2(\mathbf{n})\rangle}$ and $\Gamma_{l_il_j} = \langle \hat{T}_{l_i}(\mathbf{n})\hat{T}_{l_j}(\mathbf{n})\rangle$. We can divide integral in eq. 9.21 into two components. The first component is composed

by the first term, that is, the fourth-order Fourier momentum of the field

$$\int_{S^2} \hat{T}_{l_1}(\mathbf{n})\hat{T}_{l_2}(\mathbf{n})\hat{T}_{l_3}(\mathbf{n})\hat{T}_{l_4}(\mathbf{n})d\Omega\,, \tag{9.22}$$

giving the estimator of the trispectrum, while the second component is composed by all the remaining terms, forming a quadratic term. The effect of this quadratic term is to minimize the variance of the trispectrum, without introducing bias in the trispectrum expected value.

Taking the numerator of eq. 9.22, we obtain

$$\begin{aligned}
&\int_{S^2} T_{l_1}(\mathbf{n})T_{l_2}(\mathbf{n})T_{l_3}(\mathbf{n})T_{l_4}(\mathbf{n})d\Omega \\
&= \int_{S^2} \sum_{m_1 m_2 m_3 m_4} a_{l_1 m_1} a_{l_2 m_2} a_{l_3 m_3} a_{l_4 m_4} Y_{l_1 m_1}(\mathbf{n}) Y_{l_2 m_2}(\mathbf{n}) Y_{l_3 m_3}(\mathbf{n}) Y_{l_4 m_4}(\mathbf{n}) d\Omega \\
&= \sum_{m_1 m_2 m_3 m_4} a_{l_1 m_1} a_{l_2 m_2} a_{l_3 m_3} a_{l_4 m_4} \times G\{l_1, m_1; l_2, m_2; l_3, m_3; l_4, m_4\}
\end{aligned} \tag{9.23}$$

where $\mathcal{G}\{l_1, m_1; l_2, m_2; l_3, m_3; l_4, m_4\}$ is the fourth-order Gaunt integral,

$$\begin{aligned}
&\mathcal{G}\{l_1, m_1; l_2, m_2; l_3, m_3; l_4, m_4\} \\
&= \sqrt{\frac{(2l_1+1)(2l_2+1)(2l_3+1)(2l_4+1)}{4\pi}} \sum_{LM} (2L+1) \times \\
&\times \begin{pmatrix} l_1 & l_2 & L \\ m_1 & m_2 & -M \end{pmatrix} \begin{pmatrix} l_3 & l_4 & L \\ m_3 & m_4 & M \end{pmatrix} \begin{pmatrix} l_1 & l_2 & L \\ 0 & 0 & 0 \end{pmatrix} \begin{pmatrix} l_3 & l_4 & L \\ 0 & 0 & 0 \end{pmatrix}
\end{aligned} \tag{9.24}$$

Hence, we have

$$\begin{aligned}
&\int_{S^2} T_{l_1}(\mathbf{n})T_{l_2}(\mathbf{n})T_{l_3}(\mathbf{n})T_{l_4}(\mathbf{n})d\Omega \\
&= \frac{(4\pi)^2}{\sqrt{(2l_1+1)(2l_1+2)(2l_1+3)(2l_1+4)}} \sum_{m_1 \ldots m_4} \frac{a_{l_1 m_1} a_{l_2 m_2} a_{l_3 m_3} a_{l_4 m_4}}{\sqrt{C_{l_1} C_{l_2} C_{l_3} C_{l_4}}} \times \\
&\times \sqrt{\frac{(2l_1+1)(2l_1+2)(2l_1+3)(2l_1+4)}{4\pi}} \sum_{LM} (2L+1)(-1)^M (-1)^{-M} \times \\
&\times \begin{pmatrix} l_1 & l_2 & L \\ m_1 & m_2 & -M \end{pmatrix} \begin{pmatrix} l_3 & l_4 & L \\ m_3 & m_4 & M \end{pmatrix} \begin{pmatrix} l_1 & l_2 & L \\ 0 & 0 & 0 \end{pmatrix} \begin{pmatrix} l_3 & l_4 & L \\ 0 & 0 & 0 \end{pmatrix} \hat{Q}^{l_1 l_2}_{l_3 l_4}(L) \\
&= (4\pi)^{\frac{3}{2}} \sum_L \begin{pmatrix} l_1 & l_2 & L \\ 0 & 0 & 0 \end{pmatrix} \begin{pmatrix} l_3 & l_4 & L \\ 0 & 0 & 0 \end{pmatrix} \times \hat{Q}^{l_1 l_2}_{l_3 l_4}(L),
\end{aligned} \tag{9.25}$$

that is the same of eq. (1.70). As we have just seen, the introducing of the quadratic term make the variance of the trispectrum systematically lower then any other fourth-order statistic. The trispectrum estimator written in eq. 9.21 is then the optimal trispectrum estimator.

The asymptotic behaviour of the optimal trispectrum estimator in eq. 9.21 is analyzed in (Marinucci & Wigman 2012) and (Cammarota & Marinucci 2013) where is proved that the polyspectra of a spherical random fields behave as the normal distribution as the frequency goes to infinity

Theorem 2. *For all q such that $c_q > 0$, we have*

$$\frac{h_{2l;q}}{\sqrt{Var(h_{2l;q})}} \rightarrow_d \mathcal{N}(0,1), \quad asl \rightarrow \infty, \tag{9.26}$$

where

$$h_{l;q} = \int_{S^2} H_q(f_l(\boldsymbol{n}))d\Omega\,. \tag{9.27}$$

9.3 The Needlet Trispectrum

The aim of my PhD work was to construct the best optimal estimator for the trispectrum of a spherical random field. First, I derived the optimal estimator of trispectrum using the standard Fourier transform on the 2-sphere, that is the deconvolution by means of Spherical Harmonics. Then, in view of the bad behaviour of the Spherical Harmonics in case of incomplete sphere, I defined a new framework in which perform the deconvolution of the field, the Spherical Needlets. Now, combining the statistical robustness of Spherical Needlets with the optimal trispectrum estimator, I'm going to derive the optimal estimator for the trispectrum which is also the stronger in case of incompleteness of the sphere. A similar procedure was used for the bispectrum (Lan & Marinucci 2008b) and used to test the non-Gaussianity of the CMB (Pietrobon et al. 2009, 2010; Rudjord et al. 2009, 2010) with good results.

9.3.1 Optimal Estimator

As we already saw, the optimal trispectrum estimator is evaluated by means of combination of four Fourier components of the field $T(\mathbf{n})$:

$$T(\mathbf{n}) = \sum_{l=0}^{\infty} T_l(\mathbf{n}), \tag{9.28}$$

$$T_l(\mathbf{n}) = \sum_{m=-l}^{l} a_{lm} Y_{lm}(\mathbf{n}). \tag{9.29}$$

This components can be written by means of the Spherical Harmonics orthonormal projection operator

$$L_l = \sum_{m=-l}^{l} Y_{lm}(\mathbf{n}) Y^*_{lm}(\mathbf{n}'). \tag{9.30}$$

Convolving the field with the projection operator, one obtains

$$T_l(\mathbf{n}) = L_l * T = \int_{S^2} T(\mathbf{n}') \sum_{m=-l}^{l} Y_{lm}(\mathbf{n}) Y^*_{lm}(\mathbf{n}') d\Omega' = \sum_{m=-l}^{l} a_{lm} Y_{lm}(\mathbf{n}). \tag{9.31}$$

To obtain the form of the Needlet trispectrum, I should use the frame projection operator, analogue to the orthonormal projection operator in the frame framework

$$\sqrt{\lambda_{jk}} \sum_{l} b\left(\frac{l}{B^j}\right) L_l, \tag{9.32}$$

so that

$$\begin{aligned} T_l(\mathbf{n}) &= \int_{S^2} T(\mathbf{n}')\sqrt{\lambda_{jk}}\sum_l b\left(\frac{l}{B^j}\right)\sum_m Y_{lm}(\mathbf{n})Y^*_{lm}(\mathbf{n}')d\Omega' \\ &= \sqrt{\lambda_{jk}}\sum_{lm}\sum_{l'm'} b\left(\frac{l}{B^j}\right)a_{l'm'}Y_{lm}(\mathbf{n})\int_{S^2} Y^{l'}_{m'}(\mathbf{n}')Y^*_{lm}(\mathbf{n}')d\Omega' \\ &= \sqrt{\lambda_{jk}}\sum_{lm}\sum_{l'm'} b\left(\frac{l}{B^j}\right)a_{l'm'}Y_{lm}(\mathbf{n})\delta^{l'}_l\,\delta^{m'}_m \\ &= \sqrt{\lambda_{jk}}\sum_{lm} b\left(\frac{l}{B^j}\right)a_{lm}Y_{lm}(\mathbf{n}). \end{aligned} \tag{9.33}$$

Eq. 9.32 represent a continuous operator on the sphere. But, as it is just seen in the definition, Spherical Needlets are defined in a discrete subset of the sphere, whose elements are the cubature points. Then, we need to discretize the results of eq. 9.33, embedding them in the set of cubature points. Losely speaking, since eq. 9.33 holds for every points of the sphere, then it must holds a fortiori in a subset of S^2. Discretizing eq. 9.33, one obtains

$$T_l(\xi_{jk}) = \sqrt{\lambda_{jk}}\sum_{lm} b\left(\frac{l}{B^j}\right)a_{lm}Y_{lm}(\xi_{jk}) = \beta_{jk}, \qquad \forall\xi_{jk}\in S^2, \tag{9.34}$$

that is the definition of the random Needlets coefficients, as just seen in eq. 8.22. Then, replacing T_l with β_{jk} and discretizing the sum, I obtain the main results of this thesis, the *Spherical Needlets optimal trispectrum estimator*

$$J^{j_1j_2}_{j_3j_4} = \sqrt{\frac{4\pi}{N_{j_4}}}\sum_{k_4}\frac{:\beta_{j_1k_1}\beta_{j_2k_2}\beta_{j_3k_3}\beta_{j_4k_4}:}{\sigma_{j_1}\sigma_{j_2}\sigma_{j_3}\sigma_{j_4}}\delta_{j_1j_2j_3j_4}(k_1,k_2,k_3,k_4), \quad j_1\le j_2\le j_3\le j_4, \tag{9.35}$$

$$:\beta_{j_1k_1}\beta_{j_2k_2}\beta_{j_3k_3}\beta_{j_4k_4}: = \frac{\beta_{j_1k}\beta_{j_2k}\beta_{j_3k}\beta_{j_4k}}{\sigma_{j_1}\sigma_{j_2}\sigma_{j_3}\sigma_{j_4}} + C^{j_1j_2}_{j_3j_4k}, \tag{9.36}$$

where

$$\delta_{j_1j_2j_3j_4}(k_1,k_2,k_3,k_4) = \mathbb{I}(\xi_{j_4k_4}\in\mathcal{V}_{j_3k_3})\mathbb{I}(\xi_{j_3k_3}\in\mathcal{V}_{j_2k_2})\mathbb{I}(\xi_{j_2k_2}\in\mathcal{V}_{j_1k_1}). \tag{9.37}$$

$\mathbb{I}$ is the indicator function, different from zero only when the condition between the brackets is verified, whereas $\mathcal{V}_{jk}$ is the Voronoi cell related to the cubature point ξ_{jk}. The quadratic term is expressed as follows:

$$\begin{aligned} C^{j_1j_2}_{j_3j_4k} = &-\Gamma_{j_1j_2}\hat\beta_{j_3k}\hat\beta_{j_4k} - \Gamma_{j_1j_3}\hat\beta_{j_2k}\hat\beta_{j_4k} - \Gamma_{j_1j_4}\hat\beta_{j_2k}\hat\beta_{j_3k} \\ &-\Gamma_{j_2j_3}\hat\beta_{j_1}\hat\beta_{j_4} - \Gamma_{j_2j_4}\hat\beta_{j_1}\hat\beta_{j_3} - \Gamma_{j_3j_4}\hat\beta_{j_1}\hat\beta_{j_2} \\ &+\Gamma_{j_1j_2}\Gamma_{j_3j_4} + \Gamma_{j_1j_3}\Gamma_{j_2j_4} + \Gamma_{j_1j_4}\Gamma_{j_2j_3} \\ &-\langle\hat\beta_{j_1k}\hat\beta_{j_2k}\hat\beta_{j_3k}\hat\beta_{j_4k}\rangle, \end{aligned} \tag{9.38}$$

$$\Gamma_{j_ij_j} = \langle\beta_{j_ik_i}\beta_{j_jk_j}\rangle. \tag{9.39}$$

Some assumptions has been made to calculate the trispectrum. Following the notation used in (Lan & Marinucci 2008b) and (Marinucci & Peccati 2011), I assumed that the

cubature points are nested, i.e. for $j' > j$, $\mathcal{X}_j \subset \mathcal{X}_{j'}$ and the cubature weights are constant over k, i.e. $\lambda_{jk} = 4\pi/N_j$, where, $N_j = \text{card}\{\mathcal{X}_j\}$. Then, the role of $\delta_{j_1 j_2 j_3 j_4}(k_1, k_2, k_3, k_4)$ is to ensure that the sum runs over the unique value of k_3 such that $\xi_{j_4 k_4} \in \mathcal{V}_{j_3 k_3}$, k_2 such that $\xi_{j_4 k_4}, \xi_{j_3 k_3} \in \mathcal{V}_{j_2 k_2}$ and k_1 such that $\xi_{j_4 k_4}, \xi_{j_3 k_3} \xi_{j_2 k_2} \in \mathcal{V}_{j_1 k_1}$.

9.3.2 Mean Subtraction

In (Donzelli et al. 2012) it is shown tat in presence of nearly isotropic noise, the behavior of the linear correction term of the bispectrum, analogue to the trispectrum quadratic term, is well approximated by subtracting scale-by-scale the sky average of wavelet or Needlet coefficients. An analogue behavior for the quadratic term could allow to reduce the amount of calculation needed for its computation.

The Needlet coefficients sky average is defined as

$$\beta^*{}_j = \frac{1}{N} \sum_k \beta_{jk}, \tag{9.40}$$

then, replacing the sky average to the Needlet coefficients and rewriting the Needlet trispectrum, one obtains

$$\begin{aligned}
&\frac{1}{N} \sum_k (\beta_{j_1 k} - \beta^*{}_{j_1})(\beta_{j_2 k} - \beta^*{}_{j_2})(\beta_{j_3 k} - \beta^*{}_{j_3})(\beta_{j_4 k} - \beta^*{}_{j_4}) \\
&= \frac{1}{N} \sum_k (\beta_{j_1 k}\beta_{j_2 k} - \beta_{j_1 k}\beta^*{}_{j_2} - \beta^*_{j_1}\beta_{j_2 k} + \beta^*{}_{j_1}\beta^*{}_{j_2}) \times \\
&\times (\beta_{j_3 k}\beta_{j_4 k} - \beta_{j_3 k}\beta^*{}_{j_4} - \beta^*_{j_3}\beta_{j_4 k} + \beta^*{}_{j_3}\beta^*{}_{j_4}) \\
&= \frac{1}{N} \sum_k \beta_{j_1 k}\beta_{j_2 k}\beta_{j_3 k}\beta_{j_4 k} - \beta^*_{j_1} \left\{ \frac{1}{N} \sum_k \beta_{j_2 k}\beta_{j_3 k}\beta_{j_4 k} \right\} \\
&- \beta^*_{j_2} \left\{ \frac{1}{N} \sum_k \beta_{j_1 k}\beta_{j_3 k}\beta_{j_4 k} \right\} - \beta^*_{j_3} \left\{ \frac{1}{N} \sum_k \beta_{j_1 k}\beta_{j_2 k}\beta_{j_4 k} \right\} \\
&- \beta^*_{j_4} \left\{ \frac{1}{N} \sum_k \beta_{j_1 k}\beta_{j_2 k}\beta_{j_3 k} \right\} + \beta^*_{j_1}\beta^*_{j_2} \left\{ \frac{1}{N} \sum_k \beta_{j_3 k}\beta_{j_4 k} \right\} \\
&+ \beta^*_{j_1}\beta^*_{j_3} \left\{ \frac{1}{N} \sum_k \beta_{j_3 k}\beta_{j_4 k} \right\} + \beta^*_{j_1}\beta^*_{j_4} \left\{ \frac{1}{N} \sum_k \beta_{j_2 k}\beta_{j_3 k} \right\} \\
&+ \beta^*_{j_2}\beta^*_{j_3} \left\{ \frac{1}{N} \sum_k \beta_{j_1 k}\beta_{j_4 k} \right\} + \beta^*_{j_2}\beta^*_{j_4} \left\{ \frac{1}{N} \sum_k \beta_{j_1 k}\beta_{j_3 k} \right\} \\
&+ \beta^*_{j_3}\beta^*_{j_4} \left\{ \frac{1}{N} \sum_k \beta_{j_1 k}\beta_{j_1 k} \right\} - 3\beta^*_{j_1}\beta^*_{j_2}\beta^*_{j_3}\beta^*_{j_4}
\end{aligned} \tag{9.41}$$

where I replaced the proper indexes of the Needlet coefficients k_i with the index k, in order to simplify the notation of eq. 9.35. Eq. 9.41 shows that, even in the fullsky case, with isotropic noise, it is not possible to simplify the quadratic term with the mean subtraction approximation. Then, we have to compute all the components in order to calculate the quadratic term.

CHAPTER 10

g_{NL} Estimation

10.1 The Needlet g_{NL} Estimator

So far, I analytically derived the optimal Needlet trispectrum estimator (eq. 9.35). It is possible to use this formula in order to evaluate the magnitude of g_{NL} from the CMB data, as already done for f_{NL} (Rudjord et al. 2009; Donzelli et al. 2012). In this approach a χ^2 minimization procedure is used. Let's define

$$\chi^2(g_{NL}) = \mathbf{d}^T(g_{NL})\mathbf{C}^{-1}\mathbf{d}(g_{NL}), \tag{10.1}$$

where $\mathbf{d}$ is the data vector and $\mathbf{C}^{-1}$ is the inverse of the correlation matrix of data,

$$C_{ij} = \langle d_i d_j \rangle - \langle d_i \rangle \langle d_j \rangle. \tag{10.2}$$

The data vector $\mathbf{d}$ is defined by means of the trispectrum $J^{j_1 j_2}_{j_3 j_4}$

$$d_i = J^{j_1 j_2}_{j_3 j_4}(observed) - \langle J^{j_1 j_2}_{j_3 j_4} \rangle (g_{NL}) \tag{10.3}$$

for all the combinations of (j_1, j_2, j_3, j_4) satisfying the quadrilateral condition

$$max(|j_i - j_j - j_k|, |j_j - j_i - j_k||j_k - j_j - j_i|) \leq j_z \leq j_i + j_j + j_k, \quad i, j, k, z = 1, 2, 3, 4. \tag{10.4}$$

$J_{j_1 j_2 j_3}(observed)$ is the Needlet trispectrum of the observed CMB data, for which we want to estimate g_{NL} and $\langle J_{j_1 j_2 j_3} \rangle (g_{NL})$ is the expectation value of the Needlet trispectrum for a given value of g_{NL}, evaluated as follow. Consider a non-Gaussian collection of $\{a_{lm}\}$. Each of them is the result of the sum

$$a_{lm} = a^G_{lm} + f_{NL} a^{NG,1}_{lm} + g_{NL} a^{NG,2}_{lm}, \tag{10.5}$$

where the a^G_{lm}'s are Gaussian Harmonic coefficients while the $a^{NG,i}_{lm}$'s represent the non-Gaussian a_{lm} of order i. f_{NL} and g_{NL} are arbitrary reference values. Let's assume $f_{NL} = 0$, so that

$$a_{lm} = a^G_{lm} + g_{NL} a^{NG,2}_{lm}. \tag{10.6}$$

We have seen that the Needlet coefficients are directly related to the Harmonic coefficient (eq. 8.22). Thus we can relate non-Gaussian Harmonic coefficients to the Needlet ones:

$$a_{lm} = a^G_{lm} + g_{NL} a^{NG,2}_{lm} \longrightarrow \beta^G_{jk} + g_{NL} \beta^{NG}_{jk} = \beta_{jk}. \tag{10.7}$$

Hence, the non-Gaussian trispectrum is

$$\begin{aligned}\langle J_{j_1 j_2 j_3}\rangle(g_{NL}) &= \left\langle \sum_k \hat{\beta}_{j_1 k}\hat{\beta}_{j_2 k}\hat{\beta}_{j_3 k}\hat{\beta}_{j_4 k} \right\rangle \\ &= g_{NL}\left(\left\langle \sum_k \hat{\beta}^{NG}_{j_1 k}\hat{\beta}^{G}_{j_2 k}\hat{\beta}^{G}_{j_3 k}\hat{\beta}^{G}_{j_4 k} \right\rangle + \left\langle \sum_k \hat{\beta}^{G}_{j_1 k}\hat{\beta}^{NG}_{j_2 k}\hat{\beta}^{G}_{j_3 k}\hat{\beta}^{G}_{j_4 k} \right\rangle \right. \\ &\left. \left\langle \sum_k \hat{\beta}^{G}_{j_1 k}\hat{\beta}^{G}_{j_2 k}\hat{\beta}^{NG}_{j_3 k}\hat{\beta}^{G}_{j_4 k} \right\rangle + \left\langle \sum_k \hat{\beta}^{G}_{j_1 k}\hat{\beta}^{G}_{j_2 k}\hat{\beta}^{G}_{j_3 k}\hat{\beta}^{NG}_{j_4 k} \right\rangle \right) + \mathcal{O}((\hat{\beta}^{NG}_{jk})^2) \\ &\approx g_{NL}(\langle J^{NG,G,G,G}_{j_1 j_2 j_3}\rangle + \langle J^{G,NG,G,G}_{j_1 j_2 j_3}\rangle + \langle J^{G,G,NG,G}_{j_1 j_2 j_3}\rangle + \langle J^{G,G,G,NG}_{j_1 j_2 j_3}\rangle) \\ &= g_{NL}\langle \hat{J}_{j_1 j_2 j_3}\rangle,\end{aligned} \tag{10.8}$$

where we considered $\left\langle \sum_k \hat{\beta}^{G}_{j_1 k}\hat{\beta}^{G}_{j_2 k}\hat{\beta}^{G}_{j_3 k}\hat{\beta}^{G}_{j_4 k} \right\rangle = 0$ by definition of Gaussianity.

Having defined the non-Gaussian trispectrum, we can search for the extrema of χ^2

$$\frac{d\chi^2(g_{NL})}{dg_{NL}} = 0, \tag{10.9}$$

thus obtaining

$$g_{NL} = \frac{\langle \hat{J}_{j_1 j_2 j_3}\rangle^t \mathbf{C}^{-1} J_{j_1 j_2 j_3}(observed)}{\langle \hat{J}_{j_1 j_2 j_3}\rangle^t \mathbf{C}^{-1} \langle \hat{J}_{j_1 j_2 j_3}\rangle} \tag{10.10}$$

where t stand for *transpose* of the vector. Hence, using this formula allows to measure g_{NL} of a map knowing its trispectrum. Let's see how this is implemented in the software I wrote and what results it gave.

10.2 Software Implementation

The software I wrote to estimate g_{NL} take advantage of the C++ HEALPix libraries[1] (Hierarchical Equal Area and iso-Latitude Pixelation) (Górski et al. 2005), developed with the aim to provide subroutines useful for spherical analysis. The HEALPix code allows to analyse spherical functions by discretizing the sphere in grids of iso-latitude and equal-area cells, i.e. the pixels, and compute the spherical functions at the center of the pixels. The number of pixels in which the sphere can be divided is constrained by the condition of iso-latitude and equal-area. At the lowest resolution, the sphere is divided into 12 pixels. We can express the resolution of the grid using the parameter N_{side}, which defines the number of divisions along the side of a base-resolution pixel and must be a power of 2. Thus, $N_{side} = 1, 2, 4, 8, ...2^n$ and the number of pixels scales as

$$N_{pix} = 12 \cdot N^2_{side}. \tag{10.11}$$

In order to include the HEALPix libraries, I had to manage eq. 9.35. In fact, the summation over the cubature points of eq. 9.35 must be replaced by a summation on the center of the pixels of the sphere. Since the HEALPix partition is set finer than the cubature partition of the sphere at the maximum scale j_4, it represents an improvement

[1] http://healpix.sourceforge.net/

on the statistical significance of the results and does not introduce computational error in the results. Thus, we can rewrite the Needlet trispectrum estimator as

$$J^{j_1 j_2}_{j_3 j_4} = \sum_{k=1}^{N_{pix}} \left[\frac{\beta_{j_1 k}\beta_{j_2 k}\beta_{j_3 k}\beta_{j_4 k}}{\sigma_{j_1}\sigma_{j_2}\sigma_{j_3}\sigma_{j_4}} + C^{j_1 j_2}_{j_3 j_4 k} \right], \tag{10.12}$$

where k labels the centers of the pixels on the HEALPix grid. It is easy to see how I have dropped out a constant factor of normalization. Indeed, in the estimation of the g_{NL} parameter, this factor is elided by calculus.

Rudjord et al. (2009) and subsequently Donzelli et al. (2012) developed a software, written in `FORTRAN`, to estimate the f_{NL} parameter from the Needlet bispectrum with a χ^2 procedure analogue to that I described above. In their code, the HEALPix libraries are used efficiently and parallelization is adopted in order to decrease the computation time. Therefore, I took advantage of the solutions adopted in that code in the writing of my `C++` code for the trispectrum.

Unfortunately, the amount of memory and time required in the computation increase in the trispectrum case. Each scale j_i in the trispectrum formula (eq. 10.12) implies the calculation of an entire CMB map in which at every pixel k is assigned the corresponding Needlet coefficient $\beta_{j_i k}$. Then, assuming that the maps are stored in arrays of single precision variables (each of them has dimension 4 byte) and a resolution of $N_{side} = 512$, we have that every map requires $12 \cdot N^2_{side} \cdot 4/(1024)^2 \simeq 14\mathrm{Mb}$. For the bispectrum, the number of permutations (j_1, j_2, j_3) satisfying the triangle condition for 11 Needlet scales is about 200, then the memory required is at least 2.7 Gb. But the number of permutations (j_1, j_2, j_3, j_4) satisfying the quadrilateral condition is about 1000, thus the trispectrum estimation requires at least 14 Gb of memory. The quantity of memory required is then much greater for the trispectrum than for the bispectrum calculation.

Furthermore, we have to consider the memory necessary to the calculation of the $\Gamma_{j_i j_j}$ and $\langle \hat{\beta}_{j_1 k}\hat{\beta}_{j_2 k}\hat{\beta}_{j_3 k}\hat{\beta}_{j_4 k} \rangle$ terms of the quadratic term, adding about 1000 maps for 11 Needlet scales in the computation of the trispectrum. Thus the memory required doubles when we calculate the correction term.

In order to decrease the computational time, I implemented a parallel code using the `MPI` and `OpenMP` libraries. I run the code on the Numenor Computing Cluster of the Observational Cosmology Group at Department of Physics at University of Milano. This is composed by 8 computing nodes each with 12 Intel Xeon ES-2620 processors at 2.0 GHz with 8 Gb of RAM per core, for a total of 96 Gb per node.

10.2.1 Dataset

The g_{NL} estimation took advantage of the Planck public data, recently released by the Planck collaboration (`http://pla.esac.esa.int/pla`).

Gaussian maps were generated using the CMB power spectrum estimated by the Planck survey (Planck Collaboration et al. 2014b)(fig. 10.1). Each map is smoothed with a simulated instrumental beam with the same resolution of the Planck 70 GHz channel, i.e. $\mathrm{FWHM} = 13.01'$ (fig. 10.2) (The Planck Collaboration 2006). Furthermore, I considered two cases. In the first the sky is fully observed and no instrumental noise is added. In the second I introduced the instrumental anisotropic noise of Planck 70 GHz channel (fig. 10.3), and the sky is incomplete. The mask applied cuts the Galactic plane and remove point-sources of foregrounds, covering 30% of the sky (fig. 10.4).

999 non-Gaussian maps are generated using a sets of non-Gaussian harmonics coefficients $a_{lm} = a^G_{lm} + f_{NL}a^{NG,1}_{lm} + g_{NL}a^{NG,2}_{lm}$ created using the algorithm described in (Elsner

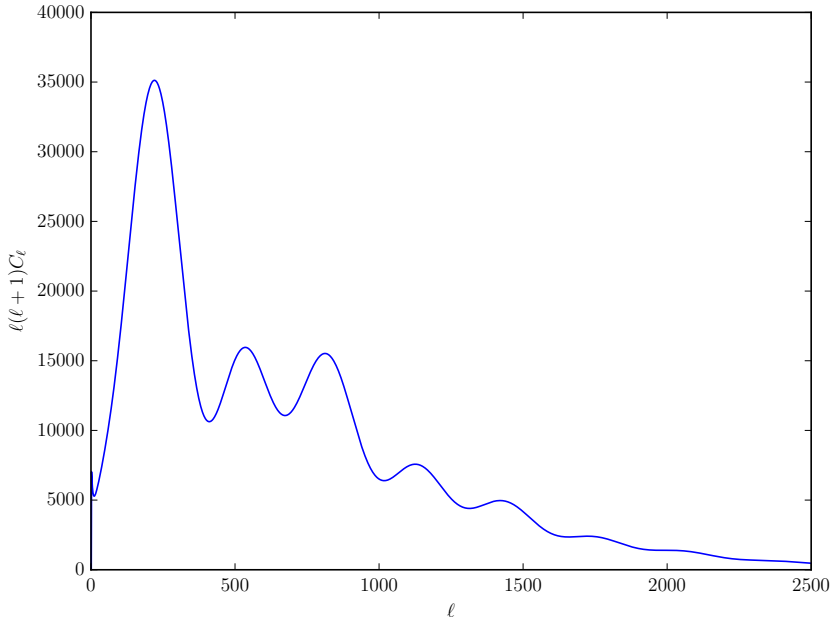

Figure 10.1: The Planck confidence spectrum. All of the peaks are clearly visible, while monopole $l = 0$ and dipole $l = 1$ are set to zero.

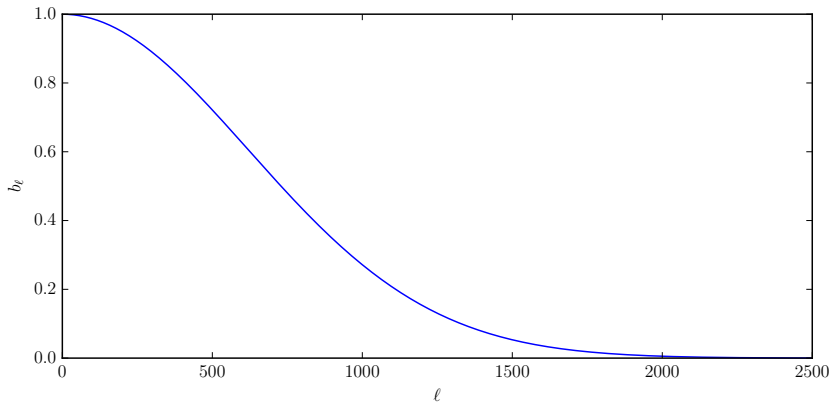

Figure 10.2: The Gaussian beam applied to data. Its shape is Gaussian, the width in real space is FWHM= 13.01′.

& Wandelt 2009). I imposed $f_{NL} = 0$, then the only contribution to the non-Gaussian a_{lm}'s is the $a_{lm}^{NG,2}$ term. Unfortunately, the $a_{lm}^{NG,2}$ term are not fully tested by the author.

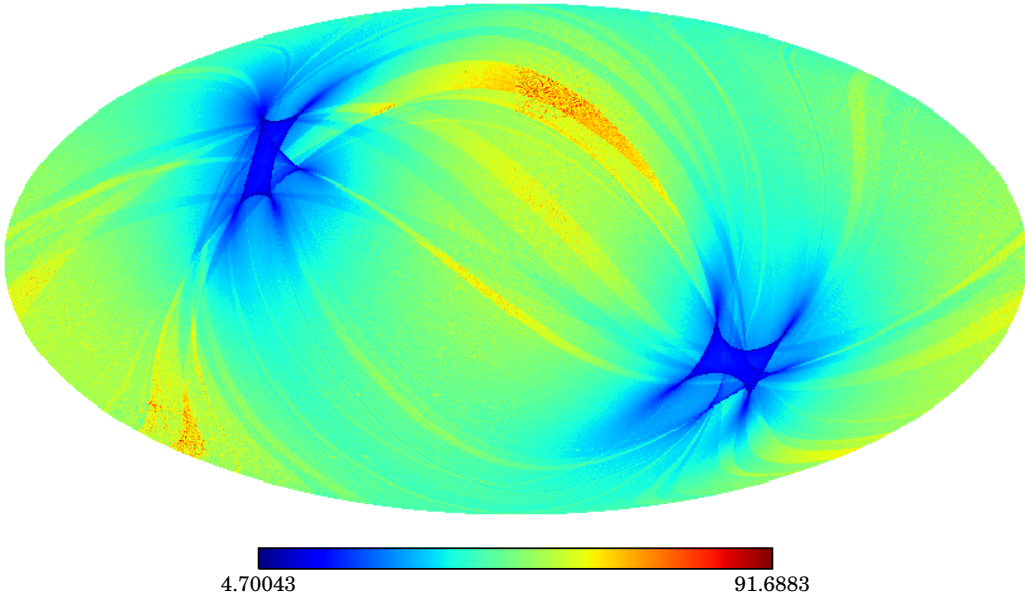

Figure 10.3: Instrumental noise of Planck 70 GHz channel. Noise is evidently anisotropic due to the number of observation per sky region. The more times Planck satellites observed one sky region, the lower is the noise in that region. The two symmetric blue region are located at the poles of Planck satellite rotation motion.

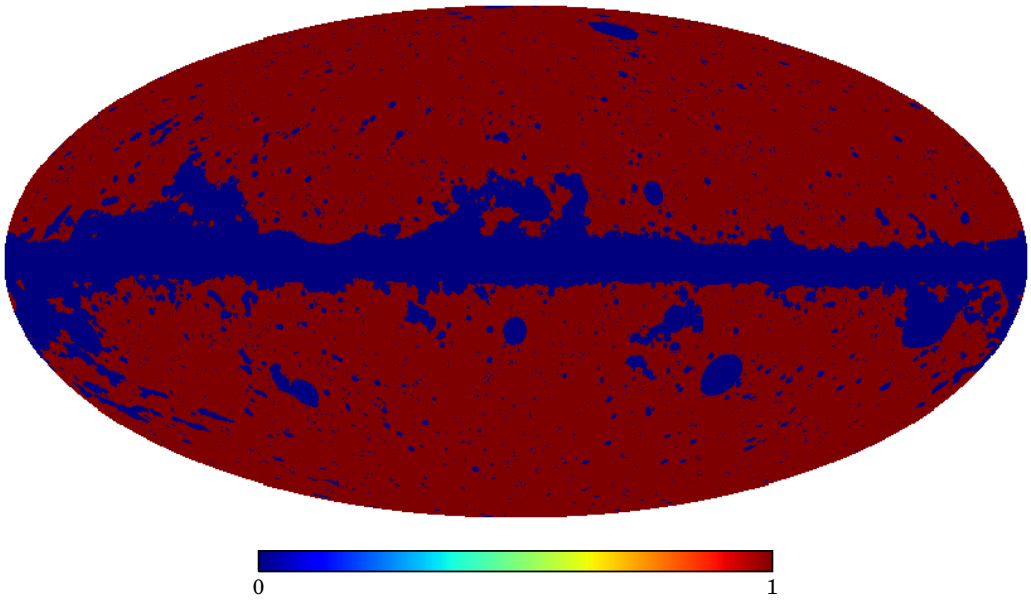

Figure 10.4: The mask used in analysis. The narrow strip covers the galactic plane and point-sources of foregrounds are removed.

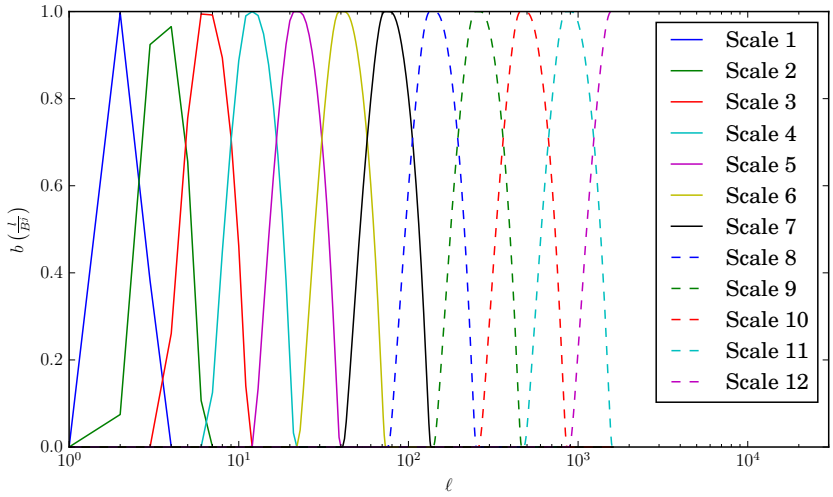

Figure 10.5: The Needlet window function calculated for 12 different scales. Each scale take in account a limited number of multipoles that grows with the Needlet scale. The sum of the square of $b(\cdot)$ for a certain multipole is 1 as required by the partition of the unity property (eq. (8.15)).

10.2.2 Software pipeline

The code is partitioned into different pieces. Each piece carries out a different task. The first piece is able to generate maps both from input C_l or a_{lm} with the aim of calculate the complete set of trispectra for each map. The procedure is simple:

1. The complete set of Needlets are generated, based on the input parameters (fig. 10.5);
2. C_l or a_{lm}, beam, noise and mask are read and in case the Needlet variance,
3. From input C_l or a_{lm} a map is generated. In the former case an input seed is required, the code is able to use a different seed to different map generating routines. To each map beam, noise and mask, and variance are applied;
4. Needlet transform is applied, giving birth to N_j new maps;
5. For each map, trispectrum is calculated;
6. Point 3-5 are repeated till the number of trispectrum required is reached.

If the aim of the process is to compute the variance, point 5 changes: each map is summed up in order to get first the variance for each Needlet scale and then the $\Gamma_{j_1 j_2}$ maps. The variance is evaluated using a formula that reduces the possibility of being affect by numerical errors, i.e.

$$\mathrm{V}ar(x)[p] = \frac{1}{N-1}\left(\sum_{i=1}^{N}(x_i[p]-x_1[p])^2 - \left(\sum_{i=1}^{N}(x_i[p]-x_1[p])\right)^2\right) \tag{10.13}$$

where x represents the Needlet coefficient map at a certain scale, p is the pixel and N is the number of maps on which the variance is calculated. To each term is subtracted the

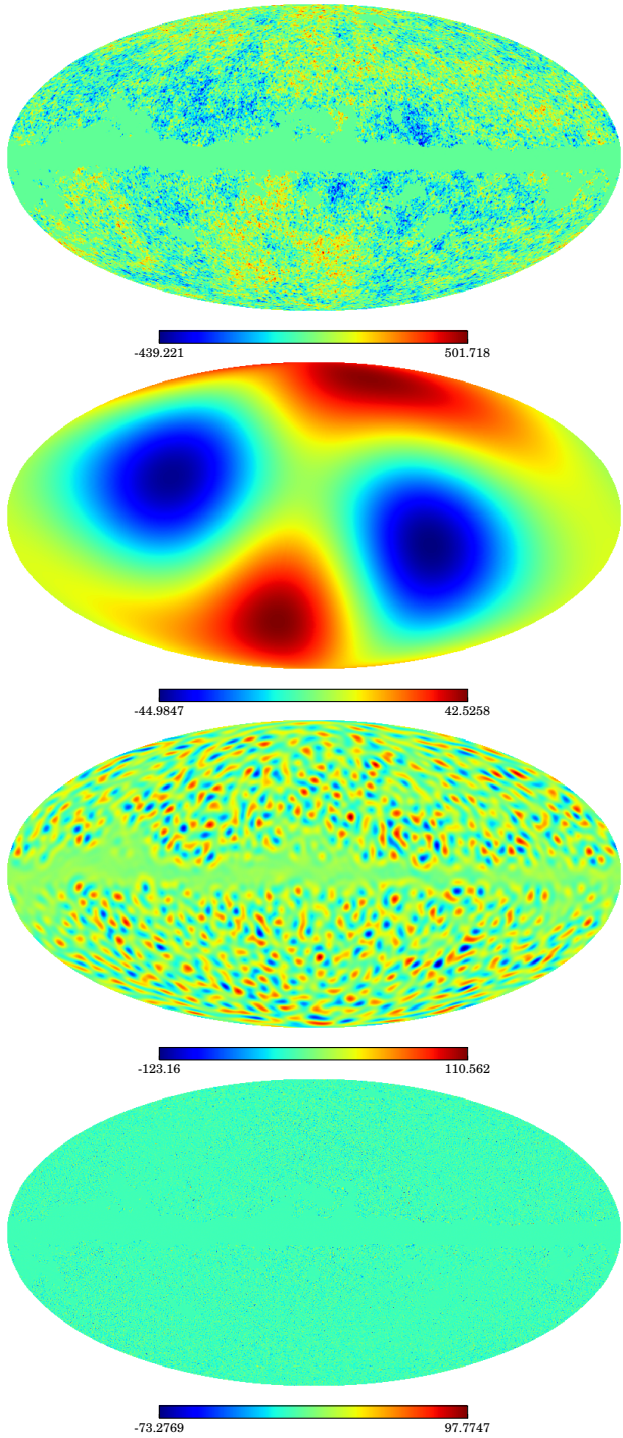

Figure 10.6: Maps used in analysis. From top to bottom, the first map is the original map, taking in account all the multipoles. The other three maps are Needlet maps evaluated for the first, the fifth and the twelth Needlet scale. The $j = 1$ map show the characteristic of a quadrupole, since it takes in account only the $l = 2$ multipole. The $j = 5$ map shows how as increasing the scale the size of the fluctuations decreases and the shape of the mask (fig. 10.4) becomes clearer. In the last map, where the only highest multipoles are take in account, the size of the fluctuations is almost invisible.

value of the first map at the same pixel, since

$$\mathrm{V}ar(x - K) = \mathrm{V}ar(x) \tag{10.14}$$

when K is constant. This subtraction allows to remove crass numerical error, allowing to obtain the exact value for the statistics we're looking for.

In order to estimate g_{NL} using the Needlet trispectrum, I followed this pipeline:

- Generate a set of simulations of Gaussian sky maps using the CMB power spectrum. These maps are smoothed with an instrumental beam and random noise is added. Then, they are then multiplied with a mask in order to remove the Galactic region and point-source of non-Galactic emission. A Needlet transform is applied to each map in order to evaluate the standard deviations of the Needlet coefficients β_{jk} and the $\Gamma_{j_1 j_2}$ maps, used in the evaluation of the trispectrum, as seen in eq. 10.12.
- Read 700 non-Gaussian simulations in order to find the mean non-Gaussian trispectrum $\langle J^{j_1 j_2}_{j_3 j_4} \rangle (g_{NL})$.
- Produce another set of Gaussian simulation. Beam, noise and mask are applied as above. After the Needlet transform, these maps are used to obtain the Needlet trispectra $J^{j_1 j_2}_{j_3 j_4}$. These trispectra are used to find the covariance matrix **C**. This converges very slowly, thus the need for a large number of simulations.
- Generate a set of simulated Gaussian maps and estimate g_{NL} from this maps in order to obtain the error bars on g_{NL};
- Read a set of 299 non-Gaussian simulations in order to estimate g_{NL} from them.

Second piece computes the covariance matrix C_{ij}. It's easy to show that the covariance matrix depend only on the measured trispectra. In fact

$$\begin{aligned} C_{ij} &= \langle d_i d_j \rangle - \langle d_i \rangle \langle d_j \rangle \\ &= \langle (J_i - g_{NL} \langle \hat{J}_i \rangle)(J_j - g_{NL} \langle \hat{J}_j \rangle) \rangle - \langle (J_i - g_{NL} \langle \hat{J}_i \rangle) \rangle \langle (J_j - g_{NL} \langle \hat{J}_j \rangle) \rangle \\ &= \langle J_i J_j \rangle - \langle J_i \rangle \langle J_j \rangle, \end{aligned} \tag{10.15}$$

where J_i represents the trispectrum at a given configuration (j_1, j_2, j_3, j_4).

Finally, the third piece computes g_{NL} implementing eq. (10.10).

10.3 Code Validation at $N_{side} = 128$

The code was validated first at $N_{side} = 128$ in order to be fast at the cost of precision. The purpose of the validation is to check if the results are consistent with g^{input}_{NL} and the error bars are consistent with the Cramer-Rao bound, in order to understand if whether or not the Needlet trispectrum is optimal. We have that for $N_{side} = 128$,

$$\sigma^{CR} \approx 6.58 \cdot 10^5. \tag{10.16}$$

A set of data was generated and analyzed four times, changing the number of Needlet scales involved, $N_j = 8, 10, 12, 14$. For the all of them, no mask or noise were added. The multipoles were bounded to $l \leq 150$.

First of all, variance was estimated over 10000 Gaussian maps, ensuring convergence. Then, 700 out of 1000 non-gaussian maps were used to estimate the non-Gaussian trispectrum $\langle \hat{J}^{j_1 j_2}_{j_3 j_4} \rangle$. The remaining 299 were used to compute a set of non-Gaussian maps with $g_{NL}^{input} = 3 \cdot 10^5$ with the aim of constraining g_{NL} for all of these. Finally, I computed 400 sets of trispectra, each of them composed by 320 trispectra, from as many maps. 50 sets were used to constrain g_{NL}, the other 350 for the slowly converging covariance matrix. The covariance matrix, indeed, was calculated using different numbers of trispectra, in order to find out when the convergence happens. In particular, I used $30, 60, 90, 120, 150, 200, 250, 300, 350$ sets in order.

It is important to note that the g_{NL}'s are distributed following a quasi-Gaussian probability function, as we expected since the convergence of the trispectrum is very slow. For this reason, the estimation of g_{NL} and $\sigma_{g_{NL}}$ were made performing a Gaussian fit on the central part of the distribution, since it is perfectly Gaussian (fig. 10.7).

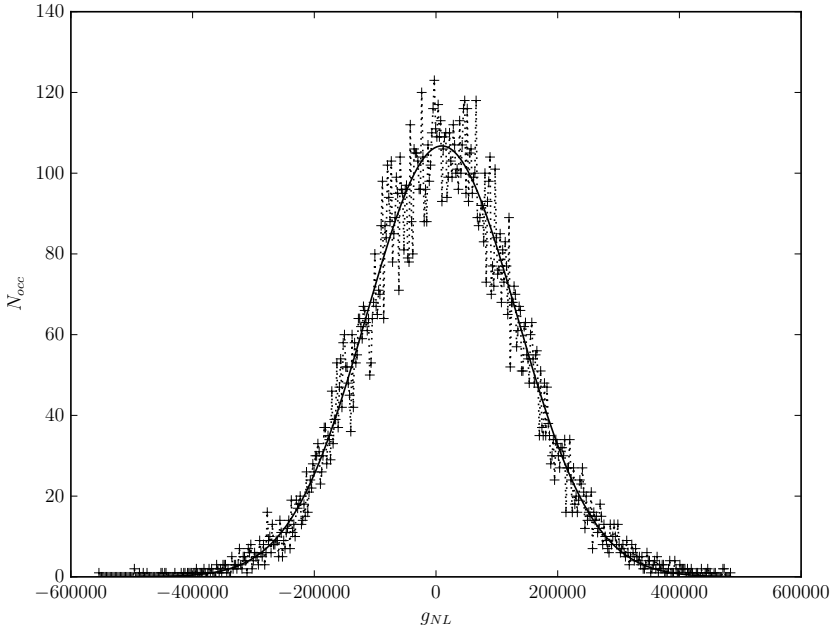

Figure 10.7: Histogram of g_{NL} using 100 bins (points) with the Gaussian fit (line) made using the central part of the histogram. It fits very well the entire distribution, thus Gaussian fit is the way I estimated g_{NL} through the analysis.

10.3.1 Gaussian Analysis

Let's list the first results, the Gaussian g_{NL} estimated using $N_j = 8$ Needlet scales varying the number of set using to estimate the covariance matrix,, N_{cov}^{set},

N_{cov}^{set}	g_{NL}	$\sigma_{g_{NL}}$
30	$(-4.0 \pm 6.7) \cdot 10^3$	$(6.85 \pm 0.07) \cdot 10^5$
60	$(-3.5 \pm 5.8) \cdot 10^3$	$(6.76 \pm 0.06) \cdot 10^5$
90	$(-2.5 \pm 5.6) \cdot 10^3$	$(6.74 \pm 0.06) \cdot 10^5$
120	$(-2.2 \pm 5.9) \cdot 10^3$	$(6.74 \pm 0.06) \cdot 10^5$
150	$(-1.9 \pm 5.9) \cdot 10^3$	$(6.74 \pm 0.06) \cdot 10^5$
200	$(-1.5 \pm 5.8) \cdot 10^3$	$(6.74 \pm 0.06) \cdot 10^5$
250	$(-1.6 \pm 6.3) \cdot 10^3$	$(6.74 \pm 0.06) \cdot 10^5$
300	$(-1.6 \pm 6.1) \cdot 10^3$	$(6.74 \pm 0.06) \cdot 10^5$
350	$(-1.5 \pm 5.6) \cdot 10^3$	$(6.74 \pm 0.06) \cdot 10^5$

The error on g_{NL} and $\sigma_{g_{NL}}$ are the standard error of the fit, which are of the same order of magnitude of the standard error of the mean

$$\sigma_{\bar{x}} = \frac{\sigma}{\sqrt{N}} \tag{10.17}$$

and of standard deviation

$$\sigma_{\sigma} = \frac{\sigma}{\sqrt{2(N-1)}}, \tag{10.18}$$

where N is the number of simulation used to estimate g_{NL} and $\sigma_{g_{NL}}$. The results show how the value of g_{NL} is always consistent with zero, within the standard error of the mean. The $\sigma_{g_{NL}}$'s, unfortunately, are quite far from the Cramer-Rao bound, approximately $6.58 \cdot 10^5$. But, there's an interesting trend. As long as we increase the number of simulations involved in the evaluation of the covariance matrix, the value of $\sigma_{g_{NL}}$ decreases. This is very likely due to the fact that the inverse covariance is biased: even though the covariance matrix estimated from N simulation is unbiased, this is not true for the inverse, which is a non-linear operation. This has been studied in (Dodelson & Schneider 2013; Andersen 2003; Hartlap et al. 2007; Taylor et al. 2013). Thus, we can fit this set of points with a suitable function to see how $\sigma_{g_{NL}}$ behaves with the increase of N_{cov}^{set}. What I found is that the best fitting function is

$$f(x) = \frac{a}{x} + b, \tag{10.19}$$

finding (fig. 10.8)

$a/10^5$	$b/10^5$
3.4 ± 0.5	6.719 ± 0.006

Thus, since the hyperbole shows an asymptotic behavior with $x \to \infty$, it is impossible for $\sigma_{g_{NL}}$ to decrease under a given value, fixed by the horizontal asymptote of the hyperbole in eq. (10.19), i.e. $y(x) = b$. Hence, the inferior limit for $\sigma_{g_{NL}}$ evaluated with $N_j = 8$ is $b = (6.719 \pm 0.006) \cdot 10^5$, well above the Cramer-Rao bound.

From fig. 10.8, we can derive interesting information. First, we observe a plateau in the data from N_{cov}^{set} on. This means that the covariance converged already with few sets of trispectra. This feature will be compared with the behaviour of the hyperbole in the other $N - j$ cases, to see in which case the covariance converges faster.

Second, the error-bars of $\sigma_{g_{NL}}$, coming from the Gaussian fit over the data, seems to high with respect to the fluctuations of the data around the fitted curve. This gives rise to some doubt on the reliability of the fitting error bars, in particular it seems plausible that the error estimated are overestimating the real error. I wrote that the errors have

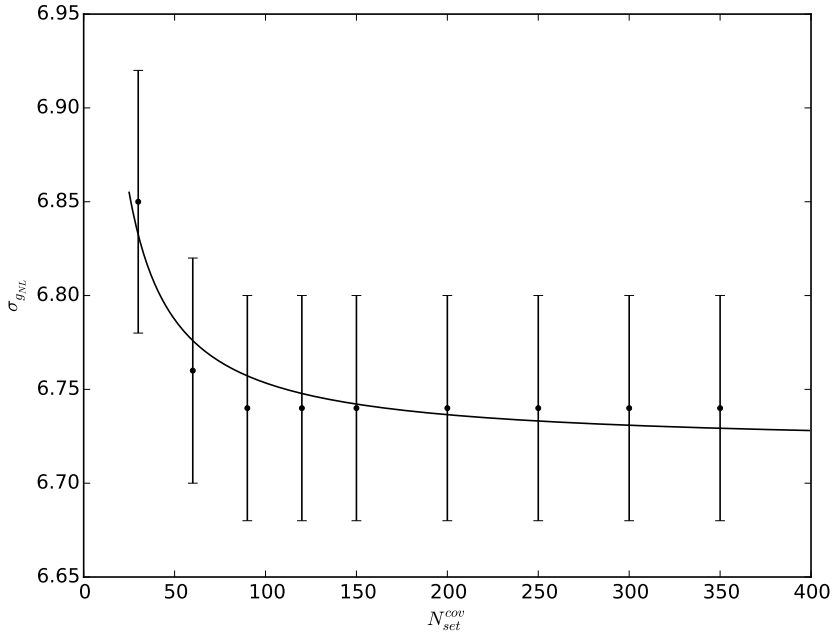

Figure 10.8: Hyperbole fit over the set of $\sigma_{g_{NL}}$ resulting from the analysis performed with $N_j = 8$. On the x-axis, the number of simulation used to compute the covariance matrix are placed. The hyperbole fit seems to be the best fitting function to the data.

the same order of magnitude of the standard error on $\sigma_{g_{NL}}$, and it is true. Can two independent way to estimate the same quantity both overestimate it? In principle, one is brought to think not, since, indeed, the two ways are independent. Since I'm a bit meticulous, I tried a third way to estimate the error of the $\sigma_{g_{NL}}$, the *bootstrap*.

Bootstrap analysis pretends to repeat an experiment using the very proper results of the experiment itself. From the data, a new set of data is extracted randomly, of the same size of the original dataset, without avoiding repetition in the random choice of the elements. This new set pretends to be the realization of a second experiment. This procedure is repeated as much as one wanted. From each set of data, mean ans σ, thus bringing to have a set of means and a set of σ's distributed according to a Gaussian distribution from which mean value and standard error can be estimated. Bootstrap thus allow to estimate the error of $\sigma_{g_{NL}}$ by pretending to repeat the analysis I performed only once. The results of bootstrap is a perfectly Gaussian distribution for the σ's with a standard error equal for each covariance matrix case,

$$\sigma_{\sigma_{g_{NL}}} = 4.3 \cdot 10^3,$$

same order of magnitude of the fit error, just a bit lower in magnitude. The difference in σ's doesn't change the fact that the errors on $\sigma_{g_{NL}}$ seem overestimated. Actually, this is not the case. The only thing I can say is that the error on $\sigma_{g_{NL}}$, just like the error on g_{NL}, depends on the number of data used for the estimation. In particular, decrease as the number of data increases. Thus, the only thing we can do to make the error bars decrease is increase the number of trispectra. Unfortunately, trispectrum computation is hard in terms of computational time, thus increasing the number of trispectra is not an option. We have to make a tradeoff between Number of trispectra and amplitudes of the

error bars. I'll come back to this point in the next section, when I'll show what happens when the analysis is performed ove $N_{side} = 2048$ maps.

Let's pass to the next case, the $N_j = 10$. Gaussian results are listed below.

N_{cov}^{set}	g_{NL}	$\sigma_{g_{NL}}$
30	$(-3.1 \pm 5.6) \cdot 10^3$	$(6.94 \pm 0.06) \cdot 10^5$
60	$(-3.2 \pm 6.1) \cdot 10^3$	$(6.80 \pm 0.06) \cdot 10^5$
90	$(-2.3 \pm 5.7) \cdot 10^3$	$(6.74 \pm 0.06) \cdot 10^5$
120	$(-1.9 \pm 6.6) \cdot 10^3$	$(6.73 \pm 0.07) \cdot 10^5$
150	$(-1.8 \pm 5.9) \cdot 10^3$	$(6.71 \pm 0.06) \cdot 10^5$
200	$(-1.6 \pm 6.3) \cdot 10^3$	$(6.71 \pm 0.06) \cdot 10^5$
250	$(-1.6 \pm 5.7) \cdot 10^3$	$(6.70 \pm 0.06) \cdot 10^5$
300	$(-1.7 \pm 6.5) \cdot 10^3$	$(6.70 \pm 0.06) \cdot 10^5$
350	$(-2.0 \pm 6.3) \cdot 10^3$	$(6.69 \pm 0.06) \cdot 10^5$

Again, the value of g_{NL} is always consistent with zero, as we expected, and the error bars on the mean are consistent with the ones of the previous case. Speaking about $\sigma_{g_{NL}}$, the results in the $N_j = 10$ case improved, with $\sigma_{g_{NL}}$ approaching to the Cramer-Rao bound. The error bars on $\sigma_{g_{NL}}$ coming from bootstrap analysis are uniformly equal to $\sigma_{\sigma_{g_{NL}}} = 4.3 \cdot 10^3$, closer to the ones coming from the Gaussian fit. Let's see the inferior limit for $\sigma_{g_{NL}}$ fitting the hyperbole over the data (fig. 10.9),

$a/10^5$	$b/10^5$
8.1 ± 0.3	6.664 ± 0.004

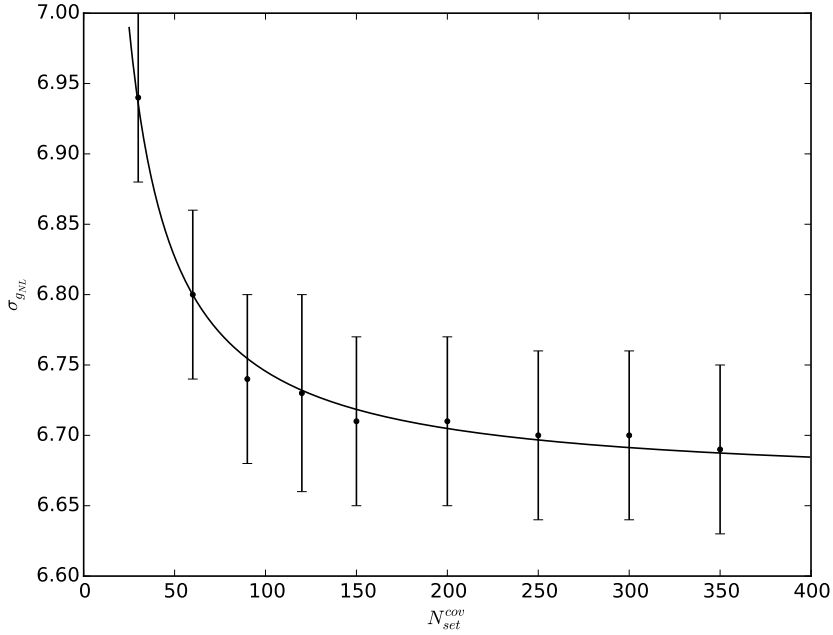

Figure 10.9: Hyperbole fit over the set of $\sigma_{g_{NL}}$ resulting from the analysis performed with $N_j = 10$. It is important to note that the plateau vanishes increasing the number of scale.

Thus, increasing the number of trispectra used in the computation of the covariance matrix, could bring to a $\sigma_{g_{NL}} \approx 6.664$, very close to the Cramer-Rao bound. The plateau

we saw in the $N_j = 8$ case tends to vanish. This means that increasing the number of scale brings the convergence speed of covariance matrix to decrease. Thus, with respect to the previous case, now more trispectra are required in order to compute a correct covariance matrix.

As we increased the number of scale, we saw an improvement in the $\sigma_{g_{NL}}$ values, approaching the Cramer-Rao bound. Let's see if the difference between them is decreased by increasing the number of scales. For $N_j = 12$ we have

N_{cov}^{set}	g_{NL}	$\sigma_{g_{NL}}$
30	$(-8.9 \pm 6.1) \cdot 10^3$	$(7.27 \pm 0.06) \cdot 10^5$
60	$(-7.0 \pm 6.5) \cdot 10^3$	$(6.99 \pm 0.06) \cdot 10^5$
90	$(-5.3 \pm 5.8) \cdot 10^3$	$(6.91 \pm 0.06) \cdot 10^5$
120	$(-4.9 \pm 5.5) \cdot 10^3$	$(6.87 \pm 0.06) \cdot 10^5$
150	$(-2.4 \pm 6.4) \cdot 10^3$	$(6.95 \pm 0.06) \cdot 10^5$
200	$(-5.5 \pm 6.0) \cdot 10^3$	$(6.82 \pm 0.06) \cdot 10^5$
250	$(-5.9 \pm 6.1) \cdot 10^3$	$(6.81 \pm 0.06) \cdot 10^5$
300	$(-5.9 \pm 5.9) \cdot 10^3$	$(6.804 \pm 0.059) \cdot 10^5$
350	$(-6.3 \pm 6.0) \cdot 10^3$	$(6.800 \pm 0.060) \cdot 10^5$

The answer is no. Although g_{NL} is almost always consistent with zero, with error bars consistent with the ones in the previous case, $\sigma_{g_{NL}}$ tends to get away from its optimal value. The bootstrap value for the error of $\sigma_{g_{NL}}$ is $4.2 \cdot 10^3$, close to the fit one, as in the previous cases. The result of the hyperbolic fit is

$a/10^5$	$b/10^5$
15.0 ± 1.3	6.76 ± 0.02

The plateau we saw in the first case is almost vanished, confirming the hypothesis of high number of trispectra required by the covariance matrix. The worsening of the $\sigma_{g_{NL}}$ are to give to the decreased power in each Needlet scale due to the increase in the number of the Needlet scales. The Needlet window $b(\cdot)$ can, in fact, be viewed as an anisotropic binning of the multipoles. The more multipoles within a bin, the more power the bin owns, thus improving the statistic. But, there's a limit in the binning. In fact, if the number of bins is too small, the resolution power of the statistics decreases thus leaving the statistics weacker, as we saw in the $N_j = 8$ case.

For completeness, I'll show also the $N_j = 14$ case.

N_{cov}^{set}	g_{NL}	$\sigma_{g_{NL}}$
30	$(3.0 \pm 6.9) \cdot 10^3$	$(8.68 \pm 0.07) \cdot 10^5$
60	$(-0.7 \pm 7.4) \cdot 10^3$	$(8.40 \pm 0.07) \cdot 10^5$
90	$(-1.0 \pm 7.4) \cdot 10^3$	$(8.33 \pm 0.07) \cdot 10^5$
120	$(-1.8 \pm 6.7) \cdot 10^3$	$(8.29 \pm 0.07) \cdot 10^5$
150	$(-2.4 \pm 7.2) \cdot 10^3$	$(8.27 \pm 0.07) \cdot 10^5$
200	$(-2.6 \pm 6.5) \cdot 10^3$	$(8.24 \pm 0.07) \cdot 10^5$
250	$(-2.9 \pm 7.0) \cdot 10^3$	$(8.22 \pm 0.07) \cdot 10^5$
300	$(-2.8 \pm 7.4) \cdot 10^3$	$(8.21 \pm 0.07) \cdot 10^5$
350	$(-2.9 \pm 7.3) \cdot 10^3$	$(8.20 \pm 0.07) \cdot 10^5$

and the result of the fit on $\sigma_{g_{NL}}$

$a/10^5$	$b/10^5$
15.5 ± 1.3	8.15 ± 0.02

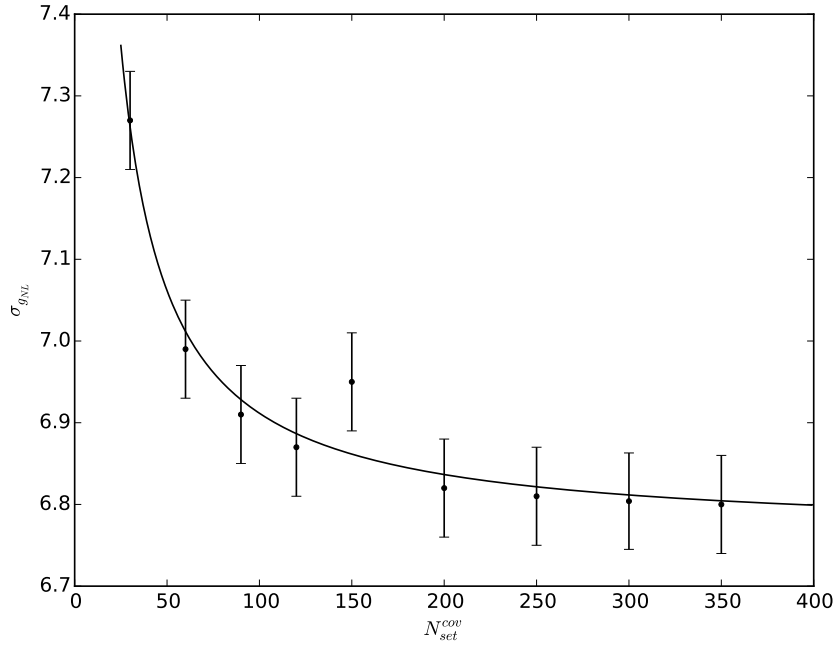

Figure 10.10: Hyperbole fit over the set of $\sigma_{g_{NL}}$ resulting from the analysis performed with $N_j = 12$.

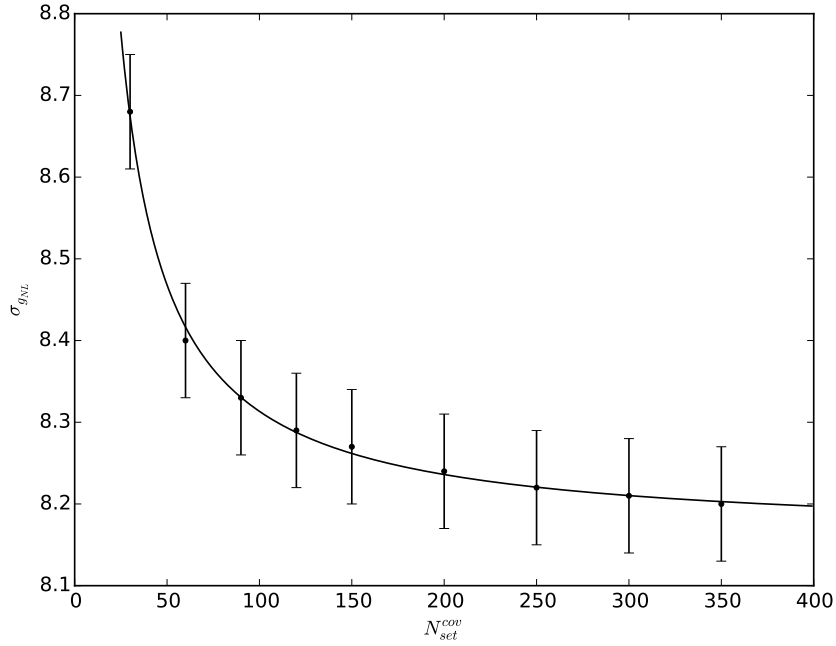

Figure 10.11: Hyperbole fit over the set of $\sigma_{g_{NL}}$ resulting from the analysis performed with $N_j = 14$.

It is important to note how the differences between points and curve in fig. 10.11 almost vanished. We can say that, increasing the number of the bins brought improvement in measuring the exact values of $\sigma_{g_{NL}}$, although the values are too high for a statistics that claims to be optimal.

10.3.2 Non-Gaussian Analysis

Let's what happens when the analysis is performed over non-Gaussian maps, with $g_{NL}^{input} = 3 \cdot 10^5$. For all the four cases, I used the covariance matrix calculated with the highest number of trispectra among the others, $N_{cov}^{set} = 350$,

N_j	g_{NL}	$\sigma_{g_{NL}}$
8	$(1.1 \pm 0.4) \cdot 10^5$	$(7.2 \pm 0.4) \cdot 10^5$
10	$(1.0 \pm 0.5) \cdot 10^5$	$(7.2 \pm 0.5) \cdot 10^5$
12	$(1.2 \pm 0.5) \cdot 10^5$	$(7.2 \pm 0.5) \cdot 10^5$
14	$(1.8 \pm 0.5) \cdot 10^5$	$(8.2 \pm 0.5) \cdot 10^5$

Taking $g_{NL} \pm \sigma_{g_{NL}}$, I found values consistent with the input. Unfortunately, the standard error of the mean shows that there is something wrong, since the values of g_{NL} are not even close to g_{NL}^{input}. As we will see later, this is due to the low resolution of the analyzed maps. In fact, increasing the resolution make the statistic stronger, as we will see further on. Furthermore, the values of $\sigma_{g_{NL}}$ are consistent with the respectively values in the Gaussian case, although higher, likely because the number of trispectra used in the analysis is quite small (only 299 trispectra).

10.4 Validation at Planck Resolution, $N_{side} = 2048$

As I have validated the code at low resolution, is time to see what happens when N_{side} is high enough to be compared with the most recent data. I'm referring to the Planck mission, which measured the sky at a very how resolution, parametrized by the HEALPix number $N_{side} = 2048$. A recent paper (Regan et al. 2015) shown that the Needlet trispectrum is suboptimal at $N_{side} = 512$, I wanted to see if this is due to the estimator itself or the low resolution maps used in that analysis.

In order to simulate the outcomes of a real experiment, I added noise and multiplied by a mask the map involved in the analysis. Furthermore, since the evaluation of trispectrum at such high resolution is really time expensive, I could analyze only one set of data using only one choice of N_j. The choice fell to $N_j = 12$, since the maximum multipole increased by a factor 10 with respect to the $N_{side} = 128$ case, $l_{max} = 1600$.

Variance was evaluated over 5000 maps. Then the non-Gaussian trispectra followed the same choices of the $N_{side} = 128$ case. Were calculated 200 sets of trispectra, 150 for the covariance matrix, 50 for the g_{NL} estimation. The number of trispectra per set is 320.

As the resolution increased, the Cramer-Rao bound decreases. thus, now $\sigma_{g_{NL}}$ has to be compared to approximately $7 \cdot 10^4$.

Thus, the results of the analysis of Gaussian maps are:

N_{cov}^{set}	g_{NL}	$\sigma_{g_{NL}}$
30	$(9.7 \pm 0.9) \cdot 10^3$	$(1.302 \pm 0.009) \cdot 10^5$
60	$(9.6 \pm 0.9) \cdot 10^3$	$(1.259 \pm 0.009) \cdot 10^5$
90	$(9.7 \pm 0.9) \cdot 10^3$	$(1.244 \pm 0.009) \cdot 10^5$
120	$(9.5 \pm 0.9) \cdot 10^3$	$(1.237 \pm 0.009) \cdot 10^5$
150	$(9.4 \pm 0.9) \cdot 10^3$	$(1.232 \pm 0.009) \cdot 10^5$

Again, the estimates of g_{NL} and $\sigma_{g_{NL}}$ are shown with the Gaussian fit error that, again, is of the same order of magnitude of the statistical standard one. Surprisingly, although $g_{NL} \pm \sigma_{g_{NL}}$ is perfectly consistent with zero, so doesn't the estimates of the exact value of the mean, as you can see in the second column of the above table. This could be due to an inefficient number of Needlet scales applied in the analysis. This is an aspet that deserve further studies in the next future.

Let's see how does the $\sigma_{g_{NL}}$ behaves. Immediately, the high difference between $\sigma_{g_{NL}}$ estimated and the Cramer-Rao bound stand out, as the former is almost twice the latter. This is another clue of an inefficient number of Needlet scales. But we can extrapolate a great information about the distribution of the $\sigma_{g_{NL}}$. Fitting the latter with the usual hyperbolic function, one obtains

$a/10^5$	$b/10^5$
2.61 ± 0.02	1.2150 ± 0.0003

Thus the lowest value $\sigma_{g_{NL}}$ can reach is $1.215 \cdot 10^5$. But we can use the hyperbolic fit for another, noble reason. In fact, if the hyperbolic fit performed over the first three points give results consistent with the fit done over 5 points, it means that 3 points are sufficient to constrain the curve, thus we can resolve the computational time issue by estimating a low number of trispectra, computing the covariance matrix and then fitting the hyperbole over the results. The results of the 3-points fit is

$a/10^5$	$b/10^5$
2.60 ± 0.02	1.2153 ± 0.0005

consistent with the 5-point cases. That's indeed a great news, thus only 90 sets of trispectra are required to perform a confident hyperbolic fit on the data. But, how much confident is the fit over 5-points? In order to test the goodness of the fit, I added 2 more points

N_{cov}^{set}	g_{NL}	$\sigma_{g_{NL}}$
40	$(9.6 \pm 0.9) \cdot 10^3$	$(1.280 \pm 0.009) \cdot 10^5$
50	$(9.6 \pm 0.9) \cdot 10^3$	$(1.267 \pm 0.009) \cdot 10^5$

so the fit is now performed over 7 points, improving its statistics

$a/10^5$	$b/10^5$
2.60 ± 0.01	1.2150 ± 0.0003

The results are perfectly consistent with the above ones. Again, I wanted to test what happens if I consider only the first points, so I fit the hyperbole over the first 4 points, obtaining

$a/10^5$	$b/10^5$
2.63 ± 0.01	1.2155 ± 0.0007

i.e. another consistent results. Thus, 60 sets are well enough in order to estimate the covariance matrix, since it is possible to constrain the value of $\sigma_{g_{NL}}$ when more trispectra are involved, by simply fitting an hyperbole. This is actually the main results of my work on the CMB trispectrum. The results of the fitting are shown in fig. 10.12

Let's see what happens when the non-Gaussian maps ($g_{NL}^{input} = 3 \cdot 10^5$) are analyzed. What we get is

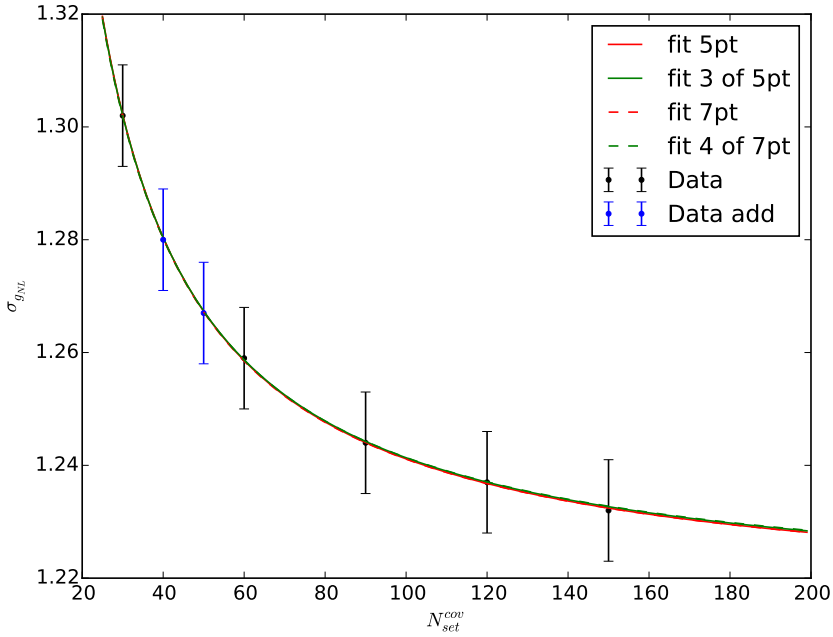

Figure 10.12: Hyperbole fit over the set of $\sigma_{g_{NL}}$ resulting from the analysis performed at $N_{side} = 2048$. The four fitted hyperbole are indistinguishable one from another, confirming by eye the consistency among them.

N_{cov}^{set}	g_{NL}	$\sigma_{g_{NL}}$
350	$(3.0 \pm 0.1) \cdot 10^5$	$(2.4 \pm 0.1) \cdot 10^5$

that is, the value of g_{NL} is perfectly constrained, although the $\sigma_{g_{NL}}$ is almost double the same statistics in the Gaussian case. This is due probably to the low number of noon-Gaussian maps involved in the analysis, just like the $N_{side} = 128$ cases, where the non-Gaussian $\sigma_{g_{NL}}$ was higher than in the Gaussian case.

I can conclude by saying that the validation of the trispectrum estimator at Planck resolution needs some more work, but the road started with this work is absolutely the right one.

Future directions

In this work I showed how to apply angular bispectrum and Needlet trispectrum estimator to LSS and CMB data respectively.

First I showed a series of known results about polyspectra, starting from their mathematical definitions, their physical description, the estimators and their variance. We saw how the angular spectrum is related to the amplitude of fluctuations, while bispectrum and trispectrum are the harmonic counterpart of the 3-point and 4-point correlation function, thus parameterizing the excess probability of finding three or four point in a give triangular or quadrilateral configuration respectively. Although they should be evaluated through an ensemble average, I showed how the simple average over the m's, describing the orientation of the multipoles, is sufficient to get the right form of the statics, even if this introduce an effect of cosmic variance, i.e. the variance of the estimator is greater at lower multipoles where the number of m's is small.

Then, I reviewed the standard cosmology and, through the Hot Big Bang model flaws, I introduced the Inflation Theory. The dynamics during inflation is due to a scalar field, the inflaton, which energy density dominates the energy content of the Universe. Fluctuation of the Inflaton were inherited by matter and radiation, seeding the Large Scale Structure of galaxies and the Cosmic Microwave Background radiation that we see today.

In Part II, I reviewed the linear and non-linear perturbation theory, in order to show how non-Gaussianity is introduced in the matter field through non-linear evolution. Then I showed how it is possible to treat a 3-dimensional field like the matter distribution as a spherical field, by convolving by a selection function and integrating along the line of sight, that is, the z coordinate. Angular estimator are re-introduced and their binned form is showed together with their binned variance. Hence, I showed the results of the analysis in which measurements of four sets of 125 spherical shell taken from a comoving simulation of 3-dimensional matter distribution. In particular, the comparison between the prediction and the estimated C_l and bispectrum. The comparison showed how the binning in redshift and the photometrical error affects our measurements, in particular the higher the bin the closer prediction and measurements are. At cost of power loss at each scale. Besides, the higher the photometrical error the worst the comparison is, and it is quite expected. In the bispectrum case, I applied the Scoccimarro-Couchman and Gil-Marin fitting formulae to compute the non-linear bispectrum, showing that the latter is better than the former. Furthermore, I found that one of the effect of the photo-z error is to destroy the collapsed triangle configuration, bring the power of the measured bispectrum to zero. In the next future, will be of interest apply the angular bispectrum estimator to real data with the aim of constrain cosmological parameters and compare

the results with predicted one. In this way, we will understand how well the bispectrum estimator can help in removing the parameter degeneracy that affect the LSS physics.

In Part III, I first reviewed the non-Gaussianity in the photon distribution, showing how we can parametrize it by means of Bardeen's potential through the non-Gaussian parameter f_{NL} and g_{NL}. Then I show the Spherical Needlet Wavelet framework and the property that makes them the closest system to the orthonormal basis of the Spherical Harmonics and the best wavelet system in order to constrain parameters from spherical distribution with missing parts. Thus, the Needlet trispectrum is derived, take advantage of the Wick theorem that allows to write a polynomial with the lowest avariance among the other polynomials of the same order. I then implemented the Needlet trispectrum in a `C++` code that was then validated. I showed that the Needlet trispectrum estimator is suboptimal, but it will be helpful in constraining g_{NL} and validates the results of other g_{NL} estimators. Furthermore, I showed that the main problem in the g_{NL} estimation is the convergence of the covariance matrix but that with a hyperbolic fit, it is possible to constrain the behavior of the converged covariance matrix even with low trispectra. Besides, the estimation of g_{NL} over non-Gaussian maps showed that the maps resolution is important, since with low-resolution maps I found impossible to recover the input g_{NL}. It will need more analysis to understand the behavior of the Needlet trispectrum with high resolution maps and different number of scales than the one used in this work. Anyway, the results of the Needlet trispectrum estimator applied to real data maps should appear in the next release of Planck papers.

The results of this work are of great importance at the light of the ongoning and the forthcoming surveys like Planck, the Dark Energy Survey (DES) and Euclid, and could help in the analysis of the physics of the odiern and the primordial Universe.

Appendices

APPENDIX A

Groups, Irreducible Representations and Diagram Formula

A.1 Basic definitions of Groups

A *group* is a set which an associative binary operation which admits an identity element and an inverse:

Definition 6. *A group G is a set of elements, denoted as $g_1, g_2 \ldots$ with a binary operation $\circ$ such that the following properties are verified:*

- $(g_1 \circ g_2) \in G$ *for all* $g_1, g_2 \in G$*;*
- *there exists an identity elemente* $e \in G$ *such that* $g \circ e = g = e \circ g$ *for alla* $g \in G$*;*
- *for all* $g \in G$*, there exist an inverse element* $g^{-1} \in G$ *such that* $g \circ g^{-1} = g^{-1} \circ g = e$*;*
- *for all* $(g_1, g_2, g_3) \in G$*, the equality* $(g_1 \circ g_2) \circ g_3 = g_1 \circ (g_2 \circ g_3)$ *is satisfied.*

The set of non-singular $n \times n$ matrices with real coefficients is called the *real general linear group*, and it is denoted by $GL(n, \mathbb{R})$. The binary operation is the ordinary matrix multiplication and the identity element is the identity matrix of order n, I_n.

Among the subgroups of $GL(n, \mathbb{R})$ of crucial importance is the *Special orthogonal group* $SO(n) = \{A : A \in GL(n, \mathcal{R}), A'A = I_n \text{ and } |\mathrm{A}| = 1\}$. The group $SO(3)$ admits a geometrical representation as the set of vector rotations in $\mathbb{R}^3$.

Let V be a normed vector space over $\mathbb{C}$. A *representation* of G in V is a homomorfism π, from G into $GL(V)$, such that the mapping $G \times V \to V : (g, v) \to \pi(g)(v)$ is continuous. Given a representation (π, V), we say that a subset $A \subseteq V$ is π-invariant if, for every $v \in A$ and for every $g \in G$, one has that $\pi(g)v \in A$. A representation π of G in V is *irreducible* if the only closed π-invariant subspace of V are $\{0\}$ and V. The Peter-Weyl Theorem states that, given a topological compact group G,

- the complete set of unitary irreducible representation of G is a countable family of $d_l \times d_l$ matrix-valued function $\pi^l, l = 1, 2, \ldots$, with d_l denoting the dimension of π_l;
- the matrix coefficients $\{\sqrt{d_l}\pi^l_{uv}(.)\}$ form an orthonormal basis of the space $L^2(G)$ of square integrable function with respect the Haar measure.

The Peter-Weyl Theorem is the theoretical cornerstone round which we shall define such fundamental objects as *Wigner matrices*, *spherical harmonics* and *Clebsh-Gordan coefficients*.

A.2 Wigner's D matrices

Wigner-s D matrices $\{D^l(g) : l = 0, 1, \ldots\}$ provide a complete set of irreducible matrix representation for $SO(3)$, having dimension $(2l + 1) \times (2l + 1)$ for every $l = 0, 1, 2, \ldots$. Several properties of these objects can be derived as special cases of the general theory of representations for compact groups.

- *Additive property*, for all $g_1, g_2 \in SO(3)$ we have

$$D^l(g_1)D^l(g_2) = D^l(g_1 g_2), \quad l = 0, \frac{1}{2}, 1, \ldots, \tag{A.1}$$

  which is equivalent to the relation

$$D^l_{mn}(g_1 g_2) = \sum_{k=-l}^{l} D^l_{mk}(g_1) D^l_{kn}(g_2). \tag{A.2}$$

- *Orthonormality*,

$$\int_{SO(3)} D^l_{mn}(g) D^{l'*}_{m'n'}(g) dg = \frac{1}{2l+1} \delta^{l'}_{l} \delta^{m'}_{m} \delta^{n'}_{n}; \tag{A.3}$$

- *Unitary Properties*,

$$\sum_m D^l_{mn}(g) D^{l*}_{mn}(g) = \delta^{n'}_{n} \tag{A.4}$$

A.3 Spherical Harmonics

Let us now introduce the class of *Spherical Harmonics*

$$\{Y_{lm}(\theta, \phi) : l = 0, 1, 2, \ldots; \ m = -l, \ldots, l\}, \tag{A.1}$$

where $(\theta, \phi) \in S^2$ labelled a point on the sphere S^2.

Definition 7. *For every integer $l = 0, 1, 2, \ldots$, and every $m = -l, \ldots, l$, the spherical harmonics function of index (l, m), written $Y_{lm} : S^2 \to \mathbb{C}$, is defined as the mapping*

$$Y_{lm}(\theta, \phi) = \sqrt{\frac{2l+1}{4\pi} \frac{(l-m)!}{(l+m)!}} P_{lm}(cos\theta) e^{im\phi}, \quad m \geq 0, \tag{A.2}$$

$$Y_{lm}(\theta, \phi) = (-1)^m Y^*_{l-m}(\theta, \phi), \quad m < 0, \tag{A.3}$$

where $\{P_{lm}\}$ denotes the associated Legendre function, which is defined in terms of the Legendre Polynomials $\{P_l : l = 0, 1, \ldots\}$ by the equation

$$P_{lm}(\mu) = (= 1)^m (1 - \mu^2)^{m/2} \frac{d^m}{d\mu^m}, \quad l = 0, 1, 2, \ldots, \ m = 0, 1, \ldots, l \tag{A.4}$$

In the sequel, for all $x \in S^2$, we shall write

$$Y_{lm}(x) := Y_{lm}(\theta, \phi), \quad x = (\sin\theta\cos\phi, \sin\theta\sin\phi, \cos\theta). \tag{A.5}$$

We shall also use $d\sigma(x)$ to denote the *Lebesgue measure* on the sphere, which, in spherical coordinates is defined as

$$d\sigma := \sin\theta d\theta d\phi. \tag{A.6}$$

The properties of Spherical Harmonics as listed below:

- *Orthonormality*: for all l, l', m, m'

$$\int_{S^2} Y_{lm}(x) Y^*_{l'm'}(x) d\sigma(x) = \delta_l^{l'} \delta_m^{m'}. \tag{A.7}$$

  As a consequence of orthonormality property we have,

$$\int_{S^2} Y_{lm}(x) d\sigma x = \sqrt{4\pi} \int_{S^2} Y_{lm}(x) Y^*_{00}(x) d\sigma(x) = 0. \tag{A.8}$$

- *Symmetry*: for all $x \in S^2$

$$Y^*_{lm}(x) \equiv (-1)^m Y_{lm}(\theta, -\phi); \tag{A.9}$$

- *Addition Formula*: for all $x \in S^2$

$$\sum_{m=-l}^{l} Y^*_{lm}(x) Y_{lm}(y) = \frac{2l+1}{4\pi} P_l(\langle x, y\rangle), \tag{A.10}$$

  where P_l is the lth Legendre polynomial and $\langle \cdot, \cdot \rangle$ denotes the usual Euclid inner product. In particular, for all $x \in S^2$,

$$\sum_{m=-l}^{l} Y_{lm}(x) Y^*_{lm}(x) = \frac{2l+1}{4\pi}. \tag{A.11}$$

- *Behaviour under rotations*: for all $g \in SO(3)$ and all $x \in S^2$, denote by $g \cdot x$ the position of x after the rotation g. Then, one has

$$Y_{lm}(g \cdot x) = \sum_{m'} D^l_{m'm}(g^{-1}) Y_{lm'}(x). \tag{A.12}$$

The most important results for the Spherical Harmonics is the *Peter-Weyl Theorem on the sphere*

Theorem 3. *For all complex-valued functions $f \in L^2(S^2)$ that is, the space of the square integrable functions on the sphere, we have*

$$f(x) = \sum_{lm} a_{lm} Y_{lm}(x), \tag{A.13}$$

where

$$a_{lm} := \int_{S^2} f(x) Y^*_{lm}(x) d\sigma(x) = (-1)^m a^*_{l-m}. \tag{A.14}$$

A.4 The Clebsh-Gordan coefficients

We can exploit the family of Wigner D matrices $\{D^l : l = 0, 1, 2, \dots$ in order to build alternative (reducible) representation, either by forming the tensor product $\{D^{l_1} \otimes D^{l_2} : l_1, l_2 \geq 0$ or by considering direct sums $\{\oplus_{l=|l_2 l_1|}^{l_2+l_1} D^l : l_1, l_2 \geq 0$, whose dimension is $(2l_1 + 1)(2l_2 + 1) \times (2l_1 + 1)(2l_2 + 1)$. There exist a unitary matrix $C_{l_1 l_2}$, known as a *Clebsh-Gordan matrix*, such that

$$\{D^{l_1} \otimes D^{l_2}\} = C_{l_1 l_2} \{\oplus_{l=|l_2-l_1|}^{l_1+l_2} D^l\} C_{l_1 l_2}^*. \tag{A.1}$$

The matrix $C_{l_1 l_2}$ is a $\{(2l_1 + 1)(2l_2 + 1) \times (2l_1 + 1)(2l_2 + 1)\}$ block matrix, whose block, of dimension $(2l_2 + 1) \times (2l + 1)$, are customarily denoted by $C^l_{l_1(m_1)l_2}$. The elements of the lth block are indexes by m_2 over rows and m over columns. More precisely

$$C_{l_1 l_2} = [C^{l.}_{l_1(m_1)l_2.}]_{m_1=-l_1,\dots,l_1;\ l=|l_2-l_1|,\dots,l_2+l_1}, \tag{A.2}$$

$$C^{l.}_{l_1(m_1)l_2.} = [C^{lm}_{l_1 m_1 l_2 m_2}]_{m_2=-l_2,\dots,l_2;\ m=-l,\dots,l}. \tag{A.3}$$

The *Clebsh-Gordan coefficients* for $SO(3)$ are defined as the collection $\{C^{lm}_{l_1 m_1 l_2 m_2}\}$ of the elements of the unitary matrices $C_{l_1 l_2}$.

These coefficients have developed in the quantum theory of angular momentum, where $C^{lm}_{l_1 m_1 l_2 m_2}$ represents the probability amplitude that two particles with total angular momentum l_1, l_2 and momentum projection on the z-axis m_1 and m_2 are couples to form a system with total angular momentum l and projection m (Liboff (1999)). Their use in the analysis of isotropic random fields is much more recent (Hu (2001)).

A.5 Diagram Formula

A *Diagram gamma* of order $(l_1, \dots, l_p)$ is a set of points $\{(j, l) : 1 \leq j \leq p, 1 \leq l \leq l_j\}$ called *vertices* and a partition of these points into pairs

$$\{((j, l), (k, s) : 1 \leq l \leq k \leq p; 1 \leq l \leq l_j; 1 \leq s \leq l_k)\}, \tag{A.1}$$

called edges, such that no vertex can be linked with itself $(j, l) \neq (k, s)$, and each pair (a, b) appears in one and only one edge. Then, if the integer $l_1 + \dots + l_p$ is odd, no diagram can be written. We denote by $\Gamma(l_1, \dots, l_p)$ the set of all diagrams of order $(l_1, \dots, l_p)$.

We say that a diagram has a *flat edge* if there is at least one pair $((i, j), (i', j'))$ such that $i = i'$. We write Γ_F for the set of diagrams hving at least one flat edge, and Γ_{F^*} for the collection of all diagrams with no flat edges. Then, the *Diagram Formula* is expressed by the following proposition:

Proposition 6. *Let $(Z_1, \dots, Z_p)$ be a centered Gaussian vector, and let $\gamma_{ij} = \langle [Z_i Z_j] \rangle$, $i, j = 1, \dots, p$, where $\langle \cdot \rangle$ denotes the ensemble average, be its covariance. Let $H_{l_1}, \dots, H_{l_p}$ be Hermite polynomials of degrees $l_1, \dots, l_p \geq 1$ respectively. Then,*

$$\langle [\Pi_{j=1}^p H_{l_j}(Z_j)] \rangle = \sum_{G \in \Gamma_{F^*}(l_1,\dots,l_p)} \Pi_{1 \leq i \leq j \leq p} \gamma_{ij}^{\eta_{ij}(G)} \tag{A.2}$$

where, for each diagram G, $\eta_{ij}(G)$ is the exact number of edges between the ith row and the jth row of the diagram G.

The Diagram Formula provides a combinatorial description of the moments associated with Hermite transformations of Gaussian random variables (Peccati & Taqqu (2010); Shyraev (1984)).

Bibliography

Abbott, L. F. & Wise, M. B. 1984, Nuclear Physics B, 244, 541

Acquaviva, V., Bartolo, N., Matarrese, S., & Riotto, A. 2003, Nuclear Physics B, 667, 119

Alishahiha, M., Silverstein, E., & Tong, D. 2004, *Phys. Rev. D*, 70, 123505

Andersen, T., W. 2003, An Introduction to Multivariate Statistical Analysis (New York: Wiley)

Antoine, J.-P. & Vandergheynst, P. 1998, Journal of Mathematical Physics, 39, 3987

Arkani-Hamed, N., Creminelli, P., Mukohyama, S., & Zaldarriaga, M. 2004, jcap, 4, 1

Armendáriz-Picón, C., Damour, T., & Mukhanov, V. 1999, Physics Letters B, 458, 209

Arroja, F., Mizuno, S., & Koyama, K. 2008, *JCAP*, 8, 15

Babich, D., Creminelli, P., & Zaldarriaga, M. 2004, *JCAP*, 8, 9

Baldi, P., Kerkyacharian, G., Marinucci, D., & Picard, D. 2006, ArXiv Mathematics e-prints

Baldi, P. & Marinucci, D. 2006, Statistics & Probability Letters, 77, 490

Baldi, P., Marinucci, D., & Varadarajan, V. S. 2007, Electronic Communications in Probability, 12, 291

Bardeen, J. M. 1980, *Phys. Rev. D*, 22, 1882

Barreiro, R. B., Hobson, M. P., Lasenby, A. N., et al. 2000, *Mon. Not. R. Astron. Soc.*, 318, 475

Bartolo, N., Fasiello, M., Matarrese, S., & Riotto, A. 2010, *JCAP*, 8, 8

Bartolo, N., Komatsu, E., Matarrese, S., & Riotto, A. 2004, *Phys. Rep.*, 402, 103

Battefeld, T. & Easther, R. 2007, *JCAP*, 3, 20

Borovkov, A. 1998, Mathematical Statistics (Gordon and Breach Science Publishers)

Buchalter, A., Kamionkowski, M., & Jaffe, A. H. 2000, *Astrophys. J.*, 530, 36

Budavári, T., Connolly, A. J., Szalay, A. S., et al. 2003, *Astrophys. J.*, 595, 59

Byrnes, C. T. & Choi, K.-Y. 2010, Advances in Astronomy, 2010

Byrnes, C. T., Sasaki, M., & Wands, D. 2006, *Phys. Rev. D*, 74, 123519

Cabella, P., Hansen, F. K., Liguori, M., et al. 2006, *Mon. Not. R. Astron. Soc.*, 369, 819

Cabré, A., Fosalba, P., Gaztañaga, E., & Manera, M. 2007, *Mon. Not. R. Astron. Soc.*, 381, 1347

Cammarota, V. & Marinucci, D. 2013, ArXiv e-prints

Casaponsa, B., Barreiro, R. B., Curto, A., Martínez-González, E., & Vielva, P. 2011, *Mon. Not. R. Astron. Soc.*, 411, 2019

Cayón, L., Martínez-González, E., Argüeso, F., Banday, A. J., & Górski, K. M. 2003, *Mon. Not. R. Astron. Soc.*, 339, 1189

Cayón, L., Sanz, J. L., Martínez-González, E., et al. 2001, *Mon. Not. R. Astron. Soc.*, 326, 1243
Chen, X. 2005, *Phys. Rev. D*, 72, 123518
Chen, X. 2010, Advances in Astronomy, 2010
Chen, X., Hu, B., Huang, M.-x., Shiu, G., & Wang, Y. 2009, *JCAP*, 8, 8
Chen, X., Huang, M.-x., Kachru, S., & Shiu, G. 2007, *JCAP*, 1, 2
Chen, X. & Wang, Y. 2010a, *Phys. Rev. D*, 81, 063511
Chen, X. & Wang, Y. 2010b, *JCAP*, 4, 27
Cheung, C., Fitzpatrick, A. L., Kaplan, J., Senatore, L., & Creminelli, P. 2008, Journal of High Energy Physics, 3, 14
Choi, K.-Y., Hall, L. M. H., & van de Bruck, C. 2007, *JCAP*, 2, 29
Cohen-Tannoudji, C., Diu, B., & Laloe, F. 1977, Quantum Mechanics (New York: Wiley)
Coles, P. & Lucchin, F. 2002, Cosmology: The Origin and Evolution of Cosmic Structure, Second Edition
Cramér, H. 1946, Mathematical Methos of Statistics (Princeton University Press)
Crocce, M., Cabré, A., & Gaztañaga, E. 2011, *Mon. Not. R. Astron. Soc.*, 414, 329
Crocce, M., Fosalba, P., Castander, F. J., & Gaztañaga, E. 2010, *Mon. Not. R. Astron. Soc.*, 403, 1353
Curto, A., Martínez-González, E., & Barreiro, R. B. 2011, *Mon. Not. R. Astron. Soc.*, 412, 1038
Curto, A., Martínez-González, E., & Barreiro, R. B. 2012, *Mon. Not. R. Astron. Soc.*, 426, 1361
Curto, A., Martínez-González, E., Mukherjee, P., et al. 2009, *Mon. Not. R. Astron. Soc.*, 393, 615
Dodelson, S. 2003, Modern Cosmology (Academic Press)
Dodelson, S. & Schneider, M. D. 2013, *Phys. Rev. D*, 88, 063537
Donzelli, S., Hansen, F. K., Liguori, M., Marinucci, D., & Matarrese, S. 2012, *Astrophys. J.*, 755, 19
Durrer, R. 2008, The Cosmic Microwave Background (Cambridge University Press)
Dvali, G., Gruzinov, A., & Zaldarriaga, M. 2004, *Phys. Rev. D*, 69, 083505
Elsner, F. & Wandelt, B. D. 2009, apjs, 184, 264
Enqvist, K. & Nurmi, S. 2005, *JCAP*, 10, 13
Enqvist, K., Nurmi, S., Taanila, O., & Takahashi, T. 2010, *JCAP*, 4, 9
Enqvist, K. & Sloth, M. S. 2002, Nuclear Physics B, 626, 395
Enqvist, K. & Takahashi, T. 2008, *JCAP*, 9, 12
Falk, T., Rangarajan, R., & Srednicki, M. 1993, *Astrophys. J. Lett.*, 403, L1
Fergusson, J. R., Regan, D. M., & Shellard, E. P. S. 2010, ArXiv e-prints
Fosalba, P., Gaztañaga, E., Castander, F. J., & Manera, M. 2008, *Mon. Not. R. Astron. Soc.*, 391, 435
Freeden, W. & Schreiner, M. 1998, Orthogonal and Non-orthogonal Multiresolution Analysis, Scale Discrete and Exact Fully Discrete Wavelet Transform on the Sphere
Fry, J. N. 1994, Physical Review Letters, 73, 215
Gangui, A., Lucchin, F., Matarrese, S., & Mollerach, S. 1994, *Astrophys. J.*, 430, 447
Geller, D. & Mayeli, A. 2007a, ArXiv e-prints
Geller, D. & Mayeli, A. 2007b, ArXiv e-prints
Geller, D. & Mayeli, A. 2009, ArXiv e-prints
Gil-Marín, H., Wagner, C., Fragkoudi, F., Jimenez, R., & Verde, L. 2012, *JCAP*, 2, 047

Górski, K. M., Hivon, E., Banday, A. J., et al. 2005, *Astrophys. J.*, 622, 759
Guth, A. H. 1981, *Phys. Rev. D*, 23, 347
Guth, A. H. & Pi, S.-Y. 1982, Physical Review Letters, 49, 1110
Hamed, N. A., Cheng, H. S., Luty, M. A., & Mukohyama, S. 2004, Journal of High Energy Physics, 5, 74
Hartlap, J., Simon, P., & Schneider, P. 2007, *Astron. Astrophys.*, 464, 399
Hashimoto, I., Mizuno, S., & Yokoyama, S. 2016a, *Phys. Rev. D*, 94, 043532
Hashimoto, I., Taruya, A., Matsubara, T., Namikawa, T., & Yokoyama, S. 2016b, *Phys. Rev. D*, 93, 103537
Havin, V. & Joricke, B. 1994, The Uncertainty Principle in Harmonic Analysis (Springer-Verlag)
Hinshaw, G., Weiland, J. L., Hill, R. S., et al. 2009, *Astrophys. J. Suppl.*, 180, 225
Hodges, H. M., Blumenthal, G. R., Kofman, L. A., & Primack, J. R. 1990, Nuclear Physics B, 335, 197
Hu, W. 2001, *Phys. Rev. D*, 64, 083005
Hu, Y. & Yan, J.-a. 2009, Acta Mathematicae Applicatae Sinica, English Series, 25, 399
Hubble, E. 1929, Proceedings of the National Academy of Science, 15, 168
Kaiser, N. 1987, *Mon. Not. R. Astron. Soc.*, 227, 1
Kaiser, N. 1992, *Astrophys. J.*, 388, 272
Kaiser, N. 1998, *Astrophys. J.*, 498, 26
Kaligotla, S. & Lototsky, S. V. 2010, ArXiv e-prints
Kamionkowski, M., Kosowsky, A., & Stebbins, A. 1997, *Phys. Rev. D*, 55, 7368
Kofman, L. 2003, ArXiv Astrophysics e-prints
Kogo, N. & Komatsu, E. 2006, *Phys. Rev. D*, 73, 083007
Komatsu, E. 2002, ArXiv Astrophysics e-prints
Komatsu, E. & Spergel, D. N. 2001, *Phys. Rev. D*, 63, 063002
Komatsu, E., Wandelt, B. D., Spergel, D. N., Banday, A. J., & Górski, K. M. 2002, *Astrophys. J.*, 566, 19
Lan, X. & Marinucci, D. 2008a, ArXiv e-prints
Lan, X. & Marinucci, D. 2008b, Electronic Journal of Statistics, 2, 332
Langlois, D., Renaux-Petel, S., Steer, D. A., & Tanaka, T. 2008a, Physical Review Letters, 101, 061301
Langlois, D., Renaux-Petel, S., Steer, D. A., & Tanaka, T. 2008b, *Phys. Rev. D*, 78, 063523
Latham, D. W. & da Costa, L. A. N., eds. 1991, Astronomical Society of the Pacific Conference Series, Vol. 15, Large-scale structures and peculiar motions in the universe
Liboff, R. 1999, Introductory Quantum Mechanics (Addison-Wesley)
Liddle, A. R. & Lyth, D. H. 2000, Cosmological Inflation and Large-Scale Structure
Limber, D. N. 1953, *Astrophys. J.*, 117, 134
Lyth, D. H. & Riotto, A. A. 1999, *Phys. Rep.*, 314, 1
Lyth, D. H. & Rodríguez, Y. 2005, Physical Review Letters, 95, 121302
Ma, Z., Hu, W., & Huterer, D. 2006, *Astrophys. J.*, 636, 21
Maldacena, J. 2003, Journal of High Energy Physics, 5, 13
Marinucci, D. 2005, ArXiv Mathematics e-prints
Marinucci, D. 2006, Annals of Statistics, 34, 1
Marinucci, D. & Peccati, G. 2010, Journal of Multivariate Analysis, 101, 77
Marinucci, D. & Peccati, G. 2011, Random Fields on the Sphere, London Mathematical

Society Lecture Note Series (Cambridge University Press)
Marinucci, D., Pietrobon, D., Balbi, A., et al. 2008, *Mon. Not. R. Astron. Soc.*, 383, 539
Marinucci, D. & Wigman, I. 2012, ArXiv e-prints
Matarrese, S., Verde, L., & Heavens, A. F. 1997, *Mon. Not. R. Astron. Soc.*, 290, 651
Mayeli, A. 2008, ArXiv e-prints
McEwen, J. D., Vielva, P., Wiaux, Y., et al. 2007, Journal of Fourier Analysis and Applications, 13, 495
Messiah, A. 1962, Quantum Mechanics (Amsterdam, Netherlands: North-Holland)
Mollerach, S. 1990, *Phys. Rev. D*, 42, 313
Narcowich, F., Petrushev, P., & Ward, J. 2006a, Journal of Functional Analysis
Narcowich, F. J., Petrushev, P., & Ward, J. D. 2006b, SIAM J. Math. Analysis, 38, 574
NASA. 2012, WEBSITE: WMAP Goals: Spectrum Fluctuations
NASA. 2014, WEBSITE: WMAP Big Bang Concepts
Padmanabhan, N., Schlegel, D. J., Seljak, U., et al. 2007, *Mon. Not. R. Astron. Soc.*, 378, 852
Peccati, G. & Taqqu, M. 2010, Wiener Chaos: Moments, Cumulants and Diagrams. A Survey with Computer Implementation (Springer-Verlag)
Peebles, P. J. E. 1980, The large-scale structure of the universe
Peiris, H. V., Komatsu, E., Verde, L., et al. 2003, *Astrophys. J. Suppl.*, 148, 213
Penzias, A. A. & Wilson, R. W. 1965, *Astrophys. J.*, 142, 419
Pezzotta, A., de la Torre, S., Bel, J., et al. 2016, ArXiv e-prints
Pietrobon, D., Balbi, A., & Marinucci, D. 2006, *Phys. Rev. D*, 74, 043524
Pietrobon, D., Cabella, P., Balbi, A., et al. 2010, *Mon. Not. R. Astron. Soc.*, 402, L34
Pietrobon, D., Cabella, P., Balbi, A., de Gasperis, G., & Vittorio, N. 2009, *Mon. Not. R. Astron. Soc.*, 396, 1682
Pilo, L., Riotto, A., & Zaffaroni, A. 2004, Physical Review Letters, 92, 201303
Planck Collaboration, Adam, R., Ade, P. A. R., et al. 2016a, *Astron. Astrophys.*, 594, A1
Planck Collaboration, Ade, P. A. R., Aghanim, N., et al. 2014a, *Astron. Astrophys.*, 571, A1
Planck Collaboration, Ade, P. A. R., Aghanim, N., et al. 2014b, *Astron. Astrophys.*, 571, A15
Planck Collaboration, Ade, P. A. R., Aghanim, N., et al. 2014c, *Astron. Astrophys.*, 571, A16
Planck Collaboration, Ade, P. A. R., Aghanim, N., et al. 2014d, *Astron. Astrophys.*, 571, A22
Planck Collaboration, Ade, P. A. R., Aghanim, N., et al. 2014e, *Astron. Astrophys.*, 571, A24
Planck Collaboration, Ade, P. A. R., Aghanim, N., et al. 2016b, *Astron. Astrophys.*, 594, A17
Planck Collaboration, Ade, P. A. R., Aghanim, N., et al. 2016c, *Astron. Astrophys.*, 594, A13
Potts, D., Steidl, G., & Tasche, M. 1996, in in Advanced Topics in Multivariate Approximation (World Scientific), 1–154
Rao, C. 1945, Bulletin of the Calcutta Math. Soc., 37, 81
Regan, D., Gosenca, M., & Seery, D. 2015, *JCAP*, 1, 013
Renaux-Petel, S. 2009, *JCAP*, 10, 12
Riess, A. G., Filippenko, A. V., Challis, P., et al. 1998, *Astron. J.*, 116, 1009
Rudjord, Ø., Hansen, F. K., Lan, X., et al. 2009, *Astrophys. J.*, 701, 369
Rudjord, Ø., Hansen, F. K., Lan, X., et al. 2010, *Astrophys. J.*, 708, 1321

Ryden, B. 2003, Introduction to cosmology
Sachs, R. K. & Wolfe, A. M. 1967, *Astrophys. J.*, 147, 73
Salopek, D. S. & Bond, J. R. 1990, *Phys. Rev. D*, 42, 3936
Santos, M. G., Heavens, A., Balbi, A., et al. 2003, *Mon. Not. R. Astron. Soc.*, 341, 623
Sasaki, M., Väliviita, J., & Wands, D. 2006, prd, 74, 103003
Scoccimarro, R. & Couchman, H. M. P. 2001, *Mon. Not. R. Astron. Soc.*, 325, 1312
Scoccimarro, R., Sefusatti, E., & Zaldarriaga, M. 2004, *Phys. Rev. D*, 69, 103513
Scodeller, S., Rudjord, Ø., Hansen, F. K., et al. 2011, *Astrophys. J.*, 733, 121
Seery, D. & Lidsey, J. E. 2007, *JCAP*, 1, 8
Sefusatti, E., Crocce, M., & Desjacques, V. 2012, *Mon. Not. R. Astron. Soc.*, 425, 2903
Sefusatti, E. & Komatsu, E. 2007, *Phys. Rev. D*, 76, 083004
Seljak, U. & Zaldarriaga, M. 1997, Physical Review Letters, 78, 2054
Senatore, L., Smith, K. M., & Zaldarriaga, M. 2010, *JCAP*, 1, 28
Senatore, L. & Zaldarriaga, M. 2011, *JCAP*, 1, 3
Shyraev, A. 1984, Probability (Springer-Verlag)
Silverstein, E. & Tong, D. 2004, *Phys. Rev. D*, 70, 103505
Simpson, F., Peacock, J. A., & Simon, P. 2009, *Phys. Rev. D*, 79, 063508
Smidt, J., Amblard, A., Byrnes, C. T., et al. 2010, *Phys. Rev. D*, 81, 123007
Smith, K. M., Senatore, L., & Zaldarriaga, M. 2015, ArXiv e-prints
Smith, S., Rocha, G., Challinor, A., et al. 2004, *Mon. Not. R. Astron. Soc.*, 352, 887
Smoot, G. F., Bennett, C. L., Kogut, A., et al. 1992, *Astrophys. J. Lett.*, 396, L1
Spergel, D. N. & Goldberg, D. M. 1999, *Phys. Rev. D*, 59, 103001
Starobinskiĭ, A. A. 1985, Soviet Journal of Experimental and Theoretical Physics Letters, 42, 152
Starobinsky, A. A. 1982, Physics Letters B, 117, 175
Suyama, T. & Yamaguchi, M. 2008, *Phys. Rev. D*, 77, 023505
Takahashi, R., Sato, M., Nishimichi, T., Taruya, A., & Oguri, M. 2012, *Astrophys. J.*, 761, 152
Taylor, A., Joachimi, B., & Kitching, T. 2013, *Mon. Not. R. Astron. Soc.*, 432, 1928
The Planck Collaboration. 2006, ArXiv Astrophysics e-prints
Verde, L., Heavens, A. F., & Matarrese, S. 2000a, *Mon. Not. R. Astron. Soc.*, 318, 584
Verde, L., Wang, L., Heavens, A. F., & Kamionkowski, M. 2000b, *Mon. Not. R. Astron. Soc.*, 313, 141
Vernizzi, F. & Wands, D. 2006, *JCAP*, 5, 19
Wang, L. & Kamionkowski, M. 2000, *Phys. Rev. D*, 61, 063504
Wiaux, Y., McEwen, J. D., & Vielva, P. 2007, Journal of Fourier Analysis and Applications, 13, 477
Wick, G. C. 1950, Physical Review, 80, 268
Yadav, A. & Wandelt, B. 2008a, in APS April Meeting Abstracts, J8001
Yadav, A. P. S. & Wandelt, B. D. 2008b, Physical Review Letters, 100, 181301
Yadav, A. P. S. & Wandelt, B. D. 2010, Advances in Astronomy, 2010

List of Publications

Refereed publications

Planck 2015 results. I. Overview of products and scientific results, Planck Collaboration, 2016, A&A, 594, A1, doi:10.1051/0004-6361/201527101
Planck 2015 results. XVII. Constraints on primordial non-Gaussianity, Planck Collaboration, 2016, A&A, 594, A17, doi:10.1051/0004-6361/201525836

Publications in preparation

Needlet Trispectrum of the CMB - Title yet TBD, Troja, A., Renzi, A., 2017
Angular Bispectrum of the LSS - Title yet TBD, Troja, A., Sefusatti, E., Crocce, M., 2017

Publications in conference proceedings

The Needlet CMB Trispectrum, Troja A., Donzelli S., Maino D., Marinucci D., 2014, Statistical Challenges in 21st Century Cosmology, 306, 48, doi:10.1017/S1743921314010813

Acknowledgments

Dopo tre anni, un mucchio di lavoro e molte difficoltà, è difficile trovare le parole giuste per ringraziare tutti quelli che mi sono stati vicini e che mi hanno dato una mano nei vari momenti che si sono succeduti. La paura di non riuscire ad elencarli tutti fa tremare le mie dita mentre digito sulla tastiera, ma proverò comunque a fare un elenco quanto più esaustivo possibile.

Innanzitutto, è giusto ringraziare le persone che mi hanno accompagnato in questo percorso dal punto di vista puramente universitario. Parto giustamente dal mio relatore, Davide, che pur non essendo pienamente coinvolto nell'ambito scientifico del mio lavoro, ha dimostrato di credere nelle mie potenzialità, permettendomi di svolgere il lavoro in piena autonomia e libertà. Non posso dimenticare i suoi consigli puntuali, che mi hanno aiutato molto più di una volta a trovare la strada verso soluzioni che sembravano lontane.

Un ringraziamento speciale va a Emiliano, che ha incarnato non solo la figura del supervisore ma anche quella del mentore (volente o nolente). Scientificamente e umanamente è stata una figura molto importante all'interno del mio percorso e penso che, davvero, non avrei potuto avere di meglio.

Non posso dimenticare, ne tantomeno ho il desiderio di farlo, Simona, la causa di tutto questo. Lei che mi ha aperto la strada verso un mondo nuovo coi suoi modi gentili e la sua pazienza illimitata. Anche se questa volta non ha dovuto sudare sette camicie per correggere un inglese scritto coi piedi, non posso non ringraziarla davvero, di tutto cuore.

Dei tre anni e mezzo necessari per arrivare fin qui, uno l'ho passato quasi interamente a Barcellona, dove sono stato accolto e trattato oltre che bene da una persona splendida come Martin, a cui non posso che dedicare un ringraziamento sentito per avermi seguito. A lui, come a tutte le persone che mi hanno accompagnato in quel periodo, fuori e dentro l'istituto di ricerca, *muchas gracias!*

La mia avventura a Milano mi ha permesso di conoscere gente splendida che, in un modo o nell'altro, mi ha aiutato ad andare avanti nel mio percorso. Nicoletta, Benedetta, Maria Chiara, Daniele, Marco mi hanno aiutato a comprendere meglio il mondo nel quale mi trovavo, per cui un grazie sentito.

A causa dei suoi innumerevoli consigli, le chiacchierate non richieste e il continuo supporto, sempre col sorriso, avevo promesso che avrei scritto un ringraziamento grosso così negli acknowledgments a lui dedicato, ma per motivi di pagina, il massimo che posso fare è questo. Grazie mille

M A U R I Z I O T O M A S I

Non dimentichiamo i miei compagni di mille avventure. Avventure permalose probabilmente, ma sempre simpatiche! Cristian, Sabrina, Jacopo e Federico! A voi un grazie speciale per aver arricchito le mie giornate con sorrisi spensierati e allegre discussioni!

E dove mettere Merate! Andrea, il cui unico difetto è la fede calcistica, Faizan colore dell'oro e cuore grande come tutta la Brianza e Matteo, che non saprò mai se sono riuscito a conquistare oppure no.

Penso che sia giusto, a questo punto, dedicare un sentito ringraziamento a tutte le persone che mi sono state vicine, nel bene e nel male. A partire dalla mia famiglia, che non ha mai smesso di credere in me nonostante tutte le difficoltà subite e provocate. Tutti i coinquilini che mi hanno tenuto compagnia, Ciccio, Alessandro, Miguel, Hugo, Jesus, Dau, Anderson, Diana e Antonio. I *veri amici del nord*, che mi hanno accolto come se ci conoscessimo da una vita e non mi hanno mai fatto sentire solo, Andrea, Nicholas, Lorenzo, Cesco, Adele, Agnese, Giulia e ancora tanti altri che elencare renderebbe davvero tutto troppo lungo! Le *Cose Raffinate* che, nonostante mi abbiano visto meno di quanto avrei voluto, sono state sempre presenti: Ivan, grazie al quale l'eurocrazia non ha più segreti per me, Gabriele, con la sua musica e la sua passione e la sua smisurata voglia di fare, Jacopo, collega, coinquilino, ma soprattutto amico. E non scordiamo il mio avvocato preferito, Domenico, con cui condivido più che una passione. Infine gli amici di una vita. Quelli che senza di loro non saresti dove sei adesso, ma allo stesso tempo non vorresti starci pur di stare con loro. Domenico, Ivan, Francesco, Alessandro. Questo ringraziamento speciale è per voi.

Ma più di tutti ringrazio lei, Veronica, la piccola Nica che ha saputo cogliere l'essenza del mio essere, nella salute e nella malattia, cercando in ogni modo di aiutarmi a giungere a quell'Io tanto cercato e mai pienamente compiuto. Le parole non sono abbastanza, ma intanto ne uso due. Grazie, davvero.